Shape memory alloys as an effective tool to damp oscillations: Study of the fundamental parameters required to guarantee technological applications.

V. Torra[1], A. Isalgue[2], M. Sade[3,4] and F.C. Lovey[3]

[1]PRG, Villarroel 162, E-08036 Barcelona, Catalonia, Spain (retired from UPC, Applied Physics Department, E-08034, Barcelona, Catalonia)
E-mail: vtorra_1@yahoo.com

[2]Applied Physics Dept., Polytechnic University of Catalonia, E-08034 Barcelona, Catalonia, Spain
E-mail: antonio.isalgue@upc.edu

[3]Metal Physics Group, Centro Atómico de Bariloche and Instituto Balseiro 8400 S.C. de Bariloche, RN., Argentina.
E-mail: lovey@cab.cnea.gov.ar

[4]CONICET, Argentina
E-mail: sade@cab.cnea.gov.ar

Number of manuscript pages (A4): 82
Number of figures: 53
Number of tables: 6
Short running title: **Shape memory alloys for dampers**

The name and full mailing address of the corresponding author.
Prof. Dr. Vicenç Torra
Applied Physics Dept., Polytechnic University of Catalonia (retired)
Address: PRG, Villarroel 162, E-08036 Barcelona, Catalonia, Spain
Phone number: +34 93 4542258 FAX number: +34 93 5334060
E-mail: vtorra_1@yahoo.com

ABSTRACT

The SMA was studied for their macroscopic application in damping for Civil Engineering. The study is a synthesis and includes an outline of the models required for the SMA simulation and some case studies using the Finite Element Analysis methods. This work is an overview that focuses in the mitigation of the oscillations in structures induced by earthquakes, and for a reduction of the oscillations amplitude in stayed cables under the action of rain, wind or traffic. The analysis needs the required conditions for each application determining the working conditions. The study includes the number of working cycles, the temperature effects and the cooling actions and, for instance, the action of the cycling frequency. The main target relates the appropriateness of the SMA for each purpose, and the suitability of the SMA device is always experimentally guaranteed. Furthermore, the applicability of the obtained results for SMA and the practical behavior of the SMA dampers were studied in international facilities. The paper includes appropriate suggestions for a correct preparation of the SMA dampers. This work outlines the effects of stress and temperature aging in NiTi, describes the particular structural effects between 18R and 6R, introduces a first attempt in the dynamic properties of the CuAlBe single crystals and summarizes some recent suggestions for damping using SMA.

Keywords: martensitic transformation, phase transitions, hysteretic behavior, damping, static and dynamic evolutions, SMA, CuAlBe, damping, aging, fatigue, thermomechanical treatment.

PART ONE

The Martensitic Transformation (MT) is the origin of the unique properties of Shape Memory Alloys (SMA) [1-2]. MT is a first-order phase transition between metastable phases with hysteresis. The transformation takes place with small displacements of the atoms and without any change in the positions of the neighboring atoms: atomic order is conserved in the transformation. The transformation can be induced by temperature or by external forces, such as traction or compression. In temperature-induced transformations, Ms (martensite start) denotes the starting temperature. The Mf (martensite finish) temperature determines the end of the transformation and As and Af denote the austenite start and the austenite finish temperatures, respectively. This part was devoted to general contents and properties of the SMA appropriate for damping of oscillations. In particular, for reduction of oscillations appeared in Civil Engineering structures.

1. Introduction

Interest in Shape Memory Alloys has been increasing over the last three decades because of the potential applications of SMA. This interest has recently been enhanced by the inclusion of standard courses on smart materials in the core engineering curriculum at many universities all over the world. Thus far, SMA have mainly been applied to the health field. For example, the classical NiTi alloys [3-4] and the newly developed Ti-based alloys have been attracting interest because their biological compatibility in practical situations. NiTi practically works as an innocuous substance in the human body. In recent years, a focused axis of Ti-based alloys (without Ni) has been in continuous research by the Miyazaki group in Tsukuba [5-8]. Several SMA applications are on the market, such as stents, chirurgical tools, orthodontic wires or bolts and elements for bone or teeth reconstruction. The number of useful and efficient applications has also increased in other fields, for instance, in automotive and consumer electronics, but still comprises a relatively small number. Several applications may be found in references [9-11].

In recent years, the potential application of shape-memory alloys (SMA) in damping devices for civil structures has attracted increasing interest. These damping devices are used to smooth oscillations, which can be produced by earthquakes, winds, rain, traffic, etc., in buildings and bridges. The pseudo-elastic effect and the hysteresis cycle that are associated with the martensitic transformation in SMA have been proposed as a mechanism for converting the mechanical energy of the oscillations into heat. Several researchers are working on using SMA in damping devices for civil engineering [12-20]. Details can be found in the reviews of R. DesRoches (Atlanta, USA) and M. Dolce (Basilicata, Italy) [21-23]. Re-centering is a problem that is encountered with the use of bearings in base-isolated buildings, for instance. Different applications have been proposed for the positive re-centering action of the pseudo-elastic effect in various papers. For example, a mixture of martensitic and pseudo-elastic bars has been considered to facilitate damping and re-centering actions.

Recently, SMA have been studied as passive elements in damping for civil structures that use the hysteresis cycle. In this case, the SMA converts the mechanical energy of the oscillations of the structure into heat that is dissipated to the surroundings. However, dampers that have been built 20 years ago have exhibited several potential difficulties[1]. When SMA dampers are to be used in

[1] Poor information is available on the NiTi dampers that were installed on the roof of the Basilica of "San Francesco d'Assisi" (in Assisi, Perugia, Italy) by the ISTECH project [28]. Ambient temperature effects on the SMA [29] are not considered to affect SMA behavior. The temperature differences between sunny summer days and cold winter days for the ceramic roof of the Basilica are probably 60 or 70 K. Using a value of 6.3 MPa/K for the Clausius-Clapeyron coefficient, the total change in the stress for a 70 K is approximately 450 MPa. Thus alloy remains in the martensite

mitigation of earthquake effects, they need to be guaranteed for their appropriate requirements. For instance the immediate list of requirements associated to the application need to be evaluated:

-the damper length need to remain invariant

The effects associated to progressive deformation on cycling need to be minimized or avoided via the appropriate training of thermo-mechanical treatment.

-self-heating not relevant or well determined.

The self-heating needs to be evaluated or quantified. The heat dissipated by the hysteresis, goes abroad by transmission to surroundings but other part increases the temperature of the specimen. The associated increase of the stress can be relevant by the action of the Clausius-Clapeyron thermodynamic equation.

-dampers with re-centering availabilities are desirable.

The pseudo-elasticity with their transformation and retransformation processes recovers their initial position. On cycling with SMA dampers the structure oscillates with reduced amplitude and recovers the original position or re-centering availability.

-oscillation's interval (earthquake + replica's): 4 to 6 minutes

The fatigue-life of the material needs to be, at least, that overcomes 1000 working cycles (the length of time of one earthquake is close to 1 minute plus N aftershocks or replicas represent (1 + N minutes). With a frequency oscillation of 1 Hz a satisfactory behavior up to 1000 working cycles was required.

-time scale, for instance, several decades between quakes.

It's necessary that the eventual time effects induced by diffusion (i.e., by precipitate accretion) or by evolution of the atomic order was avoided or quantitatively determined to be non-relevant for the expected times.

-high number of daily and yearly (summer-winter) temperature wave.

The action of 10 or more summer-winter yearly temperature (inside the house) effects would not dangerously modify the required properties of the SMA or their working capacity (the changes of transformation temperature have to be non-relevant).

The requirements for the use of SMA to damping of stayed cables are similar to the ones required in damping of earthquake effects, but the number of cable oscillations is large in comparison with the requirements for earthquakes. A strong storm can last 3 days and the number of oscillations is highly relevant. For instance, in the Iroise bridge (1 and 3 Hz of natural frequencies) or in St Nazaire bridge (18 Hz) the number of working cycles is close to 0.8 or to 4 millions. On the other hand, the time between the installation of SMA and the storms would be relatively short and remains under one year. In mitigation of the oscillations in stayed cables for bridges the main requirements are:

-the damper length need to remain invariant

The SMA creep effect needs to be minimized via appropriate training and/or thermo-mechanical treatment, as with the case of damping earthquakes.

-self-heating not relevant.

Use of short deformation (1-2 %) induces reduced temperature wave on the SMA with low stress effects, compared with the case of damping earthquakes. Analysis of series of cycles with intermediate stops corresponding to several pauses between storms is also necessary.

-dampers with recoverable behavior (re-centering availabilities) are positive.

The pseudoelastic behavior permits that the damper tracks the cable without relevant plastic (permanent) deformation, as in the case of damping earthquakes.

-larger fatigue life overcoming several millions of working cycles

---

phase in the winter and in the austenite phase in the summer without transformation, which can result in crash from the increased stress and a reduced fracture-life at higher stresses of the alloy.

In one powerful storm, in 3 or 4 days the expected number of working cycles is a function of the cable main frequencies but, in general, overcomes one million of cycles. Use of lower deformation permits an appropriate fracture-life. The requirement is different that in the case of damping earthquakes.

-daily temperature wave and, eventually, direct sunlight actions

The "room temperature" effects need to be evaluated at least for one year of continuous action. Usually, the damper might be in a less thermally protected environment compared to the damping of earthquakes, so daily temperature wave will be more relevant.

-direct rain (water) over the damper without corrosion or oxidation

The NiTi is the recommended alloy with appropriate properties that avoids the corrosive actions. The case of damping earthquake effects can be done most of the times with more protected dampers (in interior situation) and then Cu alloys might be also used.

As a consequence, the material properties have to be checked to accomplish with the requirements in each case. The many relevant parameters that must be tuned to the practical requirements of the desired applications should be carefully analyzed. These parameters can be divided into those affected by material conditions and those associated with the mechanical and the coupled thermo-mechanical aspects of the application.

- *Material condition parameters:* The pseudo-elastic behavior of a given alloy very often depends strongly on the internal state of the material. The following material characteristics should be considered: the microstructure, including the grain size, the homogeneity of the composition, precipitates, crystallographic texture, defects as dislocations, stacking faults, etc. In addition, long time aging at the working conditions can eventually change the transformation temperatures and affect phase stabilization because of atomic diffusion.

- *Mechanical parameters:* The mechanical aspects of SMA are mainly related to the hysteresis width that is associated with the pseudo-elastic cycle and the amount of the recoverable pseudo-elastic strain. The greater the hysteresis area, the larger is the dissipated energy of each cycle, which increases the efficiency of the damping device. Pseudo-elastic cycles have also generally been observed to evolve on cycling. The transformation and/or retransformation stress changes with cycling, which can diminish the recoverable pseudo-elastic strain. An asymptotic steady-state behavior can be obtained in many cases that are a useful state for the applications reviewed here. The number of cycles to fracture near the working conditions is also a fundamental parameter.

- *Coupled thermo-mechanical parameters* Critical stresses induce the pseudo-elastic effect as a function of the working temperature in accordance with the Clausius-Clapeyron (CC) equation [24-27]. The latent heat of the martensitic transformation in turn depends on the applied transformation stress. Thus, the specimen temperature depends on the conditions affecting the dissipation/absorption of the latent heat during the transformation/retransformation. These conditions are governed by the following parameters: the deformation rate, the dissipation medium of the surroundings (for example, air in a convection process), the specimen size, and so on. The pseudo-elastic behavior and the damping capacity are governed by the CC equation in two ways. One mechanism involves significant changes in the specimen temperature from either the self-heating phenomenon and/or changes in the working temperature. These two concomitant processes change the transformation stresses. Consequently, the stiffness and the resonance frequencies of structures with an integrated SMA damping device depend on the specimen temperature. The second mechanism is related to the shape of the hysteresis cycle, whereby the hysteresis area is itself dependent on the various aforementioned conditions. The considerable complexity of all these coupled phenomena dictates that the real behavior of SMA elements must be experimentally tested to fulfill the requirements of the respective application.

Hysteresis in the temperature and the stress appears because of intrinsic actions between inter-phases and dislocations, at grain boundaries and in precipitates. In stress-induced hysteresis, the internal interactions contribute to the hysteresis width. The macroscopic temperature changes produced by local temperature modifications by the absorbed / released latent heat must be accounted for. The dissipated power in the sample, which is associated with the cycling rate, heat transfer and convection also critically influence the sample temperature values. Therefore, the stress required for interface displacement changes and modifies the hysteresis width. Other specific changes may be caused by the temperature or stress aging. Figure 1 shows a temperature-induced transformation for NiTi as an example. The investigated temperature span was from 323 K to 193 K; the measured hysteresis was affected by calorimetric uncertainty and the value of temperature rate. Figure 1 A show the effect of aging at 373 K for several months for a parent to R-phase transformation: this case corresponds to approximately 20 K/year of aging. Figure 1 B shows hysteresis cycling between 100 and 300 K. The "two" hysteresis widths roughly correspond to the two consecutive NiTi transitions. The first transition that occurred in cooling the aforementioned example corresponded to the transformation from parent to R and later from R to martensite. In cooling, the uncertainty in the base line was highly significant, so that the results were purely qualitative. In heating, the two peaks overlapped, which produced minimal deformation of the integrated line.

Figure 2 shows the hysteresis cycles in stress-strain coordinates for poly-crystalline CuAlBe (A) and commercial NiTi wire (B-C) of two diameters. The investigated NiTi wire samples had lengths of 118.8 mm and 1005 mm and diameters of 2.46 and 0.5 mm, respectively. The figure shows the effects on cycling by the NiTi wire diameter. "Similar" behavior was observed for CuAlBe (A, with ε=3.14 %, ϕ= 3.4 mm and 30 cycles at 0.05 Hz) and the NiTi (B) samples after 100 cycles at 0.01 Hz. In contrast, the behavior of the thinner wire after cycling at 16 min/cycle was macroscopically different, with "flat" transformation and retransformation curves (flag-shaped mechanical cycles on stress-strain, fig 2 C). Only after a large number of faster cycles and a higher deformation strain (i.e., up to 9 %), did the hysteretic shape of the NiTi sample for the thin wire (0.5-mm diameter) resemble that of the thick wire (2.46-mm diameter).

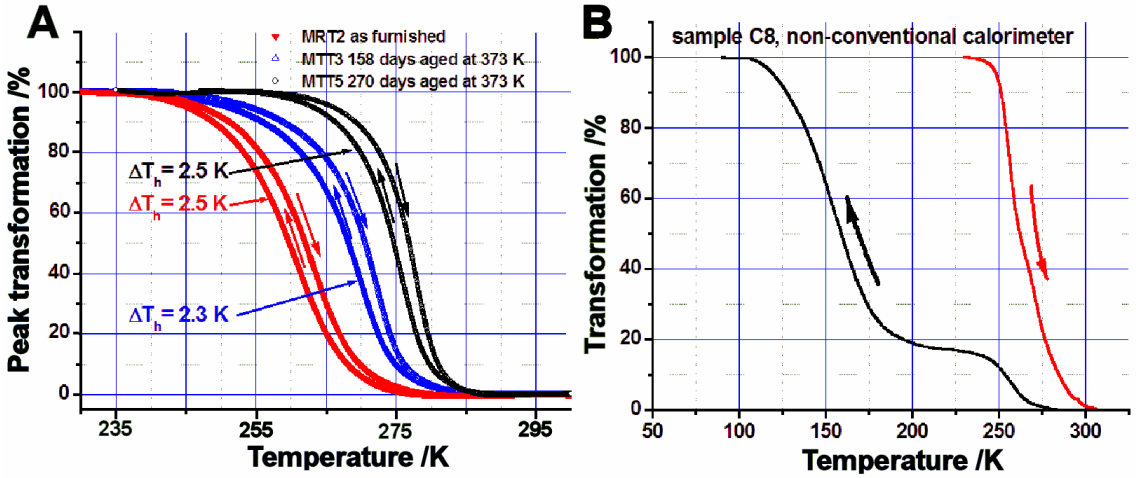

Figure 1. Hysteresis cycles determined from calorimetric measurements by temperature induced transformation of NiTi alloy (parent to R-phase)). Left: thinner hysteresis cycle in NiTi alloy for parent to R-phase transformation. Right: larger histeresis width in NiTi expanded temperature scale (from 100 to 300 K).

Let us consider in greater detail SMA applications that reduce oscillations that are induced by an earthquake in structures or are produced by wind, rain or traffic in stayed cables for bridges. The following aspects should be considered when investigating the mitigation of the effects of earthquakes in civil structures. Only several hundred cycles of a good response of the SMA damper can be expected during an earthquake [30]. A "good" response is defined as a reproducible

hysteresis cycle and a constant pseudo-elastic deformation without martensite "creep." The structure may stand for several decades between earthquakes: therefore, the material must be stable under aging at ambient temperatures over this period. Aging at ambient temperatures may eventually change the transformation temperature (i.e., Ms), as has been well established for CuAlZn, which degrades the SMA damping capacity.

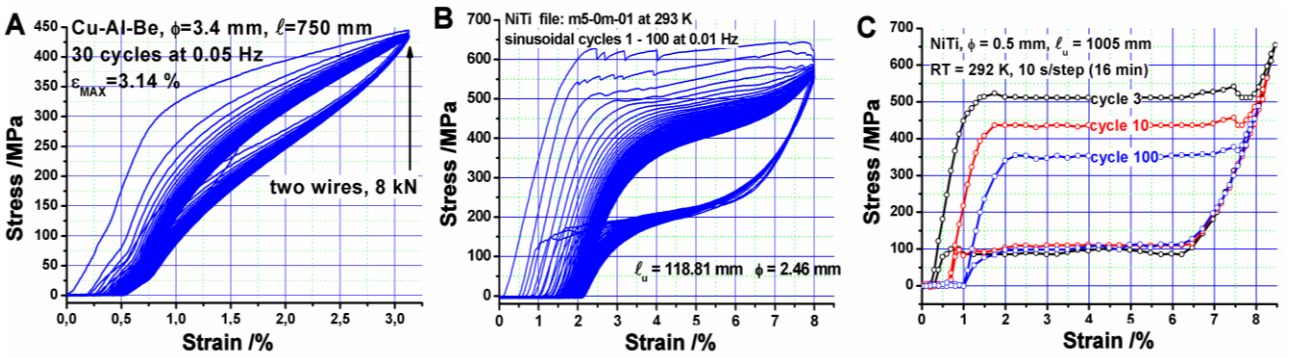

Figure 2. Hysteresis cycles in stress – strain coordinates. A: CuAlBe, homogenization 10 min. B: NiTi (2.46 mm of diameter, cycles 1 to 100). C: NiTi (0.50 mm of diameter, cycles 3, 10 and 100)

Therefore, intrinsic changes at the atomic scale caused by years of aging should be prevented. Such stabilization has been achieved with Cu-based alloys. In particular, the eventual effects of the minor actions of stress aging must be prevented, and the long-term actions induced by seasonal temperature effects must remain within the working domain. The SMA length should not evolve spontaneously with time and with the several hundreds of working cycles that are typically induced by the mitigation of oscillations. Thus, appropriate thermo-mechanical treatment should completely suppress SMA creep. SMA creep is induced by plastic deformation and/or by the stabilized martensite that is created in cycling. The effect of creep is to increase the damper length, which partially suppresses the damping effect for lower amplitude oscillations. Moreover, SMA applications require that self-heating effects and other concomitant temperature effects (from latent heat or room temperature variations), as governed by the Clausius-Clapeyron thermodynamic equation, do not completely modify the expected behavior of the SMA damper.

The damping requirements for stayed cables in bridges are more stringent than for earthquake mitigation. The number of working cycles is much higher in strong storms (e.g., the northwest winds on West European coasts, typhoons, tropical cyclones or hurricanes). A strong storm lasting three or four days can induce over a million oscillations at frequencies of several Hz. The external temperature conditions are also more severe. In earthquakes, the dampers are usually situated inside a building, where they find also protection regarding corrosion. The daily/yearly temperature wave is smoothed. The dampers in bridges are exposed to the direct action of the weather, including wind and rain: a minimum of a yearly inspection of the installed SMA dampers is required, despite the seeming inconvenience involved.

In general, "the barriers to the expanded use of SMAs include the high cost, lack of clear understanding of thermo-mechanical processing, dependency of properties on temperature, and difficulty in machining" [21]. The practical objective of this paper is to determine the requirements of the two cases of damping using SMA in civil structures (family houses and stayed cables for bridges). The core of the analysis is the study of the basic conditions that ensure that the behavior of the application is appropriate and guaranteed. Both cases for the dampers use the hysteresis cycle, but each case requires different physical conditions for the alloys. Mitigating earthquake effects requires that the SMA damper behavior be guaranteed for at least several years or decades during which the structure is at rest. A key condition for reducing the oscillation amplitude of stayed cables for bridges is a high SMA fracture-life.

The paper comprises six parts. Part One is a general introduction. Part Two reviews recent results in the literature on the use of representative models. The older Falk model [31] describes the martensitic phase transition based on the Helmholtz free energy. Several authors have made fundamental developments in this field: K. Tanaka (Japan) [32], B. Ranieki (Poland) [33], C. Lexcellent (France) [34] and Z. Moumni (France) [35]. There are also representations that are oriented to practical requirements and applications in chirurgical devices, which are directly connected with the phenomenological measurements and applications usually via Finite Element Analysis: C. Brinson (USA) [36], F. Auricchio (Italy) [37], and P. Terriault (Canada) [38].

Part Three discusses the damping of oscillations in stayed cables for bridges. In this case, the eventual wetting of the alloy disqualifies the Cu-based alloy solution because of corrosion problems, and motivates a mesoscopic study of NiTi. Part Four addresses the seismic mitigation of family houses by a CuAlBe alloy. Part Three and Part Four are dedicated to the analysis of the required "training" needed to produce the appropriate behavior. Each part studies the properties necessary for each application: A) long time aging near room temperatures; B) aging under temperature and, eventually, stress; C) cycling frequency effects on the hysteresis; and D) self-heating and forced convection from fan effects. A simulation of SMA behavior, which agreed with experimental measurements performed at experimental facilities, is also briefly discussed.

Part Five presents a brief analysis of other alloys in single crystals or in poly-crystals, which have potential damping properties. Two different types of alloys have recently been proposed for damping applications. One alloy is a Fe-based alloy, which exhibits pseudo-elastic behavior and is potentially highly useful because of its welding capability and low price. The other type of alloy is part of a group of single-crystal alloys (NiMnGa or NiFeGa) and exhibits inter-martensitic transformations in loading (i.e., two consecutive transformations are observed). This behavior allows higher deformations (up to 10 or 15 %) and a higher conversion of mechanical energy to heat. The appearance of two phases is a relatively frequent phenomenon in SMA studies. For instance, in CuAlZn, a classical Cu-based alloy, the first transformation occurs between the body centered cubic (bcc) structure and 18R, while the second transformation occurs between 18R and 6R (or fct). Part Five also presents relevant recoverable dynamic changes in CuAlBe single crystals and a potentially useful two-phase transformation. Dynamic changes in CuAlZn were observed more than 20 years ago [39]. Recently, faster changes have been discovered in CuAlBe single crystals. More recently, SMA foams of CuZnAl have also been considered for damping applications. Part Six presents conclusions and general remarks. The paper ends with acknowledgements and references.

PART_TWO

This part briefly describes the SMA models used in simulations to study the requirements of the applications described in this paper. A representative model is needed to link the measurements to the simulated analysis. The simulation focuses on the experimental behavior of the structure with and without a SMA damper. The Finite Element Analysis (FEA) of a damped structure requires a subroutine to represent SMA behavior. Several types of FEA software for simulation are available for free or can be purchased, e.g., Abaqus ANSYS, Open Sees or others. Parts Three and Four of this paper provide examples of the incorporation of SMA behavior in ANSYS by an USERMAT routine.

Each practical application requires an appropriate SMA model to efficiently simulate and predict the behavior of the structure. In the examples considered, SMA application is based on the pseudo-

elastic state of the system. The application assumes small SMA material changes in working, which correspond to well-controlled creep and an appropriate working domain in the summer to winter temperature range. At the predictive level, the representative models are used for practical simulations of SMA behavior, avoiding sophisticated treatments. General SMA models are typically used to describe complex 3-dimensional SMA behavior involving traction, compression and torsion. This work has the more limited objective of developing models that are satisfactorily and capture the actual behavior of the structure and the SMA. The model complexity is significantly reduced in comparison to that required to model the deployment of a "compressed" stent under the action of the temperature inside the human body. In general, the complexity of formulation and the difficulties encountered by the models depend on the requisite level of macroscopic description. The main objective may be the description of the behavior of a SMA spring, for example. Such a description has to capture the evolution of the material properties on cycling, the internal temperature effects induced by the external temperature changes and/or the self-heating induced by latent heat effects on the behavior of springs and stents. Here, we are mainly interested in relatively simple pseudo-elastic models with internal loops in one dimension.

Three general approaches are typically used in the representative SMA models. The first approach uses macro-scale models based on a thermodynamic formalism of the Gibbs or Helmholtz energies, in which the basic alloy parameters are extracted from experimental data. Such descriptions generally use one (or more) internal state variables, such as the martensite volume fraction. The representation includes the temperature and the strain. Further details can be found in refs. [31-32, 40] for classical materials, [41-42], and [43-44], which comprise more recent studies for SMA.

The second approach is micromechanical. These micro-macro models consider a working domain inside the sample that is averaged up to the macro-scale. This approach requires knowledge of the kinetics of the phase change and the interface motion, including the interactions between the different variants in a small material domain [45-46].

The third approach involves a limited phenomenological methodology in a 1-dimensional representation. SMA behavior is predicted by considering the pseudo-elastic work of SMA in structures. The inputs for the models and the associated equations are the Clausius-Clapeyron equation (to transform the temperature to stress) and a fit to the stress-strain hysteretic cycles, along with reasonable criteria to appropriately represent internal loops with zero or moderate pre-stresses and cycling frequencies. A phenomenological approach requires experimental data obtained under conditions similar to those of the desired application. In our case, the mean temperature, the cycling frequency and the appropriate deformation range were required.
Only a brief outline of the first and second approaches is presented here. The third approach, which was developed for use in simulations for the damping of stayed cables and of oscillations induced in structures by an earthquake, is reviewed in Parts Three and Four, respectively.

2.1. The macroscopic approach

The macroscopic approach only uses (macroscopic) thermodynamic and continuum mechanical variables: a microscopic description of the detailed processes is not given. However, some fundamental mechanisms may be introduced within this framework. Models always use some phenomenology. Falk [31] developed a representation based on the Helmholtz free energy to describe the evolution of the free energy from a one phase system to two phases, i.e., linked to the coexistence between the parent and martensite. Tanaka [41] developed thermo-mechanical constitutive equations together with an equation for the kinetics of the martensitic transformation. The phase transformation was satisfactorily simulated using the Helmholtz free energy with a dissipative term. Tanaka [47] described the deformation change in terms of the variation of three factors: the stress, the temperature and the martensite volume fraction.

For one-directional tension, the macroscopic approach relates the martensite volume fraction to the temperature and the stress. The thermodynamic potentials are strictly reversible; thus, modeling hysteretic behavior requires the inclusion of an ad hoc dissipative term for loading and a similar term for unloading. In both cases, the relations contain material constants such as the characteristic transformation temperatures. Tanaka used this model to simulate super-elasticity, one-way memory effects, and the active deformation of martensite. The model can also be used to calculate the force generated upon constrained heating (at a fixed length) of a specimen that is pre-deformed in the martensitic state.

The model was further developed in [48] by studying the cyclic properties of a Ni-Ti alloy. Four aspects of the characteristic fatigue properties were analyzed. The transformation stresses increased when the sample was subjected to thermal cycles under a constant stress and the transformation temperatures increased. The residual deformation was also observed to increase with the number of cycles, while the available elongation decreased with the number of cycles.

Raniecki et al. [49] developed a model to predict the stress-induced behavior of different titanium-nickel and copper-based alloys. This model considered the three-dimensional stress over the temperature range of the super-elastic (pseudo-elastic) state and could determine the internal loops. Later, a cyclic contribution term was added to simulate fatigue effects [50]. This model was further modified to account for experimental observations of residual (or stabilized) martensite.

2.2 The micro-macro approach

SMA exhibit complex thermo-mechanical behavior that is coupled to the different physical processes that occur in these materials. The basic phenomena include pseudo-elasticity, the temperature-dependent stress that transforms the sample, and shape memory. Pseudo-elasticity facilitates the recovery of large strains in unloading because of stress-induced phase changes. The temperature-dependent stress is governed by a Clausius-Clapeyron relationship. Shape memory enables recovery following large deformations because of temperature-induced phase changes.

These fundamental phenomena are accompanied by more complex phenomena that significantly influence the thermo-mechanical behavior. These complex phenomena include self-heating resulting from latent heat effects and hysteresis, plastic behavior and fatigue, practical tension-compression asymmetry, specimen size-dependence in thermal treatments, metastability because of diffusion at the working temperatures, and TRansformation Induced Plasticity (TRIP), among others. The dynamic phenomena are associated with heat transfer and the intrinsic phenomena are induced by evolution of the atomic order. The evolution of hysteresis cycles with stress and temperature aging for NiTi is discussed in Part Three. An experimental methodology for following the recoverable dynamic evolution of the Ms as a function of time and temperature for a CuAlBe polycrystalline material and single crystals is discussed in Part Four. Part Five summarizes the dynamic stabilization of martensite in stress-strain cycling in single crystals and the recovery of these crystals in time. While all these phenomena occur at the microscopic level in local volume material elements, most of these phenomena affect the material macroscopic response. These microscopic mechanisms cannot be neglected in constructing a detailed phenomenological description of the material behavior.

The models must be practical to be used with well-defined parameters and should be easy to adapt to FEA. The required parameters can be experimentally determined from samples or from data in the literature. The Patoor papers used a microscopic approach to obtain reliable stress-strain-temperature behavior [51-52]. These studies considered different variants of martensite in a thermodynamic potential framework. A microscopic Gibbs free energy was formulated for the

sample. This free energy was a function of the temperature, the stress tensor and the proportions of the martensite variants. Their first approach was a quadratic form. A dissipative term was added to capture hysteresis in the loading-unloading cycles [53]. The model was further modified to include the interactions among the variants of martensite within the grains [54]. The authors found good agreement between computations and the experimental behavior of the polycrystalline material.

Likhatchev [55] developed a similar formulation for inclusion in numeric routines for a one-dimensional representation, such as that by Terriault [38, 56-57], in which an USERMAT routine was constructed for compilation inside ANSYS (FEA code). The Likhatchev model predicted the macroscopic strain rate tensor under stress-controlled loading. One of the key features of the Likhatchev model was the effective temperature T*, which was a simple means of indicating whether the phase transformation was initiated by mechanical or thermal loading. The variation of the effective temperature T*, which was governed by the Clausius-Clapeyron relation, was a scalar variable incorporating the temperature and the stress tensor variations over a region.

2.3. The phenomenological approach

The models in the literature are reviewed to synthesize hybrids of the "micro-macro" approach, the general representations and the phenomenological results. The main goal is to develop a model that can be included in a computer program to efficiently simulate the desired application. The Brinson model [36, 58-59] introduced a separation between "thermal" and "mechanical" martensite. This separation into two types of martensite resulted in an improved representation of the martensite twinning effects in the total strain. The Brinson papers were a milestone in numerical (FEA) applications.

The Sun group [60] developed a general model for the main SMA behavior, such as super-elasticity and rubber-like effects. This model was based on a thermodynamic potential similar to that used by Patoor, but was developed from a macroscopic perspective, i.e., there was only one martensite species. Two types of martensite, oriented and thermal are used to explain martensite reorientation effects. Lagoudas [61-62] appropriated ideas from the older Tanaka papers. Lagoudas' model partitioned the total strain as an elastic component combined with transformation effects. This Texas A & M group developed a computational solution using finite elements to model a three-dimensional state of stress. Auricchio [12, 37, 63-64] developed a relatively simple model to model the large strains of the martensite transformation. This model, together with a FEA code, was adopted by ANSYS into a standard subroutine [63].

Obtaining agreement between models and experimental results is a long-standing and difficult problem. A short description of these difficulties can be found in several interesting papers. Ben Mekki and Auricchio [12] used a model similar to a bilinear representation of the hysteresis cycle, which might induce misunderstandings. The model, predicted a reduction in the amplitude of the larger oscillations of a simulated oscillating cable but not of the minor amplitudes. The oscillation decayed to fixed amplitude that was governed by the elastic component of the model. The oscillation energy of the elastic component remained constant. However, experiments performed in facilities showed that the oscillation amplitude decayed practically to zero in a short time [65]. Another general difficulty is associated with size effects, i.e., SMA diameter effects. A series of papers, which included experimental studies, explored a relatively wide range of diameters: 1-mm diameter wire samples [35] and 2-mm diameter wire samples [66] have been investigated without comparative analysis. Scaling up from one diameter to another does not reproduce experimental results for NiTi (see Section 3.9). Experimental results for one wire diameter are difficult to apply to other diameters of SMA wires (usually for the NiTi alloy).

In phenomenological modeling, the material constants of a model are fit to a series of experimental results. This representation does not address the physical phenomena that cause the martensitic transformation. The model always uses a detailed analysis of the hysteretic behavior and/or the temperature effects as an "operational" method. A phenomenological model cannot "predict" material behavior: the phenomenological model only attempts to reasonably reproduce the dynamics of structures, in this case. This approach may not be able to capture the effects of different cross-sections and dissimilar lengths: Part Three shows that NiTi samples with different lengths and diameters exhibited completely different transformation rates (in mm/s) for the same deformation rate (in 1/s), and the transformation behavior is different. The transformation behavior depends on the local temperature and self-heating from latent heat effects, dissipation and heat transmission to the surroundings. However, phenomenological models can rapidly compute pseudo-elastic behavior. Efficient computation is necessary for appropriate implementation into FEA software for multiple applications. The main contribution of this work is the visualization of the necessary experimental results. SMA should always satisfy the application requirements. Experimental trials to measure SMA behavior are completely essential. Later, a hysteretic behavior was built into the model to agree with the experimental results.

Terriault's study includes a phenomenological macroscopic model for "krigeage" [67] within both bilinear and cubic representations. These simple models provide a satisfactory representation of pseudo-elastic behavior. The bilinear model is widely used. The cubic model was implemented into ANSYS via the user-defined subroutine USERMAT. This feature enables users to augment the material library with their own constitutive relations that are written in FORTRAN, compiled and linked to the ANSYS software [68]. The USERMAT routine is especially useful for simulating new materials with behavior that was not included in the original software package. The simulations in this study used the cubic representation to model the SMA dampers. The bilinear model was only used as a final comparison. Part Three described a methodology to satisfactorily represent internal loops within the cubic model approach. Other possible fits to the hysteretic behavior are available. For instance, neuronal networks and fuzzy rules have been proposed for CuZnAl single crystals in refs. [69-70].

Recently, modeling has a tendency to approach the experimental behavior in very concrete situations, or for concrete phenomena, regarding specific applications of the SMA. For instance, [71] adapt the situation for modeling a 3-D, load-biased problem; [72] applies finite elements for approaching the behavior of a perforated plate; the effect of a laminar microstructure (martensite bands) is considered in [73]; ratcheting (accumulation of residual deformation when mechanically cycling in stress control) due to different mechanisms of plastic deformation is treated in [74]; non-local effects (which could be related to heat wave in the material when transforming) are considered in [75]. Even simulation of thermal properties of composites with SMA are experimentally measured and then computed with finite element modeling in [76]. Also, the effects of rate of transformation, linked to temperature dependence, continue to be perfected in models as [77].

Micromechanics modeling taking into account precipitates in the SMA has been undertaken by Lagoudas group [78]. The effect of cycling on the microstructure of the SMA has been also considered, as a possible justification of the evolutive behavior [79]. Further on, the possibility of plastic deformation of martenite by twinning has been considered, with experiments and models, by Sehitoglu et al. [80].

One-dimensional models continue to be considered useful because they allow a faster computation. The effects of temperature, giving a "(Lüders) band-like" structure of transformation in NiTi, are considered in [81].

The possibilities of multiple phase transformation have been included in some previous models, to allow for a refinement of 3-D behavior, by Auriccio group [82]

Different groups working in this area have published approximately five hundred papers over the last few years on the improvement and application of these models. Several reviews are available in the literature [83-87]. However, open questions still remain, including time or rate effects in the transformation process and size effects. Modeling has mainly focused on thin wires with hysteresis cycles that exhibit a "plateau" in transformation and retransformation. The experimental behavior of thick wires is highly affected by heat transfer and thermal coupling with the surroundings that induces an associated plastic deformation, i.e., SMA creep.

A useful synthesis of existing models in [88] concluded that very simple models, such as that of Auricchio, which uses 7 parameters, can produce fairly accurate results. However, the details of the experimental behavior were not fully accounted for. Much more complex models, such as that of Lexcellent (which uses more than 20 parameters) can improve agreement with the experimental data. Even state of the art models cannot completely represent the internal loops. The stress and temperature aging effects are completely out of the scope of these representations. Atomic diffusion effects are always neglected in these models.

The heat and the entropy balance are difficult. In the literature appear some misunderstandings on the First and the Second Thermodynamic Laws of Thermodynamics. Ref. [89], for example, states "According to literature *two major heat sources* come into play during phase change: *latent heat*, which seems to be the predominant heat source, and *intrinsic dissipation*." The "intrinsic dissipation" in the stress-strain cycle is actually the hysteresis energy in the heat balance for the transformation and retransformation processes at different stresses:

$$Q_{\beta \to m} + Q_{m \to \beta} = \oint \vec{f}\, d\vec{x} \qquad (1)$$

The mechanical hysteretic energy of a temperature-induced cycle is zero. In this case, the transformation is induced by the temperature without any external forces. The driving force for a temperature-induced transformation/retransformation is related to the entropy increase that is induced by the same quantity of heat being absorbed and released at different temperatures [90].

2.4 Part Two: Summary

It is difficult to provide a concise description of the SMA representative models because the formalism of these models depends on the intended application. Fundamental studies have used a thermodynamic description of the phase transition with hysteresis. A more practical approach has been to model the SMA elements of a device or structure. Real situations require a combination of a macroscopic approach based on the Helmholtz free energy, a micro-macro approach for the interactions between the martensite plates, and a phenomenological approach. The round-robin [88], established by the Sittner group in Praga, was developed from the MAFESMA project of the European Science Foundation. The analysis showed that for thin wires (0.1-mm diameter), a phenomenological model using 7 parameters produced reasonable agreement with experiments. Increasing the number of parameters in a macroscopic model cannot produce considerable improvement. The models have never accounted for parasitic effects that are induced by diffusion, such as recoverable Ms tracking or monotonic aging effects. State of the art semi-phenomenological models, such as those of Brinson, Patoor and Terriault, have used algorithms that are converted into FEA methods.

PART_THREE

Increasing the quality of life is one of the main goals of smart materials and systems. The suppression or reduction of external perturbation phenomena, such as wind, rain or traffic that induce cable oscillations is a practical problem for bridges. The oscillations induce progressive damage and crash of the steel fibers, reducing the cable life. A classical example is the Dongting Lake Bridge over the Yang-Tse River, which opened in 2002 [91] because of strong wind and rain storms that induced large oscillations in the large bridge cables. The bridge was immediately retrofitted using Magneto-Rheological dampers of LORD [92-93].

Potential or practical damage to the cables of some "old" French bridges has also been observed. The FP014-SMARTeR: Shape Memory Alloys to Regulate Transient Responses in civil engineering (SMARTeR: 2006-09) was a European Science Foundation (ESF) project that used SMA to damp stayed cables [94]. Specific objective of the project included the damage sustained by the Iroise Bridge (1994) over the Elorn River (near Brest) and by the St. Nazaire bridge (1975) over the Loire River (near Nantes) (http://fr.wikipedia.org/wiki/Pont_de_Saint-Nazaire, 2013). Several cables were changed for the St. Nazaire bridge.

Oscillations are also observed at low winds speeds. For winds under 10 km/h, minor oscillations (near 10 mm) were observed in the large cables (110 m between the piers) of the Echinghen Viaduct (1997), which is situated on the A16 toll highway near Boulogne in NW France. The cables sustained accumulated damage. Decreasing the amplitude of the oscillations can increase the practical lifetime of the cables. Damping oscillations requires the use of appropriate passive or semi-active dampers in the structure. Semi-active devices [9], which were used for the MR dampers of Dongting Lake Bridge, need guaranteed electrical power and appropriate technical computing supervision, i.e., for software and hardware.

This Part discusses the use of pseudo-elastic NiTi wires to damp stayed cables [95]. NiTi metallurgy has been studied elsewhere [96]. The SMA damper is a passive device [9] that exploits the SMA hysteresis cycle. Our study focuses on the experimental requirements of the application and correspondingly investigates the SMA properties. First, the cable requirements are outlined. Next, the experimental measurements of the SMA wires are used to provide data on the required conditions for the fracture life, depending on external temperature effects and self-heating mechanisms, the cycling frequency and the wire diameter. The study includes the seasonal temperature effects. The final section describes the characteristics of a phenomenological model that is used to simulate partial and internal loops in the SMA application as a damper for facilities' cables and a portico structure. Finally, temperature aging mechanisms are discussed, as well as temperature and stress actions.

3.1 Damping of stayed cables in bridges: SMA damper application requirements

The Iroise Bridge is a toll-free highway bridge with a length of 200+400+200 m. The separation between the piers has a "classical" length, i.e., approximately 400 m (see figure 3). The cable lengths generally exceed 200 m and the cable tension is approximately 1000 kN. The structural characteristics indicate that a smooth SMA action can induce small changes in the distribution of forces in the structure, i.e., the dampers can produce only minor changes at the oscillation frequencies. It is critical that the damper does not modify or induces only minor changes in the static and dynamic response of the structure. The force induced by the damper action, which is projected to be approximately orthogonal to the cable axis, should remain in the neighborhood of 10^{-3} of the force inducing the stress in the cable. The force scale indicates that a damper built by a

set of one or more wires exerts forces of approximately 1 kN on the cable. A large set of thin SMA wires is unsuitable because of the practical difficulties of installing such wires. Wrapping several turns of a long thin wire around the ends would result in undesirable parasitic thermal interactions between the wires and an increased risk of failure because of high length of thin wire exposed. For this configuration, the crash of a single thin wire part would destroy the damper.

This Part ends with a brief description of the required damper structure based on the results from the experiments in the facilities. There are two possible damper positions. One possibility is to place the damper between the platform and the cable. Another possibility is to install the damper between two cables. In the second case, the oscillations clearly have a more complex effect on the SMA damper. Thus, the actions can be reduced to traction only by using appropriate links between the SMA and the cable. Biaxial or bending actions on the SMA damper are generally expected. The study and analysis of such actions are out of the scope of this paper.

Figure 3. The Iroise Highway Bridge with 2+2 lanes between Brest and Plougastel, France. (Reprinted from Engineering Structures vol. 49, V. Torra, C. Auguet, A. Isalgue, G. Carreras, P. Terriault, F.C. Lovey: Built in dampers for stayed cables in bridges via SMA. The SMARTeR-ESF project: A mesoscopic and macroscopic experimental analysis with numerical simulations, pages 43-57 (2013), with permission from Elsevier).

A damper on a bridge is directly exposed to wind and rain. NiTi exhibits the desirable characteristic of low oxidation under the action of the weather. The damper is affected by the external temperature and daily and yearly temperature variations. The damper may be subjected to a practical temperature differential of approximately 60 K, i.e., between 30 or 40 °C (313 K) in summer and -20°C (253 K) in winter, such as in Western Europe. The martensitic transformation releases and absorbs latent heat in working and releases the hysteretic energy for each working cycle. The effect of these actions induces local heating/cooling that is associated with the cycling behavior. A study should be conducted on the temperature effects associated with working cycles and their frequency and deformation and on the eventual heat transmission to the surroundings by convection. A moderately complex analysis is needed to model the potential effects of aging on the alloy. The model uses a simplification of the behavior of SMA pre-stressed wires to prevent bending or compression. Our work was extended to two diameters (2.46-mm and 0.5-mm diameters) to study diameter effects and scaling of the results.

The oscillation frequencies were a function of the stress used to position the cable, the mass per unit length and the steel and the supplementary materials that constituted the cable. In some cases, a polymeric tube is refilled with concrete or wax to protect the steel wire strands. A cable at 1 Hz, under the action of a strong storm lasting of three or four days, requires a working damper with a fracture-life of over a half a million cycles. The fracture-life increases proportionally at higher frequencies. The fracture-life is the relevant parameter for this application. A spontaneous increase in the damper length (i.e., by SMA creep) in working is completely unacceptable. SMA creep, i.e., a net increase in the SMA length up to a value "A", results in oscillations with an amplitude up to "A" that are not smoothed.

In standard NiTi studies, the alloy is generally prepared by complex thermo-mechanical treatments, such as cold working and strain annealing. Our study is motivated by a civil engineering application, so the complexity of the pre-treatments needs to be reduced to facilitate the use. The necessary length of the wires was more easily obtained directly from a guaranteed furnisher, which minimized the local treatment required. For several bridges, one would require 100 dampers of several meters of SMA wire, i.e., with total lengths of 100 to 1000 m.

3.2. Experimental: materials and methods.

The experimental analysis focused on the NiTi SMA alloy for two fundamental reasons: the alloy resistance to wet oxidation and the relative ease of acquiring long wires of the alloy. The study used a 2.46-mm diameter wire (A wire) and a similar 0.5-mm diameter wire (B wire) for comparative and "scaling" purposes. Wires with smaller diameters (0.2 and 0.1 mm) were used in studies on a minor cable in "an indoor laboratory." The stress-induced transformation force in the A wire after several cycles was approximately 2 kN. The same force for the B wire was approximately 80 N (see Section 3.9). Lengths of 125 and 500 mm were investigated for the A wire and of 125 and 1000 mm for the B wire. Different sets of measurements were carried out for three slenderness ratios (ℓ/r) of 50, 200 and 2000 to study the thermo-mechanical effects on cycling. Further, an A wire with a length of 4140 mm (with a ℓ/r over 3000) was used in all the measurements performed in ELSA (European Laboratory for Structural Assessment, Joint Research Center, Ispra, Italy). Usually, applications for NiTi wires use thin wires with cross sections under 1 mm^2. These wires induce stress forces situated near 1-200 N, which are extremely small for civil engineering applications.

The NiTi alloy was provided by SAES Getters (Milan, Italy) via a subsidiary company Memry Corp. (Bethel CT, USA) and was previously provided by Special Metals Corp. (New Hartford, New York, USA). The surface of the samples was finished with a light (gray) oxide surface (for the 2.46-mm diameter A wires) or with black oxide (for the 0.5-mm diameter B wires). The nominal As temperatures for the A and B wires were similar at 248/247 K and 243 K, respectively.

The purpose was to try to use industrial product, as the number of dampers needed for a large Civil Engineering work might imply around a km of wire. Also, reproducibility during time of service was considered important. For example, for the A wire, two different batches in different years, the furnisher certificates indicate the composition and impurities from table 1.

The as furnished A wire was tested in traction. The failure was ductile, and happened at 1200 MPa, and near 20% strain. It was considered that ductile fracture was preferable to enhancing some other properties, because of the application in Civil Engineering, to avoid failures without advertising.

Table 1. NiTi wires of 2.46 mm diameter alloy data from the furnisher certificates. In all cases, other impurities were: H<0.005%, Fe<0.05% weight, each of the groups: (Si, Cr, Co, Mo, W, V, Nb, Al, Ba); (Zr, P, Cu, Hf, Ag, Pb, Bi, Ca); and (Mg, Sn, Cd, Zn, Sb, Sr, Na, As, Be), where in

amounts of less than 0.01% weight. According to the certificates, Ti was to balance the composition.

Date	Ni % weight	C ppm weight	O ppm weight	As (fully annealed)
March, 2007	55.99	379	246	247
April, 2005	56.00	380	167	246

As previously mentioned, the fatigue life is a critical parameter for the application. The stress-strain-temperature-time studies were also highly relevant. The study was conducted using a conventional MTS 810 at room temperature (near 293 K) in an air-conditioned room. The MTS had a chamber, which was constructed in-house, to maintain moderate temperatures (between 293 and 323 K). Simple protective structures were built for studies of the minor transformation steps to prevent parasitic actions by the air-conditioning equipment and the associated temperature variations. Two devices, INSTRON 5567 and INSTRON 1123, were used with two cooling-heating standard thermal chambers, 3119-005 (203 to 523 K) and 3110, respectively. The equipment was selected to perform measurements at working temperatures between 240 and 373 K. The equipment was also appropriate for determining the Clausius-Clapeyron coefficient (i.e., 6.3 MPa K^{-1} in [27]) and to investigate seasonal effects. One stress –strain equipment computer controlled was fabricated in-house to study the longer (1 m) B wire samples at approximately room temperature (below 313 K).

One or two K thermocouples (from OMEGA) were wrapped around the samples for local time-temperature analysis. Wrapping prevents local compositional changes induced by spot welding, but introduces supplementary noise: the "mean" reading corresponded to a SMA wire length in the 2-4 mm range. A zero-point was used: the signal was digitized from Digital MultiMeter (DMM) Agilent U1251A, transmitted by a proprietary program and stored in a PC. The stress-temperature aging measurements were performed using adapted devices that were constructed in-house. Cheaper temperature chambers were built for the aging experiments at 373 K.

3.3. Summary of microstructure observations

This section describes the minor analysis of the microstructure of the polycrystalline 2.46-mm diameter NiTi wire. The microstructure of the wire was observed by transmission electron microscopy. A Philips CM200 LaB_6 transmission electron microscope was used [97]. The observed structure of the furnished and cycled samples was similar: the structure was complex, with a large quantity of grain boundaries, dislocations and martensite. The results for the 2.46-mm diameter wire are shown in figure 4. The weak 001- and 200-type reflections, associated with the B2 structure of NiTi (figure 4 A), indicated that the wire was textured along the <111> direction. The microstructure shown in figure 4 B appears as small grains and sub-grains with a minimum size of approximately 80 nm. Scarce precipitates of TiC and Ni_3Ti_2 were also observed, but are not shown.

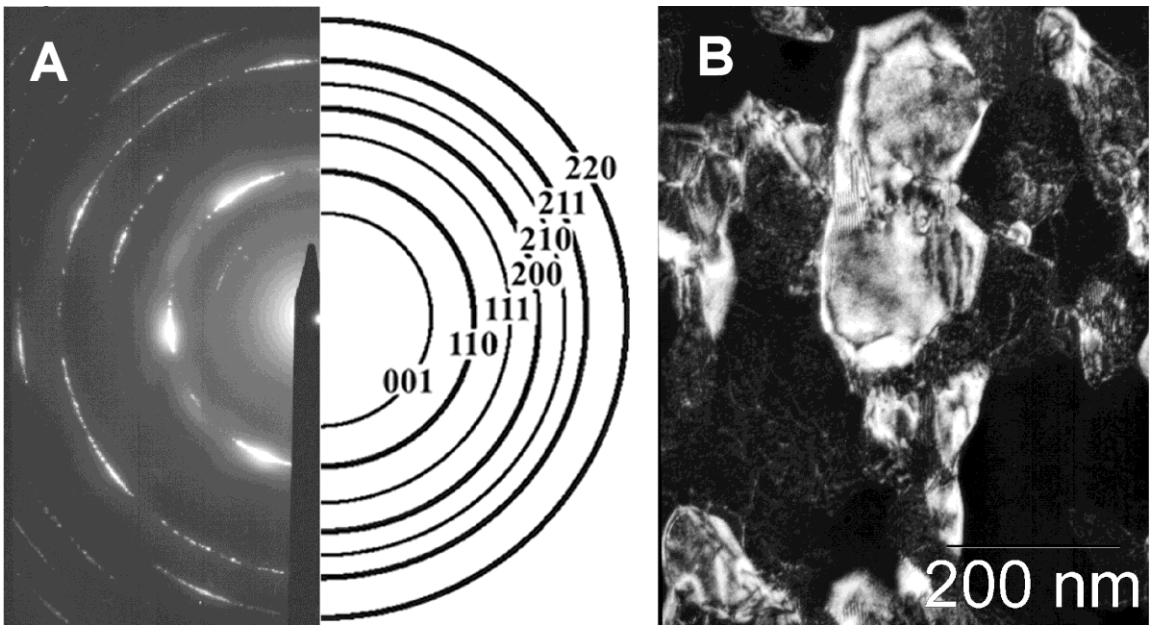

Figure 4. TEM study of the NiTi wires of 2.46 mm. (a): Electron diffraction pattern of the NiTi wire along the wire axis. Texture along the <111> is evident. (b): Dark field image taken with a small part of the 110 type ring in the left. Grains and sub-grains, as smaller as about 80 nm, can be observed (Reprinted from Canadian Metallurgical Quarterly, vol 52-1, V. Torra, A. Isalgue, C. Auguet, G. Carreras,F.C. Lovey, P. Terriault, Damping in civil engineering using SMA part 2 - Particular properties of NiTi for damping of stayed cables in bridges, pp. 81 - 89 (2013), with permission from Pergamon.)

3.4. NiTi fracture-life.

The relevant damping parameter, the fracture-life of the alloy, must be long to reduce the amplitude of the oscillations in stayed cables. We focused on the most convenient and ease deformation path for the NiTi wires i.e., pure traction. Other deformation paths, including compression, torsion, bending and buckling, were inappropriate for the desired application. The complex action of these deformation paths reduces the fracture-life of the alloy. Figure 5 shows the results of several fracture-life tests, which were obtained in traction for NiTi samples with lengths of 120 and 500 mm, at 293 K, using 2.46-mm diameter wire. The associated stresses are important for relatively high deformations, e.g., between five and eight per cent. Related tests determined a fatigue life that was under 30000 cycles. This lower fracture level (short life) was unacceptable for SMA use in dampers of stayed cables. As the fracture-life strain increases when the stress decreases [98], the stress and deformation were observed to decrease for several samples, along with the hysteresis energy. Reducing the deformation to approximately 1 % reduced the net force in the sample to 1 kN at stresses near 200 MPa. This force value brought the fracture-life of the samples into the realm of practical application. An acceptable fracture-life is between 3 and 5 million working cycles. Sample crash generally appears near or inside the grips most likely via a coupling between the cycling effects and the internal deformation induced by the grips pressure.

The experimental data and approximate Basquin law fit [98-99] are presented in figure 5. The stress reduction increased the number of working cycles. When the fracture-life exceeded 0.5 million cycles, the deformation remained below 1.5 %. It was always possible to create small hysteresis cycles at low strains (less than 0.5 %) and reduced loads, i.e., from zero stresses to less than 250 MPa. The triangles in figure 5 were associated to temperature cycling measurements for several constant stresses for wires of 0.6 mm of diameter with a strain situated between 1 and 3 %. For external stress near 100 MPa, the number of working cycles overcomes 350000 working cycles.

The Basquin law describes the fatigue life of standard materials. This formalism considers the maximal stress (σ_{MAX}) to be linear in a negative power of the number of fatigue-life cycles (N_f). Fitting the experimental points with the Basquin law results in equation 2:

$$\sigma_{MAX} = A + B*(N_f)^{-a} = 170 + 7920.9*(N_f)^{-0.398} \qquad (2)$$

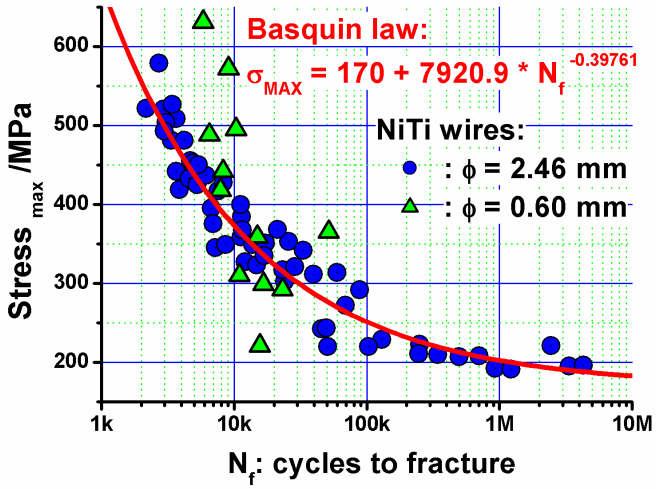

Figure 5. The stress against the fatigue results for traction only in NiTi (dots: 2.46 mm of diameter) including the Basquin law fit. Triangles: partial analysis by temperature cycling for 0.6 mm diameter wire.

The main difference between the SMA and classical materials is the higher value of the "a" exponent (a ≈ 0.40). The higher value of "a" compared to the classical values (1/8 > a > 1/16) suggests that the fatigue-fracture process was effectively controlled by the parent to martensite transition. The deformation was produced by the martensitic transformation instead of by the dislocation glides of standard materials. Therefore, less dislocations are expected to be created when cycling SMA materials at lower deformations (i.e., near 1 %) and stress (near 200 MPa), resulting in a longer life**.** There was satisfactory agreement between the experimental points and the Basquin law over the full range of the data. The main parameter in the fracture-life was the maximal stress value. The measurements were performed for several deformations and different sample preparations. The tests were performed on samples "as furnished" at room temperature, on samples in a liquid bath of paraffin or water, on aged samples at 373 K and with strains between 0.5 and 8 %. The NiTi SMA experimental data in the literature correspond to data for bits in the health care field. For example, orthodontic tests using bits involve highly complex deformations, including rotating-bending and bending-bending and/or compression, bending, torsion or buckling. Studies on wires for bone fixation and fundamental studies on wires have also been reviewed [100-105]. Recently, two reviews synthesizing fracture results in NiTi have been published [106-107].

3.5 SMA creep

SMA creep is the increase in length resulting from a combination of the creation of dislocations and, eventually, retained martensite. Progressive SMA creep must be suppressed in working by an appropriate thermo-mechanical treatment. The experimental analysis used 2.46-mm diameter "as furnished" wire. The maximal stress of the first cycle, at an eight percent of deformation, was approximately 3 kN or 600 MPa. The thermo-mechanical treatment began at 100 working cycles, which was induced by the action of a sinusoidal strain of up to 8 % at 0.01 Hz, for samples with an available length of approximately 120 mm.

The sample remains inside the action of a fan (air speed near 1-2 m/s) that activates the forced convection in the sample. The treatment diminishes the initial transformation stress to 1 or 2 kN and situates the permanent deformation (SMA creep) up to 2 %. See, for instance, the figure 6 A. After the 100 cycles, the shape of transformation approaches to an inverted S-shape similar to the cycles in polycrystalline CuAlBe [95, 108] (see, for instance, the Part Four). The retransformation was submitted to minor changes. The maximal hysteresis width is reduced from 400 to near 200 MPa, and the dissipated energy is reduced to 1/3 (figure 6 B). In series of the first 100 working and continuous cycles, an intermediate stop in the fan for several cycles (producing a lower heat transfer, free convection on the sample) induces changes in the hysteretic behavior. The figure 6 A visualizes a reduction in the hysteresis width (see, the arrows) associated to several cycles with the fan "off" (free convection) in comparison with the other cycles with the fan "on" (forced convection).

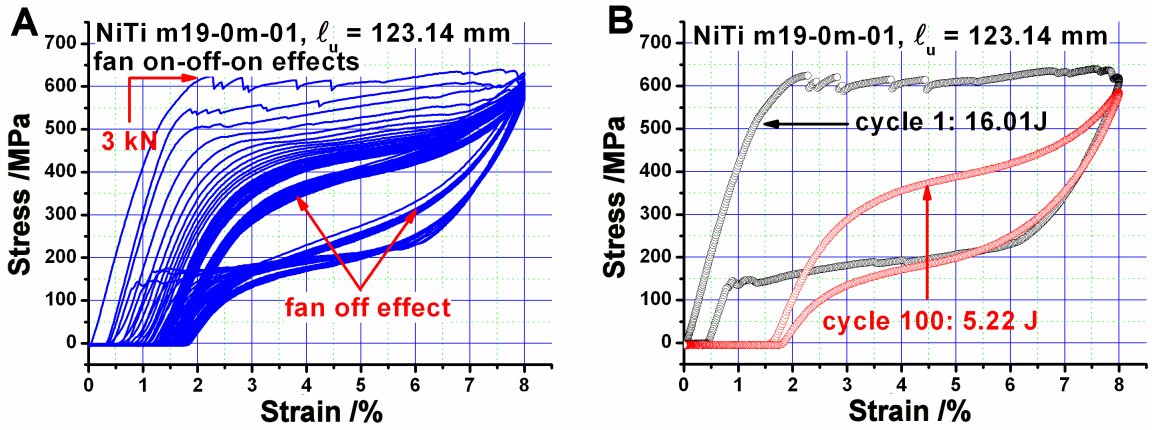

Figure 6. Cycling effects for wire of 2.46 mm. 100 cycles realized with sinusoidal strain up to 8 % at 0.01 Hz (100 s/cycle) with a fan addressed to sample. (a): the arrows shows the fan off effect. (b): Shape and frictional energy for cycles 1 and 100. The SMA creep effect was close to 2 %. (Reprinted from Canadian Metallurgical Quarterly, vol 52-1, V. Torra, A. Isalgue, C. Auguet, G. Carreras,F.C. Lovey, P. Terriault, Damping in civil engineering using SMA part 2 - Particular properties of NiTi for damping of stayed cables in bridges, pp. 81 - 89 (2013), with permission from Pergamon.)

3.5.1 Stops and SMA creep

The creep increased progressively for the initial sets of cycles. The creep increased up to 2 % in the first 100 training cycles, as shown in figure 6 A. This increase represents the dominant creep behavior. The SMA creep also increased as the maximal room temperature increased or as the cycling frequency increased, which contributed to self-heating in the samples and the stress. The maximal creep was approximately 2.5 %, as shown in figure 7 A.

Figure 7 A shows an example of the SMA creep evolution. The SMA creep increased by 2.0 % in the initial set of 100 working cycles, when the transformation stress was more relevant. The final value of each set of cycles was fitted by an exponential (these data points are shown as triangles). Later, after 2000 cycles, the mean creep value remained constant at approximately 2.5 %. These observations were associated with sets of cycles at different amplitudes and cycling frequencies (up to 16 Hz) that were separated by pauses. Each set of cycles showed an initial decrease in the creep (which is shown by the empty circles in figure 7 A), which was equivalent to a highly reduced parent recovery, as shown in figure 7 B. The experimental results showed that, following a small pause of 540 s, the first cycle required supplementary stress compared to the stress of the last cycle

of the previous set. The measurements showed an increase in the hysteretic energy over the first cycles of the subsequent set of working cycles. At a low cycling rate (i.e., frequencies close to 0.01 Hz), the "recovery" could be associated with temperature actions. The experimental results showed that the measured creep in the 2.46-mm diameter samples did not exceed 2.5 %, so that appropriate training to approach 2.5 % creep should guarantee SMA behavior for the desired applications. Figure 8 A shows the stop effects in a continuous series of working cycles.

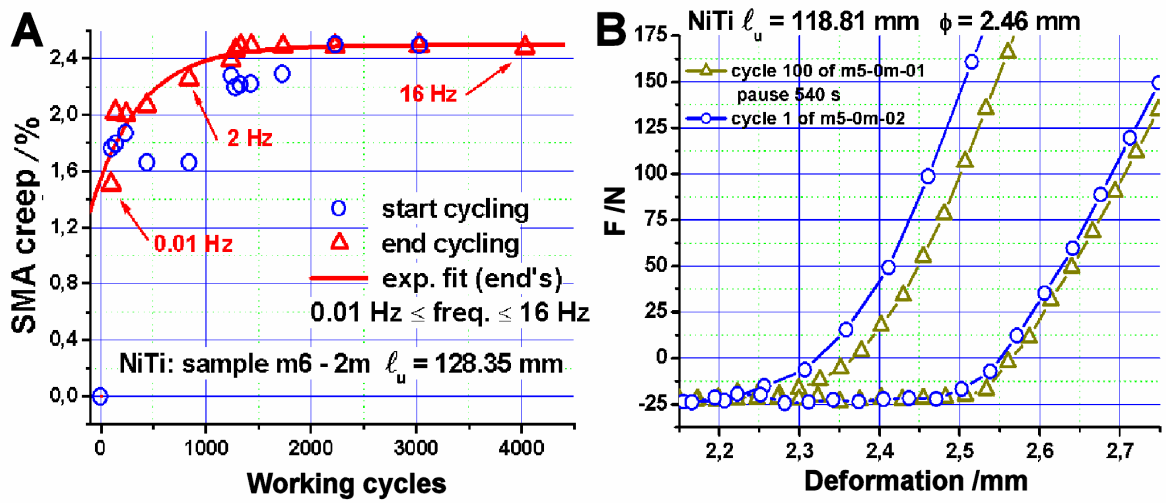

Figure 7. Increase of the SMA creep for larger series of working cycles. (a): Creep evolution against the number of working cycles realized by several sets of cycles at different frequencies (between 0.01 and 16 Hz). Empty dots: initial value for each set of cycles. (b): Changes in creep in the first cycle of a set of cycles. The expanded deformation scale (by empty dots) visualizes the minor creep reduction after one pause of 540 s.

Figure 8 A shows that the stops in the cycling process modify the hysteretic behavior. This minor action increases the hysteretic energy for the next set of the working cycles. Figure 8 (A and B) shows the stop effects for samples with approximately 120-mm lengths, at strains of 0.76 and 1.2 %, respectively. The change for the first cycle could have corresponded to 100 % of the dissipated energy, but this effect was insignificant for thousands or millions of working cycles. The energy changes in figure 8 B were related to fluctuations in the practical limits of displacement resolution of the MTS equipment. The series of measurements in figure 8 B were not performed continuously over four months, but with several placement-replacement actions on the sample with the minor positioning uncertainty. The dissipated energy associated to figure 8 B situates near 0.5 MJ.

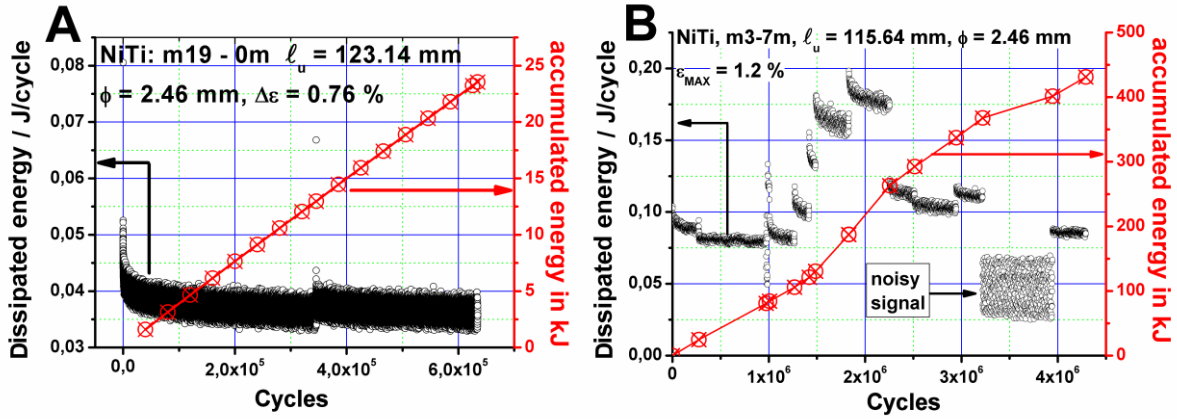

Figure 8. Pauses effect in the dissipated energy. A: Energy/cycle when cycling at 4 Hz for a low strain (0.76 %). The accumulated energy for 600000 cycles of this low strain overcomes 23 kJ. B: Series of 4.5 million of working cycles for 1ow strain: 1.2 %, and the accumulated energy (near 0.5 MJ).

3.6. Cycling frequency effects: temperature and convection actions

Unique temperature effects were observed in cycling for the samples [109]. Sinusoidal strain cycles (at 0.01 Hz) with 8 % deformation induced temperature waves in the sample (figure 9 A) with an amplitude of ± 10 K. The amplitude was similar at different positions in the sample. Suppression of the fan action (reducing heat transfer from forced convection to free convection) increased the oscillation amplitude up to ± 15 K. Figure 9 B shows the temperature wave that was induced by the conditioned air (upper section). The "a" shows the effect of one stop in the cycling on the dissipated energy (middle section) and the oscillations induced by the conditioned air. The temperature waves also affected the force values (bottom section) in accordance with the Clausius-Clapeyron equation.

The fluctuations in the energy of the hysteresis cycle (between 5 and 10 %) decreased because of the room-temperature wave produced by the start (and stop) of the cooling phase of the air-conditioning. The maximal values of the oscillatory behavior of the hysteretic energy for minor cycles were associated with the minimal room temperature values, in agreement with the Clausius-Clapeyron equation. The local change in the dissipated energy decayed rapidly, so that the start-stop action was not significant for modeling the SMA behavior.

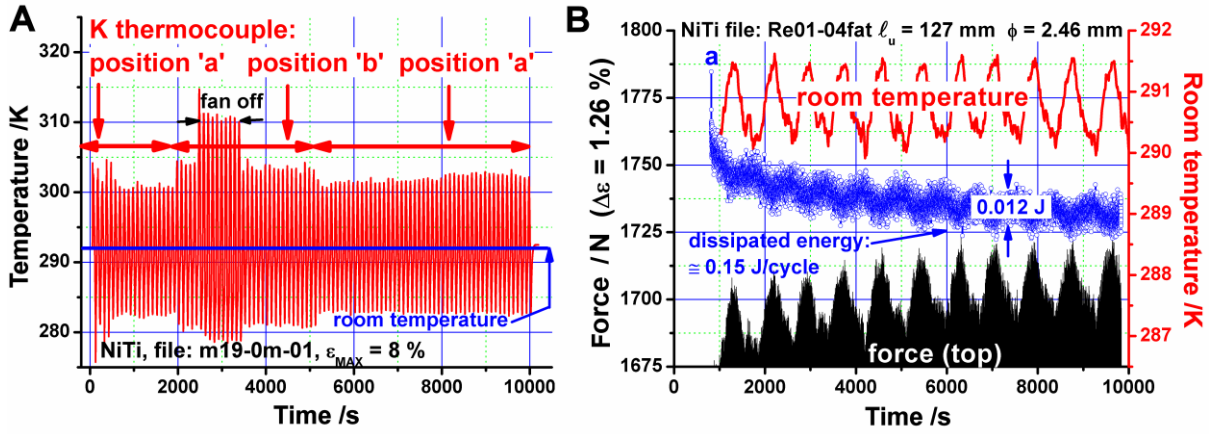

Figure 9. Fan and pause effects on cycling. A: effect of the thermocouple position and of the fan on - off in the sample temperature, cycling at 0.01 Hz and maximal deformation of 8 %. B: temperature oscillation induced by the conditioned air (top). Action of a previous pause (a) in the dissipated energy and oscillations by the actions of the conditioned air (middle). Oscillations in the force by the conditioned air (bottom).

3.6.1 Cycling and self-heating effects

Self-heating was extremely significant for the 2.46-mm diameter wires. Figure 10 shows the temperature increase for two strains when cycling (A. 8 % and B: 1.8 %). The mean sample temperature increased progressively with the cycling frequency due to the hysteresis cycle that converted mechanical work to heat. The local temperature in the sample oscillated around the external room temperature only during cycling at approximately 0.01 Hz or lower. For cycling frequencies of 3 Hz and deformations up to 8 %, the sample temperature increased more than 25 K for an associated stress of approximately 150 MPa, modifying the fracture-life of the samples. For cycling frequencies up to 10 Hz and deformations of 1.8 %, the temperature increase was lower: the temperature increase was approximately 10 K and 20 K (with the fan (forced convection) and without the fan (free convection), respectively). The maximum transformation stress followed the temperature behavior of the specimen (see figure 10 B). The amplitude of the oscillations of cables on bridges, primarily induced by wind or rain, would not exceed 1 % of the SMA element length.

For frequencies up to 10 Hz, the temperature increase, with wet air circulating over the SMA, is predicted to remain below 5 K.

Remark: The temperature reading frequency was 6.5 Hz, which only represents a mean value for cycling frequencies over 2 Hz. The figure 10 B shows the mean temperature against time: the readings induce a ripple for cycles at 1 or 3 Hz.

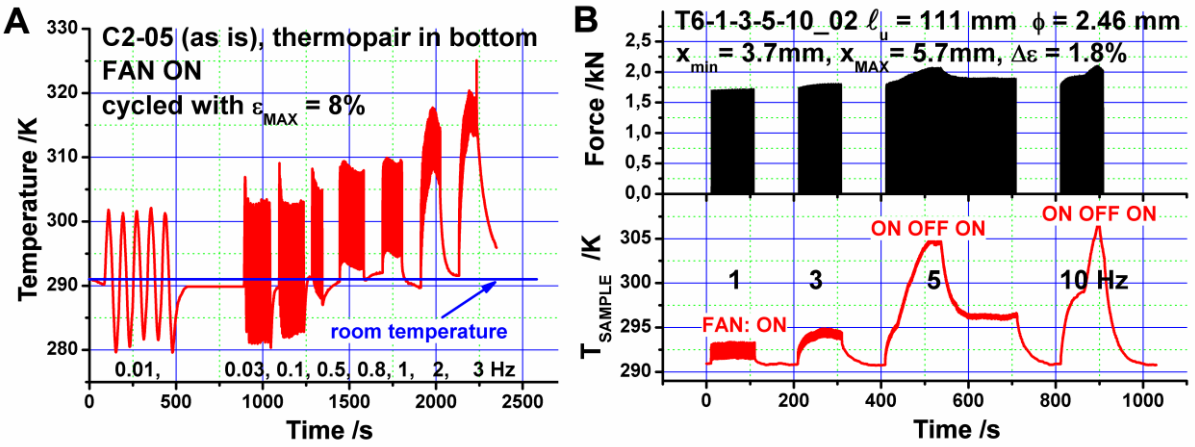

Figure 10. Temperature effects and cycling frequency. A: For maximal deformation 8 % and several cycling frequencies (0.01, 0.03, 0.1, 0.5, 1, 2 and 3 Hz. B: Frequency effects (up to 10 Hz) for a maximal deformation of 1.8 % and actions of fan "on" and fan "off". Up: Force against time. Bottom: Temperature against time for fan "on" and "off".

3.6.2. Convective actions: the fan effects

The self-heating of the SMA specimen on cycling depended on forced air convection (by the fan) that was used to dissipate the heat. The "fan off" state (heat transfer reduced to free convection) increased the maximal stress (figure 11) associated with the self-heating as shows the temperature in figure 9 A, and the Clausius-Clapeyron coefficient for these wires.

However, the "fan on-off" effect on the hysteresis cycle was not clearly evident, as shown by figures 12 and 13. Figure 12 A shows the "fan-off" effect: an energy reduction of 33 % was observed for on the first series of 100 cycles at 0.01 Hz. In figure12 B, a similar series of cycles was performed on a previously cycled and aged sample. In this case, the energy reduction was lower and approximately 10 %. For a trained sample, the dissipated energy changes associated with external wind variations did not appear to be very significant (within a 10 % uncertainty).

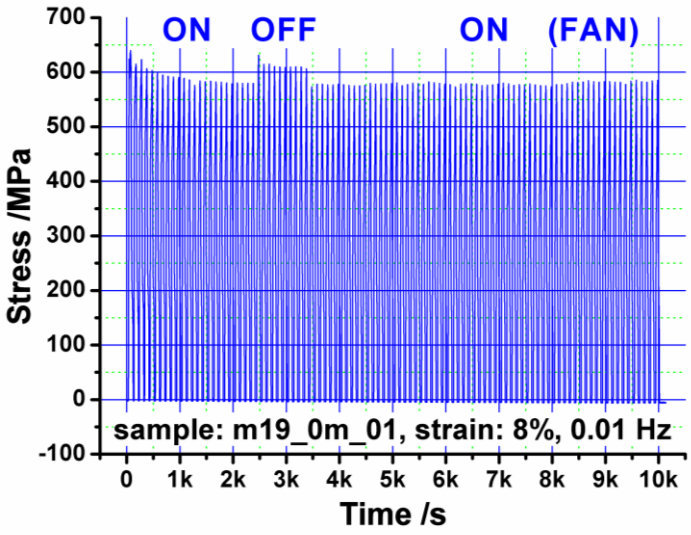

Figure 11. Stress against the time cycling at 0.01 Hz and a strain of 8 %. Initial transitory and the fan ON and fan OFF effect are clearly visualized.

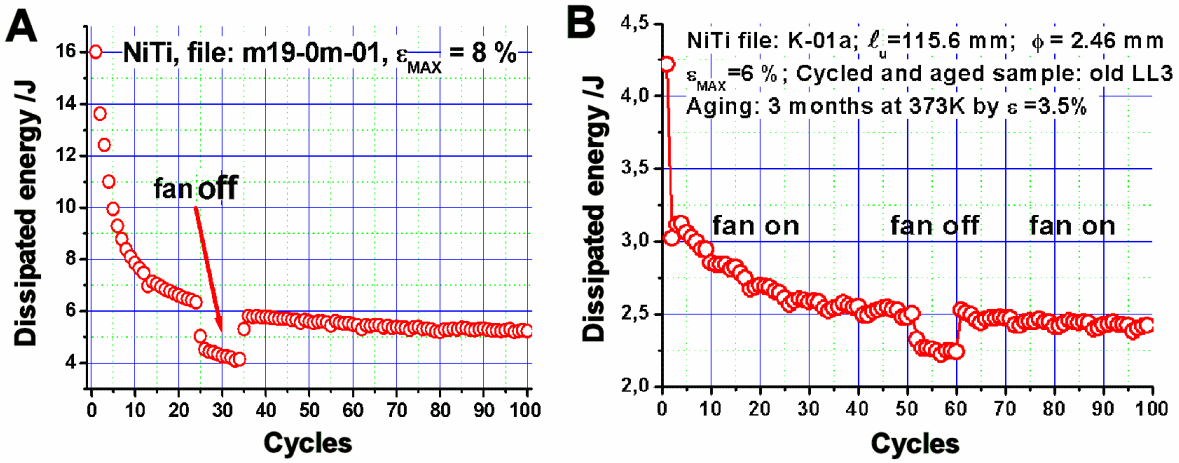

Figure 12. Hysteresis cycles in stress and strain realized with fan "on" and "off". A: Sample as furnished, cycles 24 and 31. B: cycles 45 and 55 in a previous cycled sample (several thousand or working cycles).

The fan effect on the stress-strain coordinates and the reduction in the stress and strain for cycled samples can be clearly seen in figure 13. At other cycling frequencies, a similar but reduced fan effect was observed. The fan effect may be related to compensatory amounts of released and absorbed latent heat in the "fan-off" (free convection) cycles compared to the "fan-on" (forced convection) cycles and to pseudo-adiabatic behavior. Ref. [110] showed wider hysteresis when latent heat was released to the surroundings before the start of retransformation compared to a more adiabatic cycle. In the first series of "fan-on" (forced convection) cycles, the partially localized transformation resulted in self-heating and required more stress because the wire was under room temperature from the previous cycle, but less cold than when there is only free convection. In retransformation, the specimen was somewhat cooler (because of forced convection) and required a lower stress: the width of the hysteresis cycle increased. The frequency of 0.01 Hz for the A samples was unique in producing the maximal hysteresis (see Section 3.6.3 below).

Figure 14 shows a plot of the temperature versus time for several cycling frequencies up to 3 Hz, for a maximal deformation of 8 %, with progressively increasing creep. The temperature increase associated with the 8 and 16 Hz cycling frequencies, at reduced net deformations of 1 and 0.8 %, respectively, remained under 10 K.

The figure 14 (A and B) visualizes the temperature against the cycling frequency up to 3 Hz for maximal deformation of 8 % with the progressive increase of the creep: from 0 to 2 % in the first 100 cycles and increased to 2.5 % in the last series of working cycles. The figure 14 C shows the temperature increase associated to 8 and 16 Hz using reduced net deformations of 1 and 0.8 % that, respectively, remains under 10 K.

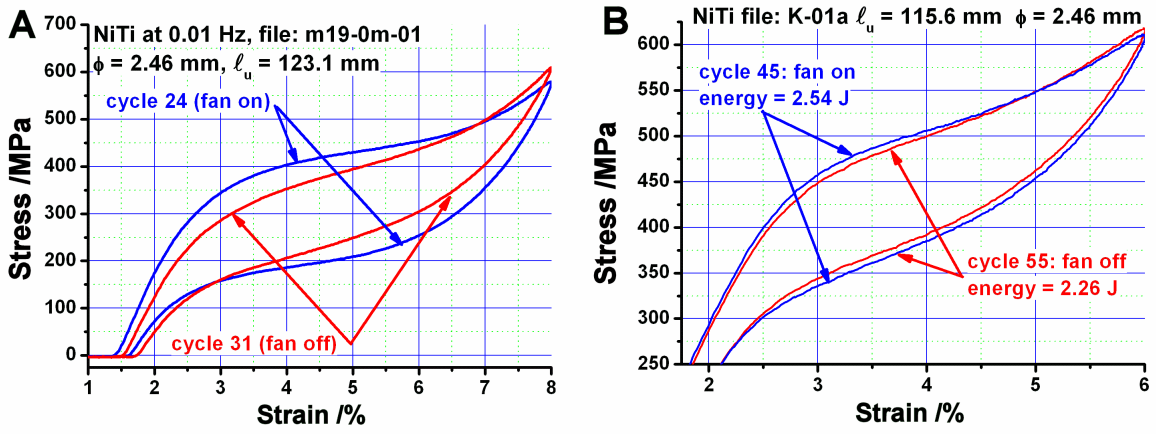

Figure 13. Hysteresis cycles for the same samples of the figure 12.

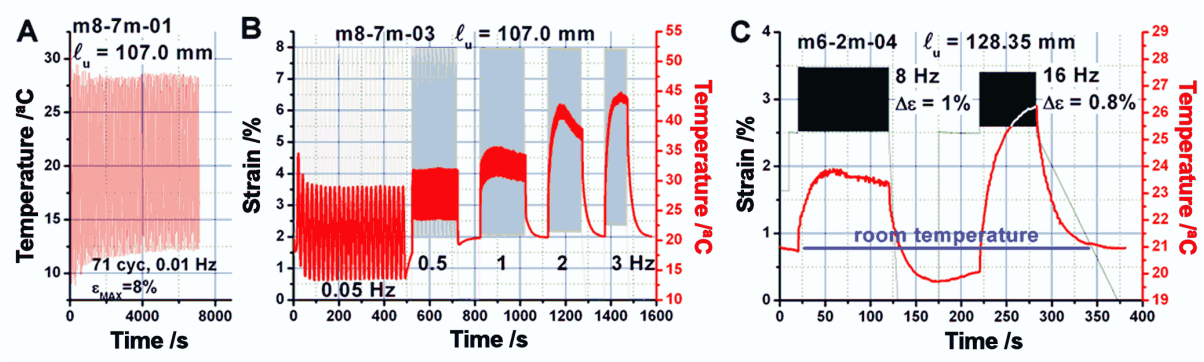

Figure 14. The temperature, frequency and creep effects. A: Changes in temperature for 8 % strain in cycles at 0.01 Hz. B: Strain and temperature for progressive increased frequency (up to 3 Hz) for available strains between 2 and 8 %. C: Temperature effects for faster cycling and reduced deformation: cycling frequency at 8 and at 16 Hz for respective strains of 1 and 0.8 %.

The main difference between samples with few cycles and highly cycled samples can be attributed to two mechanisms. The first mechanism was the distribution of the transformation throughout the entire sample (see below), while the second mechanism was associated with the SMA creep (2.5 %), which induced a latent heat reduction of approximately 30 % (i.e., 100*2.5 / 8 = 31 %). In terms of the entropy production in a pseudo-steady cycling state, the fan action induced more irreversibility (more heat transfer) and increased the entropy: the system response was to increase the hysteresis cycle energy.

3.6.3. Cycling frequency and hysteresis width

The hysteresis cycle was studied as a function of the cycling frequency for a maximal deformation of 8 %. The study was performed for sinusoidal cycles ranging from 3×10^{-5} Hz (33333 s) up to 3 Hz. Representative results are shown in figure 15. The plot of the hysteresis versus the frequency exhibits a "symmetric" shape [110-111] that is associated with the maximal deformation of 8 %. The A and B points were determined for the initial and the final cycles in the first set of measurements (dots). After a larger series of working cycles of mixed strains (up to 8 %), a subsequent analysis was performed (see the up-triangles in the figure 15). The results for the two sets showed similar approximately Gaussian behavior, with a maximum at 0.01 Hz. Analysis for the thin wires showed that the frequency of the maxima increased with the decrease in the wire diameter [110]. In practical damping applications, the working frequencies start near 1 Hz and the value is a function of the structure.

At extremely low frequencies, the heat produced in the transformation was completely dissipated to the surroundings and the sample temperature always remained at room temperature. The self-heating was almost zero for this slow process and the temperature effects were also negligible. The temperature rise upon progressively increasing the frequency up to 0.01 Hz. Larger and smaller forces were required for transformation and retransformation, respectively, as per the Clausius-Clapeyron coefficient. The hysteretic energy at 0.01 Hz decreased progressively with the increase of the SMA creep (see A, B and the triangles in figure 15). The dots in figure 15 correspond to a strain of 8 % and the triangles correspond to a net strain of 6.4 %, at a creep of 1.6%. Simulation of the SMA behavior requires careful examination of the frequency effects of the dissipated energy. For instance, experimental analysis of the dissipated energy associated to expected deformations and frequencies of the cable.

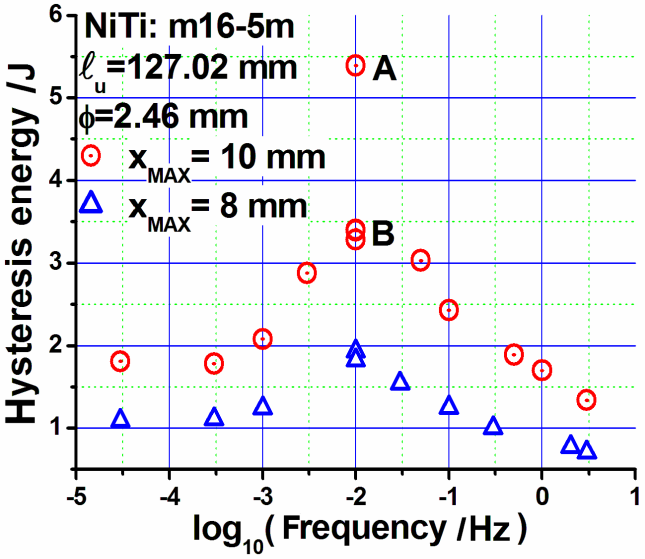

Figure 15. Hysteretic energy for two series of hysteresis cycles with a maximal strain 8 % in the same sample against the cycling frequency (up to 3 Hz). Dots: initial measurements (strain up to 8 %). Triangles: after several thousands of cycles. Net strain up to 8 %: the creep was suppressed.

3.6.4. Distributed transformation effects

The effects of cycling and the changes in heat transfer for a series of working cycles were determined by testing several standard and long samples. Figure 16 corresponds to a sample with a length of 508 mm. In this study, the sinusoidal strain (up to 8 %) was converted to strain steps (30 steps of 4 s in file 01) that were separated by pauses (196 s) with simultaneous measurement of the sample temperature by two thermocouples. The K-pairs were situated at 25 mm and 275 mm on the bottom grip (i.e., the bottom and "middle" positions of SMA wire). A new cycle (file 05) with 24 strain steps was initiated after a series of 100 working cycles at 0.01 Hz. Reducing the number of steps from 30 to 24 suppresses the SMA creep. Figure 16 A shows that the reduction of the stress steps, the hysteresis width and the energy were associated with the evolution of the transformation process for the complete set of the cycles. Each strain step induced a force step that corresponded to the temperature effect that was induced by the transformation step. Figure 16 B shows the temperature versus time for the measurements in figure 16 A. The temperature for file LL2-01 in figure 16 B exhibited slight oscillatory behavior that could be related to the room-temperature oscillations that were induced by the conditioned air. The measurements showed a reduction in the temperature-transformation pulses and a small increase in the other pulses. The main effect was the homogenization of the temperature steps that corresponded to 100 working cycles. The "fast" strain steps used a deformation of 0.27 % (1.35 mm in 4 s), so that the macroscopic action for a larger

sample was related to “one” minor transformation in the entire sample. The temperature was similar to that measured by the other K-thermocouple.

A progressive increase in the number of martensite domains with the deformation rate in cycling has been reported in the literature. This behavior was shown in the figure 2 b of a paper published by Y.J. He and Q.P. Sun [112]. If the local temperature for each front is assumed to be divided by the number of active domains of transformation (numbered from 1 to N), an increase in the number of domains results in the reduction of the local temperature that is associated with the transformation: figure 16 A shows that the stress peaks, which were mainly related to thermal actions, exhibited a clear reduction from cycle 1 to cycle 13.

Figure 17 shows the temperature effects for cycles at 2 Hz and a low net deformation of 0.59 % (3 mm) that were obtained after a larger number of working cycles. Similar temperature oscillations were measured in the two thermocouples at the bottom and middle of the sample (0.6 and 0.8 K, respectively). These low deformations appear to have affected the entire sample. In the first cycles, the transformation was localized in a portion of the sample, as indicated by the temperature peaks in figure 16 B. After a relatively high number of working cycles, similar temperature oscillations for reduced deformation in the entire sample were consistent with a distributed transformation that corresponded to a larger fracture-life. The transformation could be considered to be homogeneously distributed throughout the sample.

Using the same sample lengths, reducing the oscillatory strain resulted in a more complex transformation distribution than a pure homogeneous distribution. In particular, for deformations less than 2 mm (near 0.4 %) and close to the elastic regime, the measurements showed different behavior for the long samples: a portion of the sample underwent the transformation, while the rest of the sample remained in the elastic regime.

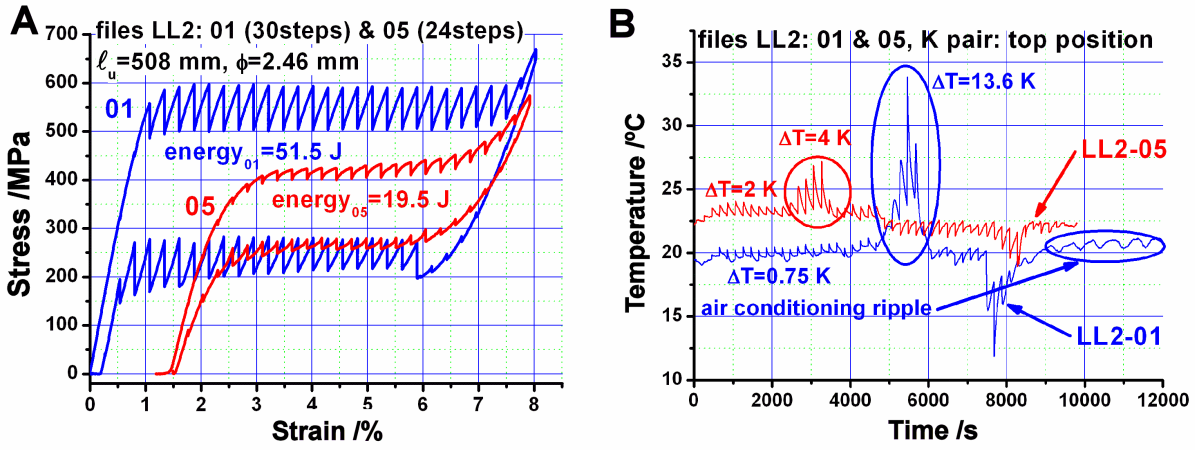

Figure 16. Results in two cycles realized by strain steps using a larger sample (508 mm). 11 cycles were realized between the files 01 and 05. (1): stress against strain. (2): temperatures detected near the top position for the files 01 and 05. The temperature associated to the dissipation decreases and the step effects increase.

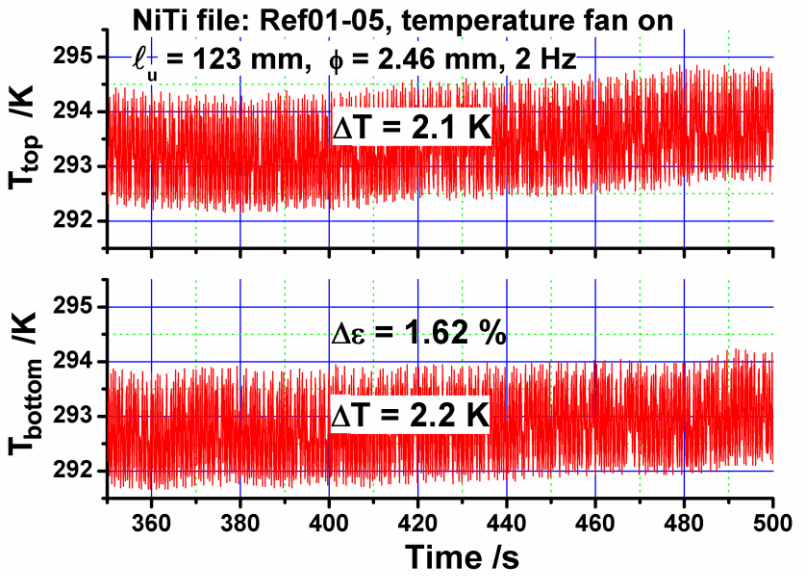

Figure 17. Cycling effects with a deformation of 1.62 %. Bottom: bottom thermocouple. Top: top thermocouple.

3.7. Seasonal temperature effects

Temperature variations between winter and summer modify the position of the hysteresis cycle in the stress-strain-temperature diagram. For the flat cycles of thin wires, the retransformation process does not occur at low temperatures, resulting in damper failure. Following sample transformation, the retransformation cannot be recovered and the SMA remains in the martensite phase. Appropriate training of the wire (2.46 mm of diameter) with approximately 100 or more working cycles before building the damper can prevent two parasitic effects: the creep remains invariant and the hysteretic behavior is converted to an S-shaped cycle.

Damping behavior was studied using external cooling-heating with the INSTRON equipment. To prevent parasitic creep effects, a previously cycled sample with an estimated "accumulated creep" of 2.5 % was used at a maximal net deformation of 5 %. The behavior of the sample temperature versus time and the associated hysteretic energy are shown in figure 18 A. The sample was cycled by ramps of 5% for a complete cycle of 20 s. The upper portion of figure 18 A shows the energy corresponding to all the working cycles and the lower portion shows the sample temperature as measured by a K-thermocouple. Figure 18 B shows that the measured cycles had a reasonable dissipated energy at several temperatures. At a low temperature, the low deformation portion of the SMA remained in the martensite phase and the available deformation was reduced. At 258 K the hysteresis cycle starts after the 2.5 %.

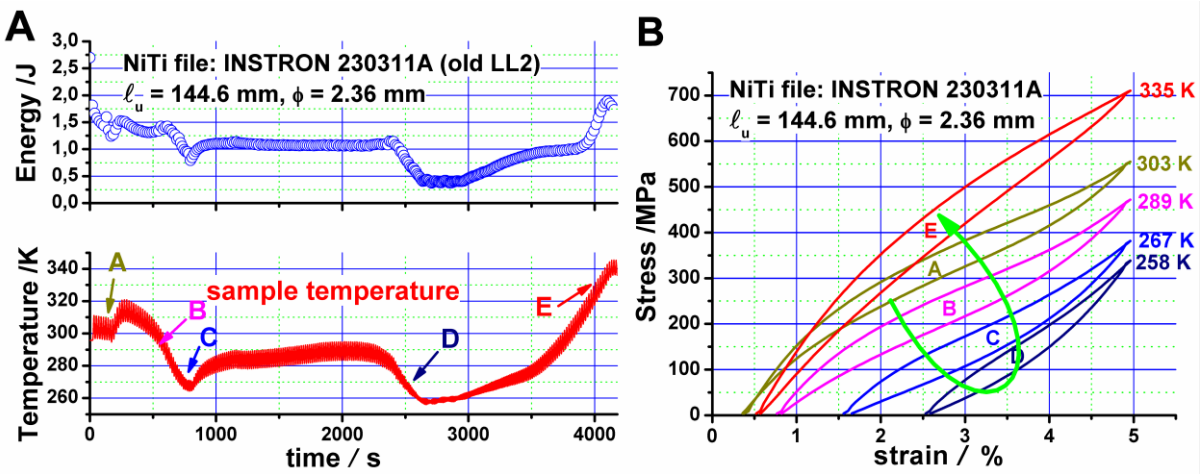

Figure 18. External temperature effects on cycling. A: Energy and sample temperature against time. HTT: High temperature effect. B: Hysteresis cycles for several working temperatures. "a": Grips adaptation. Arrow: hysteretic evolution associated to the effects of decreased and increased temperature, from cycle A to cycle E.

The experimental analysis showed that an S-shaped cycle (i.e., with a stress variation from 0 to 600 MPa) is advantageous for damper applications. Using a thin wire with flat behavior in the winter can situate the wire in the martensite phase without retransformation, resulting in no damping. The extended stress for transformation in the S-shaped cycles was associated with a larger temperature working domain. A stress of 600 MPa with a Clausius-Clapeyron coefficient near 6.3 MPa/K corresponded to a temperature span of 95 K. In practice, the working temperature domain would be reduced to 2/3 of this value, i.e., to 60 K or less. The stress-aging increases the working temperature domain (see, the section 3.10).

3.8. Energies at reduced strains: the frequency effect.

A larger fracture-life is expected at reduced stress (i.e., near 200 MPa), which corresponds to a low strain (i.e., under 1.5 %). An analysis was performed on the dissipated energies at reduced strains (under 2.5 %) and the frequency effects (figure 19 A, B and C). Figure 19 A shows the hysteresis cycles for several strains from 0.8 to 2.5 %. The energy was fitted (figure 19 B) by a second-order polynomial without a linear term. It was necessary to avoid negative energy values when fitting the lower strains. Figure 19 C shows strains of 1.5 % for frequencies between 0.5 to 18 Hz. The measurements were corrected for artifacts in strain by the MTS 810, associated with the increased frequency. At this level, the experimental observations showed that the hysteretic energy decreased linearly with the cycling frequency at low strains.

Using SMA with initial pre-stressing and with initial pre-strain ($\boldsymbol{\varepsilon_i}$), the SMA length changes from an initial strain $\boldsymbol{\varepsilon_i}$ to a final strain $\boldsymbol{\varepsilon_f}$. A rough estimate of the energy difference of the SMA (E_{SMA}) between the initial and final strain $E_{SMA}(\varepsilon_i \rightarrow \varepsilon_f)$ states is as follows:

$$\mathbf{E_{SMA}\,(\varepsilon_i \rightarrow \varepsilon_f) = E(\varepsilon_f) - E(\varepsilon_i)} \qquad (3)$$

The experimental results provided satisfactory data for the simulation of the dissipated energy as a function of the oscillation amplitude (figure 19 A and B). An evaluation of the cable frequencies is also necessary. The frequency values associated with the cable oscillating with the SMA damper should be determined (see, the section 3.11). A linear change in the energy with the cycling frequency was observed. The fit in figure 19 C permits an acceptable calculation of the energies including the effect of the damper in the cable frequency.

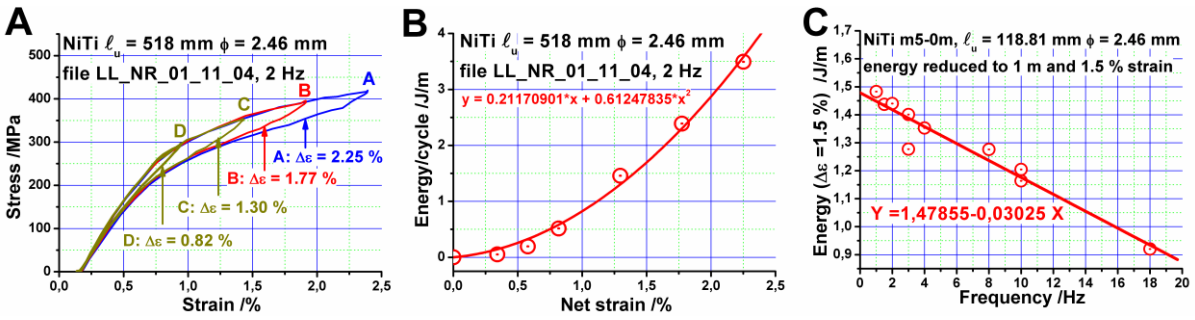

Figure 19. The hysteretic energy against deformation and frequency for 2.46 mm of diameter. A: Series of cycles realized at 2 Hz with deformation up to 2.25 %. B: Parabolic fit to the energies against the deformation. C: recalculated series of measurements to well established strains against the cycling frequency. At constant deformation (1.5 %) the calculated points fit satisfactorily by one straight line up to 18 Hz.

3.9. Scaling of the wire diameter

For comparative purposes, several samples of wire B (with a diameter of 0.5 mm) were studied. Figure 20 A and B shows the effects of cycling on a NiTi 0.5-mm diameter wire, at 16 minute/cycle and at 20 s/cycle, respectively, using ramps (i.e., a constant strain rate dε/dt). Cycling this wire reduced the creep evolution for the same number of cycles. Wires with two diameters (2.46 mm and 0.5 mm) were compared by scaling the measurements in figure 20 B in terms of the cycling and thermal characteristics. The frequency ratio was 1/5 of the diameter ratio. For the 0.5-mm diameter wire, time and diameter scaling could not reproduce the change in the SMA stress-strain behavior from horizontal cycles to S-shaped cycles. The internal NiTi properties were the critical determinants of the SMA creep values and the shape of the transformation for the wires with different diameters.

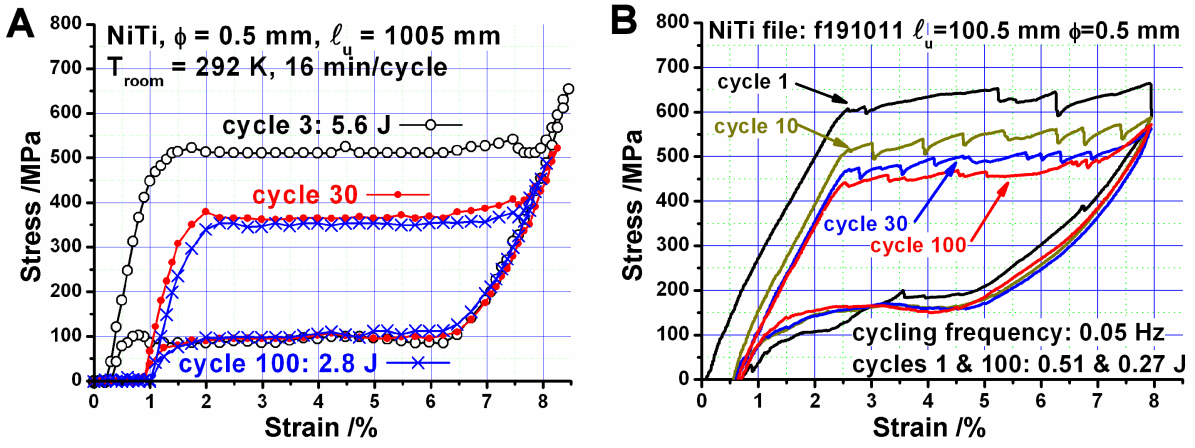

Figure 20. Cycling effects for wires of 0.5 mm. A: Slow cycles (3, 30 and 100) at 16 min/cycle. Cycle 3: 5.6 J, cycle 100: 2.80 J. B: Cycles at 0.05 Hz in a shorter sample. Cycles 1, 10, 30 and 100. The ripple in cycle 1 was the nucleation effect. The accumulated SMA creep not overcomes 1.5 %. Cycle 1: 0.95 J, cycle 100: 0.38 J.

Supplementary measurements were carried out in this work using a wire diameter of 0.1 mm. The creep deformation was negligible. The two cases in figure 20 show that the SMA creep did not exceed 1 or 1.5 % for 100 working cycles. The cycles always showed the classical flat parallelogram shape of the classical NiTi wires and the hysteresis width remains close to 250 MPa..

Note: The ratio between the thermal mechanisms in a wire of length ℓ with a diameter d is related to the ratio between the bulk effects ($(\pi/4)\ d^2\ \ell$) and the heat losses ($\pi\ d\ \ell$).

In seeking a "natural" scaling of the time and cross-section of the wires, the diameter ratio was not found to be an appropriate scaling parameter for the NiTi wires studied. Grain diameter effects and/or cold working effects in the wire preparation by the furnisher were the determining factors. The experimental measurements suggest that extrapolation is rather difficult and that each diameter requires particular study due to internal differences.

3.10. Stress and temperature aging

This study was performed under "extreme" conditions to determine the upper limit of the effects of aging. Continuous aging was studied at a temperature of 373 K. The calorimetric and transformation temperature from resistance curves in figure 21 show a monotonic and irrecoverable change in the Rs temperature of approximately 20 K/year. The figure 21 B shows that a reduction of the "aging" temperature (i.e., near 200 days) not reduces the transformation temperature. This specific behavior for the used alloy nearly did not affect the critical transformation stress or the stress-strain hysteretic behavior. Therefore, the effect of temperature aging on damping could be neglected [113-114].

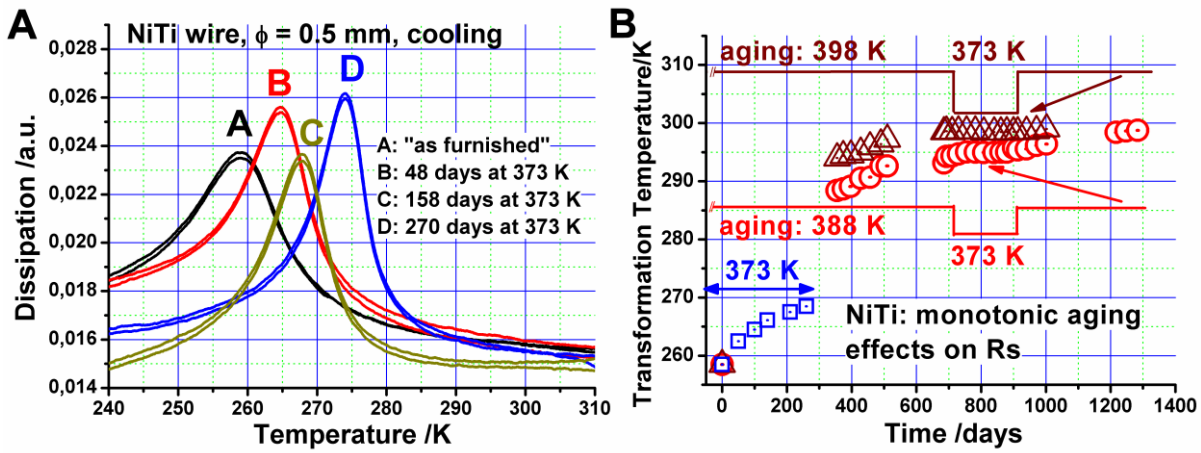

Figure 21. A: Calorimetric measurements of temperature aging effects at 273 K on Rs. A: as furnished. B: 48 days. C: 270 days. B: Transformation temperature from electrical resistance measurements, monotonic increase of the observed transformation temperature against aging time, at temperatures of 373 K, 388 K and 398 K. For the two later aging temperatures, a decrease to 373 K does not produce a recovery of transformation temperature.

Experiments were performed to ensure that the static pre-stress aging [115-116] was practically not relevant for the SMA state for damping oscillations in cables. A preliminary analysis was performed using type B wires (0.5-mm diameter). After one month, a half-transformed sample exhibited a small step in the stress-strain curve. The stress was reduced in the martensite portion of the sample, so that increasing the amount of transformation required an additional stress. Several devices were developed for a more in-depth study with type A wires (2.46-mm diameter) (see figure 22). Figure 22 A shows the static device. The sample was fixed firmly by the cubes A_1 and A_1'. When the bolt D_1 turned in an appropriate direction, the axis B_1 progressively separated A_1 from A_1', increasing the length of the sample. Figure 22 B shows the element situated directly in the MTS. First the stress on the sample was reduced to zero. Later, the lateral bolts C_1 and C_1' were used to fix the A_1 and A_1' cubes in place. The grips of the equipment were used to fix the C_1 - C_1' axis. The oscillatory behavior of the MTS produced vertical oscillatory displacements of the bottom grip and the sample. The bottom axis in C_1' could slip because of sample displacement. For

instance, suppressing any increase in the sample length of the sample from SMA creep or compressive action. The x at figure C represents the position of the room temperature thermocouple and the two empty dots represent the positions of the two K-thermocouples in the sample. The wires did not increase in diameter at the ends (unlike bone samples) and the cubes fixed the sample position. Small holes in the cubes enabled the lateral bolts of C_1 and C_1' to fix the cubes. Fixing the sample with the two cubes and the associated C_1 and C_1' bolts, which were firmly held by the hydraulic grips, facilitated the sample measurements. A series of systematic measurements was planned in advance. The samples were accordingly positioned in the MTS or INSTRON equipment. Figure 22 C also shows the positioning in the sample in the MTS equipment and relative to the surroundings, the fan (F_1), the room-temperature sensor (x) and the two wrapped thermocouples (empty dots), which were used to measure the sample temperature.

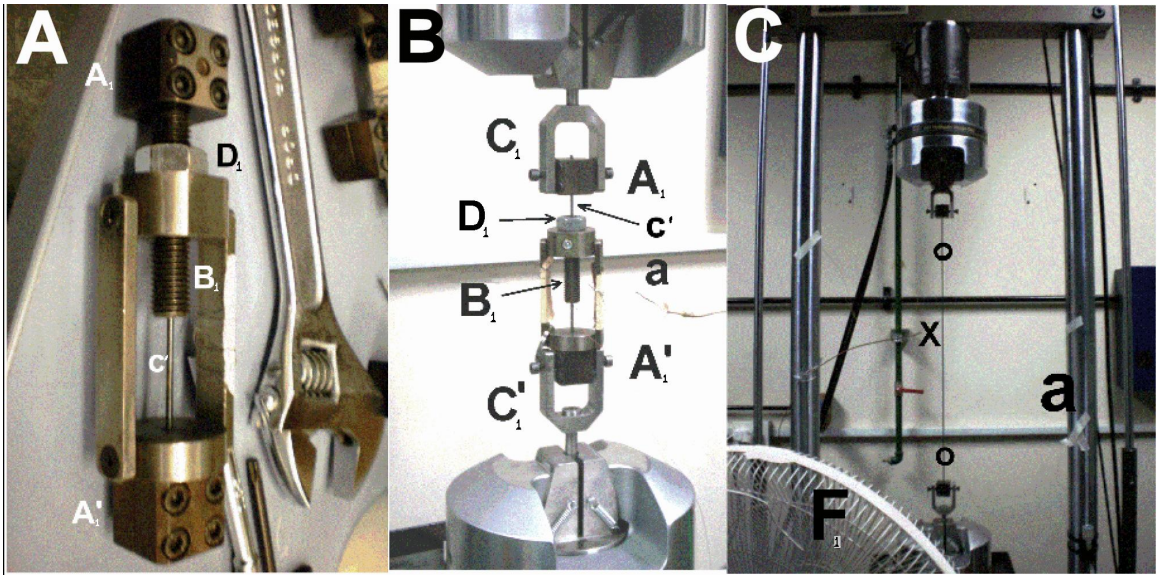

Figure 22. The static stress-temperature-aging studies. A: Pre-stressing device for samples with length close to 160 mm. A_1 and A_1': the cubes that fasten the ends of the sample "c' ". B_1 and D_1: screw and the associate bolt; turning allows the change of the sample length. B: Working in traction using conventional equipment (i.e., one MTS 810). A_1 and A_1' the cubes fixed in C_1 and C_1' (the MTS supports); B_1: screw; c': SMA wire; D_1: bolt. C: Study of a length wire; a: room temperature thermocouple; F_1: fan unit; o: K-thermocouple; "x": near the sample K-thermocouple.

Figure 23 shows several examples of the effects of stress-temperature aging. Figure 23 A shows an "as furnished" sample that was subjected to a strain of 4.5 % for 3 months. The figure shows that the first cycle was clearly affected by aging. After 100 cycles, the changes in the shape of the hysteresis curve modified the aging effects. Changes in the sample were reduced and/or suppressed in the 100th cycle. Figure 23 B shows a virgin sample that was subjected to a 6.8 % strain (near complete transformation) for 7.5 months, resulting in a reduction of the hysteretic width. The total stress is increased, compared to a standard sample, from 600 to 900 MPa (i.e., 40 MPa/month), in qualitative agreement with the results in Figure 23 A (with minor time and minor strain %). Figure 23 C shows a previously cycled sample that was subjected to a 6.8 % strain for 1.5 months for which the total stress increased from 600 to 850 MPa. Later, the sample was stored at room temperature under no applied stress for an additional year. A new series of working cycles was performed: figure 23 C shows the reduction in the changes in the sample at the new 100th cycle. The results in Figure 23 A reflect the effect of re-positioning on the sample.

The measurements showed that the effects of aging effect were greater for previously cycled samples. In the virgin samples, the induced actions partially disappeared in the training cycles (i.e., 100 cycles at 0.01 Hz for a strain of 8 %). In any case, several months at 373 K with strain of 8% modify the hysteretic behavior. Advancing the transformation required a progressive increase of the

stress of up to 50 % (from 600 to 900 MPa). The stress-temperature-time actions induced "permanent" or irrecoverable structural changes in the samples. These effects remained in a sample after one year at room temperature without any applied stress (i.e., figure 23 C). These effects are not practically relevant for the use of dampers in the desired application. One year of working in a cable at the maximal temperature during sunny summer days (i.e., 40 °C or 313 K) did not exceed 30*86400 ~ 2.6×10^6 s, i.e., 30 days. Moreover, the typical pre-stress was approximately 1 kN (i.e., 200 MPa). Under these conditions, at reduced temperatures, stresses and times, the effect of static stress-temperature aging can be neglected.

External temperature changes were shown to be insignificant in aged stressed samples. After appropriate stress-temperature aging, the S-shaped behavior was associated with a working domain of 800-1000 MPa. Under these conditions, the associated temperature interval exceeded 125-150 K, compared to 95 K for the samples with a stress of 600 MPa that were used in section 3.7. Annual temperature changes of 60-80 K can be "absorbed" by a damper constructed of aged wires. A specific study of the fracture-life of these aged samples is necessary but remains out of the scope of this work.

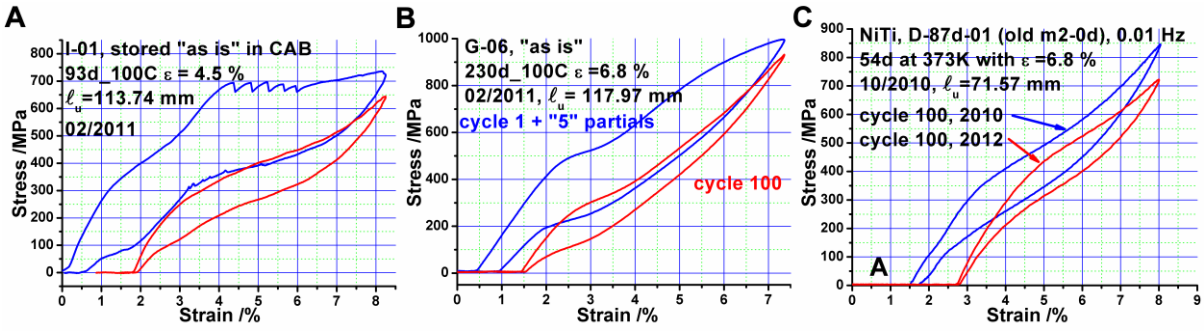

Figure 23. Temperature-stress aging in NiTi. A: cycle 1 and 100 in a sample with 3 months at 4.5 %. B: Cycle 1 and 100, sample with 7.5 months at 6.8 %. C: cycle 100 after an aging of 1.5 months at 6.8 % in a previously cycled sample. Cycle 100, 2012 was the cycle 100 of a series of working cycles realized after a year at room temperature and stress-free.

3.11. Studies on NiTi SMA in experimental facilities

Three measurement studies were carried out at the experimental facilities. One study (in September 2009) was conducted on cable No. 1 at the ELSA Laboratory. ELSA is a part of the Institute for the Protection and Security of Citizens (IPSC) in Ispra (Italy) at the Joint Research Centre (JRC) of the European Commission. Two studies were conducted in October 2009 and in December 2010 at the "Institut Français des Sciences et Technologies des Transports, de l'Aménagement et des Réseaux" (IFSTTAR), Bouguenais, near Nantes, France using 50-m length and 57-mm diameter steel cable without any additional damping materials.

3.11.1. ELSA measurements

A series of measurements was conducted on the cable investigated (see, a general overview of experimental system in figure 24). ELSA cable No. 1 was 45 m in length (cable length: L). The cable was built from 4 sets of wires (of a 15-mm diameter) inside a protective polyethylene tube with an external diameter of 75 mm that was refilled with wax. The ELSA cable was inclined at 21° and subjected to 250 kN of the traction force. Only one 2.46-mm diameter NiTi SMA wire was used (see figure 25): after training, the used wire length was 4140 mm. For a maximum peak-to-peak oscillation amplitude of 120 mm, the strain in the SMA wire did not exceed 3 %. Damping typically reduces the oscillation amplitude by half. When the maximum amplitudes were reduced to one-half or less (± 30 mm), the damped strain remained under 1.5 %. The hypothetical strain for file s071 without a SMA was 2.7 %. During working, the strain in the SMA was relatively low: file

s079 in figure 26 exhibited a maximum strain of approximately 1.3 %. This value was reasonable in terms of the large SMA fracture-life.

A vertical force was tentatively applied by hand to the cable at 27 % of its length to induce oscillations at resonant frequencies. The SMA damper was also installed vertically at 22 % of the cable length. Figure 26 shows the effect on ELSA cable No. 1 (which was 45 m long) and the associated frequencies. Figure 26 A shows the comparatively free and damped oscillations from measurements of s071 and s079. At steady state, the SMA damper reduced the oscillation amplitude by 1/3. The fracture studies showed that the SMA length was consistent with a larger fracture-life [117]. A Fast Fourier Transform (FFT) with and without a SMA (figure 26 B) showed that frequency changes from 1.8 to 2.03 Hz were induced. The action of the damper on the structure was extremely reduced: the overall change in frequency did not exceed 10 %.

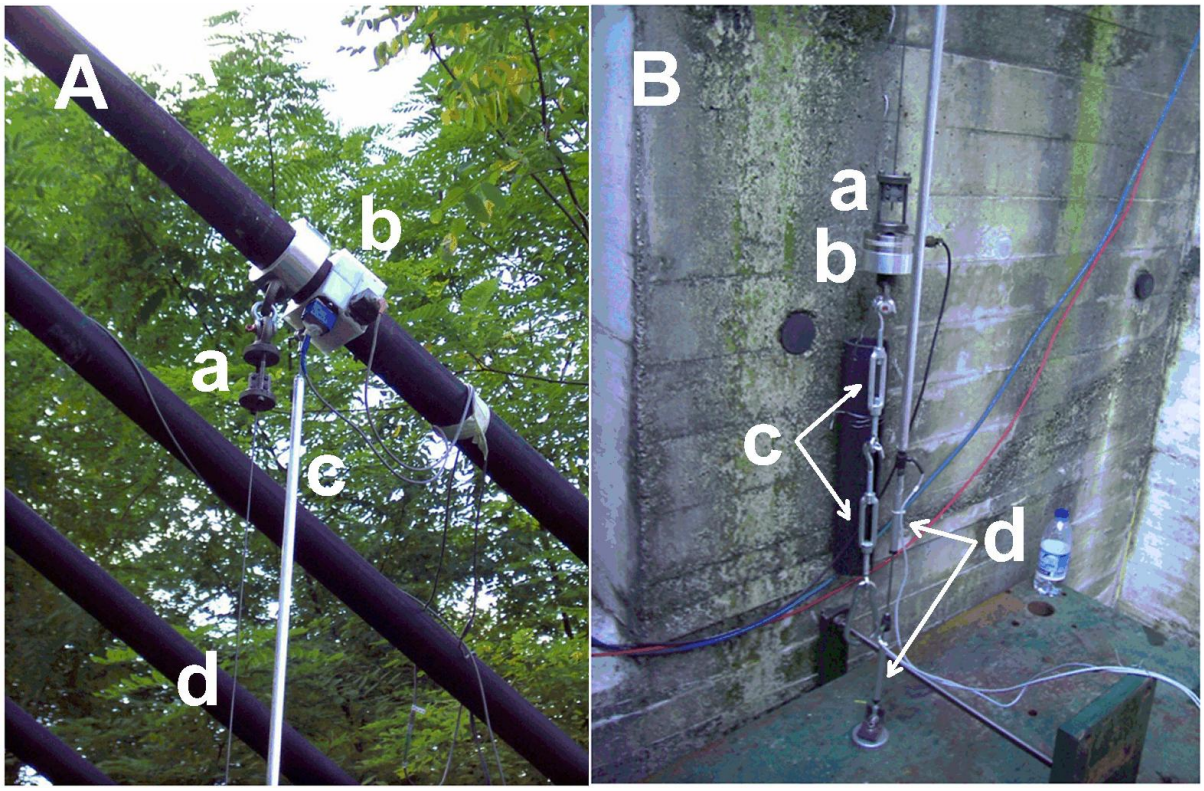

Figure 24. The ELSA cable No 1 and the mock-up. A: Devices in the attached to cable No 1. A: SMA fixing device (see, figure 25). b: accelerometers. c: bar connecting the LVDT situated in the bottom. D: SMA wire. B: devices in the bottom. a: fixing device for the SMA wire. b: force sensor on the SMA. c: tensor devices for the SMA wire. d: the addition of two LVDT ensures appropriate measurements.

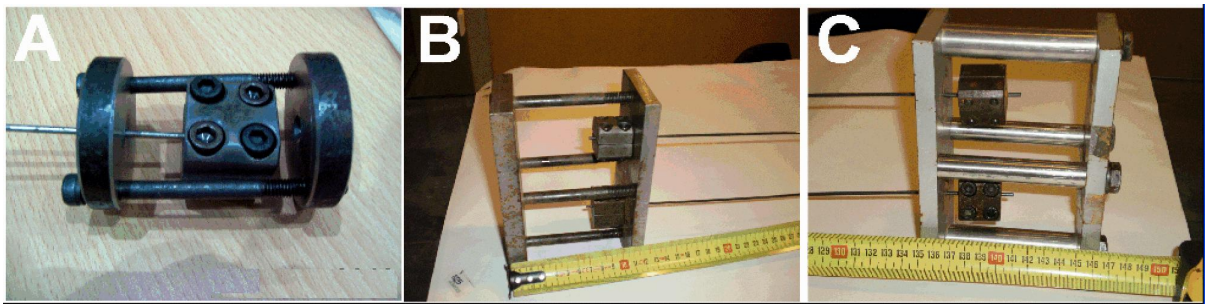

Figure 25. Fixing devices for the SMA wire for only traction connections. A: used for a single wire (similar with the outlined in figure 17). B and C: used in IFSTTAR; permits simultaneously one, two and three SMA wires.

The time-frequency analysis (shown as dots in figure 26 A) shows that the use of the SMA wire affected a small change in the frequencies with time. According the shape of the hysteresis cycle the SMA stiffness (k_{SMA}) progressively decreased with increasing strain. The macroscopic observed frequency corresponded to the parallel actions of the SMA stiffness and the cable stiffness (k_{cable}). At lower strains, the effect of the SMA decreased when the strain increased and vice versa in the retransformation. Progressive increases in the oscillation amplitude induced increased deformation (in the parent to martensite transition). The overall effect was that the SMA progressively reduced the overall strength with a small decrease in the frequency (i.e., from 10 to 45 s, see figure 26 A). In the martensite to parent transition, the effect of the SMA was to increase the strength and the local frequency (i.e., from 50 to 90 s, in figure 26 A).

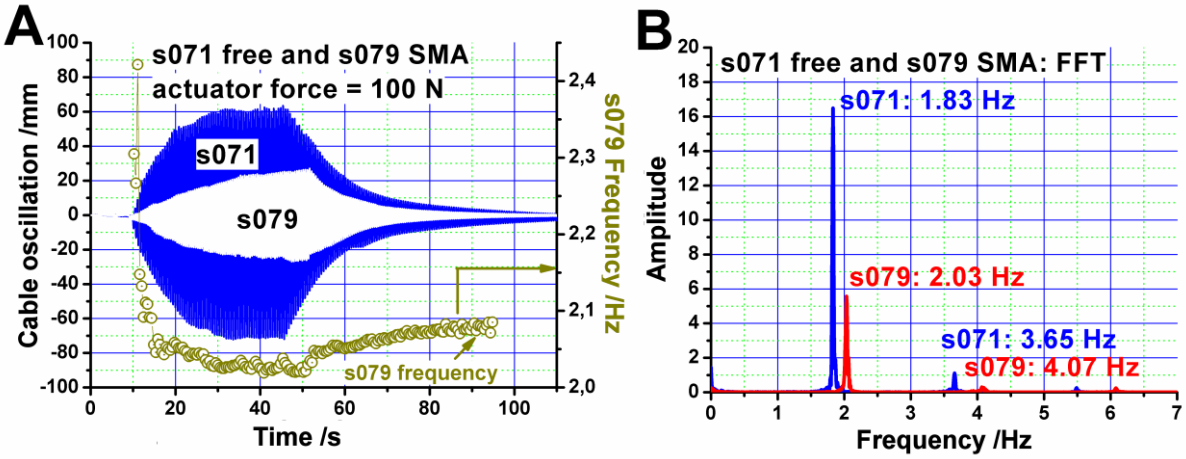

Figure 26. ELSA, cable No 1: experimental ELSA cable oscillations (measurements s071 and s079). A: equal excitation (98 N) at resonance frequencies without and with SMA damper. Dots: direct calculation of the frequency against time in the measurement s079. B: frequencies determined by the FFT.

3.11.2. Measurements performed at the IFSTTAR facility.

Only transient measurements were conducted on the IFSTTAR cable, which had a length (L) of 50 m under 1000 kN (figure 27). A force f was applied orthogonally to the cable to produce an appropriate displacement. The force was then suppressed suddenly, resulting in cable oscillations that slowed and progressively were slowed down. The oscillatory motion was established by the decay of the Heaviside step function. Figure 28 shows the locations of the actuator and the detector at the center of the cable (at L/2); the action of the force was a Heaviside step function with a magnitude of 4 kN. In this case, two trained 2.46-mm diameter wires with lengths of approximately 1260 mm were used (figure 27 B). This SMA wire length did not correspond to a large fracture-life. The available experimental wire was shorter than the wire length required for a large fracture-life [117]. The appropriate SMA length (ℓ) for an IFSTTAR damper should be 3 m for a displacement of approximately 1 or 1.5 % of the peak-to-peak oscillation amplitude.

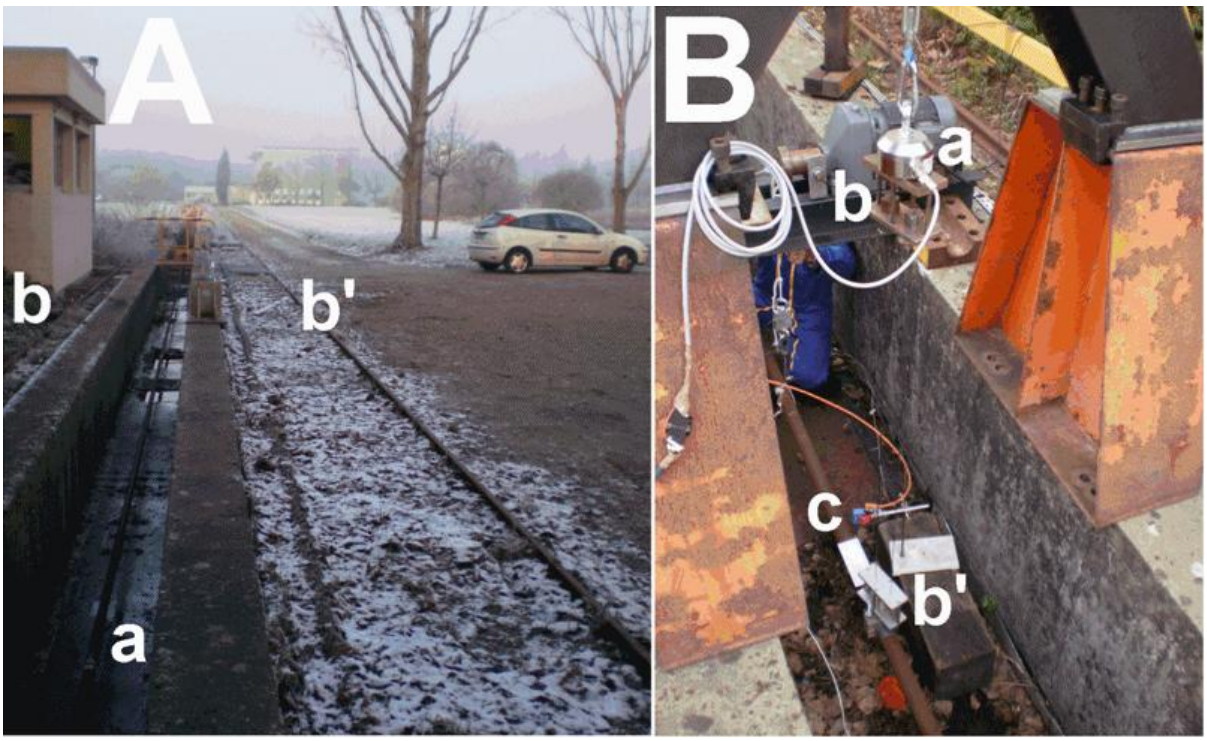

Figure 27. The IFSTTAR cable. A: general overview. a: the 50 m cable. b and b': rails for displacement of the motorized Laboratory equipment. B: measurements devices. A: force sensor on the SMA. b and b': fixing the SMA (see, the figure 25). c: laser sensor determining the position of the cable against time. (Reprinted from Engineering Structures vol. 49, V. Torra, C. Auguet, A. Isalgue, G. Carreras, P. Terriault, F.C. Lovey: Built in dampers for stayed cables in bridges via SMA. The SMARTeR-ESF project: A mesoscopic and macroscopic experimental analysis with numerical simulations, pages 43-57 (2013), with permission from Elsevier)

The damping measurements from 2010 showed a small increase in the time constant value compared to the measurements performed in 2009. For the first set of measurements, which were performed at the center of the cable at L/2, the oscillations decreased to "zero" in time intervals of approximately 10 s (see figure 28).

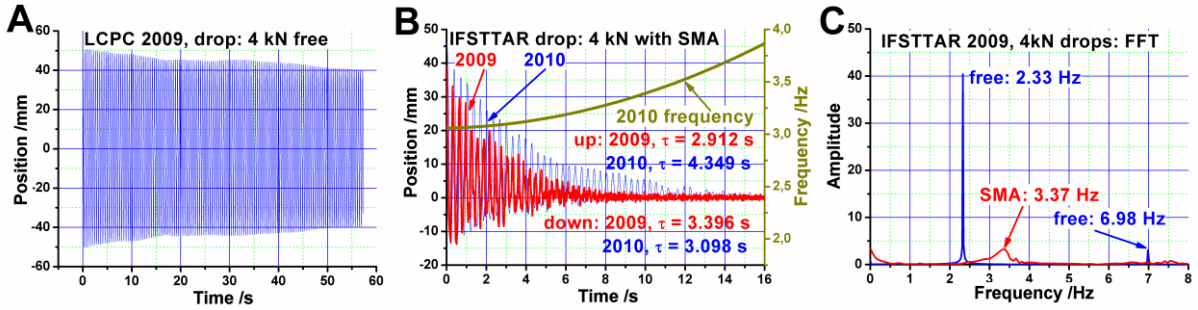

Figure 28. Measurements in the IFSTTAR cable associated to a Heaviside step. A: free oscillations. B: oscillations using the SMA damper in 2009 and in 2010 campaigns. Upper line: fit to local frequency changes. C: frequency spectrum by the FFT to free (A) and damped (B-2009) signal.

The 2010 measurements were performed for different positions of the cable actuator and the measurement sensor (L/4, L/8, …). The damping action of SMA was clearly effective at each position, but became progressively less intense. Figure 28 B shows the evolution of the frequency with time corresponding to the action of the SMA (Δf was approximately 0.7 Hz). The FFT (see figure 28 C) results showed a change of 1 Hz between the free and the damped cable, as well as a corresponding reduction in the oscillation amplitudes. The more relevant change in the frequencies from approximately 2 to 3 Hz, or an increase of 40 %, was associated with the use of 2 wires, under a smaller pre-stress, but more force on the cable that in the ELSA measurements. The training at

ELSA included 100 working cycles, while the training at IFSTTAR used only 20 slow cycles that increases the SMA strength. The decay in the IFSTAR cable was similar to that observed in the ELSA cable. For the IFSTTAR cable, the oscillation amplitude was transitory and decayed: the effect of the SMA on the cable was to increase the overall strength and the static and the time-frequency values.

3.12. Simulation: a phenomenological model for SMA behavior

The numerical simulation of damper behavior required models that satisfactorily capture the properties of the SMA wires. Simulating SMA behavior by Finite Elements analysis using ANSYS required the development of a dedicated routine called USERMAT. Two versions of the routine were implemented based on phenomenological models of the hysteresis cycle. The first version used a rudimentary representation of the bilinear model and is denoted by "a" in figure 29 A. The "elastic" line Oa denotes a net deformation up to 1.1%. The second version that is shown in the figure was based on the cubic model and produced predictions that agreed completely with the experimental cycles at low strain. The bilinear model behaved elastically at deformations up to 1 %, so the simulated damper did not convert mechanical energy into heat and the calculated oscillation amplitude remained constant. Reference 12 provides an example of the use of the bilinear model in SMA damping of the oscillations of stayed cables: a fast initial decay of the oscillation amplitude was calculated. At later times, the oscillation amplitude remained constant (see, below, an example in figure 31 A).

The experimental measurements in figure 29 A showed energy absorption for strains as low as 0.4 %: the bilinear model clearly cannot capture such phenomena. The experimental cycles motivated the development of a phenomenological cubic model. The model is called "cubic" because the loading and unloading paths of the cycle are represented by polynomial cubic equations. The model was constructed using four points from the loading and unloading paths of an experimental curve. Both paths were constructed by using the same first (M_0) and last (M_e) points. Two other points for the loading path (L_1 and L_2) and for the unloading path (U_1 and U_2) were selected from the experimental curve. In the example considered, the coordinates were extracted from the data represented in figure 29 A (see table 2).

Table 2. Data for the cubic fits.

Point	**M_0**	**M_e**	**L_1**	**L_2**	**U_1**	**U_2**
ε (m/m)	0	0.0636	0.0166	0.043	0.0112	0.045
σ (MPa)	0	531	252	350	52	200

The coefficients, c_0 to c_3, of the cubic polynomial equation $\sigma = c_3 \varepsilon^3 + c_2 \varepsilon^2 + c_1 \varepsilon + c_0$ were determined by forcing the curve to pass through the four selected points. Of course, different polynomial equations were obtained for the loading and for the unloading paths. Very good agreement with the experimental data was obtained by selecting appropriate data points.

3.12.1. Constructing partial loops

Partial loops could be immediately constructed using the bilinear model. At the return point of the "transformation" line, the path was parallel to the elastic parent (or martensite) up to the arrival at the retransformation path. When the external load did not exceed the end point of the elastic regime ("a" in figure 29 A), the hysteretic area was zero and the damper did not produce any damping action. With the bilinear model, the initial and the final section of the loop were usually equal in slope. For partial loops, the path was parallel to M_0-a.

Constructing partial or internal loops within the cubic model is fairly complex and requires a working hypothesis. For partial cycles inside the hysteresis cycle, another polynomial equation was derived by selecting the data points and the slope at the beginning and end of the partial cycle. Partial cycles starting at ε* were generated by fitting a fourth-degree polynomial (curve B in figure 29 B)) to the three points ε*, a, and O, which corresponded to the return point, 20 % of the associated deformation (O-a) and the origin (O) of the hysteresis cycle. The fit used two slope values from the retransformation curve at M and at O (i.e., s_1 and s_2). The return point of the internal loop ε^r used two transformation slope values (at O and at M) and at the three points, ε^r, b and M. The fit (curve C) remained relatively close to ε*. The choice of 20 % for the initial (a) and residual deformation (b) corresponded to a satisfactory asymptotic fit of the calculated curves to the experimental data. Experimental tests were performed to compare the experimental energy with the calculated energy for the partial loops. The differences between the experimental and calculated energies were under 20 %. The complete hysteretic cycle was used in this approach. The reduced transformation cycles can always be fitted as well, as described in Section 3.8.

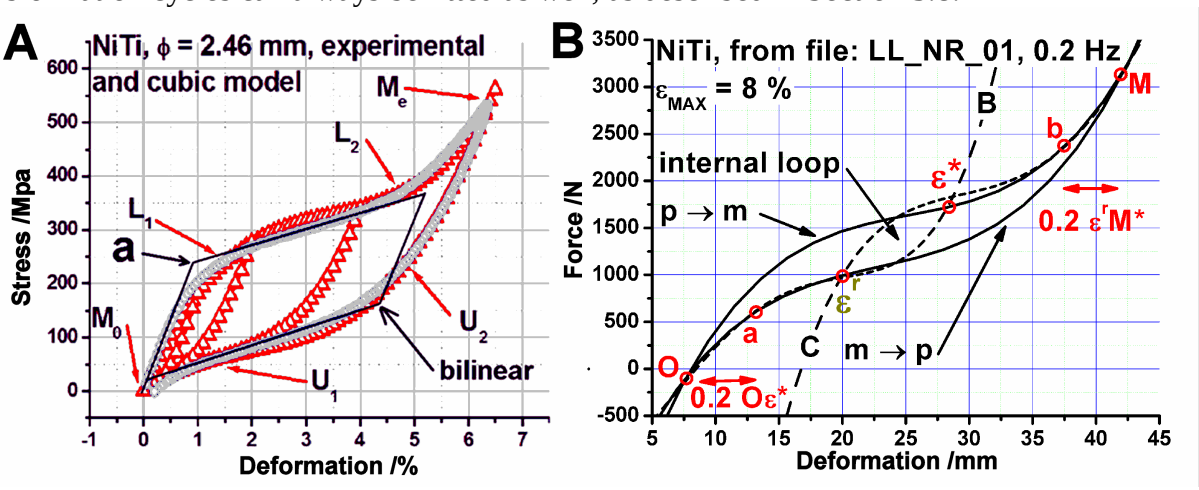

Figure 29. Bilinear and cubic models in SMA simulation. A: Cubic fit and bilinear model (OABCD). B: partial loop as measured and calculated using a fourth order polynomial.

In addition to simulations, the dissipated energy of the SMA damper can be directly evaluated using a quadratic fit of the hysteretic energy plotted against the SMA deformation. For the level of pre-stressing used, the phenomenological approach was used to calculate the frictional energy by multiplying the experimental maximal displacements of the cable by the energy extracted from fitting the energy versus deformation curve in figure 19 B. The result was used for the appropriate cable frequency determined via the figure 19 C.

3.12.2. Simulation of the ELSA experimental measurements

The ELSA cable was 45 m long and inclined at 21° from the floor to a high position in the ELSA main building. Figure 30 shows the simulation results for the ELSA cable. The tension in the cable was 250 kN, the simulations actuator (a vertical force) was applied to the cable at 27% of its length (near the end of the cable on the floor). The SMA damper was installed vertically at 22% of the cable length on the same side. The model was built using finite element software ANSYS 13.0 with a Mechanical APDL interface. The cable was represented by 100 beam elements (BEAM3 element type) and both extremities were clamped (i.e., the displacements and rotation were set to zero). The cable data showed that the cable cross-section was made of four stranded steel cables (E = 200 GPa), each with a 15-mm diameter, that were inserted into a polyethylene sheath (E = 600 MPa) with a 3.5-mm thickness and a 76-mm external diameter. The sheath was filled with wax (E = 27 MPa). The cable had a mass per unit length of approximately m_L = 9.8 kg/m.

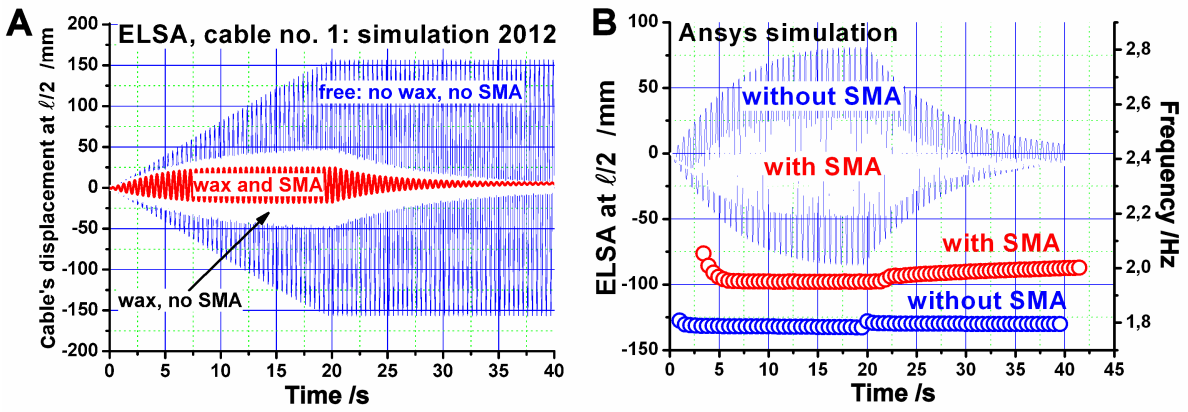

Figure 30. ELSA, cable No 1, displacements at the center. A: Simulation with wax (free cable) and with a damper by only one wire of SMA. The situation without wax was unavailable from experiments, but is shown here as simulation. B: direct determination of the frequencies on the ANSYS simulation. The experimental behavior is shown in fig. 26 A

Given the dimensions and the material properties of the cable, the Stiffness-Inertia (EI = 35 400 Nm^2) and Stiffness-Area (EA = 1.3×10^8 N) products were calculated for the entire cable cross-section. An equivalent density ρ*, Young's modulus E* and inertia moment I* were defined to simulate a uniform circular beam with the same properties as a cable made of different materials. Given the cable length and cross section of L = 45 m and A = 0.0045 m^2, respectively, and the following known values for the products of the real cable (m_L = ρ*A = 9.8 kg/m, E*I* = 35 400 Nm^2, E*A = 1.3×10^8 N), the equivalent properties of the cable were ρ* = 2175 kg/m^3, E*= 29 GPa and I* = 1.2×10^{-6} m^4.

The damper was modeled as a single bar element (LINK180 element type), which was attached to the cable at one end and pinned to the ground at the other end. The damper was considered to be a single NiTi wire, which was 4 m long with a 2.46-mm diameter. The SMA behavior was described by the cubic model and implemented in ANSYS through the USERMAT architecture. The cable was excited by a sinusoidal force varying between 0 and 100 N, at a frequency of 1.81 Hz for the free cable and a frequency of 2.04 Hz when a damper was used. After 20 s of excitation, the force was released and the cable oscillated freely for another 20 seconds. The numerical approach calculated the behavior of the "steel cable" alone, the effect of the wax and the action of the SMA damper: the frequencies were directly evaluated from the simulation results with and without the SMA. The experimental results agreed perfectly with the simulation, showing the relevant and clear effects of damping by the SMA for stayed cables embedded in wax inside a polyethylene sheath.

3.12.3. IFSTTAR cable simulations

The transitory behavior of the IFSTTAR cable was measured. In this case, the cable started oscillating under the action of a Heaviside step function. The situation was dynamically different from the measurements performed at ELSA where the oscillations were induced by periodic and resonant actuations. At IFSTAR, forces of 1, 2, 3 or 4 kN were used to displace the cable. A sudden termination of the force (corresponding to a Heaviside decay function) produced spontaneous oscillations that decayed because of the action of frictional forces on the cable.

The simulation for the IFSTAR cable was similar to the ELSA simulation but was adapted to the IFSTTAR horizontal cable, which was 50.5 m long with a mass per unit length of 16.1 kg/m. The IFTSAR cable was made of steel (E=200 GPa) with an initial tension of 960 kN. The cross-section of the cable was made of 159 stranded wires forming a core and 7 additional layers. The outer diameter, cross-sectional area and moment of inertia were 55.6 mm, 1936 mm^2 and 3.03×10^{-7} m^4,

respectively. Figure 31 summarizes the simulation results. Figure 31 A shows the results obtained by using the bilinear model, which inaccurately predicted the damping effect for the small oscillation amplitudes. Figure 31 B shows that the cubic model produced results that were similar to the experimental measurements.

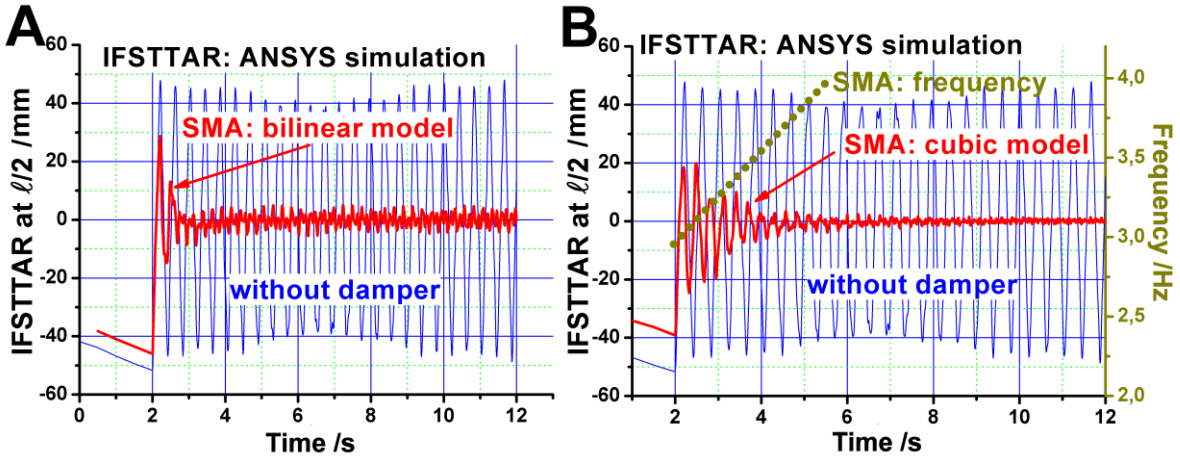

Figure 31. Simulation: free and damped oscillations. A: bilinear SMA model. B: cubic SMA model. Dots: evolution of the frequency from the simulation.

3.13. Constructing a SMA damper

A SMA damper should be constructed to realize the desired damping action in the requisite cables. It is necessary to establish appropriate criteria for an SMA length that corresponds with the requisite fracture-life. Two requirements are mandatory for an appropriate and efficient damper. The first requirement is related to the length of the SMA wires that will be used with a large number of working cycles. The SMA dampers are required to damp the oscillation amplitude by half or less. Let "x" denote the acceptable residual amplitude after damping. The required length (ℓ) for the SMA wires, which must endure the anticipated millions of working cycles, must ensure that the oscillation amplitudes do not exceed 1 %. The length (ℓ) can be related to the oscillation amplitude (x) as follows:

$$0.010\,\ell = x(NiTi) \qquad (4)$$

Table 3 shows the available data for the cables at ELSA and IFSTTAR and an indoor cable at the Pavia University [118-119], which was used to provide an extreme comparison. The Pavia university cable was a thin steel cable with a 2-mm diameter to which several lead balls were attached to increase the cable inertia to reduce the experimental frequencies to approximately 5 Hz. The cable uses one SMA wire with 0.1 mm of diameter.

Table 3. Dampers in ELSA, IFSTTAR, and Pavia.

facility.	L m	SMA (wires)	length(ℓ) mm	NiTi SMA ϕ in mm	σ (cable) in MPa	traction force	f_{SMA} near	cable diameter	Δx mm	f Hz
ELSA	45	1	4140(*)	2.46	283	250 kN	1.5 kN	4*15 mm	60	2
IFSTTAR	50	2	1260(X)	2.46	390	1000 kN	3 kN	57 mm	50	3
Pavia	2.36	1	1229(**)	0.1	43	133.8 N	2 N	2 mm	40	5

(*) appropriate length with larger fracture life.

(^{X}) shorter length inducing reduced fracture life.
(**) fracture life that requires deeper study

For the second requirement, the SMA force was compared to the dynamic forces in the cables, which were considered to act in the same direction for the purposes of a rough estimate. An appropriate level of damping was obtained with a 0.1-mm diameter SMA NiTi wire. The experimental results were similar to the ELSA results. The basic concept is that the ratio of the dynamic forces in the cables, which are associated with the oscillation amplitude, the frequency and the cable mass, was similar to the force ratio for the SMA dampers. The ratio between the cross-sections could be considered or the ratio between the wires (N) multiplied by the cross-section.

The ratios between the Pavia cable and the ELSA cable were as follows:

$$Dynamic\ \ force\ ratio = \frac{F_{Pavia\ cable}}{F_{ELSA\ cable}} = \frac{(\rho\ \pi\ r^2 L\ \omega^2\ \Delta x)_{Pavia\ cable}}{(\rho\ \pi\ r^2 L\ \omega^2\ \Delta x)_{ELSA\ cable}} = 0.0012$$

$$\frac{force_{SMA\ Pavia\ cable}}{force_{SMA\ ELSA\ cable}} = \frac{\left(\pi * r^2\right)_{SMA\ Pavia\ cable}}{\left(\pi * r^2\right)_{SMA\ ELSA\ cable}} = 0.0016 \qquad (5)$$

The calculated ratios show that the proposed approach is fairly satisfactory. To identify the two ratios, the SMA cross-section for a new damper is calculated as follows:

$$\frac{F_{new\ cable}}{F_{ELSA\ cable}} = \frac{force_{SMA\ new\ cable}}{force_{SMA\ ELSA\ cable}} = \frac{cross\ section_{SMA\ new\ cable}}{cross\ section_{SMA\ ELSA\ cable}} \Rightarrow$$

$$cross\ section_{SMA\ new\ cable} = \left(\pi * r^2\right)_{SMA\ ELSA\ cable} \frac{(\rho\ \pi\ r^2 L\ \omega^2\ \Delta x)_{new\ cable}}{(\rho\ \pi\ r^2 L\ \omega^2\ \Delta x)_{ELSA\ cable}} \qquad (6)$$

The number N of SMA wires with the same cross-section is given by

$$\frac{force_{SMA\ new\ cable}}{force_{SMA\ ELSA\ cable}} = \frac{N\ \left(\pi * r^2\right)_{SMA\ new\ cable}}{\left(\pi * r^2\right)_{SMA\ ELSA\ cable}} = N \qquad (7)$$

Using formula (7), the number (N) of SMA wires with equal diameters is given by

$$N = \frac{F_{new\ cable}}{F_{ELSA\ cable}} = \frac{(\rho\ \pi\ r^2 L\ \omega^2\ \Delta x)_{new\ cable}}{(\rho\ \pi\ r^2 L\ \omega^2\ \Delta x)_{ELSA\ cable}} \qquad (8)$$

When the IFSTAR cable was used as the "new cable", the value of N was 1.8: the measurements used two wires (N=2). Equations 4 and 6 (or 4 and 8) are rough estimates for the length and cross-section or number of equivalent SMA wires that could be used to construct a satisfactory SMA damper.

3.14 Part Three: Summary

The experimental results showed that the polycrystalline NiTi wires exhibited satisfactory characteristics for damping the oscillations of stayed cables. After obtaining appropriate lengths of 2.46-mm diameter wires, the wires must be initially trained. 100 working cycles at 0.01 Hz can be used for this initial training. For such training, the SMA creep induced an irrecoverable increase of approximately 2 % in the length. Subsequent creep was practically negligible. After training, the coupling effects between the external cooling, self-heating and the hysteretic shapes were reduced. Using smaller deformations (i.e., below 1 or 1.5 %) resulted in an appropriate fracture-life that exceeded several million of working cycles. Pauses in between the series of working cycles induced local changes in the hysteretic behavior: for larger numbers of cycles, these changes were negligible. The hysteretic shape after training was approximately S-shaped. This behavior can enable SMA dampers to be used outside in the Western Europe, i.e., between 253 and 313 K. Stress-aging studies have shown that a monotonic and permanent hysteretic shape change up to 800-1000 MPa can enable a SMA damper to function in climates as in south Canada (233 to 313 K).

Simulation of the cable behavior required the use of the cubic model and appropriate rules to build internal loops to satisfactorily represent the partial and internal loops in the hysteresis cycle. The classical bilinear model cannot be used for small deformations, i.e., for strains below 1 %. Using the cubic model and the Clausius-Clapeyron equation, if required, with ANSYS generated a complete picture of the behavior of the free cables and the cables with the SMA dampers. Comparing the behavior of the standard ELSA and IFSTTAR cables with the thinner cable at Pavia University enabled rules for damper preparation to be formulated that can be adapted to any cable.

PART FOUR

One of the most important damping applications in civil engineering involves the smoothing of oscillations induced by earthquakes in civil structures. Earthquakes can induce severe oscillations in steel structures that can eventually result in permanent deformations by plastic effects. In masonry and concrete structures, brittle fracture can induce catastrophic results. Thus, the oscillation amplitudes induced by earthquakes must be lowered by approximately half or less (i.e., the oscillation energy must be, at least, decreased to 25 % of the original energy) to reduce or suppress the damage to the structure that can be caused by larger amplitude oscillations. The main application for SMA dampers [9] is to reduce the oscillation amplitude to a level that circumvents the plastic deformation of steel. Such an analysis requires that assumption for the intensity of the earthquake and their effect to the structure. In this work, satisfactory damping effects were determined for earthquakes that were assumed to remain under 7.0 or 7.5 on the Richter scale [19, 120].

4.1 Introduction

The damping of oscillations requires the use of appropriate passive or semi-active dampers in a structure. Classical solutions use plastic elements in steel or tuned mass devices coupled with hydraulic dampers [9]. Dampers may use magneto-rheological fluids with computerized control of an external magnetic field to modify the fluid “viscosity” in semi-active assemblies. The use of semi-active elements requires permanent service, i.e., a continuous supply of electrical power and regular technical support for software and/or computing and control requirements. Permanent service is usually available for large buildings or skyscrapers. SMA alloys offer the advantage of passive damping devices that are controlled by a hysteresis cycle. These devices can be built to

work without external energy and computerized control. These conditions require that the properties of the material remain fairly unchanged [19]. For example, the material properties should be unaffected by seasonal (summer-winter) temperature changes over the expected period of inactivity (typically, tens of years). The SMA should then be able to respond effectively when an earthquake induces oscillations in the structure.

In general, successful use of SMA [121] requires a deep and clear knowledge of the effective conditions required for each application and the actual responses of the SMA under these conditions. For instance, the use of a pre-stressed material that can improve the performance of damping devices is not typically an appropriate solution for Cu-based alloys. This limitation arises because Cu-based alloys stabilize martensite over time, producing unexpected paths in the phase coexistence trajectories. The best alternative is to build an appropriate mechanical device that creates a pre-stressed state with the energy extracted from the induced oscillations at the beginning of the earthquake. This alternative approach was described in reference [108].

While NiTi can be used for damping, this analysis was performed on a poly-crystalline CuAlBe SMA for the low strength steel structures that are used in family homes [122]: the number of working cycles for earthquake damping is limited and the Cu-based alloy is cheaper than NiTi.

A family home was composed of two sections of one and two floors. A roof garden was located in the section with one floor, increasing the load on this section. Using porticos in the structure of the house enabled the dampers to be allocated to the diagonals of the lateral porticos. In this study, the structure investigated corresponded to a practical allocation of the dampers.

The first-order phase transition with hysteresis in the SMA is governed by thermodynamic laws, such as the Clausius-Clapeyron equation, whereby increased transformation stresses in coexistence zone are induced in the summer relative to the winter. However, dampers are usually situated inside a house, which smooth the amplitude of the daily and annual external temperature waves. The fatigue behavior, the long-time temperature aging effects and the effects of self-heating for cycling at approximately 1 Hz were studied in this paper. The action of the damper on an experimental steel portico is presented at the end of the paper: an inverted U-shaped structure, 247 cm high and 410 cm long with a two ton loading was studied. The effect of externally-induced oscillations with and without a SMA is described, showing that a CuAlBe SMA and NiTi wires can efficiently mitigate induced oscillations. A FEA simulation of the portico with and without CuAlBe and NiTi using ANSYS is briefly summarized at the end of the paper.

4.2 Experimental

A CuAlBe alloy [123] was studied for damping earthquake-induced oscillations. The wires were provided by a Research Center of TREFIMETAUX, France in 2003 and by NIMESIS, France in 2004 and from 2005 to 2009 from the original casts. The reference data for the AH140 (Trefimetaux) cast were as follows: Ms = 255 K; Mf = 226 K; As = 253 K; and Af = 275 K. The corresponding chemical composition in mass per cent was as follows: Al = 11.8; Be = 0.5; and Cu = 87.7. The A140 cast for CuAlBe had a Clausius-Clapeyron coefficient of approximately 2.2 MPa/K [27]. Several lengths of the wires were used in testing i.e., from 150 to 900 mm, usually with a 3.4-mm diameter [95]. The furnisher dispatched the CuAlBe alloy after direct extrusion (at 1173 K) of the wires and cooling by a water stream at room temperature. The as furnished alloy had a mixture of $\alpha + \beta$ phases. A large progressive and permanent residual deformation was induced in the alloy under stress because of SMA creep and plastic deformation of the α phase.

Practical application of the alloy requires a homogenization process, such as conventional heating to 1123 K for several minutes (i.e., 10, 20, 30 or 40 minutes) to ensure homogenization in the beta

phase and an increase in the grain growth. Following homogenization, the specimen was quenched in water at room temperature (i.e., 293 K) [124]. Further long-time aging of 1 or 2 months at 373 K resulted in a more stable Ms value (see Section 4.3). An additional month (or more months) of aging at 353 K was found to improve the stability of the material, i.e., a steady state could be obtained with a lower tendency toward Ms evolution. To attain a steady state by aging required an extremely long time, as shown in Section 4.3. This aging process induced a slow decrease of the CuAlBe Ms temperature, as shown in figure 2 of [125]. The experimental analysis was improved to ensure good results for the long samples that were required for the application. Table 3 describes the sets of standard cycles with progressively higher deformations that were used in the thermo-mechanical treatments (in traction only). The steel axis shown in the left and right sections of figure 32 is appropriate for pure traction experiments and can easily slip inside the brass cylinder that supports the SMA wires to prevent compression, bending or buckling. The main part of the measurements was conducted using two "Universal Testing Machines" (the INSTRON and MTS) with temperature chambers, as indicated in Section 3.2. The force exerted on a sample with a diameter of 3.4 mm, for strains up to 3.14 %, ranged between from 0 to 4 kN/wire (and up to 450 MPa in figure 2 A in Part One).

The single crystals used in this study had a similar composition to the polycrystals of Cu-11.4 wt % Al-0.53 wt% Be (22.63 at %Al, 3.15 at % Be); the crystals were provided by Nimesis (France) and were likely induced by the semi-industrial Bridgmann method. Several wires that were 1.3 mm in diameter and approximately 200 mm long were used for the experiments described here. The single crystals were oriented 7 degrees from the $[001]_\beta$ direction to the $[011]_\beta$ direction, as determined by the Laue X-Ray method. Specimens with different lengths were obtained from the single crystal by cutting with a low speed saw: 60-mm long samples were used for mechanical testing and 10 to 20 mm long samples were used for the electrical resistivity measurements.

The single crystal samples were heat-treated as follows: the samples were heated for 900 s at 1110 K and quenched into water at 373 K. After approximately 60 minutes at this temperature, the samples were air cooled and then mechanically and electrolitically polished (using 7 steps at 9 V in a solution of 15 % nitric acid in methanol). To determine the temperature range of the pseudo-elasticity, the martensitic transformation temperatures for the heat-treated condition were determined. Sample A1 (Table 1) was studied by electrical resistivity measurements using the four-point method. The following characteristic temperatures were obtained: M_s = 296 K, M_f = 246 K, A_s = 270 K and A_f = 302 K. A complementary measurement performed after maintaining the specimen at 373 K for 4 additional hours did not show any noticeable variations in the transition temperatures. Therefore, 1 h at 373 K was selected as the appropriate aging treatment for attaining a stable starting condition for further mechanical tests over the time scale used for the inter-martensitic analysis.

Mechanical tests were performed with the Instron 5567 and the temperature chamber, as described in Part Three. Tensile specimens with a free length of 40 mm between the grips were used. The deformation was measured by an extensometer MTS 632.13F-20 with a gage length of 10 mm, which was attached to the central portion of the specimen to prevent parasitic deformation of the measurement device. The tests were performed at a crosshead speed of 0.1 mm/min to prevent temperature effects associated with the heat of transformation. This speed corresponded to a mean strain rate of 4.2×10^{-5} 1/s. The load was determined using a Load Cell Instron 2525-810 with a ±1 kN maximum load. The test temperatures were measured by a Chromel-Alumel thermocouple that was spot-welded to the specimen. The thermocouple was calibrated with a temperature calibrator, AMETEK model ETC 400-A12.

4.3 Ambient aging effects in CuAlBe alloys

Cu-based alloys, such as CuZnAl single crystals, show a slow transformation-temperature evolution as the room temperature varies in time. The Ms tracks the room temperature with a well-defined time constant and temperature-dependence. The Ms is an experimentally recoverable parameter, which depends on the external room temperature. Further details can be found in [39]. The Ms temperature of the CuAlBe polycrystalline alloy evolves when the parent phase is aged at different ambient temperatures and at different times. The change in the Ms for CuAlBe is opposite to that for CuZnAl, i.e., the $(dMs/dT_{room\_temp})_{CuAlBe}$ is positive and negative for CuZnAl. Thus, at steady state, the Ms depends on seasonal temperature changes.

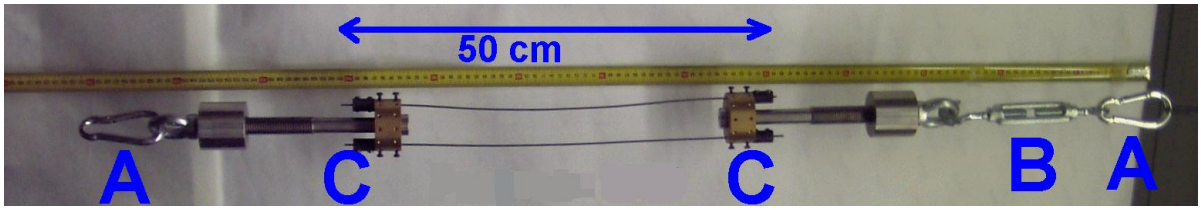

Figure 32. Photograph of a SMA damper. The device shows only two SMA wires. A: clamps. B: eventual pre-stressing device. C: elements with holes for several SMA wires. The SMA wires and the steel axis can slip avoiding any compressive part in the working cycles.

This temperature-time effect on the alloy can be studied by electrical resistance measurements of the Ms transformation temperature: relatively fast cooling-heating cycles must be used to circumvent maintaining the CuAlBe alloy under several "constant temperatures". A rough but reliable estimate of the Ms value as a function of time can be determined from the intersection of the martensitic transformation with the electrical resistance-temperature curves (see figure 33). The arrows in figure 33-A indicate a reproducible method of determining the Ms value: the intersection of the arrows indicates the resistance branch of the parent phase. The other arrow indicates the inflexion point in the heterogeneous zone (containing the parent and martensite phases). Sets of measurements have shown that an alloy situated inside family homes is not significantly affected by several years of summer-winter temperature cycles. Figure 33-B shows that the Ms evolved with time and the aging temperature. For a summer temperature of 303 K and a winter temperature of 278 K, the maximum oscillation of the Ms value would be less than 13.5 % of 25 K (i.e., below 5 K). Figure 33-B also shows that the Ms value of the alloy reached an asymptotic value after two months of aging at temperatures over 353 K. After reaching steady state, the Ms tracked the external room temperature.

For aging at temperatures close to or under 373 K an increase of 20 K (i.e., from 373 to 353 K in figure 33 B) in the room temperature induced an asymptotic increase of 2.5 K in the Ms [125]. The temperature oscillations corresponded to annual summer-winter changes are highly damped by the time constants. The peak-to-peak amplitude of the annual summer and winter oscillation inside one house, i.e., 20 K, can induce minor ripples in the Ms (of approximately 1 K).

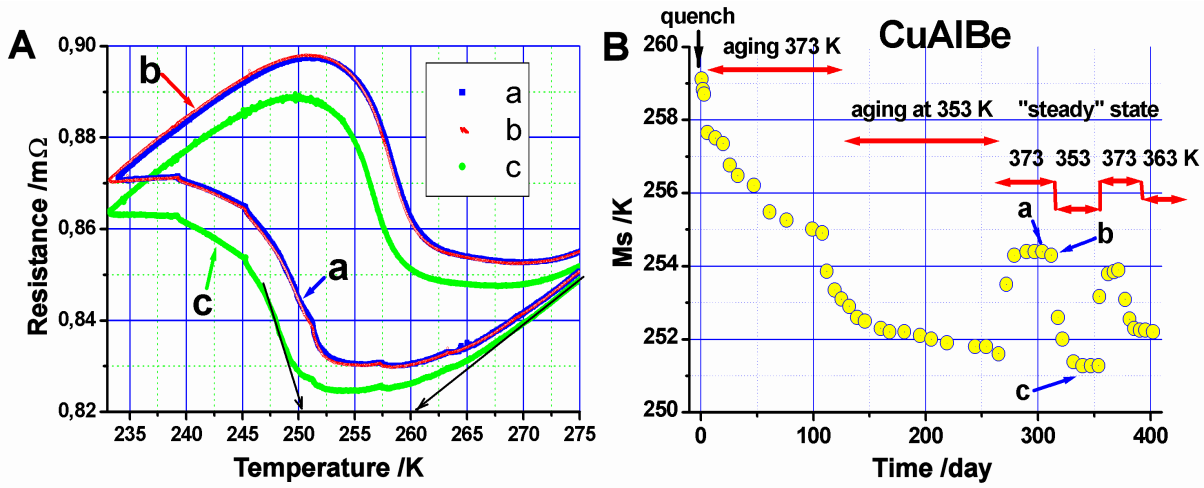

Figure 33. Hysteresis cycle evolution due to temperature and time aging. A: Hysteresis cycle in resistance against temperature (after aging at 373 K (a and b), and at 353 K (c) (at right). The resistance cycles (a, b, c) are associated to the Ms temperatures established by the a, b, c dots in right part. B: The Ms evolution against time after quench and aging at 373 and 353 K. Further aging at 373 and 353K shows the tracking action on the Ms (reproduced with permission from [125], Isalgue A, Fernandez J, Torra V, Lovey FC. Conditioning treatments of Cu–Al–Be shape memory alloys for dampers. Mat Sci Eng A Struct 2006; 438–440: 1085–8).

Depending on the quality of the experimental data, several time constants (τ_1, τ_2, τ_3, …) can be extracted; two time constants, i.e., τ_1 and τ_2, can be extracted from the measured evolution of the Ms during aging, i.e., τ_1, and τ_2, of a CuAlZn single crystal alloy [see references 39 and 109, for example]. Aging in a polycrystalline CuAlBe alloy induces slow phenomena and only one time constant could be determined. This time constant τ_1 depends on the temperature (table 1) through the activation energy. The relationship between the time constant and the temperature is given by

$$\mathrm{Log_e}(\tau_1) = -3.472 + 5740 / T \quad (T \text{ in K and } \tau_1 \text{ in s}) \qquad (9)$$

The Ms value can be extracted from resistance measurements. The resistance can be decomposed in two terms: a phonon contribution and an atomic order contribution (R*). The α parameter is a temperature coefficient associated with the phonon contribution. The resistance can be written as follows:

$$R(T, \text{order}) = R^*(\text{order}(T)) + \alpha\,(T - T_{RT}) \qquad (10)$$

At steady state, when the temperature is stable and constant at a value T_{RT} over a long time (), the Ms is only a function of T_{RT}:

$$Ms_\infty = Ms(T_{RT}, t=\infty) \qquad (11)$$

Setting the time origin after an infinite time under fully steady conditions (at constant temperature), the room temperature T_{RT} becomes equal to an "order" temperature $T_1(t)$, which represents the actual ordered state:

$$T_1(t \Rightarrow -\infty \rightarrow 0) = T_{RT}(t = 0) \qquad (12)$$

Following a temperature step between T_a and T_b, the Ms evolved exponentially with a time constant τ_1 that depended on the final temperature value T_b. This experimental result is described by

equation (13). The behavior of T_1, which is not restricted to evolve with $T_{RT}(t)$, under an externally varying temperature can be determined by the solution of the following differential equation:

$$\frac{dT_1}{dt} = -\frac{1}{\tau_1(T)}\left(T_1 - T_{RT}\right) \qquad (13)$$

The differential equation shows that T_1 tracks T_{RT}. The solution following a step in T_{RT} is an exponential in $T_1(t)$. When the process involves N independent order parameters, equation (13) is replaced by a set of N independent differential equations. Experiments have found two order parameters for the CuAlZn single crystal. A similar formalism can be applied whereby two differential equations must be solved and the evaluation of the Ms is given by the following equation:

$$Ms(t) = Ms(t=0) + \sum k_i \{T_i(t) - T_{RT}(t)\} \qquad (14)$$

The k_i coefficients were determined from the comparison between the calculated values and the experimental results [39]. For CuAlBe, the solution of the differential equation (13) for $T_{RT}(t)$ is used in the numerical solution for $T_1(t)$ (the order temperature); the solutions for $T_{RT}(t)$ and $T_1(t)$ can be converted to an expression for the Ms time evolution as follows:

$$M_s\left((t), T_{RT}(t)\right) = M_s\left(t=0, T_{RT}(t=0)\right) + k_1\left(T_1(t) - T_{RT}(t)\right) \qquad (15)$$

k_1 can be determined from the experimental results for a temperature step. The value of k_1 for the CuAlBe SMA was 0.135 [108]. Values of time constants at different temperatures for polycrystalline CuAlBe are also given in table 4. Installing dampers inside a house reduces the effects of the temperature changes over the summer and winter. For steady changes of 30 K, the ΔMs was found to be 2.7 K. Thus, the time-temperature effect was negligible.

Table 4. Diffusion phenomena and asymptotic temperature effects on Ms for the CuAlBe alloy.

Parameters	**Alloy: CuAlBe [9]**
τ_1 from measures	1.95 days at 373 K
τ_1 from measures	4.63 days at 353 K
τ_1 extrapolated	116 days at 293 K
Activation Energy	5740 K
$100\Delta Ms/\Delta T_{RT}$	13.5

4.3.1 SMA creep effects

Shape memory alloy creep has been found to occur during cycling in the pseudo-elastic range. SMA creep consists in the accumulation of residual deformation, and is associated (as in Section 3.5) with the maximal stress. The stress value was increased by the imposed deformation and by the local temperature values, which were induced by the room temperature or by self-heating. The creep reduced the recoverable pseudo-elastic elongation of the material and increased the sample length at zero stress, leading to a deterioration of the damping capacity and a loss of re-centering capacity when the creep increased during working. As with the cable oscillations, creep in the working cycles caused malfunctioning of the damper: the small amplitude oscillations were not smoothed.

For specimens with standard heat treatment, a short homogenization time and a short aging time at 373 K, the creep increased to over 2.5 % at a maximum imposed strain of approximately 6 % [126-

127], as shown in figure 34. The figure shows that when small deformations were imposed (at approximately 3 percent or less), the creep remained near 0.50 %.

Longer homogenization times (i.e., 40 minutes at 1123 K) were associated with large grain growth [112 128] and increased fragility. In a civil structure, the required damper lengths should exceed 700 mm (750 mm in section 4.7), so that the SMA could not satisfy the expected fracture-life that was obtained for sample lengths of 100 or 150 mm. Large grains produce good results in laboratory measurements, but poor results for industrial samples with an immediate crash. Some ductility is highly desirable for industrial application. This situation occurs relatively frequently in studies of SMA behavior. The laboratory tests produce satisfactory results, but cannot be easily extended to industrial applications. Testing in the real world is always recommended.

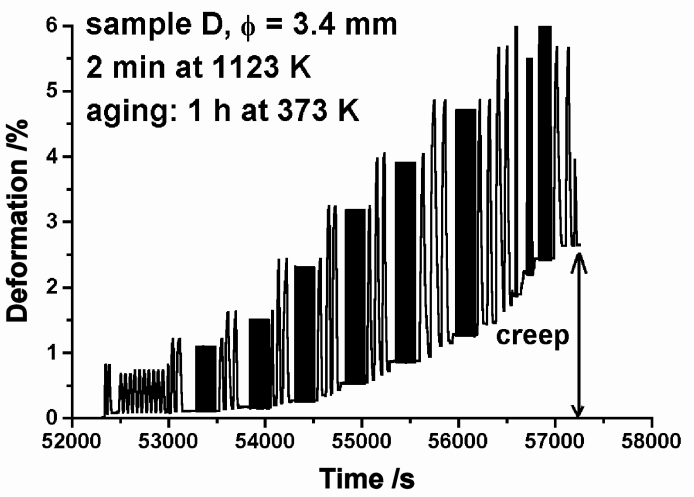

Figure 34: Progressive deformation on cycling. Standard heat treatment: two minutes at 1123 K and 1 hour of aging at 373 K. (Reprinted from ref. [19], with permission from Elsevier)

To satisfy the damper requirements, studies were carried out at different homogenization times (10, 20, 30 and 40 minutes). Better results were obtained for a homogenization time of 10 minutes at 1103 K, followed by water quenching, a similar aging process over 1 or 2 months at 373 K and aging for an additional month at 333 K (as shown in the figure 33 B). The creep value depends on the homogenization time and the thermo-mechanical treatment of the samples.

Figure 35 A illustrates a case where the deformation imposed on the specimen was gradually increased from approximately 0.8% to 5.5 % by the strain steps shown in table 2. Figure 35 A shows an initial series of cycles (a) at 307 K up to a deformation of 3.14 % with a creep of 0.5 %. Later, at room temperature (294 K) (b), the creep remained constant for deformations under 4 %. The creep increased at the end of the cycling process (c). For the fatigue measurement in (d), only a small increase in the creep from 1.5 to 1.8 % (i.e., approximately 0.3 %) could be observed. Figure 35 B provides the complete sets of cycles and the total creep versus the number of cycles. After the complex training (a+b+c) the final mean net value of the creep was 1.5 % (the effect of the grips in the initial sample positioning produced a creep of 0.3 %). Thus, the creep decreased in comparison to that for a progressive deformation of up to 6 %, as shown in figure 34 (in this case 2.7 %).

For a systematic analysis, the different cycling steps were divided into modules that were characterized by three parameters: the strain, the cycling frequency and the number of cycles. The set of modules that were used in a series of near exhaustive measurements are listed in table 5. The cycling frequency was relatively fast (0.5 and 0.25 Hz), but somewhat lower than that expected in a civil structure. Figure 36 A shows the hysteretic energy corresponding to the measurement of the fatigue evolution in (d) of figure 35 A. The fatigue measurement (shown by an arrow) showed a

decrease (25 %) in the energy after 1000 cycles of work, which was mainly associated with the small increase in creep in cycling (see figure 35 B) or a minor decrease of the hysteresis width.

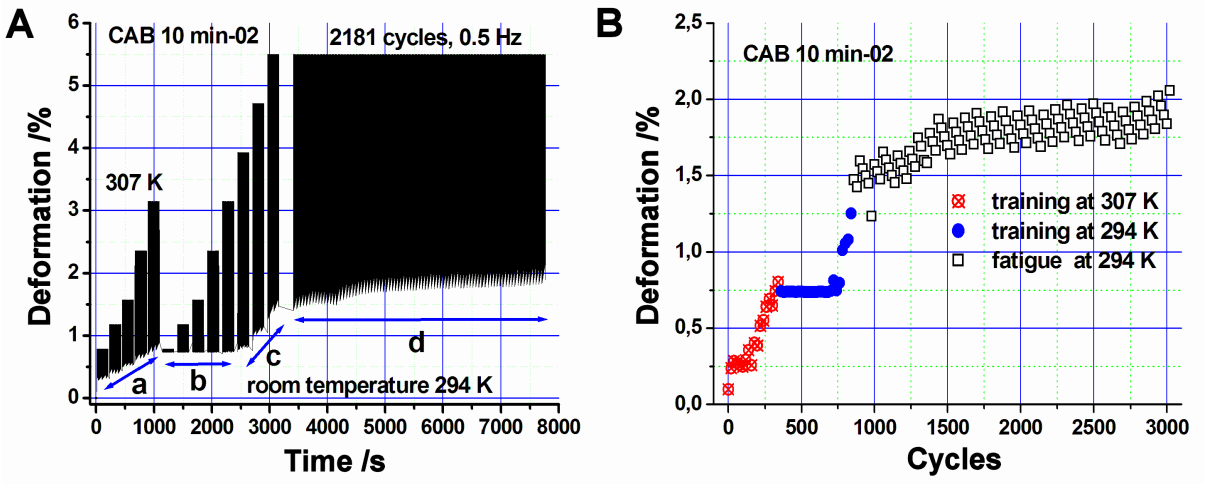

Figure 35. CuAlBe wire of 3.4 mm of diameter (Trefimetaux-France: cast AH140) with short homogenization time (10 min) and extended aging (two months at 373 K). Left: three series of working cycles: two of "training" as a, and b+c and one of the fatigue as d) performed with one MTS equipment using the strains described in Table 2. Right: progressive strains versus time showing the growing of SMA creep.

Two sets of cycles are shown in figure 36 B. The first series comprised 100+10 cycles at 0.01 Hz and the subsequent series of cycles to fracture (3616 cycles) was performed at 0.5 Hz. The smaller deformation value (3.14 %) corresponded to 0.75 % from sample adaptation to the grips and 0.4 % of creep from the cycling part. While 3 % deformation is considered to be "sufficient" for samples that were used directly, the more sophisticated thermo-mechanical treatment described in the caption of figure 35-A allows a 4 % deformation.

In the figure 36 B two sets of cycles are performed. First a series of 100+10 cycles at 0.01 Hz and, later, one series of cycles to fracture (3616 cycles) at 0.5 Hz. The global deformation (3.1 %) includes 2.3 of net strain 0.7 % of grips adaptation and 0.2 % of creep in the cycling part. When 3 % is "sufficient", it is possible to use directly the samples, the more sophisticated thermo-mechanical treatment outlined in the caption of figure 35 A permits 4 %.

Table 5. Sets of modules (with their code) for the cycling procedures used in the systematic analysis of SMA creep and fatigue. (f = 0.79% in strain). The M1 was used to check mechanical setup of grips in the machine testing.

Code	Amplitude (mm)	Strain (%)	Freq. (Hz)	Cycles on the samples (N)
M1	1**f*	0.79	0.50	Usually 4 or 5
M2	1.5**f*	1.18	0.50	100
M3	2**f*	1.57	0.50	100
M4	3**f*	2.36	0.50	100
M5	4**f*	3.14	0.25	50
M6	5**f*	3.93	0.25	50
M7	6**f*	4.71	0.25	50
M8	7**f*	5.50	0.25	50

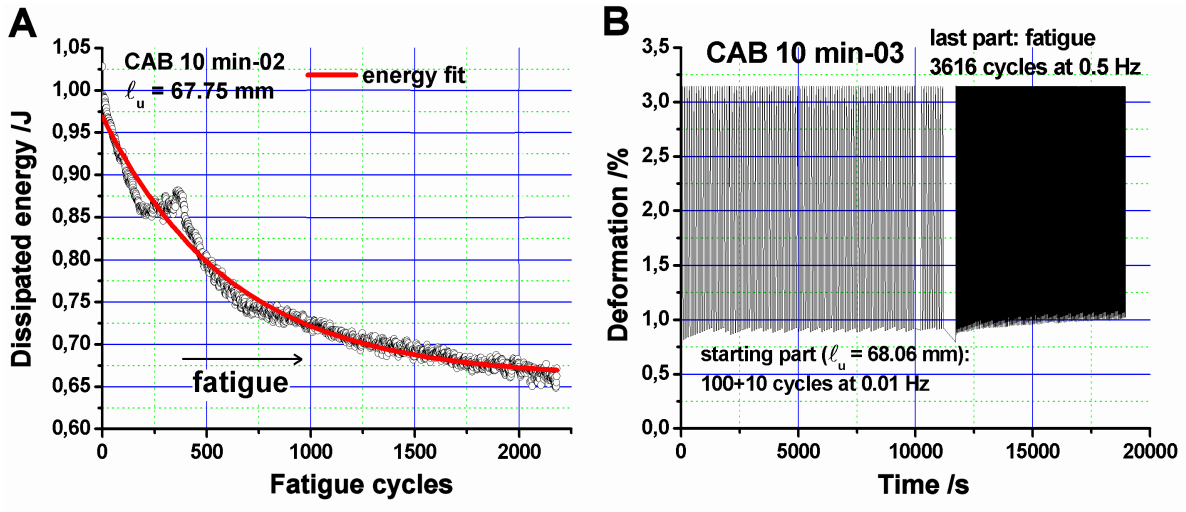

Figure 36. CuAlBe alloy in wires of 3.4 mm of diameter {Trefimetaux (France): cast AH140} subjected to quench after a short homogenization (10 min) and long aging (1 month at 373 K). A: hysteretic energy corresponding to part d of figure 35 A. In the fatigue part, cycling at 0.5 Hz, (part d) the net deformation was close to 4 %. B: Fatigue analysis after training at 0.01 Hz, sample with 2 months of aging at 373 K and with net deformation of 2.14 %

SMA creep is caused by permanent sample deformation that is induced by grain accommodation in response to the shape change induced by the martensitic transformation. Two mechanisms operate simultaneously: dislocation creation and the appearance of stabilized small martensite plates by the dislocation stress field. The stabilized martensite can be recovered via appropriate re-heating at intermediate temperatures [124], giving a partial recovery of creep. Cycling after recovering immediately induces an equivalent creep if the sample has memory (i.e., local deformations) of the previous actions.

4.4 Fatigue life and fracture in CuAlBe

The fatigue life of the 3.4-mm diameter CuAlBe wires were analyzed following two stages of complete Thermo-Mechanical Treatment (TMT). The first stage consisted of homogenization and aging processes, as described in parts 4.2 and 4.3. In the second stage of heat treatment (or training), a series of modules from M1 to M5 at 318 K were carried out, as indicated in table 4. The fatigue life was then measured at room temperature (293 K), as shown in figures 36 and 37.

First, a series from M1 to M6 or M7 was conducted to reach a nearly asymptotic SMA creep. Then, the specimen was cycled to fracture at M6 (figure 37 A). The life to fracture (for a net strain of approximately 3 %) in the samples increased at a lower amplitude deformation (or lower transformation stresses) in fatigue. Figure 37 A shows an initial step in the SMA creep that corresponded to the sample adaptation to the grips, but the actual creep was similar to that in figure 35 (for the set of cycles in “a”). The intrinsic creep obtained by this method remained below 0.3%. The frictional energy decreased with the number of cycles (figure 37 B) for two series of consecutive cycles: a portion of the first series is shown in figure 37 A.

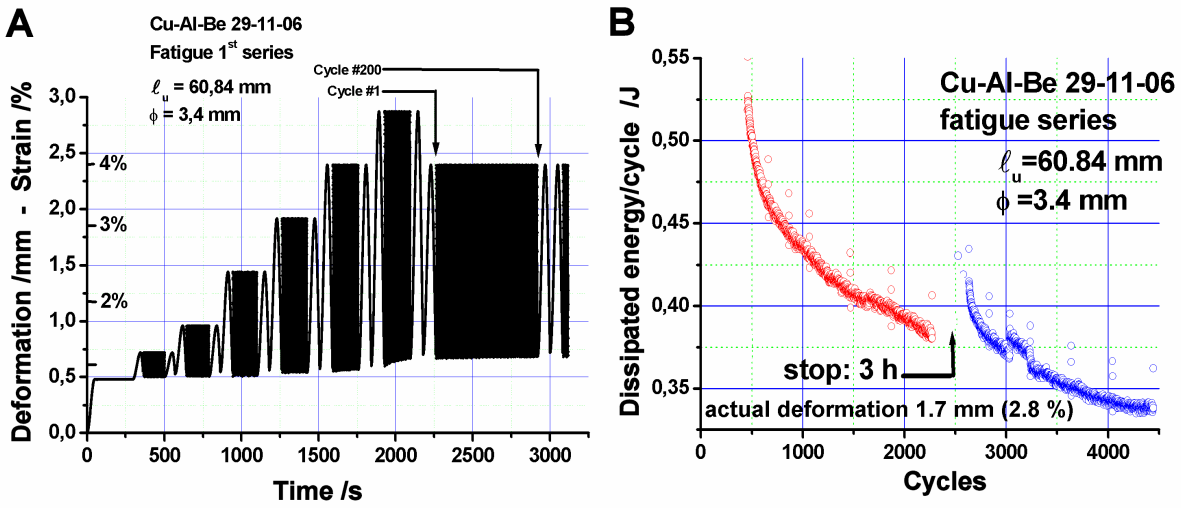

Figure 37. Initial part of the fatigue study using a polycrystalline CuAlBe wire of 3.4 mm of diameter. A: Initial sets of cycles between M1 and M7, later 200+2000 cycles of fatigue when using M6. B: Evolution of the frictional energy on cycling (only the fatigue part is included) for two sets of consecutive similar cycles as is outlined in the left figure.

Figure 38 synthesizes the results on the number of cycles to fracture for the CuAlBe samples that were studied under different heat treatments and cycling frequencies. The martensitic transformation stress was higher for short homogenization times. For a homogenization time of 10 min at 1123 K, a stress of approximately 450 MPa was induced at 3 % strain, as shown in figure 2 A. The cycling procedure shown in figure 35 A reduced the maximum stress for cycling and therefore increased the fatigue life. The fatigue life exceeded 1000-2000 cycles, which is generally sufficient to damp earthquake oscillations in small buildings, such as family homes. The range of stresses that were measured in the fatigue tests was highly dependent on the homogenization time of the heat treatment, i.e., the stresses depended on the grain diameter.

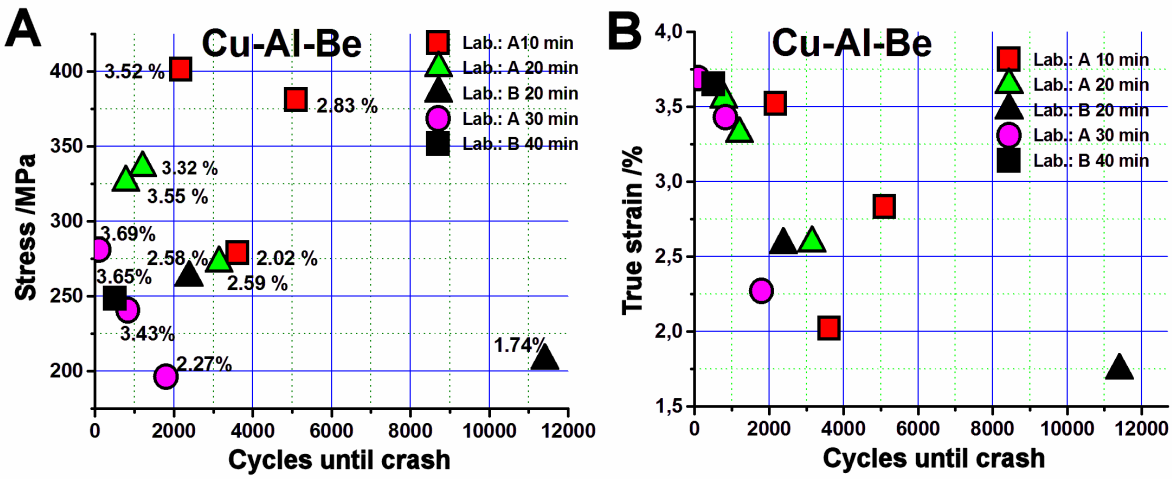

Figure 38. Fatigue tests for CuAlBe using wires with 3.4 mm of diameter. Fatigue cycling was realized at 0.5 Hz. The strain values are the true or net strain: the permanent deformation or SMA creep is subtracted. A: stress against the number of cycles for five different treatments realized in two laboratories (Lab A (UPC-Barcelona) and Lab B [CAB-Bariloche]). B: Associate true strain against the number of cycles to fracture

4.5 Frictional energy dependence on the number of cycles

The frictional contribution of the damper is related to the integral of the hysteretic cycle, which corresponds to the conversion of mechanic energy into dissipated heat [27, 122]:

$$\oint \vec{f} \cdot d\vec{x} = \text{frictional energy} = \text{dissipated heat} \qquad (16)$$

Figures 36-A and 37-B show the results for the series of cycles to fracture, for which the energy progressively decreased with the number of cycles N. Fitting the curve with one, or two for greater accuracy, exponentials sufficed for a rough description of the behavior. The dissipated energy for strains up to 3 % decreased progressively with the working cycles. After 2000 working cycles, the energy decreased by approximately 30 %. At low strains, i.e., 1-2 %, the dissipated energy remained practically constant with cycling [129]).

4.6 Testing CuAlBe SMA dampers: computational experiments

A house was considered, composed of two sections of one and two floors, which were separated by an internal garden (figure 39). The garden was located on the roof of the section with one floor, increasing the load on this seemingly lighter section. Three porticos in the one-floor section of the house enabled the dampers to be allocated to the diagonals of the lateral porticos. In this study, the investigated structure corresponded to a practical allocation of the dampers.

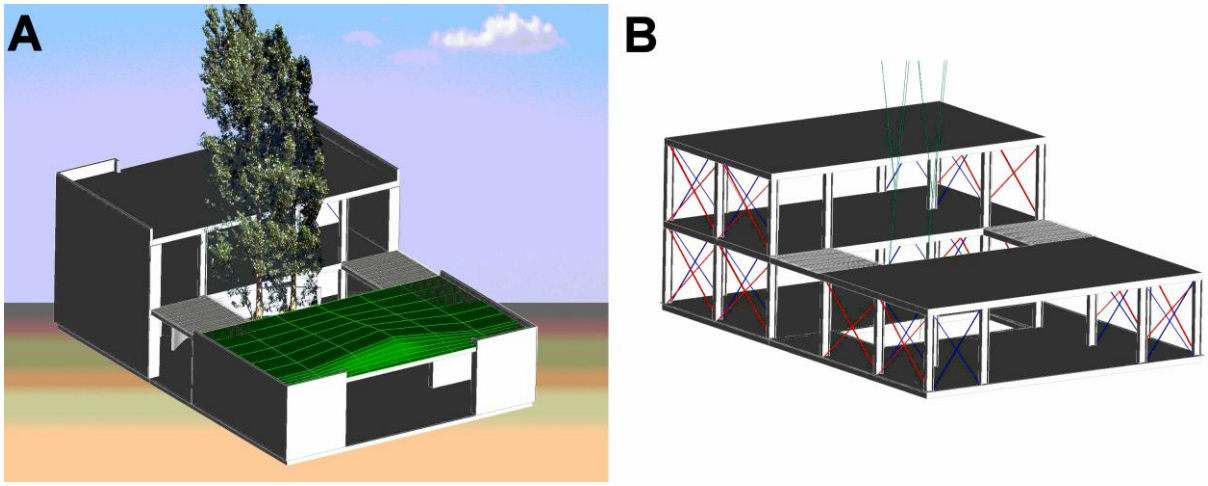

Figure 39. A: Outline of the family house. The structure was used for simulation of the SMA dampers behavior under "El Centro" earthquake. B: Potential position of the dampers in the portico diagonals (Reprinted from ref. [19], with permission from Elsevier).

The simulation of the structure, with and without dampers, was performed using standard Finite Element Analysis (FEA) by ANSYS. The first simulation was performed for a one family home with a steel structure and a relatively heavy garden on the roof (using a 60 cm soil layer). The behavior of such a structure could be representative of other structures with heavy masses on top of the structure (for instance, emergency generators on top of a building). Appropriate pillars and beams were considered for the porticos: HEB (H-shaped cross section of beams, [130]) 140 and 200 were used for the columns and HEB 240 and IPN (I-shaped cross section of beams, [131]) 160 were used for the beams (as shown in figure 40 A). The roofs were built by depositing a concrete slab over a thin corrugated steel plate to fill the space between the beams. An acceleration spectrum for the "EL CENTRO" earthquake (figure 40 B) was used as an input to the simulation of the response of the structure and the appropriated loads with and without dampers. The main objective was to use the dampers to reduce the undamped oscillation amplitude by half and to ensure that the damped amplitudes did not overcome the plastic deformation threshold of the steel parts (the beams and columns) of the structure.

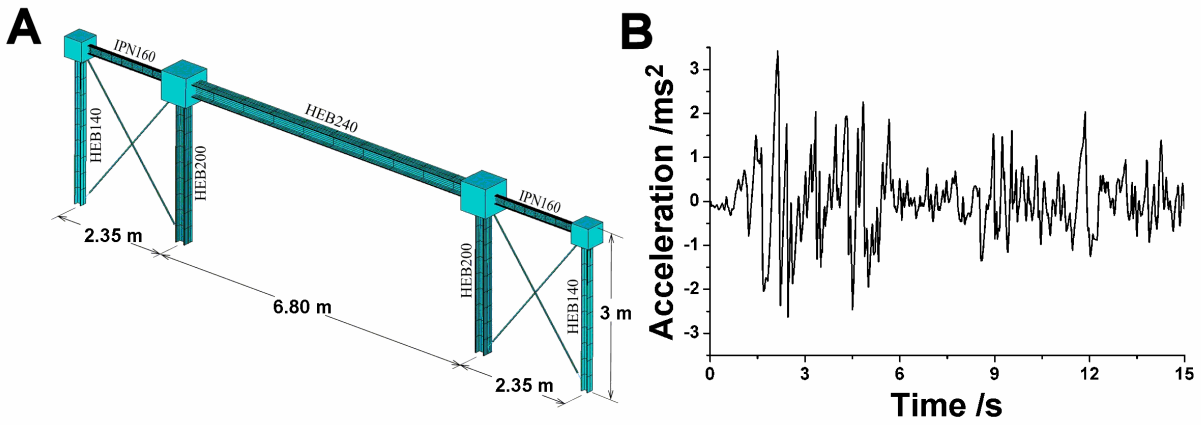

Figure 40. A: Schematic view of the studied portico. The cross bars on the lateral portico outlines the dampers. B: Acceleration pattern induced by "El Centro" earthquake (Reprinted from [19], with permission from Elsevier).

The bilinear model cannot satisfactorily describe complex trajectories in hysteresis cycles. The CuAlBe SMA behavior was simulated with ANSYS using a Merge of 9 Bilinear Models that were organized mechanically in parallel (M9BM) that fits well the highly complex trajectories of experimental data [19]. Good results for the mechanical cycles were obtained at a reduced computation time. The "cubic" model (Section 3.12) could also have been used in the portico simulations. The figure 41 shows the association in parallel (A) of the 9 bilinear models for the simulation of the partial and internal loops of CuAlBe SMA. The figure shows the comparison between the experimental measurements dots) and the calculated cycles (line).

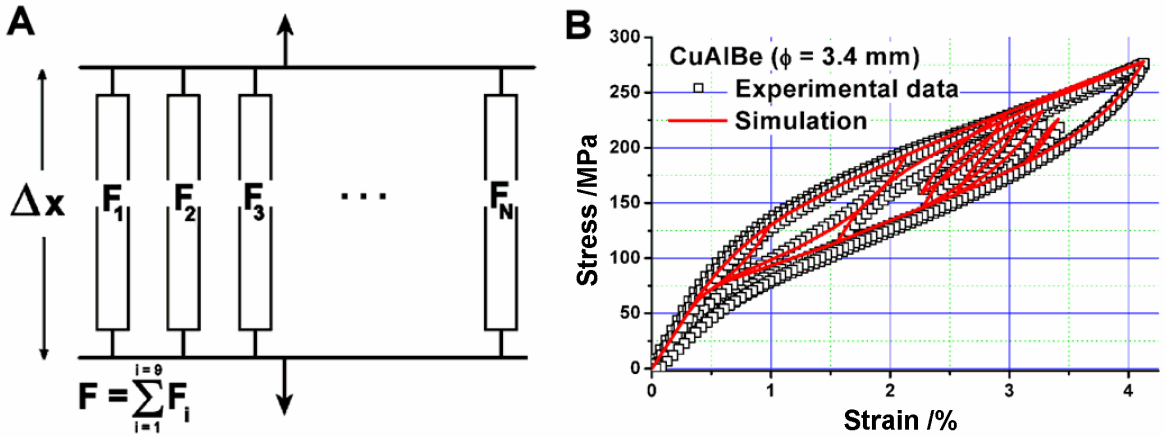

Figure 41. Modeling complex cycles. A: bilinear models used in the simulation. B: comparison between the M8BM model (line) and the experimentally measured loops (dots) in the hysteresis cycles for CuAlBe.

The Clausius-Clapeyron equation was also used as input to the simulation to model the effects of the room temperature (i.e., temperature variations from summer to winter). The results of the energy absorbed by the dampers showed that pre-stressed dampers (clearly under 1 kN/wire) were clearly more efficient in absorbing the oscillation energy.

A general recommendation is that the forces induced by the dampers on the porticos should not exceed approximately 20-30% of the dynamic forces exerted on the porticos without dampers. Therefore, the resonant frequencies of the structure would be altered only slightly by the presence of the dampers (corresponding to a change of approximately 15% in the frequencies). The length of the SMA wires must be tuned based on the effective deformation that is induced in the diagonals by the earthquake and reduced by the dampers.

The SMA dampers in the simulation were situated in the diagonals, at the left and right sides of the structure arches: the structural response with and without dampers was then compared. The optimal damping for the El Centro earthquake was obtained by using dampers made of 25 CuAlBe wires with a 3.4-mm diameter and a 600-mm length. In the optimal case, the simulation showed that the maximum displacement (vibration amplitude) of the top of the portico was reduced from 6 cm without dampers to approximately 3 cm with dampers. The first positive result was the reduction of the vibration amplitude by half, which implies that 25% of the oscillation energy without dampers remained (i.e., an energy reduction of 75 %). A second very important result was that the limit for plastic steel deformation was attained for the steel portico without dampers, resulting in a permanent displacement of approximately 1 cm. With the dampers, the plastic steel limit was not attained and the initial positions were recovered after the event, i.e., the dampers left the structure unchanged and no additional re-centering was needed. In principle, only the dampers would need to be checked, adjusted or replaced after a moderate event (such as an earthquake measuring 6 or 7 on the Richter scale).

The computation was also performed with pre-stressed dampers. Thus, the initial "elastic or nearly elastic" component of the SMA stress-strain behavior (see figure 41 B) was reduced and the dampers started working at very low displacements. The absorbed mechanical energy (which was converted to heat by the dampers) nearly tripled with 1% pre-straining and a reduced maximum oscillation amplitude. From a purely mechanical perspective, pre-stressing has clear advantages: however, the properties of Cu-based SMA are such that several years in a pre-stressed material state can induce spontaneous martensite stabilization that modifies (by a local increase of transformation temperatures) the SMA hysteretic behavior via a partial, or even total suppression of the retransformation process.

Preventing permanent pre-stressing has been a convenient means of circumventing the inevitable difficulties associated with stabilization after several years of reduced transformation (at an overall strain of 0.5 %). An automatic device has been developed in the literature that uses the compressive component of the oscillation amplitude to reduce the effective length of the SMA wires, while increasing the absorbed energy when needed [108, 132]. The set-up (a passive element) acts as a pseudo-semi-active device without an external energy supply.

4.7 Testing the CuAlBe SMA damper: experiments

A partial test of the SMA behavior was carried out with a "shaking table" in 1-dimension (see figure 42). The steel portico (consisting of a 4.10-m long HEM-120 beam and 2.47-m high HEB-100 pillars) and the lateral protective structures were built by TAMANSA (08050 Gavà, Catalonia, Spain). The portico was mounted over a chariot with wheels that were protected by supplementary reinforced walls to prevent "out-of-plane" oscillations. A hydraulic system moved the chariot in back and forth with sinusoidal displacements. Two inverted V-shaped light beams were fixed to the chariot to facilitate direct measurement, via a LVDT-HBM sensor, of the beam net displacement (with respect to the chariot basis). The maximum load used over the portico was approximately 2 metric tons. A reference wall of concrete blocks was used to subject the actuator that displaces the chariot-portico device. The dampers (see figure 42-A) were installed in the portico diagonals and joined to the frame with steel cables. In the example described, the actuator induced nominal accelerations of 1.2 m/s^2 and created oscillations of 2 or 3 Hz at the portico because of resonances (unloaded vs. loaded portico). The effective accelerations were similar to higher "EL CENTRO" accelerations.

Figure 43 shows the oscillating behavior of the portico beam under the action of the external actuator, which generated 40 sinusoidal oscillations at 1 Hz (shown in the bottom section of the figure for the structure without the SMA), and the reduced oscillations under the action of the SMA

damper (top section of figure 43). In this example, the two dampers (one for each diagonal) were each built using two CuAlBe SMA wires that were 3.4 mm in diameter and 750 mm in length. The figure clearly shows the relevant amplitude reduction by the SMA dampers. A 80 % of reduction in the oscillating energy converted from mechanical energy to heat. In this case, a low pre-stressing (of 0.08 MPa) was used. The deformation corresponded to the displacement of the portico beam was measured by a LVDT sensor, i.e., the beam net displacement. The effect of the SMA damper was relevant in the comparison between the residual signals after the actuator was stopped. Figure 43 shows that, with the SMA, the residual oscillations were practically reduced to zero in less than 5 s.

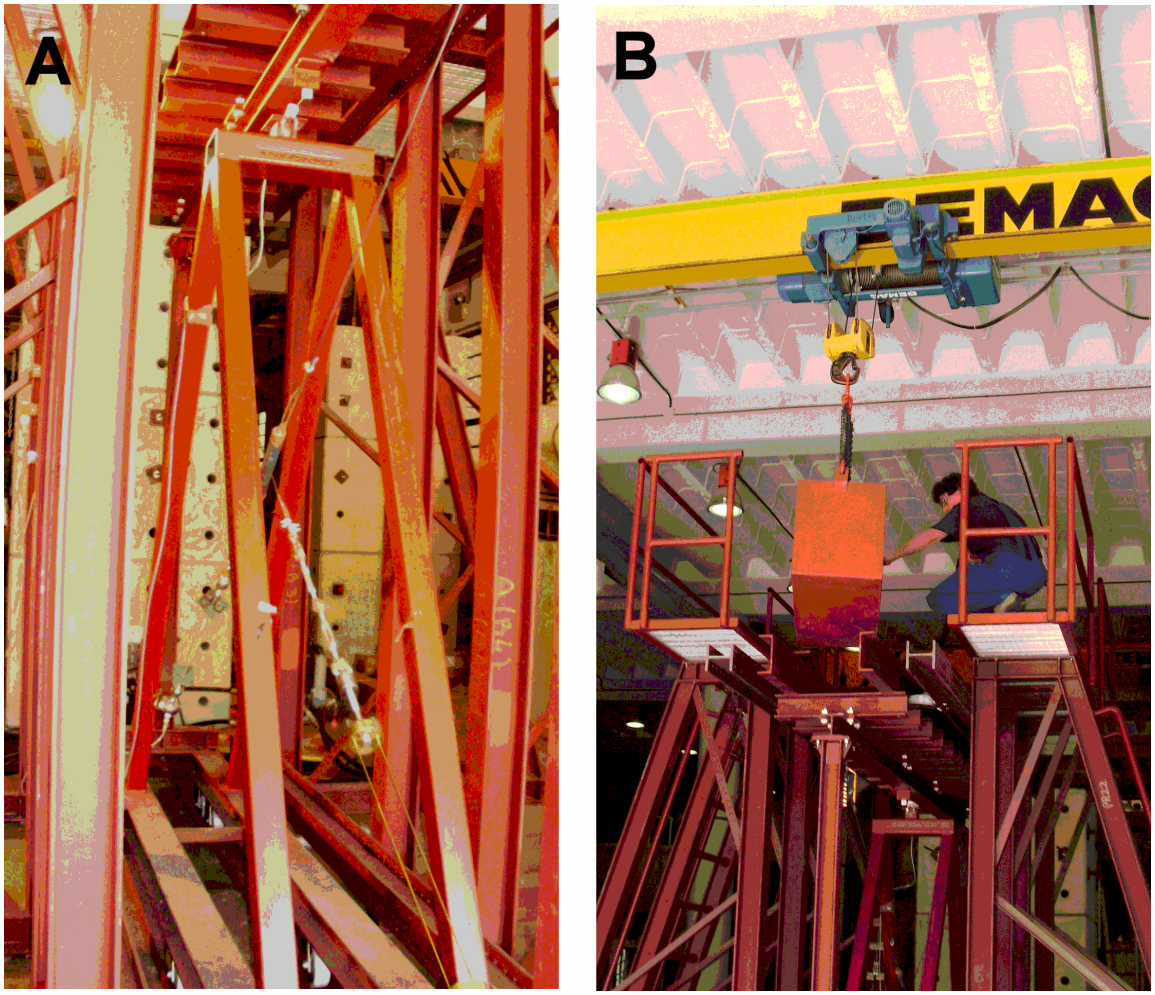

Figure 42. A: In the upper part of the inverted V-shaped against the portico-beam one HBM-LVDT sensor determines the relative position against time. The picture shows CuAlBe SMA dampers in the portico diagonals. In the rear, the reference wall (by concrete blocks) can be observed. B: positioning the loads in the top of the portico.

Figures 43 and 44 show examples of the oscillations with and without SMA for loads situated near 1000 kg. The frequency change in the structure by the SMA actions not seems relevant. The measurements showed a change in the relative significance of the different frequencies. The dampers installed in the portico diagonals were built to produce approximately 30-40 % of the dynamic forces that were expected to be induced by the earthquake oscillations. The SMA length (for an expected maximum pseudo-elastic strain below 4 %) was chosen to provide the expected strain during the damping event.

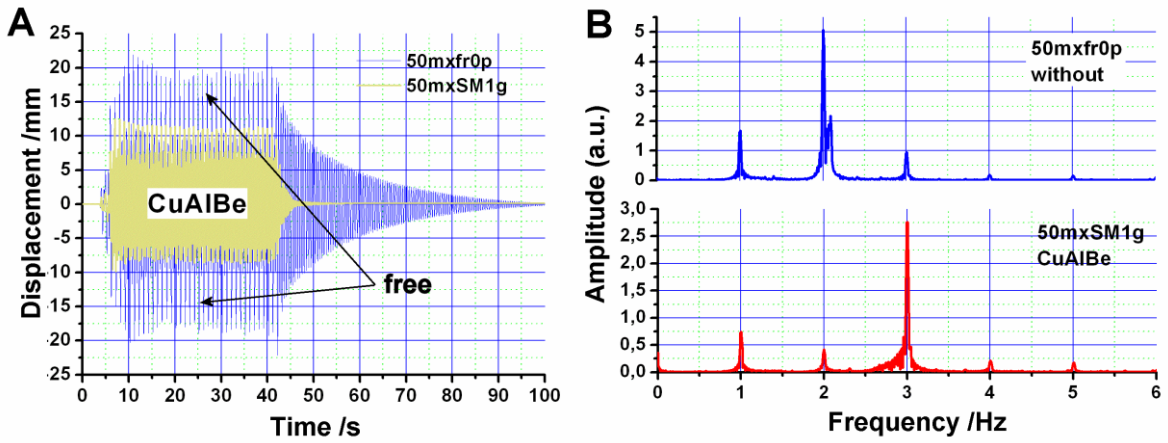

Figure 43. A: Oscillation amplitude in the portico beam (half load), without and with CuAlBe SMA damper visualized in figure 32 and 42 A. B: frequencies via FFT, top: without SMA, bottom: with SMA

The action of the SMA was important: the "steady" signal was reduced to 1/3 of its value in the undamped case. This dynamic effect was highly significant. After the actuator was stopped, the oscillations with SMA were clearly reduced. The action of the portico created significant frequencies at 1.7 Hz and an additional harmonic at 2 Hz (and small signals at 3 and 4 Hz). The behavior of the beam frequencies showed that beats appeared without dampers. The action of the SMA reduced the oscillation amplitudes and reduced the frequency spectrum to that of the actuator signal (1 Hz) and the upper harmonic frequencies (2, 3, and 4 Hz). Similar results could be obtained by fabricating the dampers from NiTi wires. Figure 44 shows the experimental results for dampers that were each constructed of two trained 2.46-mm diameter NiTi wires, with similar lengths as the CuAlBe dampers. Computed results with ANSYS and the 9-element model indicated previously can be found, for different earthquakes, in fig. 12 to 16 of [19].

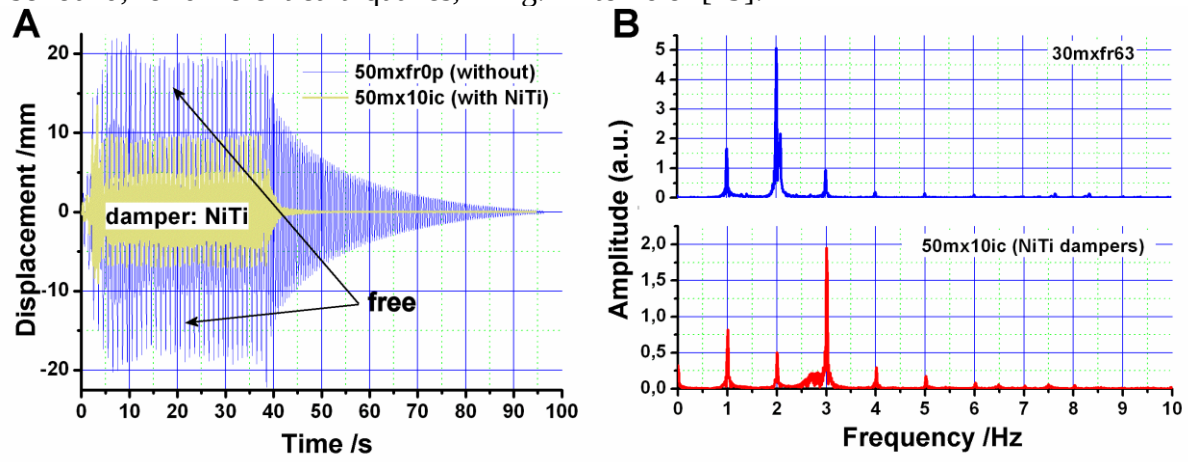

Figure 44. Oscillation amplitude in the portico beam (half load), without and with NiTi SMA A: oscillations induced without and with the SMA damper. B: frequencies determined by FFT.

4.8 Part Four: Summary

The experimental analysis of wires of CuAlBe polycrystalline material showed satisfactory behavior for damping civil structures. The preparation of the samples required an initial homogenization between 1073 and 1123 K over several minutes (i.e., 10 minutes or less), followed by quenching to room temperature. Subsequent aging at 373 K for two months conveniently reduced the spontaneous evolution of the transformation temperature. The fluctuations of the daily and annual temperature were negligible for dampers situated inside a house. The fracture analysis of up to 2000 working cycles for deformations up to 3 % was appropriate for oscillations induced by

earthquakes. Using SMA in a portico application produced satisfactory damping. The amplitude of the oscillations was reduced to between ½ and 1/3 of the undamped amplitude. Experimental measurements showed that NiTi was also suitable for damping. Similar experimental results were obtaining by using dampers constructed of two wires of CuAlBe or NiTi.

Simulation by ANSYS produced a similar reduction in the amplitude of the oscillations (to between ½ and 1/3 of the undamped amplitude). The SMA model that was used in simulation was either a cubic fit to the experimental data, along with the Clausius-Clapeyron coefficient, or a simplified phenomenological superposition of 8 bilinear elements. The use of FEA expands the available options for a satisfactory simulation with different accelerograms. That is, FEA enables computer experiments to be performed at an evidently low cost and includes the possibility of optimizing the damper position in the structure.

PART FIVE

In recent years, research on damping applications by SMA has attracted increasing interest. This part of the paper discusses a brief and partial synthesis of studies of other alloys, of single crystals or poly-crystals, which have potential damping applications. Single-crystal alloys, such as NiMnGa or NiFeGa, can undergo larger deformations (i.e., up to 15 % or more) induced by two-phase transformations, which translates to more efficient damping in each working cycle. The inter-martensitic transformation is a relatively frequently encountered phenomenon in SMA studies. For classical Cu-based alloys, such as CuAlZn, the first transformation appears between the quenched austenitic structure (a high-temperature body centered cubic (or bcc) phase, which orders into a $L2_1$ structure, and 18R, which is a slightly monoclinic structure with 18 basal planes in its conventional cell. If the sample is correctly oriented, a second transformation takes place, i.e., a tensile-stressed 18R single crystal transforms into a fct structure, which is usually called 6R because of the number of basal planes in its conventional cell. CuAlBe single crystals have recently emerged as a potentially useful system that undergoes two-phase transformations, similar to CuZnAl, with interesting differences that are related to the mechanical properties of the phases involved and to the pertinent recoverable dynamic changes. Experiments performed more than 20 years ago showed dynamic changes in CuAlZn single crystals. These results were obtained by observing the displacements of single interfaces under varying temperature and/or stress actions [39]. At the end of this study, two research directions are briefly explored. The first research direction is a preliminary description of CuZnAl foams which are potentially useful in bearings for base isolated buildings. The second research direction summarizes the current knowledge on Fe-based alloys. These alloys are useful because of their welding capability and projected low price.

5.1. Improvements in SMA for damping: inter-martensitic transformations

Increased recoverable deformations can increase the hysteretic energy resulting in more efficient damping. Large deformations are advantageous for oscillation mitigation. At the same oscillation amplitude, using a SMA with two consecutive transformations requires smaller lengths of the SMA wires and produces more effective damping by increasing the hysteretic energy. The appearance of two phases has been a recurrent subject in the study of SMA single crystals. Fifty years ago, a second phase transformation was discovered in Cu-based alloys, increasing the complexity of SMA behavior. Studies in the literature have typically focused on SMA material properties without explicit investigation of practical damping requirements. Such analyses do not address the required fatigue-life, dynamic effects as describes the Section 5.3 and the ultimate parasitic effects of temperature oscillations from summer to winter.

Research studies have typically investigated only the progressive transformation from one form of martensite to another form in stress-induced transformations. A typical transformation path relates the parent (bcc) to martensite (i.e., 18R) and later to another form of martensite (i.e., fct). This transformation has also been observed in CuAlNi (see, for instance, page 34 in reference [1]). The "coexistence" of two different phases has been observed in poly-crystals and in temperature-induced transformations [133]. These results apparently violate the thermodynamic phase rule, i.e., 3 simultaneous solid phases co-exist for only one component. This apparent contradiction can be rationalized considering the distribution of internal stresses instead of considering the entire sample. Each constant-stress portion of the sample is considered to be a thermodynamic system, i.e., the parent and martensite$_1$ or the parent and martensite$_2$. Monoclinic martensite (18R) and hexagonal martensite (2H) "coexist" but are formed directly from the parent phase under different internal stresses.

This particular transformation is observed in temperature cycling in temperature under no external stress (i.e., at constant external pressure). In cooling, "islands" of the non-transformed beta-phase appear between plates of 2H variants. With progressive cooling, a fine morphology has been observed in the islands, which has been associated with several variants of the 18R monoclinic martensite phase [39, 133]. Similar "coexistence" of two martensites has been observed in the stress-induced transformation of single crystals of CuAlNi. If pseudo-elastic cycles are performed at increasing test temperatures, the hysteresis decreases because of the formation of smaller amounts of 2H compared to the proportion of 18R. Pseudo-elastic cycling under tensile stress is unfavorable to the appearance of 2H martensite, instead favoring the austenite-18R transformation. This behavior is the macroscopic result of the "relative stability between martensitic structures and its evolution due to stress-strain cycling" as discussed in references [134-135]. The complexity associated with small changes is a classic phenomenon in martensitic transformations.

The Cu-Al-Ni system has been deeply analyzed in the last decades and phase transformation diagrams have been presented for single crystals [1]. Depending on the alloy composition 18R or 2H martensite will form and the 6R martensite is also obtained by tensile stressing an 18R single crystal if the required tensile axis is correctly selected. However, the brittleness of the system is a disadvantage if applications as those here discussed are considered. Due to this reason we will not further comment on this system in this work.

A great increase in the available deformation was observed in CuAlZn, first in relation to the bcc-18R transition and later for the 18R-6R transition in traction or the 18R-2H transition in compression. A study performed in the seventies [136-137] investigated the appearance of two consecutive transformations for CuAlZn. This interesting mechanical behavior has been observed in austenitic single crystals that transform to 18R. If the test is performed under tensile stress, the obtained 18R exhibits the 18-6R transition for tensile axes closer than 24 degrees to the [100] orientation, while the 2H phase is formed if the 18R single crystal is tensile-stressed at orientations of the tensile axis far from the [100] orientation without a stress plateau or compressed in a conveniently re-oriented direction [138-139]. The temperature dependence of the 18R-6R transformation is extremely weak. This property is particularly useful for applications that are subjected to ambient temperature changes.

In recent years, the use of these consecutive transformations in new alloys (NiMnGa, NiFeGa) with higher hysteresis has become potentially useful for damping oscillations of structures. Further details can be found in references [140-142]. The study of classical and innovative alloys always requires an in-depth analysis of the basic properties of the SMA. The use of two consecutive phase transformations in oscillation mitigation is a subject that was mainly studied (in 2007-08) in single crystals of NiFeGa and NiMnGa by the Sehitoglu group in Urbana, USA. In particular, ref [140] reported that the number of working cycles to fracture exceeded 10000 for deformations of 10 % for

NiFeGa single crystals. Such results may have wider earthquake mitigation applications. Only cost presents an eventual obstacle for the practical application of these materials. Practical study requires that the dynamic effects not appear in the samples.

5.1.1 Two consecutive phase transformations in CuAlZn

Two consecutive transformations were observed in the seventies for Cu-Zn alloys [143-144]. This system exhibits a tensile stress-induced martensite-martensite transition, which is temperature-independent, but composition-dependent. Experiments have shown that an appropriately oriented single crystal of martensite transforms into an ordered structure similar to a fcc structure. However, the transformation temperatures for the austenite-martensite transition in the binary system were rather low for practical applications.

Ternary Cu-based alloys exhibit more practical transformation temperatures. Barceló et al. [145-146] studied the CuZnAl system and extended the previous results for the binary alloy. The Critical Resolved Shear Stress (CRSS) for the appearance of 6R martensite was found to be a function of the Al composition and the electronic concentration (e/a). The CRSS decreased for high amounts of Al at a constant e/a and increased at higher e/a and a constant Ms. A rather weak effect of the temperature on the stress that induces 6R has been detected. The weak temperature dependence of the 18R-6R transformation is particularly useful for applications that are subjected to daily and annual external temperature waves.

The 18R-6R transition in a single crystal of a ternary CuZnAl alloy showed a larger stress width compared to the hysteresis for the austenite-18R transition. An example of this transition can be seen in [145]: a first well-defined plateau during the 18R-6R transition, at stress under 50 MPa, strain up to 4%, then a nearly linear increase of stress to 250 MPa at 6% strain, and a further plateau to 15% strain (at 250 MPa), on unloading a first retransforming plateau at 120 MPa from 13.5 to 11.5% strain, then linear decrease of stress with decreasing strain to 40 MPa, 10% strain, and final decrease of stress with strain to nearly 0 stress at near 3% strain, showing a large deformation obtained during this transformation and larger hysteresis. An additional consideration is the effect of orientation and the stress mode on the plastic behavior of the 18R martensite. Orientations close to the $<100>_{\beta}$ direction lead to the formation of the 6R phase if the stress is applied in a tensile mode. However, if the orientation of the tensile axis separates more than 24 degrees from the $<100>_{\beta}$ direction, the plateau is non-existent and a rather brittle fracture occurs together with the formation of a hexagonal phase [147]. In compression, a single 18R structure is formed and further compression induces a plastic deformation [148]. This result precludes the use of this stress mode for applications requiring pseudo-elasticity.

An interesting feature of the 18R-6R transition involves the permanent deformation that is usually observed after an austenite-18R-6R cycle. This retained deformation is indicative of plastic deformation, as discussed in [149]. The leading result is that a smaller tensile stress is required to plastically deform 6R than the stress required to induce 6R martensite. Thus, plastic deformation is simultaneous with the martensite-martensite transformation. A recent and interesting solution to this problem was reported in [150]. The authors showed that introducing nanoprecipitates increased the plastic yield stress of the 6R martensite, thereby separating 6R formation from its plastic deformation. Thus, complete recoverability was obtained. Interesting recent results have also shown a highly stable stress-strain behavior at frequencies of approximately 1 Hz [151]) up to 2000 cycles. These results are of potential interest for damping applications.

5.2 Local structural change in CuAlBe induced by loading.

In the practical dampers studies, the experiments focused on the polycrystalline CuAlBe alloy without the appearance of two consecutive phases. The recoverable deformation was approximately 3.1%, and the increased deformation induced progressive SMA creep and fracture in the sample (as described in section four). Analysis of the fundamental behavior was performed on single crystals. Three types of results were obtained: (1) the appearance of additional martensite at higher loads, (2) slight structural distortion of the stress induced 18R martensite (see Section 5.3) and (3) a faster cycling evolution associated with "dynamic stabilization". This is an even stronger effect when compared with the quasi-static stabilization obtained from similar numbers of vacancies.

Depending on the thermo-mechanical treatment, pseudo-elasticity in a polycrystalline material is imperfect because the strain is not completely recovered upon unloading. An increase in the applied load leads to progressive permanent deformation or "SMA creep." This cans the result of plastic deformation, the presence of retained martensite or both mechanisms acting simultaneously. This effect was observed and quantified in section three for NiTi and in Part Four for polycrystalline CuAlBe. Polycrystalline Cu-based alloys show strong effects from the interaction between the martensitic transformation and the grain boundaries. This interaction usually enhances micro-plasticity, leading to higher amounts of retained martensite [20]. In Part Four, the experimental approach for polycrystalline CuAlBe exhibited SMA creep associated with progressive maximum strain.

Single crystals of Cu-based alloys constitute an interesting material where the mutual interaction of martensitic stress induced transformations and diffusion related phenomena give rise to complex mechanical behavior for both static and dynamic conditions [152-153]. The stabilization of martensite, changes in vacancy concentration and the ordering or reordering of the parent phases have been reported as potential mechanisms [154-155]. Changes in the order of the parent phase affect the martensitic transformation temperatures [156]. Section 5.4 describes tracking the transformation temperature versus the time and the external temperature for polycrystalline and single crystal materials of several Cu-based alloys. The stabilization of martensite [157] modifies the critical stresses and the morphology of stress-strain curves. Different portions of a specimen undergo different degrees of stabilization associated with the time spent in the martensitic state, and the effect induces a triangular shape in the hysteresis curves of the CuZnAl and CuAlBe single crystals [152-153, 158]. Furthermore, the kinetics of the diffusive phenomena is controlled by the martensite stabilization and by changes in parent material recovery, such as pseudo-elastic cycling [152-153]. For the CuAlBe system, the pseudo-elastic fatigue of single crystals exhibits a non-homogeneous decrease in the critical stresses and mechanical hysteresis during cycling [153, 159]. In the following section, a brief revision of the basic characteristics of the pseudoelastic behavior of CuAlBe single crystals is presented. Temperatures between 303 and 393 K were considered, as well as excursions down to 203 K. The M_s of the samples is near room temperature.

One of the features of the CuAlBe alloy is the appearance of a second transition. The consecutive transformation of bcc to 18R martensite and then to 6R martensite produces a larger deformation and a more relevant hysteresis for use as a practical damper. However, a deeper understanding of the bcc to 18R martensite cycling phenomena is needed. Using several samples, a study was performed using electrical resistance to determine the transformation temperatures and stress-strain measurements in order to evaluate the mechanical behavior. Figure 45 A shows the stress-strain curves corresponding to a complete β phase to 18R martensite transformation and partial 18R martensite to 6R martensite transition obtained at 303 K and 393 K, respectively. These temperatures correspond to a temperature difference T-Ms = 7 K and 97 K, respectively. From these measurements, the critical transformation stresses for both transformations are well defined. Moreover, a slight departure from linearity is observed for the obtained curve at 303 K for intermediate stresses, following the β phase to 18R martensite transition. The σ-ε curves in figure 45 A shows a different hysteresis associated with the β phase to 18R martensite transition for both

the selected temperatures. This suggests that 393 K is the maximum temperature that can be considered to avoid any overlapping between the stresses induced from the β phase to 18R martensite and 18R martensite to 6R martensite transitions.

Figure 45 B outlines the stress-strain (σ-ε) curves for several temperatures between 303 and 393 K. For each cycle, the maximum stress is larger than the stress required to complete the transformation to 18R martensite but is slightly lower than that required to induce the creation of 6R martensite. The maximum deformation towards the end of the 18R transformation shows little evolution between 125 and 175 MPa stress levels. The observed change in the $\varepsilon^{\beta\text{-}18R}$ deformation of the pseudoelastic stage with temperature is rather unusual because it should depend only on the composition and the orientation of the tensile axis of the sample, both of which are not affected by temperature. However, a similar strain has been reported for 2H martensite in Cu-Zn-Al alloys subjected to applied stress [160]. The justification information obtained from 2H martensite can be used for 18R martensite is that although both structures differ in their stacking sequence, the basal plane is the same. The possible explanation for the distortion is a change in the cell parameters of the basal plane from a similar variation in parameters that takes place in both structures. In Cu-Zn-Al alloys, a strain of 0.8 % for the 2H martensite was attributed to changes in the lattice parameters due to a possible second order phase transition [160].

From a series of tensile tests at several test temperature, the Clausius-Clapeyron coefficient from the parent to 18R martensite is 1.92 and 1.84 MPa/K from 300 K to 400 K, respectively. Detailed analysis of this structural evolution indicates the appearance of a structural distortion with slight temperature dependence, such as 0.42 MPa/K. The associated entropy change of the structural distortion was 2% of the complete transformation:

$$\Delta S^{18R\text{-}18R'} \approx 0.02\ \Delta S^{\beta\text{-}18R} \quad (17)$$

This small entropy change explains the departure from linearity for the Clausius-Clapeyron coefficient ($d\sigma^{\beta\text{-}18R}/dT$) as a function of temperature [161]. The 18R martensitic transition shows negligible hysteresis within the experimental resolution, which is different from most reported martensitic transitions in Cu-based systems.

Reference [161] includes a detailed analysis of these phenomena. Moreover, the mechanical hysteresis corresponding to the β phase to 18R martensite transformation increases with the test temperature as the overlap between the β phase to 18R martensite transformation and the structure distortion of the 18R phase increases. The hysteresis width increases from 5 to 13 MPa when the temperature rises from 300 to 390 K. The fit of the hysteresis width versus the temperature was parabolic and in agreement with the appearance of the structural distortion.

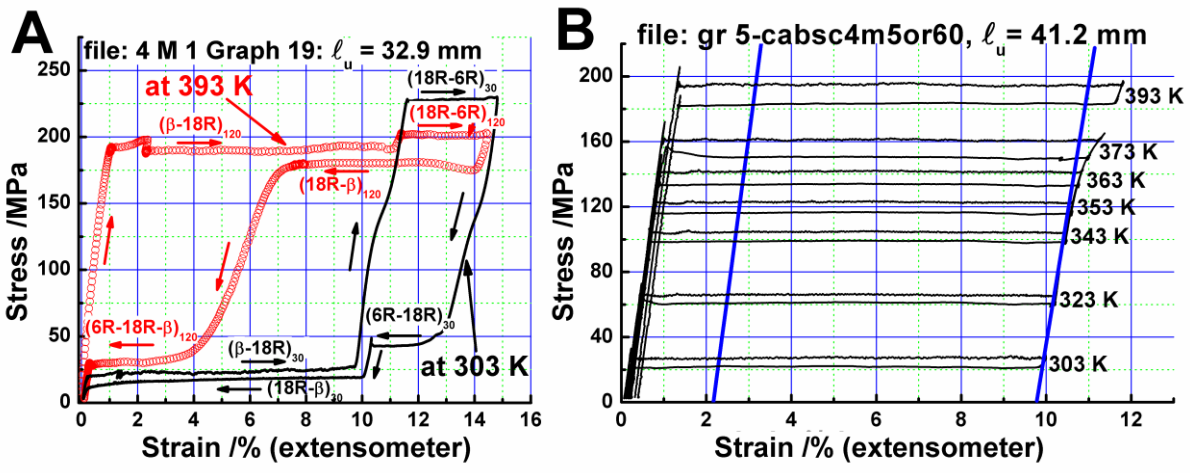

*Figure 45. CuAlBe single crystal. A: Sample A2 at 303 and 393 K. σ-ε curves corresponding to a complete β-18R transformation followed by a partial 18R-6R transition. Crosshead speed: 0.1 mm/min (strain rate: 5 * 10^{-5} s^{-1}). B: Stress- strain curves at several test temperatures for sample A3. Strain rate: 4 * 10^{-5} s^{-1}. The maximal tensile stress for each one approaches 200 MPa that overcomes the required stress for one complete β-18R transition.*

5.3. Dynamic and recoverable stabilization of CuAlBe

Pseudoelastic cycling of CuAlBe single crystals causes a strong mechanical evolution after a few hundred cycles [152, 159]. Figure 46 shows the main features that characterize pseudoelastic cycling in the samples; several σ-ε curves obtained from sample "cabsc1m4" at 353 K with a crosshead speed of 0.1 mm/min are shown [159]. An obtained reference cycle was found to deform the sample up to 10.5% for a crosshead speed of 0.1 mm/min; pseudoelastic cycling was then performed at 10 mm/min until a deformation of 8.3% was reached.

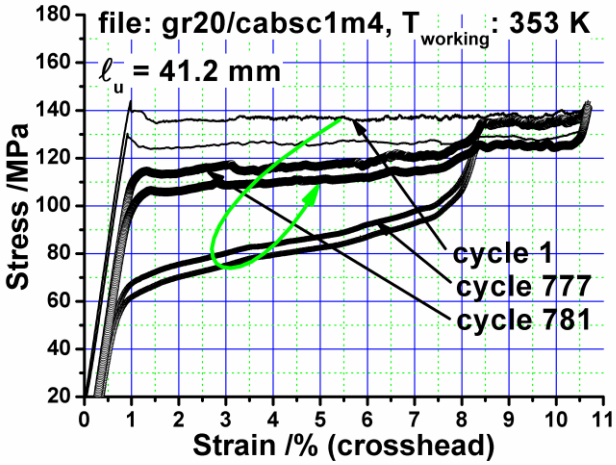

Figure 46. The σ-ε curves obtained for sample cabsc1m4 at T = 353 K. Cycles 1 and 777, previous and after rapid cycling respectively. Crosshead speed 0.1 mm/min, ε in the x axis obtained from the crosshead speed. Cycles 2 to 776 (not shown in fig) performed at 10 mm/min. Cycle 781 obtained after partial recovery of the β phase during 2 days. The big arrow visualizes the dynamic cycling effect.

After the rapid cycling, slow cycling was performed to check the recovery of the sample. As part of the sample did not transform during the rapid cycling, this part of the stress-strain curve provides the reference behavior. The main changes that take place in the stress-strain curves are the following:

a) The critical stress levels needed to transform and re-transform decreased as the number of cycles increased. These decreases differ for different amounts of deformation, are larger for parts of the samples that transform at an earlier stage and are negligible for the last part of the sample to transform. The consequence of this behavior is a strong increase in the slope during the transition stage, which changes with the number of cycles, N.
b) A decrease in the hysteresis to half of the original value after 777 cycles was observed. If the Clausius-Clapeyron relationship at the test temperature of 353 K is considered, the hysteresis corresponds to 5.3 K for cycle 1 and decreases to 2.8 K after 777 cycles.
c) After stopping the pseudoelastic cycling, the critical stresses start to increase in the direction of the values present before the cycling.
d) A decrease in the critical stresses needed to transform any remaining austenite is also obtained.

e) The permanent deformation increased with the number of cycles, and a partial recovery is also observed after rapid cycling is stopped.

A more detailed example concerning the evolution of the cycling and recovery of the β phase [159] obtained for sample "cab2m1" is presented in figure 47 A. The test temperature in this case was 353 K, and the crosshead speed during cycling was 10 mm/min. After 1000 rapid cycles were performed at this temperature, cycling at a new crosshead speed of 0.1 mm/min showed a strong decrease in the critical stress required to transform. The critical transformation stress $\sigma^{\beta\text{-}18R}$ decreased from 120 MPa to approximately 60 MPa for 1% deformation, which is equivalent to a 30 K increase in the Ms temperature. This amount of dynamic stabilization of the martensite is at least one order of magnitude larger than the static stabilization obtained at the same temperature and was obtained in shorted time intervals. Rapid cycling leads to an asymptotic behavior. An example is observed in figure 47 B performed at 353 K. See, below, the particular effects of the lower temperature (333 K) on the dynamic actions.

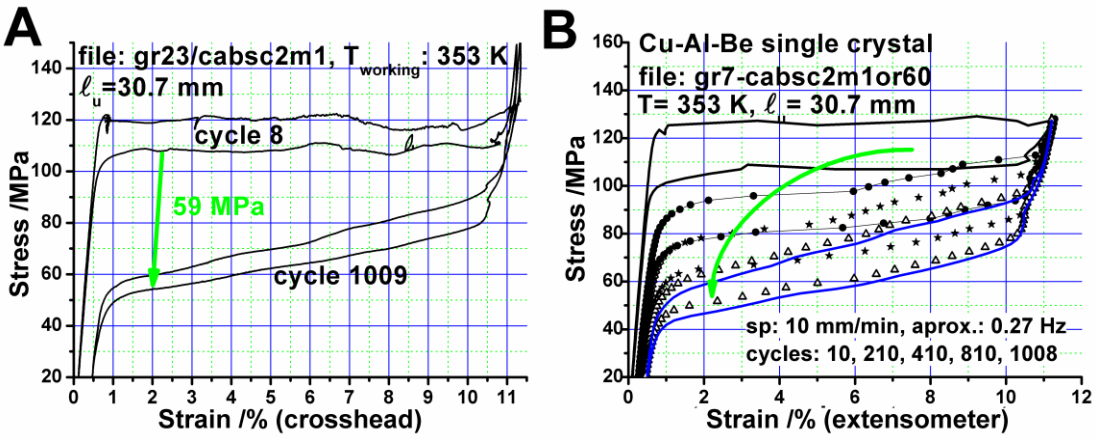

Figure 47. A: σ-ε curves corresponding to N= 8 and 1009, before and after rapid cycling. Crosshead speed 0.1 mm/min. ε in x axis obtained from extensometer. 1000 cycles in between at 10 mm/min. Dynamic stabilization = 59 MPa (29.5 K) Hysteresis of cycles 8 and 1009 equal to 11.8 MPa and 5.39 respectively. B: Rapid cycles obtained for sample cabsc2m1 at 353 K. Crosshead speed 10 mm/min. Cycles 10, 210, 410, 810 and 1008 are plotted. An asymptotic behavior is approached as shows the big arrow.

The evolution of the critical stresses after the rapid cycling has stopped is shown in figure 48 as a function of time. The behavior can be fitted to an exponential growth curve with a time constant larger than the one obtained for the martensite dynamic stabilization (time constants of 780 min and 150 min, respectively). The strong difference in time constants can be explained considering that the recovery of the austenitic structure takes place under quasi-static conditions, while the time constant which describes the martensitic stabilization corresponds to an enhanced dynamic effect. [152, 159].

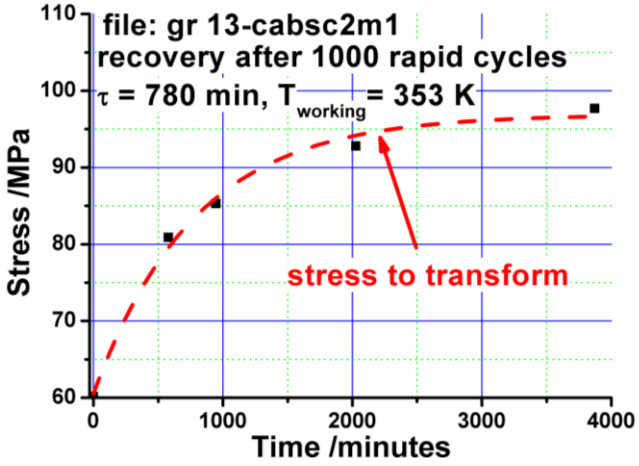

Figure 48. Applied stresses to transform measured as a function of time. Start point corresponds to the end of 1000 rapid cycles. Exponential decay fit is shown together with the obtained constant time. Stresses obtained at aprox. 2% ε in the pseudoelastic transition stage from cycles performed at a crosshead speed = 0.1 mm/min.

Two additional experiments were performed for strong stabilizations, and the results are shown in figure 49. Figure 49 A shows the results obtained from 3000 cycles performed at a test temperature of 333 K for a crosshead speed of 20 mm/min (frequency = 0.11 Hz) and for deformations of up to 5%. Most of the cycled portion of the sample stabilizes during cycling. A similar experiment was shown in figure 49 B, where pseudoelastic cycling strongly stabilizes part of the sample after 1303 cycles, and a strong recovery was observed after holding the sample at the same temperature in the parent phase. Rapid cycles are plotted as dashed lines, and slow cycles (0.1 mm/min, i.e., $2.8*10^{-4}$ Hz) are plotted as solid lines.

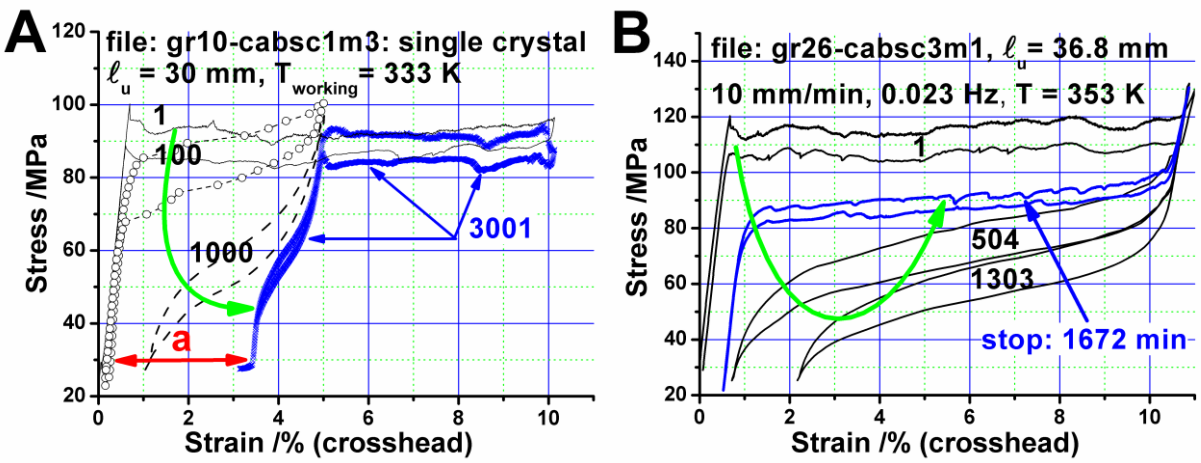

Figure 49. Dynamic stabilization and recovery. A: Cycle 1 and the first cycle after 3000 rapid cycles are shown in solid lines (crosshead speed 0.1 mm/min). Cycles 100 and 1000 performed at 20 mm/min are plotted in dots and in dash line respectively. Test temperature is 333 K. The arrow shows the evolution associate to cycling process (1 to 3001). a: dynamic stabilized martensite. B: Slow cycles obtained at crosshead speed 0.1 mm/min: N=1 and one "recovered" cycle obtained 1672 minutes after 1303 rapid cycles. Two rapid cycles are shown (N= 504 and 1303) at crosshead speed 10 mm/min). The arrow shows the evolution associate to "fast" cycles and to recovery related with one stop close to 28 h.

The main results from the pseudo-elastic cycling experiments are that the inhomogeneous dynamic stabilization of martensite was followed by recovery when the cycling is stopped. Both of these

facts indicate that diffusion plays a significant role. This behavior was similar to that reported for CuZnAl single crystals tested at temperatures greater than room temperature and for CuAlBe single crystals [152-153]. This behavior is explained considering the stabilization of the stress induced martensite and the recovery of the beta phase once the re-transformation takes place. As the time interval that each portion of the sample remains as beta phase martensite is different, the decrease in the critical stresses will also be different, causing a slope in the σ-ε curve at the transformation stage. These concepts allow modeling of pseudoelastic cycling for both systems [152-153].

Similarly, an overlapping of two diffusive mechanisms was sufficient to explain the change in slope in the stress strain curves for CuZnAl single crystals. One noticeable point concerning CuAlBe single crystal behavior is that the stabilization under static conditions with an equilibrium concentration of vacancies is not a significant factor, which causes difficulties in properly measuring the kinetics under static conditions for temperatures lower than 373 K. However, stabilization in these alloys can be obtained if the concentrations of vacancies are large enough, such as after quenching. Moreover, quenching through Ms has led to a so-called hyperstabilization effect, which increases Ms considerably more than the normal stabilization phenomenon [158, 162-167]. Different mechanisms have been proposed to be responsible for the stabilization in CuAlBe alloys; however, none have been able to explain all of the reported results.

The experiments presented so far do not allow to precisely assessing the physical mechanism behind the dynamic stabilization. Moreover considering that the initial amount of vacancies should be close to the equilibrium concentration, differing from the start conditions usually used to explore the behavior associated to the stabilization of martensite in these alloys. This point will not be further analyzed here and in fact it is still unknown which structure should be the final one after the stabilization of the martensite [168]. A last point we would like to emphasize is the noticeable difference in the kinetics constants if static and dynamic stabilization are compared. Tidu et al. [168] explain the strong stabilization as a consequence of the structural change of martensite which is not complete in each cycle and an inherited disorder in the β phase. However it is still an open question why this does not occur under static conditions. Two options have been considered here: the creation of vacancies during cycling and the movement of vacancies due to the interface movement [169]. A related discussion on a similar phenomena observed in CuZnAl was presented in [170].

The experimental results suggest that for damping the decay of critical stresses cannot be considered completely appropriate. This fact reduces progressively the hysteretic energy. Moreover, the partial stabilization and, later, the slow recovery (temperature dependent) inhibit the use of the alloy. In fact, when the initial part of the transformation remains directly in martensite the damper cannot smooth the reduced oscillations. This particular situation that requires more analysis at faster cycling frequencies close to actual ones in damping of civil engineering (i.e., from 0.25 to 10 Hz) suggest that the dynamics effects on the CuAlBe single crystal do not favors their use, at least if only the austenite-18R cycle is considered.

5.4 Ms tracking of external temperature by Cu-based alloys

Parts Three and Four indicate that the used SMA shows some aging effects at moderate temperatures. This has been attributed to diffusion processes in the materials. In CuAlBe, aging induces a recoverable tracking effect, but only non-recoverable monotonic actions are observed for NiTi. Actually, the alloys are obtained by specific thermo-mechanical treatments and the martensitic transformations are performed between meta-stable phases.

The results from the measurements of the electrical resistance of the hysteresis curve in Cu-based alloys are presented in table 5. Some results obtained for CuAlZn single crystals are found in

reference [39]. In this case, the Ms increased after quenching. It was possible to make a prediction of the Ms against the time and the temperature ("room or surroundings temperature") from the evaluated time constants versus temperature (equation 18) and the solution of the differential equation associated with the hidden order temperature ($T_i(t)$) by equation 19:

$$\tau_i = exp(A_i + B_i / T) \quad (i = 1, 2, \ldots) \tag{18}$$

$$\frac{dT_i(t)}{dt} = -\frac{T_i(t) - T_{RT}(t)}{\tau_I(T_{RT})} \tag{19}$$

By integrating $T_i(t)$, it is possible to evaluate Ms using equation 20 and reference values (T_{ref} and the $Ms(T=T_{ref})$):

$$Ms(t) = Ms(T=T_{ref}) + \sum a_i (T_i(t) - T_{ref}) \tag{20}$$

Figure 50 shows an example of the excellent agreement between the experimental and the calculated evolution for Ms in the CuAlZn single crystal [39, 171-172].

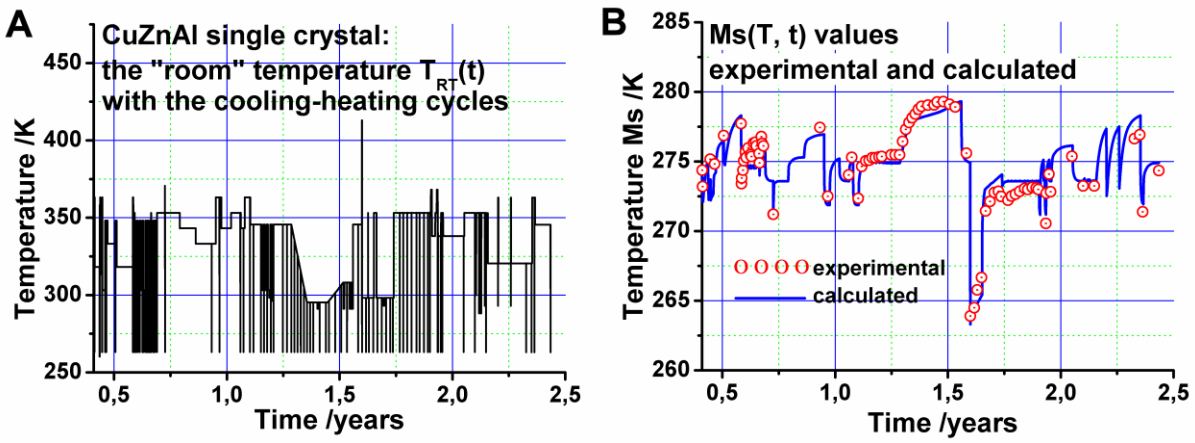

Figure 50. More than two years of Ms measurements for the Ms tracking in CuAlZn single crystal. A: "room" temperature against time with the cooling-heating cycles for Ms measurements. B: experimental measurements (dots) and simulated value using the equations 18, 19 and 20.

Figure 51 shows the recoverable evolution of a CuAlBe single crystal sample. After one homogenization at 1123 K for 300 s, the sample was quenched in water at 373 K. Later, the Ms was evaluated using a cooling-heating process lasting approximately 2.5 h. The sample always remained at one of the specified temperatures shown in figure 52 (either 348, 353, 373 or 378 K). The evolution of Ms permit a rough approach to be performed for determining the time constant and the activation energy (see table 6).

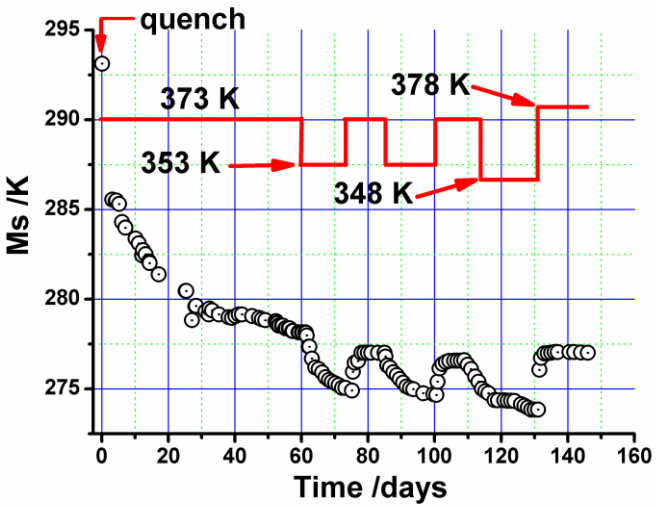

Figure 51. Recoverable actions in Cu-based SMA. "Room" temperature (up-line) and time effects on Ms values (dots) for a single crystal of CuAlBe.

Additionally, a single crystal of Cu-10.3 wt%, Al-4.3 wt%, Ni, with an initial transformation temperature of 238.2 K was studied. The alloy was homogenized at 1173 K for 300 s, before being quenched in room temperature water at and stored at room temperature (approximately 293 K) for nine years prior to taking the measurements. Figure 52 shows the Ms transformation temperatures versus time for a CuAlNi sample stored at 368 and 388 K. The small electrical resistance (approximately 20 mOhm) and the jerky transformation (parent to γ or hexagonal phase) produced more dispersion in the results than for the previously analyzed cases or thermo-elastic. The available results (including the scatter) are found in table 6. After quenching, the Ms increased, as was observed for the CuAlZn. However, a slow change in the transformation temperature with time was detected, and the amplitude of the change appears to be lower than for CuZnAl and the evolution time constant appears to range for months for the studied temperatures.

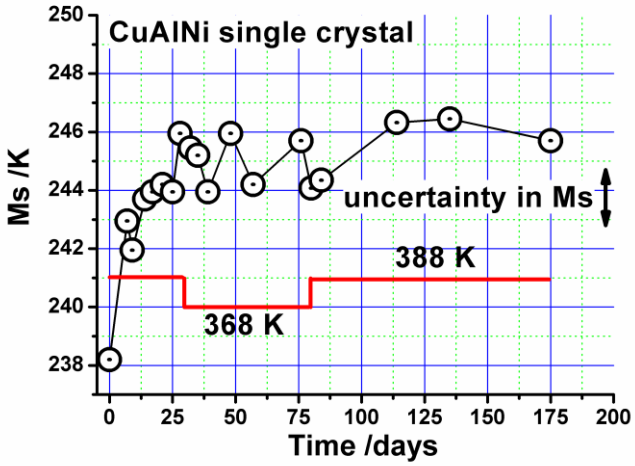

Figure 52. Measured transformation temperature (open dots) for the CuAlNi sample kept at the indicated temperatures. The lines are only visual guides.

Table 6. Cu-based alloys. Calculated values of time constants (τ_1 and τ_2) and activation energies.

CuZnAl (single cristal) [39,	T and τ_1	T and τ_2	activation energy	activation energy

153, 154]	373 K and 0.39 h	373 K and 13.1 h	13630 K	10330 K
CuAlBe poly-crystal [see, Part Four]	373 K and 1.73 d	- - -	5740 K	
CuAlBe single-crystal	373 K and 0.62 d	- - -	$12*10^3$ K	- - -
CuAlNi single-crystal	388 K and 20 d (*)	- - -	$1.4*10^4$ K (*)	- - -

(*) larger uncertainty

5.5 Eventual substitution of steel-rubber bearings with CuAlZn SMA foams.

The classic damping devices for base isolated buildings are bearings built with a series of steel and rubber discs. Usually the bearing, in the vertical axis, includes a cylindrical lead core that increases the hysteresis energy. The bearing works under the permanent load induced by the weight of the structure. The oscillations produced by the floor movement induced during an earthquake include both vertical and horizontal oscillations. The damping effect on the bearing was mostly associated with the shear oscillations caused by horizontal oscillations of the floor. In particular, the bearings smoothes the horizontal oscillations, but any recovery or re-centering actions are clearly limited or negligible. One possibility is to use SMA as a substitute material, including SMA foams to take advantage of the positive re-centering effects.

SMA CuZnAl foams with an Ms temperature below room temperature (Ms = 10°C) were synthesized [173-174] using the method described in reference [175]. Small millimeter-sized silica spheres were immersed in a molten alloy. Afterwards, the material cooled down and solidified when removed from the furnace. The foam is an open-cell structure, and the Cu-Zn-Al is a polycrystal.

The foams were tested in compression using an INSTRON 1123 mechanical testing machine, whereas other samples were tested using an MTS 810 servo-hydraulic machine for several different deformation ranges. The foams exhibited good pseudo-elastic behavior, as shown in figure 53 for more than 1000 working cycles. For the number of working cycles examined (1000) the increased permanent deformation (SMA creep) was not relevant. The foams were studied for different frequency conditions up tom 10 Hz. The material presents several advantages if we think of possible applications. The synthesis is direct. The starting material is cheaper than the most important possible competitor alloys. The CuZnAl foams do not need any training after preparation. The mentioned material would constitute a good possible candidate for damping applications substituting the rubber in bearings. In the actual “state of the art”, the full reliability and the shear response requires further study.

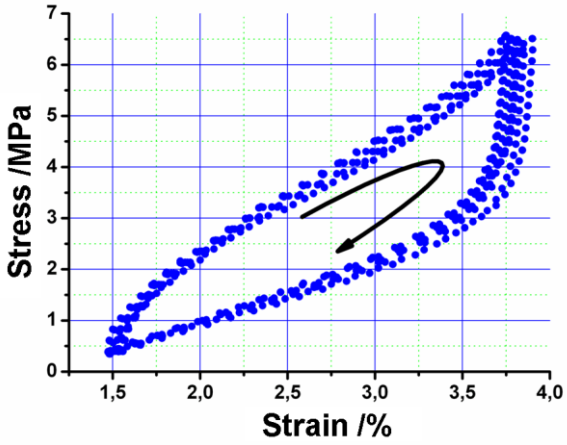

Figure 53. CuZnAl foam that shows a reduced degradation with working cycles. 1000 cycles of compressive stress strain representation. Representation of the cycles 100, 200, 300, …1000.

5.6. Expected improvements in SMA for damping: Use of the Fe-based alloys.

The possibility of using shape memory steels as damping materials has been the object of several studies. Most of these studies have focused on the damping properties of Fe-Mn-based shape memory alloys (SMAs). These alloys exhibit good overall material properties such as high ductility and workability, high strength and moderate to high corrosion resistance. Fe-Mn-based alloys are weldable using standard methods, and their cost is relatively low when compared to NiTi alloys [176-177]. The austenite phase of the Fe-Mn-based SMAs is fcc (γ). Alloys containing less than 14 wt.% Mn transform to bcc martensite (α') upon cooling, whereas for alloys with Mn contents in excess of 14 wt.%, hcp martensite (ε) is formed. Alloys with superior shape memory properties belong to the group containing more than 14 wt.% Mn [176].

Sato et al. identified the damping potential of these alloys based on the results of internal friction experiments on Fe-Mn-Si-Cr alloys [178]. From this, binary Fe-Mn alloys were found to have high damping properties on small amplitude vibrations. Lee et al. performed a long-term systematic effort in this field and identified the Fe-17 wt.% Mn alloy as the one with the best damping properties [179-181]. Additionally, a specific damping capacity (SDC) [2] of approximately 30% was measured for this material, and the SDC was found to be independent of the temperature and the vibration frequency between 0°C to 60°C and 10 Hz to 10^4 Hz, respectively [180]. The authors attribute the main damping effect to the movement of the γ/ε interfaces and the movement of partial dislocations at the ends of stacking faults. Other authors have studied the effects of alloy additions and pre-deformation on the damping properties. Jee et al. [182] reported on the effect that cold rolling had on the damping properties of a ternary Fe-Mn-Si alloy. It was found that while cold rolling increased the damping capacity, it also produced significant anisotropy [182]. Jun et al. studied Fe-Mn-Co alloys and reported that the addition of Co was beneficial to the SDC [183]. However, the effects of carbon and nitrogen additions were found to be disadvantageous for the SDC [184-185]. In general, all of the studies agree that partial dislocations movements (either at the ends of stacking faults or at γ/ε boundaries) are the main source of damping for small amplitude vibrations [179-180, 183, 186].

Despite their documented ability to mitigate small amplitude vibrations, Fe-Mn-based SMAs are considered unsuitable for seismic protection due to their poor pseudoelastic recovery properties, specifically caused by the γ/ε martensitic transformation in these materials being predominantly

[2] SDC defined by 100 $W_{hysteresis}/W_{transformation}$.

non-thermoelastic. Early studies have shown very restricted pseudoelastic behavior [187-189], usually related to low shape recovery properties. However, recent developments on these alloys related to the introduction of NbC precipitates [190-191] and pre-deformation at intermediate temperatures [174 192] resulted in materials with excellent shape memory properties and extended pseudoelastic ranges [193-195]. In particular, Sawaguchi et al. showed that a Fe-Mn-Si-Cr alloy containing a small amount of tiny NbC precipitates could be deformed by cycling between tension and compression [196], reaching a SDC of 80% for cycles with 1% deformation amplitude. Although further work in this area is necessary, this result opens possibilities for the application of these materials as elements in absorbing structures or in composite materials [197-198]. Recently, new Fe-based materials with extraordinary pseudoelastic properties have been presented [199-200]. In one case, the material is a complex and textured Fe-28Ni-17Co-11.5Al-2.5Ta alloy containing ordered Ni-Al bcc precipitates. The samples exhibit a 13.5% of pseudo-elastic recoverable strain over a huge stress-strain hysteresis loop [199]. The other case is for alloy Fe-34Mn-15Al-7.5Ni (wt.%). This alloy has the pseudoelastic behavior nearly temperature independent between 223 K and 423 K [200]. The applicability of these materials in real-world devices will be determined by the ability to produce them at an industrial scale, which is not clear at this moment. Furthermore, an appropriate study to determine the damping characteristics, such as the number of available working cycles, is necessary. For the present "state of the art" [201] it appears that the Fe-based alloys are close to application and eventual use in dampers.

5.7 Part Five: Summary

This section is devoted to new improvements in SMA: The two-phase transformations, to particular static and dynamic properties of CuAlBe single crystal and to improved SMA dampers. The inter martensitic transformations was first discovered in single crystals of CuZn in the 1970s. Biphasic transformations offer interesting deformation ranges and larger hysteresis appropriate for damping. Recently, the Sehitoglu group established the potential use of single crystals of NiMnGa and NiFeGa as dampers.

Studies of the polycrystalline CuAlBe alloy suggests potential success in applications such as dampers in structures for smoothing the oscillations induced by earthquakes. The alloy requires homogenization, quenching and aging to adequately stabilize the transformation temperature. Comparative analyses between single-crystals and polycrystalline CuAlBe showed faster tracking of the external temperatures by the single crystals. A partial study of other Cu-based alloys is included in this section (CuAlNi).

The extended analysis of the CuAlBe single crystal establishes the particular appearance of a second martensite (6R) and the emergence of an intermediate transition between martensite (18R) and martensite (6R), a "three-phase" behavior. A detailed study of the single crystals establishes the dynamic stabilization phenomena, a recoverable phenomenon that is clearly coupled to the external temperature.

The use of steel-rubber bearings for base isolated buildings requires a periodic change of the rubber, on the order of every 15 years. A compressive study of the CuAlZn foam offers one eventual solution. In addition, another solution may be found in Fe-based alloys, and the "state of the art" is described here. Recently, Fe-based alloys have received significant interest and seem to be one possible solution for low priced dampers in structures. The applicability of these materials was determined through the possibility of producing them at industrial scales and through building damping requirements.

PART SIX

6. Conclusions and remarks

The paper was devoted to the applications of Shape Memory Alloys in civil engineering, particularly NiTi and CuAlBe SMA alloys that permit appropriate efficiency in damping oscillations induced in structures. The first study focused on the oscillations induced in fixed cables by wind, rain or traffic. For this case, NiTi (2.46 mm diameter) avoids faster oxidation from rain or wetting and requires less preparation, such as 100 relatively slow cycles at 0.01 Hz. After the mechanical treatment, the alloy shows S-shaped hysteresis behavior that permits reasonable working in different temperatures, such as seasonal changes. For the damping of oscillations induced by earthquakes, the use of CuAlBe is an interesting possibility. In this case, the dampers were situated inside of a house and the wetting effects were irrelevant. Appropriate homogenization heat treatment for 2-10 min at 1093-1123 K, followed by quenching to room temperature and subsequent aging for one or two months at 373 K yields an alloy with constant properties for deformations up to 3.1%. Below, we outline of the principal conclusions and remarks for each section of the paper.

6.1. Modeling of the SMA behavior (the Part Two)

1) Recently, several groups working with SMA models have focused their attention on algorithms for FEA methods, such as models to simulate the SMA behavior and their insertion in device applications.

2) In general, the basic models use a large amount of parameters and the simulation of complex paths on the hysteretic behavior is difficult. The effect of temperature and stress aging was not considered by these studies.

3) To some phenomenological extent, bilinear or cubic models that include the Clausius-Clapeyron coefficient with rules to estimate internal loops permit an ease in the approach to applications. Most of the simulations consider completely invariant SMA behavior. Furthermore, this phenomenological approach implicitly considers that the previous experimental studies guarantee the invariance.

6.2. Remarks on the experimental results and the simulations for damping of the stayed cables (the Part Three).

1) The use of NiTi SMA requires a detailed knowledge of the behavior according to the requirements of the application. In particular, for damping stayed bridge cables, fatigue life is a major concern. The fracture life was determined to be four millions cycles for deformations near or less than 1%.

2) Cycling induces SMA creep, which, for 2.46 mm diameter wires, is 2.5%. The pauses between sets of cycles induce parasitic effects associated with minor recoverable creep. The associated energy effects are irrelevant for the standard number of working cycles. Previous pre-conditioning of the SMA wires, such as 100 cycles with a deformation of 8% at 0.01 Hz was necessary to achieve “reproducible” behavior.

3) The temperature effects induced by the cycling frequency were critical to determining the hysteresis width. Moreover, the fan used for the laboratory work or the wind in the external surroundings modifies the hysteresis width. The fan effect on cycling is reduced for cycled samples.

In actual working conditions, some wind and/or moisture is always expected and the effect of a fan in the "off" state was irrelevant.

4) The temperature analysis establishes that the partial or reduced transformations are fully distributed in the entire sample. This distributed effect can be considered the origin of the larger fracture for low deformations and loading.

5) The aging at permanent higher strain modifies the state of the samples to have an increased strength (up to 50%) and a steeper hysteresis. The practical effects of small amount of pre-strain in a damper do not modify the expected behavior of the damper. The stress-temperature aged samples furnish a new application via the increase the temperature span available (130-140 K) in comparison with the S-shaped cycles (90 K).

6) The use of pre-conditioned wires allows the successful use of SMA dampers under the cooling and heating associated with yearly temperature changes (seasonal effects). The maximum temperature range studied was approximately 80 K (between 253 and 333 K).

7) The evolution of the dissipated energy versus the strain for deformations less than 2.5% suggests a satisfactory representation using a quadratic fit. Moreover, the measurements establish a linear reduction of the energy versus the frequency.

8) The used SMA dampers reduce the amplitude of oscillations more than 50%. The effects of the SMA and the wax in the ELSA cable are similar to the SMA actions. Moreover, the SMA shows excellent damping behavior in the IFSTTAR cable.

9) The oscillations in the IFSTTAR cable were produced by Heaviside decay. The simulation visualized the limitations of the classical bilinear representation of the hysteretic behavior and suggested a more accurate model. The third degree (or cubic) model used two separate polynomial fits. One was used for the transformation and the other for the retransformation. The partial cycles and the internal loops were determined via qualitative rules from the cubic fits.

10) The simulation of the cables using the cubic model agreed with the experimental results, suggesting that the algorithms can be included as a part of the programs built for new bridges.

11) The time-frequency analysis shows a minor evolution of the amplitude with the cable oscillations. Their evolution was associated with the behavior of the SMA. The mean stiffness of the SMA decreases with a progressive transformation. This minor effect associated with the constant cable stiffness increases the frequency with the oscillation amplitude.

12) The length and the number of wires of an effective damper were established from the results established in the ELSA cable. The expected length of SMA wires and the cross section (or number of equal wires) is outlined.

6.3. Remarks on the experimental results and the simulations for damping oscillations induced by earthquakes (the Part Four).

1) Using a CuAlBe damper for smoothing oscillations induced by earthquakes is an interesting possibility. The alloy requires more preconditioning that the NiTi. The dampers were situated inside of a house, so wetting effects were irrelevant and the daily and seasonal temperature changes were minimized. Appropriate heat treatment by quenching in room temperature water after 2-10 minutes at 1093-1123 K and subsequent aging for one or two months at 373 K yields an alloy with constant properties for deformations up to 3.1%.

2) The study of CuAlBe shows a minor and slow evolution dependent of time and temperature that tracks the room temperature. The evolution of Ms can be modeled by similarity rules that are established for other Cu-based alloys, such as CuAlZn.
3) The results obtained in the application of the SMA to a realistic house are as expected. The SMA damper reduces the oscillation amplitude to 50 or to 33%. The energy, associated with the square of the oscillation amplitude, was reduced by 75% or by 90%, respectively.

4) Simulations using the cubic model for the SMA show behavior similar to the experimental measurements.

6.4. Remarks on the static and dynamic effects in CuAlBe single crystals, to CuZnAl foams and to Fe-based alloys (the Part Five).

1) Careful analysis of the tension-deformation study in CuAlBe single-crystals establishes the appearance of ***a minor phase transformation*** (named 18R') between the parent-18R and the 18R-6R. The observations show a reduced entropy change.

2) Relatively fast cycles of the partial transformation at 353 K show a dynamical evolution of the transformation stress in the cycled zone, called *a dynamic stabilization*. The evolution was asymptotical for each temperature. After a period without stress, recovery began. The evolution can be considered an "activated process" with a time constant of 780 minutes (13 h). Working at 323 K, the effect was increased and part of the transformed zone remains as dynamically stabilized martensite. However, after a sufficient time interval without stress the material recovers to the parent phase. The process was controlled by a time constant of one day. The cycling evolution suggests that the CuAlBe single crystals were not appropriate for damping. The analysis suggests that any single crystal need to be carefully studied to ensure that not shows the dynamic stabilization.

3) The CuAlZn foam is one tentative improvement to dampers composed of classic steel-rubber-lead bearings. The experimental preparation furnished satisfactory alloys. In the actual "state of the art", the compressive experimental behavior was satisfactory with no relevant stabilization.

4) The research into the preparation of Fe-based alloys to determine their workability and soldering difficultly is in progress. An interesting evolution in the practical approach was discovered by the Kajiwara group in 2005. In the last four or five years, positive steps have been taken and the approach to commercialize wires, bars and slabs is expected in the next two to four years.

This work is a consequence of a series of articles published by V Torra and coworkers in Journal of Thermal Analysis and Calorimetry (Metastable effects on martensitic transformation in SMA, parts I- IX) the last years. We are grateful to the editors of the Journal for the possibility to synthetize this lifetime work.

Acknowledgements

Research work realized in the frame of the projects "Construcción 22/2006" (M. Fomento, Spain) and SMARTeR (ESF 2007-09 and MICINN BIA2006-27041-E, PR2008-0235) and AGAUR: BE-1-DGR-2009-00480. The relevant support of Dr. G. Magonette and coll. in ELSA (EU, Ispra, Italy) and, also, of Dr. L. Dieng and coll. in the IFSTTAR (Bouguenais, Nantes, France) for the

measurements done in their Institutions is gratefully acknowledged. Some measurements were performed in an indoor thinner cable in the Pavia University. The support of Prof. F. Casciati and A. Marzi in Pavia, Italy was acknowledged. The support of P. Riquelme in the series of measurements performed in the "Centro Atómico" of Bariloche, Argentina, in the last 25 years, and of J. Lafuente and T. Garcia for the portico measurements in the "Lab. de Construcció" (ETSECCPB-UPC) in Barcelona was decisive. The 15 years cooperation with prof. P. Terriault at EST Montreal (Quebec, Canada) on simulation and FEA was extremely fruitful. The authors are indebted by the support of foams-grup in CAB: Drs. P. Arneodo, A. Baruj, G. Bertolino and H. Troiani, and for the parts associated to Fe-based alloys and in foams of CuAlZn. Prof. M. Ahlers and Dr. J.L. Pelegrina, their indefatigable support in more than twenty years of positive discussions focused in martensitic transformations, is gratefully acknowledged. We thank also the referees' suggestions, and the editorial office indications.

References.

[1] Otsuka K, Wayman CM. Eds. Shape Memory Materials. Cambridge: Cambridge University Press; 1998

[2] Wayman CM, Shape memory and related phenomena. Prog Mater Sci 1992;36:203-24

[3] Otsuka K, Ren X. Physical metallurgy of Ti-Ni-based shape memory alloys. Prog Mater Sci 2005;50(5):511-678

[4] Mohammad HE, Mandi H, Majid T, Bhaduri SB. Manufacturing and processing of NiTi implants: A review. Prog Mater Sci 2012;57(5):911-46

[5] Ishida A, Sato M, Takei A, Miyazaki S. Effect of heat treatment on shape memory behavior of Ti-rich Ti-Ni thin films. Mater T JIM 1995; 36(11):1349-55

[6] Kim JI, Kim HY, Hosoda H, Miyazaki S, Satoru H. Mechanical Properties and Shape Memory Behavior of Ti-Nb Alloys. Mater T JIM 2004;45(7):2443-8

[7] Kim JI, Kim HY, Hosoda H, Miyazaki S. Shape Memory Behavior of Ti–22Nb–(0.5–2.0)O (at%) Biomedical Alloys. Mater T JIM 2005;46(4):852-7

[8] Kanetaka H, Hosoda H, Shimizu Y, Kudo T, Zhang Y, Kano M, Sano Y, Miyazaki S. In Vitro Biocompatibility of Ni-Free Ti-Based Shape Memory Alloys for Biomedical Applications. Mater T JIM 2010;51(10):1944-50

[9] Janocha H, Ed. Adaptronics and smart structures. Berlin: Springer; 1999.

[10] Kohl M, Microactuators. Berlin: Springer Verlag 2004

[11] Van Humbeeck J, Non-medical applications of shape memory alloys. Mat Sci Eng A-Struct 1999;273–275:134–148

[12] Ben Mekki O, Auricchio F. Performance evaluation of shape-memory-alloy superelastic behavior to control a stay cable in cable-stayed bridges. Int J Nonlinear Mech 2011; 46(2): 470-7

[13] Torra V, Isalgue A, Auguet, Carreras G, Lovey FC, Terriault P, Dieng L. SMA in mitigation of extreme loads in civil engineering: Damping actions in stayed cables. In: Cheng YS, Lucas M, Applied Mechanics and Materials, Durnten-Zurich: Trans Tech Publications Inc,2011;82:539-44

[14] Sharabash AM, Andrawes, BO. Application of shape-memory alloy dampers in the seismic control of cable-stayed bridges. Eng Struct 2009; 31(2):607-16

[15] Casciati S, Faravelli L. Structural Components in Shape-memory Alloy for Localized Energy Dissipation. Comput Struct 2008;86:330-9

[16] Yunfeng Z, Songye Z. Seismic Response Control of Building Structures with Superelastic Shape-memory Alloy Wire Dampers. J Eng Mech-ASCE 2008;134(3):240-51

[17] Alam MS. Youssef MA. Nehdi M. Utilizing shape-memory alloys to enhance the performance and safety of civil infrastructure: a review. Can J Civil Eng 2007;34(9):1075-86

[18] Yawny A, Sade M, Eggeler G. Pseudoelastic cycling of ultra-fine-grained NiTi shape-memory wires. Z Metallkd 2005;96:608-18.

[19] Torra V, Isalgue A, Martorell F, Terriault P, Lovey FC; Built in dampers for family homes via SMA: an ANSYS computation scheme based on the mesoscopic and the microscopic experimental analysis. Eng Struct 2007;29:1889–902.
[20] Auguet C., Isalgué A., Lovey FC., Martorell, F. and Torra, V., Metastable effects on martensitic transformation in SMA Part 4. Thermomechanical properties of CuAlBe and NiTi observations for dampers in family houses. J Thermal Anal Calorim 2007;88:537–48
[21] DesRoches R, Smith B. Shape memory alloys in seismic resistant design and retrofit: a critical review of their potential and limitations. J Earthquake Eng 2004;8(3):415-29.
[22] Dolce M, Cardone D. Mechanical behaviour of shape memory alloy s for seismic applications 1. Martensite and austenite NiTi bars subjected to torsion. Int J Mech Sci 2001;43:2631–56
[23] Dolce M, Cardone D. Mechanical behaviour of shape memory alloys for seismic applications 2. Austenite NiTi wires subjected to tension. Int J Mech Sci2001;43:2657–77
[24] Wollants P, Debonte M, Roos JR. A thermodynamic analysis of the stress induced martensitic transformation in a single crystal. Z Metallkd 1979;70:113-7
[25] Wollants P, Roos JR, Delaey L. Thermally- and Stress-Induced Thermoelastic Martensitic Transformations in the Reference Frame of Equilibrium Thermodynamics. Prog Mater Sci 1993;37(3):227-88
[26] Wollants P, Roos, J, Otsuka K. On the thermodynamic-equilibrium of stress-induced martensitic transformations. Z Metallkd 1991;82(3):182-5
[27] Isalgue A, Torra V, Yawny A, Lovey FC. Metastable effects on martensitic transformation in SMA Part VI. The Clausius–Clapeyron relationship. J Thermal Anal Calorim 2008; 91(3): 991–8
[28] project ENV4-CT95-0106, http://ec.europa.eu/research/press/2001/pr0510en.html)
[29] Indirli M, Castellano MG. Shape Memory Alloy Devices for the Structural Improvement of Masonry Heritage Structures. Int J Architect Herit 2008;2(2);93-119
[30] Ozbulut OE, Hurlebaus S, DesRoches R. Seismic Response Control Using Shape Memory Alloys: A Review. J Intel Mat Syst Str 2011;22:1531-49
[31] Falk F. Model free energy, mechanics, and thermodynamics of shape memory alloys. Acta Metall 1980; 28:1773–80
[32] Mori T, Tanaka K. Average stress in matrix and average elastic energy of materials with misfitting inclusions. Acta Metall 1973;21(5):571–74
[33] Raniecki B, Tanaka K. On the thermodynamic driving force for coherent phase transformations. Int J Eng Sci 1994;32(12):1845–58
[34] Raniecki B, Lexcellent Ch, Tanaka K. Thermodynamic models of pseudoelastic behaviour of shape memory alloys. Arch Mech 1992;44(3):261-84
[35] Moumni Z, Wael Zaki W, Nguyen QS. Theoretical and numerical modeling of solid–solid phase change: Application to the description of the thermo-mechanical behavior of shape memory alloys. Int J Plasticity 2008; 24(4): 614–45
[36] Brinson LC. One-Dimensional Constitutive Behavior of Shape Memory Alloys: Thermomechanical Derivation with Non-Constant Material Functions and Redefined Martensite Internal Variable. J Intel Mat Syst Str 1993;4(2):229-42
[37] Auricchio F, Taylor RL, Lubliner J. Shape-memory alloys: macromodelling and numerical simulations of the superelastic behavior", Comput Method Appl M 1997;146(3):281-312
[38] Theriault P, Terriault P, Brailovski V, Gallo R. Finite element modeling of a progressively expanding shape memory stent. J Biomech 2006;39:2837-44
[39] Lovey FC, Torra V. "Shape memory in Cu-based alloys: phenomenological behavior at the mesoscale level and interaction of martensitic transformation with structural defects in Cu-Zn-Al. Prog Mater Sci 1999;44(3):189-289
[40] Abeyaratne R, Knowles J. 1993. A continuum model of a thermoelastic solid capable of undergoing phase transitions. J Mech Phys Solids 1993;41:541–571
[41] Tanaka T. A thermomechanical sketch of shape memory effect: one-dimensional tensile behavior. Res Mech 1986;18:251–6

[42] Tanaka K, Nagaki S. A thermomechanical description of materials with internal variables in the process of phase transitions. Arch Appl Mech 1982;51:287–99
[43] Zaki W, Moumni Z. A 3D model of the cyclic thermomechanical behavior of shape memory alloys. J Mech Phys Solids 2007;55:2427–54
[44] Zaki W, Moumni Z. A three-dimensional model of the thermomechanical behavior of shape memory alloys. J Mech Phys Solids 2007;55:2455–90
[45] Patoor E, Berveiller M. Lois de comportement et calcul de structures en alliage à mémoire de forme. In: Technologie des Alliages à Mémoire de Forme. Cachan(France): HERMES 1993;195–224
[46] Patoor E, Eberhardt A, Berveiller M. Thermomechanical behavior of shape memory alloys. Arch Mech. 1988;40:775–94
[47] Tanaka K. A Phenomenological Description on Thermomechanical Behavior of Shape Memory Alloys. J Press Vess-T ASME 1990;112:158-63
[48] Tobushi H, Iwanaga H, Tanaka K, Hori T, Sawada T. Stress-Strain-Temperature Relationship of TiNi Shape Memory Alloy Suitable for Thermomechanical Cycling. JSME Int J 1992; 35(3) Ser I:271-7
[49] Raniecki B, Lexcellent C. RL-Models of Pseudoelasticity and their Specification for some Shape Memory Solids. Eur. J. Mech., A/Solids 1994;13(1):21-50
[50] Bourdon G, Lexcellent C. Thermodynamic modeling of the cyclic behaviour in tension of TiNi and CuZnAl shape memory alloys. J Phys IV Col. C3 1994;4:145-150
[51] Patoor E, Eberhardt A, Berveiller M. Thermomechanical Behaviour of Shape Memory Alloys. Arch. Mech 1988;40(5-6):775-794
[52] Patoor E, Bensalah MO, Eberhardt A, Berveiller M. Thermomechanical behaviour determining of shape memory alloys using a thermodynamical potential optimizing. Rev Metall-Paris 1993; 90:1587-92
[53] E. Patoor, A. Eberhardt, M. Berveiller. Micromechanical Modelling of Superelasticity in Shape Memory Alloys. J Phys IV Coll. C1 1996;6:277-92
[54] Siredey N, Patoor E, Berveiller M, Eberhardt A. Constitutive equations for polycrystalline thermoelastic Shape Memory Alloys - Part 1: Intragranular interactions and behaviour of the grain. Int J Solids Struct1999; 36:4289-315
[55] Likhachev VA. 'Structure-Analytical Theory of Martensitic Unelasticity. J Phys IV 1995;5:137_42
[56] Paradis A, Terriault P, Brailovski V. Modeling of residual strain accumulation of NiTi shape memory alloys under uniaxial cyclic loading, Comp Mater Sci 2009;47:373–83
[57] Terriault P, Brailovski V. Modeling of Shape Memory Alloy Actuators Using Likhachev's Formulation. J Intel Mat Syst Str 2011;22(4):353-68
[58] Brinson LC. One-Dimensional Constitutive Behavior of Shape Memory Alloys: Thermomechanical Derivation with Non-Constant Material Functions and Redefined Martensite Internal Variable. J Intel Mat Syst Str 1993;4(2) 229-42.
[59] Brinson LC, Huang MS. Simplifications and comparisons of shape memory alloy constitutive models. J Intel Mat Syst Str 1996;7(1):108-14
[60] Sun QP, Hwang KC. Micromechanics Modelling for the Constitutive Behavior of Polycristalline Shape Memory Alloys (part I and II). J. Mech. Phys. Solids 1993;41(1):1-33
[61] Boyd JG, Lagoudas DC. Thermomechanical Response of Shape Memory Composites. J Intel Mat Syst Str 1994;5:333-346
[62] Lagoudas DC, Bo Z, Qidwai MA. A Unified Thermodynamic Constitutive Model for SMA and Finite Element Analysis of Active Metal Matrix Composites", Mech Compos Mater St 1996;3:153-79
[63] Auricchio F; Taylor RL. Shape-memory alloys: Modelling and numerical simulations of the finite-strain superelastic behavior. Comput Method Appl M 1997;143(1-2):175-94
[64] Auricchio F, Lubliner J. A uniaxial model for shape-memory alloys. Int J Solids Struct 1997;34(27):3601-18

[65] Torra V, Lovey FC, Terriault P. Experimental study of damping in civil engineering structures using smart materials (Cu-Al-Be – NiTi SMA). Applications to steel portico and to stayed cables for bridges (The SMARTeR project). In: Barros R, Preumont A. editors. School and Symposium on Smart Structural Systems Technologies, S(3)T, Faculdade de Engenharia da Universidade do Porto; 2010, p. 369-99
[66] Zaki W, Moumni Z. A three-dimensional model of the thermomechanical behavior of shape memory alloys. J Mech Phys Solids 2007;55:2455-90
[67] Terriault P, Meunier MA, Trochu F. Application of Dual Kriging to the Construction of a General Phenomenological Material Law for Shape Memory Alloys", J Intel Mat Syst Str 1997;8:605-17
[68] ANSYS Mechanical APDL Programmer's manual, ANSYS inc. documentation, Release 13.0, November 2010.
[69] Isalgue A, Pelegrina JL, Torralba A, Torra VR, Torra V. Meso-scale model of a Cu-Zn-Al single crystal SMA. Mechanics of phase transformation and SMA, LC. In: Brinson LC, Moran B, editors. New York: ASME; 1994, p. 71-84
[70] Isalgue A, Lovey FC, Pelegrina JL, Rogueda C, Torra V. Experimental studies, modeling and simulation of the hysteresis in SMA single crystals: The stress, strain, temperature and time coordinate space. J. Phys IV 1995;5:C2-471-6
[71] Sung Young, Tae-Hyun Nam, Thermodynamic constitutive model for load-biased thermal cycling test of shape memory alloy, Mat Res Bull 2013; 48:5110–5114
[72] Bashir S. Shariat, Yinong Liu, Gerard Rio, Finite element computational modelling and experimental investigation of perforated NiTi plates under tension, Mat Res Bull 2013; 48:5099–5104
[73] Weiguo Li, Xueliang Shen, Xianghe Peng, A Constitutive Description for Shape Memory Alloys with the Growth of Martensite Band. *Materials* 2014; *7*:576-590; doi:10.3390/ma7010576
[74] Chao Yu, Guozheng Kang, Qianhua Kan, Crystal plasticity based constitutive model of NiTi shape memory alloy considering different mechanisms of inelastic deformation. International Journal of Plasticity 2014 54:132–162
[75] K.M. Armattoe, M. Haboussi, T. Ben Zineb, A 2D finite element based on a nonlocal constitutive model describing localization and propagation of phase transformation in shape memory alloy thin structures. International Journal of Solids and Structures 2014; 51:1208–1220]
[76] Feifei Cheng, Liangfa Hu, Junuthula N. Reddy, Ibrahim Karaman, Elizabeth Hoffman, Miladin Radovic, Temperature-dependent thermal properties of a shape memory alloy/MAX phase composite: Experiments and modeling. Acta Mater 2014, 68:267–278
[77] Andani, Masood Taheri; Elahinia, Mohammad, A rate dependent tension-torsion constitutive model for superelastic nitinol under non-proportional loading; a departure from von Mises equivalency.
SMART MATERIALS AND STRUCTURES 2014; Vol. 23, 1, Article 015012 (JAN 2014)
[78] T. Baxevanis, A. Cox, D. C. Lagoudas, Micromechanics of precipitated near-equiatomic Ni-rich NiTi shape memory alloys. Acta Mech 2014; 225:1167–1185
[79] Benafan O., Noebe RD., Padula II SA., Brown, DW., Vogel S., Vaidyanathan R., Thermomechanical cycling of a NiTi shape memory alloy-macroscopic response and microstructural evolution. International Journal of Plasticity 2014; 56:99–118
[80] J. Wang, H. Sehitoglu, Twinning stress in shape memory alloys: Theory and experiments, Acta Mater 2013; 61:6790–6801
[81] Dorian Depriester, Anne Maynadier, Karine Lavernhe-Taillard, Olivier Hubert, Thermomechanical modelling of a NiTi SMA sample submitted to displacement-controlled tensile test, International Journal of Solids and Structures 2014; 51:1901–1922
[82] F. Auricchio, E. Bonetti, G. Scalet, F. Ubertini, Theoretical and numerical modeling of shape memory alloys accounting for multiple phase transformations and martensite reorientation. International Journal of Plasticity 2014; 59:30–54

[83] Lexcellent C, Torra V, Raniecki B. Hysteresis behavior of Thermoelastic Alloys – Some Shape-Memory Alloys Models. J Phys III 1993;3(7):1463-77
[84] Janke L, Czaderski C, Motavalli M, Ruth J. Applications of shape memory alloys in civil engineering structures - Overview, limits and new idea. Mater Struct 2005;38: 578-92
[85] Wilson JC, Wesolowsky MJ. Shape Memory Alloys for Seismic Response Modification: A State-of-the-Art Review. Earthq Spectra 2005;21(2):569-601
[86] Lagoudas DC. Editor, Shape Memory Alloys: Modeling and Engineering Applications. New York; Springer 2008
[87] Terriault P. Shape Memory Alloys: Fundamentals, Modeling and Applications and Constitutive equations and Finite elements. In: Brailovski V, Prokoshkin S, Terriault P, Trochu F, editors. Université du Québec-ETS-Montreal; 2003 : p 549-634 and 635-684
[88] Sedlak P, Sittner P, Heller L, Pilch J. Evaluation of SMA roundrobin. In: Barros R, Preumont A. editors. School and Symposium on Smart Structural Systems Technologies, S(3)T, Faculdade de Engenharia da Universidade do Porto; 2010, p. 263-271
[89] Morin C, Moumni Z, Zaki W. A constitutive model for shape memory alloys accounting for thermomechanical coupling. Int J Plasticity 2011; 27:748–767
[90] Torra V, Tachoire H. "Martensitic transformations in shape memory alloys. Successes and failures of thermal analysis and calorimetry", Thermochim. Acta 1992;203:419-44
[91] http://en.wikipedia.org/wiki/Dongting_Lake_Bridge (2014)
[92] http://www.lord.com/Products-and-Solutions/Magneto-Rheological-(MR).xml (2012)
[93] Chen ZQ, Wang XY, Ko JM, Ni YQ, Spencer Jr BF, Yang G. MR damping system on Dongting Lake cable-stayed bridge. In: Liu, S-C editor. Proceedings of the SPIE; 2003, Vol. 5057, p. 229-235
[94] http://www.esf.org/activities/eurocores/completed-programmes/s3t/projects.html (2013)
[95] Carreras G, Isalgue A, Torra V, Lovey FC, Soul H. Metastable effects on martensitic transformation in SMA - Part V. Fatigue-life and detailed hysteresis behaviour in NiTi and Cu-based alloys. J Therm Anal Calorim 2008;91(2):575-9
[96] K. Otsuka and X. Ren. Mechanism of martensite aging effect. Scripta Mater 2005;50(5):511-678
[97] Condó AM, Lovey FC, Olbricht J, Somsen Ch, Yawny A. Microstructural aspects related to pseudoelastic cycling in ultra fine grained Ni-Ti, Mat Sci Eng A-Struct 2008; 481-482:138-41
[98] Ashby MF, Jones DRH. Engineering Materials. An introduction to their properties and applications, Oxford, England; Pergamon Press; 1980, p. 136-7
[99] Basquin OH. The exponential Law of endurance tests. Proc Am Soc Test Mater Proc 1910; 10:625-30
[100] Tobushi H, Hachisuka T, Yamada S, Lin P-H. Rotating-bending fatigue of a NiTi Shape Memory Alloy wire. Mech Mater 1997;26:35-42
[101] de Azevedo MG, Fonseca R, Lopes VT. The influence of high amplitude cycling straining on the behaviour of superelastic NiTi. Int. J. Fatigue 2006;28:1087-91
[102] Maletta C, Furgiuele F. Analytical modeling of stress-induced martensitic transformation in the crack tip region of nickel–titanium alloys. Acta Mater 2010; 58:92-101
[103] Baril Y, Brailovski V, Terriault P. Fatigue properties of superelastic Ti-Ni filaments used in braided cables for bone fixation. Adv. Sci. Tech 2008;**57:**235-40
[104] The NiTi wire Smartflex_ 150 marketed by SAES Getters was used throughout the experimental campaign. The wire has a diameter of 0.150 mm: Mammano GS, Dragoni E. Functional fatigue of Ni–Ti shape memory wires under assorted loading conditions. Adv Sci Tech 2013;78:40-5
[105] Miyazaki S, MizukoshiK, Ueki T, Sakuma T, Liu YN. Fatigue life of Ti-50 at.% Ni and Ti-40Ni-10Cu (at.%) shape memory alloy wires. Mat Sci Eng A-Struct1999; 273:658-63
[106] Pelton AR. Nitinol Fatigue: A Review of Microstructures and Mechanisms. J Mater Eng Perform 2011; 20(4-5):613-7

[107] Robertson SW, Pelton AR, Ritchie RO. Mechanical fatigue and fracture of Nitinol. Int Mater Rev 2012; 57(1) 1-36
[108] Torra V, Isalgue A, Martorell F, Lovey FC, Terriault P. Damping in Civil Engineering Using SMA. Part I: Particular Properties of CuAlBe for Damping of Family Houses. Can Metall Quart 2010;49(2):179-90
[109] Torra V, Auguet C, Isalgue A, Lovey FC, Sepulveda A, Soul H, Metastable effects on martensitic transformation in SMA Part VIII. Temperature effects on cycling. J Thermal Anal Calorim 2010; 102:671-680 (DOI: 10.1007/s10973-009-0613-3)
[110] Soul H, Isalgue A, Yawny A, Torra V, Lovey FC. Pseudoelastic fatigue of NiTi wires: frequency and size effects on damping capacity. Smart Mater Struct 2010;19(8):1777-1783
[111] He Y-J, Sun Q-P.: Frequency-dependent temperature evolution in NiTi shape memory alloy under cyclic loading. Smart Mater. Struct 2010;19: 115014 (9pp) doi:10.1088/0964-1726/19/11/115014
[112] He Y-J, Sun Q-P. Rate-dependent domain spacing in a stretched NiTi strip. Int. J. Solids Struct 2010; 47(20):2775-83.
[113] Auguet C, Isalgue A, Lovey FC, Pelegrina JL, Ruiz S, Torra V, Metastable effects on martensitic transformation in SMA. Part III. Tentative temperature effects in a NiTi alloy. J Thermal Anal Calorim 2007; 89:537–542
[114] Auguet C, Isalgue A, Torra V, Lovey FC, Pelegrina JL, Metastable effects on martensitic transformation in SMA. PART VII. Aging problems in NiTi. J Thermal Anal Calorim 2008; 92:63–71
[115] Weighardt SC, Maier HJ, Chumlyakov Y. Dependence of Functional Degradation on Crystallographic Orientation in NiTi Shape Memory Alloys Aged Under Stress. Poster session: P2-22, September 4-9, 2011, ICOMAT, Osaka, Japan
[116] Torra V, Auguet C, Isalgue A, Carreras G, Lovey FC, Metastable effects on martensitic transformation in SMA: Part IX. Static aging for morphing by temperature and stress. J Thermal Anal Calorim 2013; 112:777-780 (DOI 10.1007/s10973-012-2585-y)
[117] Torra V, Auguet C, Isalgue A, Lovey FC, Terriault P. The SMA was a tool for damping the induced oscillations in civil structures. Application to earthquake mitigation in family homes and to stayed cables for bridges. Applications of Transformations to Smart System I, September 9, 2011, ICOMAT, Osaka, Japan
[118] Casciati S, Marzi A. Experimental studies on the fatigue life of shape memory alloy bars. Smart Struct Syst 2012;6(1):73-85
[119] Faravelli L, Fuggini C, Ubertini F. Toward a hybrid control solution for cable dynamics: theoretical prediction and experimental validation. Struct Control Hlth 2010;17(4):386–403
[120] http://earthquake.usgs.gov/learn/topics/measure.php (September 2014)
[121] Torra V, Isalgue A, Lovey FC. Microstructure and thermodynamics of the martensitic transformation. Can Metall Quart 2000:39(2):207-16
[122] The family house structure was created by Rosa Maria Torra and calculated by Alfonso Vera, architects (2008). Respective e-mail: rmtorra@coac.net and averagq@coac.net.
[123] Zhang YF, Camilleri JA, Zhu SY, Mechanical properties of superelastic Cu-Al-Be wires at cold temperatures for the seismic protection of bridges. Smart Mater Struct 2008; 17 (2): Article Number: 025008
[124] Montecinos S, Cuniberti A. Thermomechanical behaviour of CuAlBe shape memory alloy. J Alloy Compd 2008;457: 332-336
[125] Isalgue A, Fernandez J, Torra V, Lovey FC. Conditioning treatments of Cu–Al–Be shape memory alloys for dampers. Mat Sci Eng A Struct 2006; 438–440: 1085–8
[126] Auguet C., Isalgué A, Lovey FC, Martorell F. Torra V. Metastable effects on martensitic transformation in SMA. Part 4. Thermomechanical properties of CuAlBe and NiTi observations for dampers in family houses. J Therm Anal Calorim 2007; 88 (2): 537–48

[127] Torra V, Pelegrina JL. Isalgue A, Lovey FC. Metastable effects on martensitic transformation in SMA (I) Recoverable effects by the action of thermodynamic forces in parent phase. J Therm Anal Calorim 2005; 81: 131–5
[128] Sepulveda A, Muñoz R., Lovey FC., Auguet C., Isalgue A. Torra V. Metastable effects on martensitic transformation in SMA. Part II. The grain growth effects in Cu–Al–Be alloy J Therm Anal Calorim 2007; 89 (1): 101-7
[129] Casciati F, private communication (2009).
[130] http://www.celsa.com/Pdf/productos/perfiles_heb.pdf (September 2014)
[131] http://www.celsa.com/Pdf/productos/perfiles_ipn.pdf (September 2014)
[132] Terriault P, Torra V, Fischer C, Brailovski V, Isalgue A. Superelastic Shape Memory Alloy Damper Equipped with a Passive Adaptive Pre-straining Mechanism. Proceedings of the 9th Canadian Conference on Earthquake Engineering (9CCEE), Ottawa, 26-29 June 2007, p. 1489-96.
[133] Van Humbeeck J, Van Hulle D, Delaey L, Ortiz J, Segui C, Torra V. A two-stage martensite transformation in a Cu-13.99 mass % Al-3.5 mass % Ni alloy. Mater T JIM 1987; 28 (5):383-91
[134] Gastien R, Corbellani CE, Sade M, Lovey FC. Thermal and pseudoelastic cycling in Cu–14.1Al–4.2Ni (wt%) single crystals. Acta Mater 2005; 53:1685–91
[135] Gastien R. "Fatiga pseudoelastica en aleaciones de CuAlNi" PhD thesis, Univ. Nac. Buenos Aires, August 2005 (in Spanish).
[136] Barceló, G.; Ahlers, M.; Rapacioli, R. The stress induced phase transformation in martensitic single crystal of CuZnAl alloys. Z Metallkd 1979; 70 (11): 732-38.
[137] Sade M. Deformation mechanisms in martensitic single crystals, Ms thesis, Instituto Balseiro, U.N.de Cuyo, 1980 (in Spanish).
[138] Sade, M.; Rapacioli, R.; Lovey, F.; Ahlers, M. An 18R to hexagonal transformation in CuZnAl. J Phys IV 1982; 43:C4-647-52.
[139] Tolley, A.; Ríos Jara, D.; Lovey, F.C. 18R to 2H transformations in Cu-Zn-Al alloys. Acta Metall 1989; 37(4):1099-108.
[140] Efstathiou C, Sehitoglu H, Kurath P, Foletti S, Davoli P. Fatigue response of NiFeGa single crystals. Scripta Mater 2007;57(5):409–12.
[141] Efstathiou C, Sehitoglu H, Carroll J, Lambros J, Maier HJ. Full-field strain evolution during intermartensitic transformations in single-crystal NiFeGa. Acta Mater 2008; 56(15):3791–99.
[142] Hamilton RF, Sehitoglu H, Aslantas K, Efstathiou C, Maier HJ. Inter-martensite strain evolution in NiMnGa single crystals. Acta Mater 2008; 56(10) 2231-6
[143] Arneodo W, Ahlers M. Plastic deformation of martensitic Cu-Zn single crystals. Scripta Metall 1973; 7(12):1287-94
[144] Arneodo W, Ahlers M. The martensitic transformation in β Cu-Zn. Acta Metall 1974; 22(12):1475-80
[145] Barceló, G.; Ahlers, M.; Rapacioli, R. The stress induced phase transformation in martensitic single crystal of CuZnAl alloys. Z Metallkd 1979; 70(11):732-38
[146] Ahlers, M.; Barceló, G.; Rapacioli, R. The stress induced transformation between orthorhombic and face centered martensite in CuZn alloys. Proc. Int. Conf. on martensitic transformations-ICOMAT 79. Cambridge, Massachusetts, USA (24-29 June 1979) 277-82
[147] Sade M, Rapacioli R, Lovey FC, Ahlers M. An 18R to hexagonal transformation in Cu-Zn-Al. J Phys IV 1982; C4-43:647-52.
[148] Cuniberti, A.; Romero, R.; Ahlers, M. The plastic deformation of long range ordered 18R martensitic single crystals of Cu-Zn-Al alloys. Scripta Metall Mater 1992; 26(3):495-500
[149] A. Cuniberti, R. Romero. Slip systems in Cu-Zn-Al martensitic phases. Mat Sci Eng A Struct 1999; 273–275:362–5.
[150] F. de Castro Bubani, M. Sade, F. Lovey. Improvements in the mechanical properties of the 18R <-> 6R high-hysteresis martensitic transformation by nanoprecipitates in CuZnAl alloys. Mat Sci Eng A Struct 2012; 543:88– 95

[151] F. de Castro Bubani, Marcos Sade, Francisco Lovey, Mechanical Behavior Under Cyclic Loading Of The 18r-6r High-Hysteresis Martensitic Transformation In Cuznal Alloys With Nanoprecipitates. Submitted (2013) to Mat Sci Eng A Struct.
[152] Yawny A, Lovey FC, Sade M. Pseudoelastic fatigue of Cu-Zn-Al single crystals: The effect of concomitant diffusional processes. Mat Sci Eng A Struct 2000; 290:108-21.
[153] N.Siredey,A.Eberhardt. Fatigue behavior of Cu-Al-Be shape memory single crystals. Mat Sci Eng A Struct 2000; 290:171-9.
[154] Mañosa L, Jurado M, González-Comas A, Obradó E, Planes A, Zarestky J, Stassis C, Romero R, Somoza A, Morin M. A comparative study of the post-quench behaviour of Cu-Al-Be and Cu-Zn-Al shape memory alloys. Acta Mater 1998; 46:1045-53.
[155] Pelegrina JL, Ahlers M. Influence of a constant stress during isothermal beta phase ageing on the martensitic transformation in a Cu-Zn-Al shape memory alloy. Scripta Mater 2004; 50:423-7.
[156] Rapacioli R, Ahlers M. The influence of short-range disorder on the martensitic transformation in Cu-Zn and Cu-Zn-Al alloys. Acta Metall 1979; 27(5):777-84.
[157] Abu Arab A, Ahlers M. The stabilization of martensite in Cu-Zn-Al alloys. Acta Metall 1988; 36(9):2627-38.
[158] González CH, De Araújo CJ, Cuadros NF, Guénin G, Morin M. Study of martensitic stabilisation under stress in Cu-Al-Be shape memory alloy single crystal. Mat Sci Eng A Struct 2004; 378:253-6.
[159] Sade M, Lovey FC, Torra V, Yawny A. Pseudoelastic cycling in Cu-Al-Be single crystals: Interaction with diffusive phenomena. ESOMAT 2009, Prague, 06036 (2009), DOI:10.1051/esomat/200906036, published by EDP Sciences 2009; (www.esomat.org)
[160] Arneodo Larochette P, Condó AM, Ahlers M. Stability and Stabilisation of 2H martensite in Cu-Zn-Al single crystals. Philos Mag 2005; 85:2491–525.
[161] Sade M, Yawny A, Lovey FC, Torra V. Pseudoelasticity of Cu–Al–Be single crystals: Unexpected mechanical behavior. Mat Sci Eng A Struct 2011; 528:7871– 77,
[162] Kustov S, Pons J, Cesari E, Morin M. Two-stage reverse transformation in hyperstabilized β'_1 martensite. Scripta Mater 2002; 46:817-22
[163] Gonzalez CH, Guénin G, Morin M. Effects of martensitic stabilization in Cu-Al-Be shape memory alloys. J Phys IV 2003; 112:561-6.
[164] Kustov S, Pons J, Cesari E, Van Humbeeck J, Morin M. Stabilization and hyperstabilization of Cu-Al-Be β'_1 martensite by thermal treatment and plastic deformation. Mat Sci Eng A Struct 2004; 378:283-8
[165] Dunne D, Morin M, Gonzalez C, Guenin G. The effect of quenching treatment on the reversible martensitic transformation in CuAlBe alloys. Mat Sci Eng A Struct 2004; 378:257-62
[166] Dunne D, Ireland K, Gonzalez C, Morin M, Guenin G. Hyperstabilisation of martensite in Cu-Al-Be alloys. Mat Sci Eng A Struct 2006; 438-440:339-42
[167] Sapozhnikov K, Golyandin S, Kustov S, Cesari E. Defect-assisted diffusion and kinetic stabilization in Cu-Al-Be β´1 martensite. Mat Sci Eng A Struct 2008; 481-482:532-7
[168] Tidu A, Eberhardt A, Bolle B, Moreau F, Heizmann JJ. Orthorhombic lattice deformation of CuAlBe shape-memory single crystals under cyclic strain. J Appl Crystallog 2001; 34:722-9.
[169] Cingolani E, Stalmans R, Van Humbeeck J, Ahlers M. Influence of thermal treatments on the long range order and the two way shape memory effect induced by stabilization in Cu-Al-Be single crystals. Mat Sci Eng A Struct 1999; 268:109 -15
[170] Sade M, Malarría J, Yawny A, Lovey FC. Bulk and surface defects in fatigued Cu-Zn-Al single crystals. Proceedings of the XVIII Conference on Applied Crystallography, Wisla, Poland, 4-7 Sept. 2000; Editors: H. Morawiek and D. Stróz, World Scientific; pp.153-170.
[171] Isalgue A, Torra V. Ms-evolution in Cu-Zn-Al SMA. Predictable temperature and time actions on parent phase. J Phys IV 1997; 7:C5-339–44
[172] Isalgue A, Torra V. Order processes in Cu-Zn-Al shape memory alloys - Quantitative approach to Ms values by resistance measurements. J Therm Anal Calorim 1998; 52:773–80.

[173] Bertolino G, Arneodo Larochette P, Castrodeza EM, Mapelli C, Baruj A, Troiani HE. Mechanical properties of martensitic Cu-Zn-Al foams in the pseudoelastic regime. Mater Lett 2010; 64:1448–50.
[174] Bertolino, G., Gruttadauria, A., Arneodo Larochette, P., Castrodeza, E.M., Baruj, A., Troiani, H.E. Cyclic pseudoelastic behavior and energy dissipation in as-cast Cu-Zn-Al foams of different densities. Intermetallics 2011; 19(4):577-85
[175] Castrodeza EM, Mapelli C. Processing of brass open-cell foam by silica-gel beads replication. J Mater Process Tech 2009; 209:4958–62.
[176] Kajiwara S. Characteristic features of shape memory effect and related transformation behavior in Fe-based alloys. Mat Sci Eng A Struct 1999; 273–275:67–88
[177] Wan J, Chen S. Martensitic transformation and shape memory effect in Fe-Mn-Si based alloys. Curr Opin Solid St M 2005; 9:303–12
[178] Sato A, Ozaki K, Watanabe Y, Mori T. Internal-Friction Due To Epsilon-Gamma Reverse Transformation in an Fe-Mn-Si-Cr Shape Memory Alloy. Mat Sci Eng A Struct 1988; 101:25-30
[179] Lee YK, Jun JH, Choi CS. Damping capacity in Fe-Mn binary alloys. ISIJ Int 1997; 37:1023-30
[180] Baik SH. High damping Fe-Mn martensitic alloys for engineering applications. Nucl Eng Des 2000; 198:241-52
[181] Baik SH, Kim JC, Han DW, Kim TH, Back JH, Lee YK. Fe-Mn martensitic alloys for control of noise and vibration in engineering applications. Mat Sci Eng A Struct 2006; 438-440:1101-5
[182] Jee KK, Ito K, Shin MC. Damping Capacity In Fe-27mn-3.5si Alloy. ISIJ Int 1994; 34:912-916
[183] Jun JH, Kong DK, Choi CS. The influence of Co on damping capacity of Fe-Mn-Co alloys. Mater Res Bull 1998; 33:1419-25
[184] Baik SH, Kim JC, Jee KK, Shin MC, Choi CS. Transformation behavior and damping capacity in Fe-17%Mn-X%C-Y%Ti alloy. ISIJ Int 1997; 37:519-22
[185] Lee YK, Baik SH, Kim JC, Choi CS. Effects of amount of epsilon martensite, carbon content and cold working on damping capacity of an Fe-17% Mn martensitic alloy. J Alloy Compd 2003; 355:10-6
[186] Okada H, Sahashi H, Igata N, Miyahara K. Effects of ε martensite and nitrogen on the damping property of high strength Fe–Cr–Mn alloys. J Alloy Compd 2003; 355:17-21
[187] Wang XX, Zhang CY. Pseudoelastic behavior in an Fe-Mn-Si-Ni-Co shape memory alloy. J Mater Sci Lett 1998; 17:1795-6
[188] Zhao C. Superelasticity and two-way shape memory effect in an Fe-Mn-Si-Cr-Ni-N alloy. J Mater Sci Lett 2000; 19:1711-3
[189] Matsumura O, Sumi T, Tamura N, Sakao K, Furukawa T, Otsuka H. Pseudoelasticity in an Fe–28Mn–6Si–5Cr shape memory alloy. Mat Sci Eng A Struct 2000; 279:201-6
[190] Baruj A, Kikuchi T, Kajiwara S, Shinya N. Effect of pre-deformation of austenite on shape memory properties in Fe-Mn-Si-based alloys containing Nb and C. Mater T JIM 2002;43: 585-8
[191] Kajiwara S, Baruj A, Kikuchi T, Shinya N. Low-cost high-quality Fe-based shape memory alloys suitable for pipe joints. In: Smart Structures and Materials. Proc. of SPIE 2003, San Diego, CA. Book editor: Lagoudas DC. 2003; 5053: 250-61
[192] Baruj A, Troiani HE. The effect of pre-rolling Fe-Mn-Si-based memory alloys: Mechanical properties shape and transmission electron microcopy examination. Mat Sci Eng A Struct 2008; 481-482:574-7
[193] Sawaguchi T,Kikuchi T, Kajiwara S. The pseudoelastic behavior of Fe-Mn-Si-based shape memory alloys containing Nb and C. Smart Mater Struct 2005; 14:S317-22
[194] Baruj A, Bertolino G, Troiani HE. Temperature dependence of critical stress and pseudoelasticity in a Fe-Mn-Si-Cr pre-rolled alloy. J Alloy Compd 2010; 502: 54-8
[195] H. C. Lin HC, Wu SK, Peng YT, Cheng TC, Lin KM. Pseudoelasticity of thermo-mechanically treated Fe–Mn–Si–Cr–Ta alloys. J Alloy Compd 2012; http://dx.doi.org/10.1016/j.jallcom.2012.02.029

[196] Sawaguchi T, Sahu P, Kikuchi T, Ogawa K, Kajiwara S, Kushibe A, Higashino M, Ogawa T. Vibration mitigation by the reversible fcc/hcp martensitic transformation during cyclic tension-compression loading of an Fe-Mn-Si-based shape memory alloy Scripta Mater 2006; 54:1885-90
[197] Watanabe Y, Miyazaki E, Okada H. Enhanced Mechanical Properties of Fe-Mn-Si-Cr Shape Memory Fiber/Plaster Smart Composite. Mater T JIM 2002;43:974-83
[198] Wakatsuki T, Sato H, Watanabe Y, Maruyama T. Development of Fe-Mn-Si-Cr Shape Memory Alloy Machining Chips Reinforced Smart Composite (Transformations and Microstructures) Tetsu-To-Hagane/J Iron Steel Res Int 2006; 92: 562-566
[199] Tanaka Y, Himuro Y, Kainuma R, Sutou Y, Omori T, Ishida K. Ferrous Polycrystalline Shape-Memory Alloy Showing Huge Superelasticity. Science 2010; 327:1488-90
[200] T. Omori T., Ando K, Okano M, Xu X, Tanaka Y, Ohnuma I, Kainuma R, Ishida K. Superelastic Effect in Polycrystalline Ferrous Alloys. Science 2011; 333:68-71
[201] Cladera A, Weber B, Leinenbach C, Czaderski C, Shahverdi M, Motavalli M. Iron-based shape memory alloys for civil engineering structures: An overview. Const. Build. Mater. 63 (2014) 281–293

Figure 1
Click here to download high resolution image

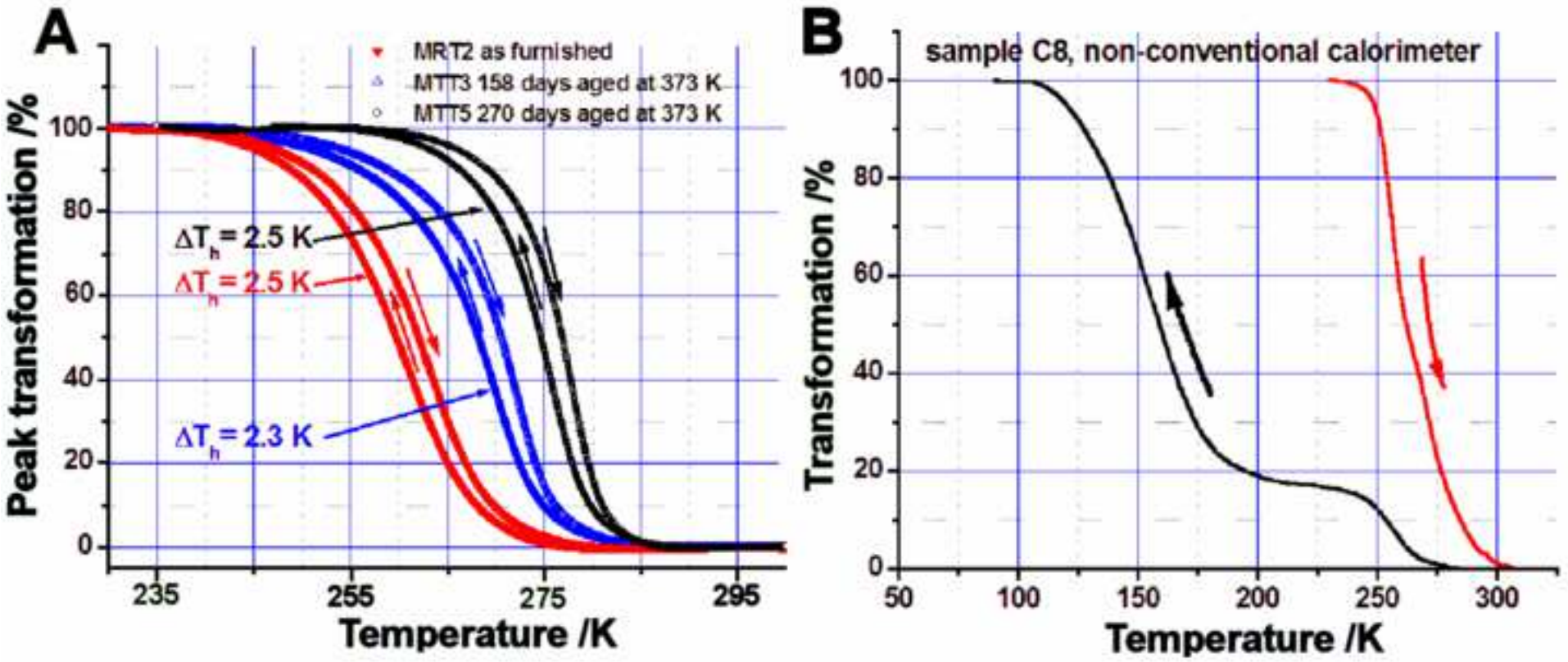

Figure 2
Click here to download high resolution image

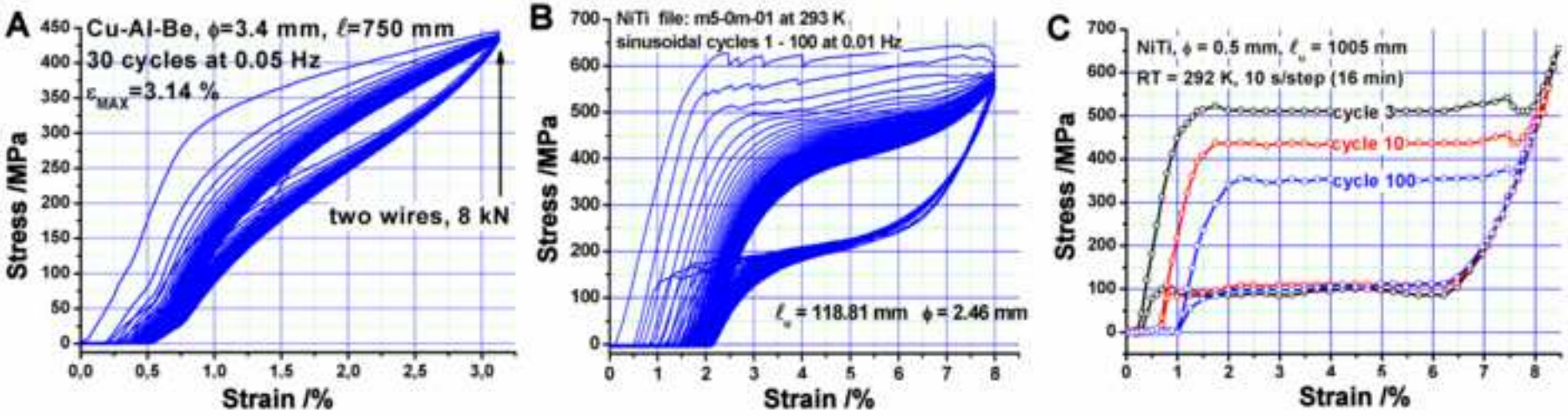

Figure 3
Click here to download high resolution image

Figure 4
Click here to download high resolution image

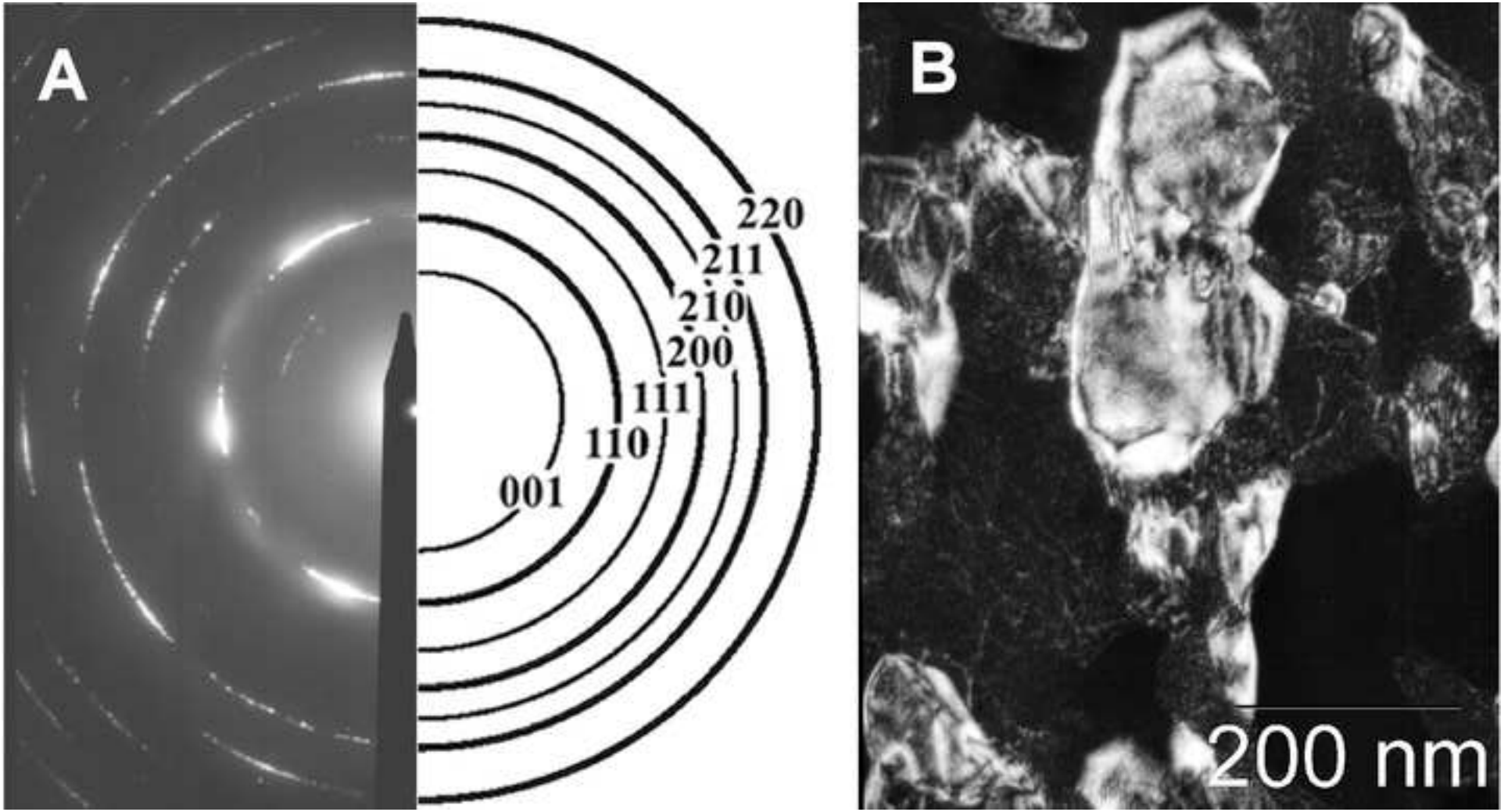

Figure 5
Click here to download high resolution image

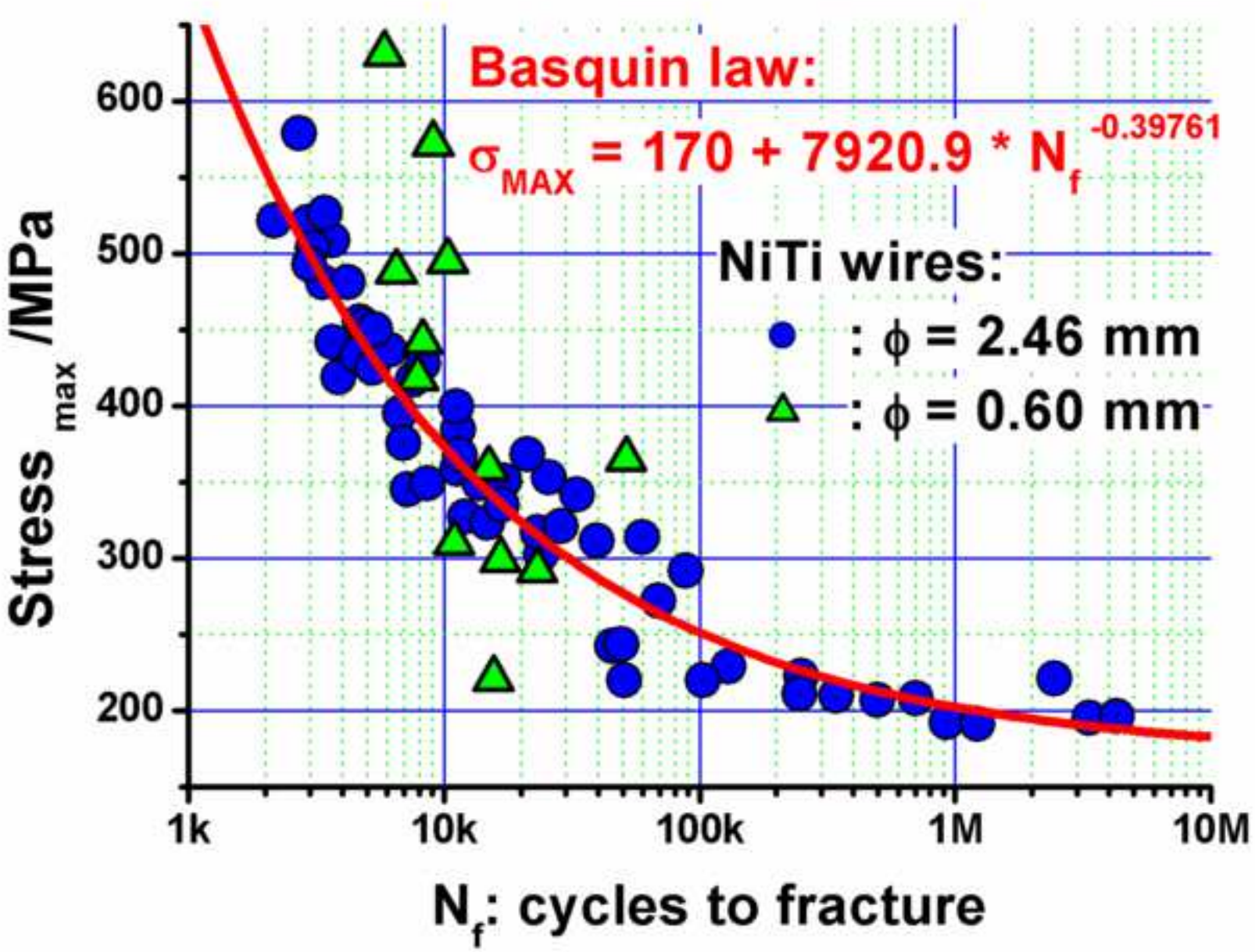

Figure 6
Click here to download high resolution image

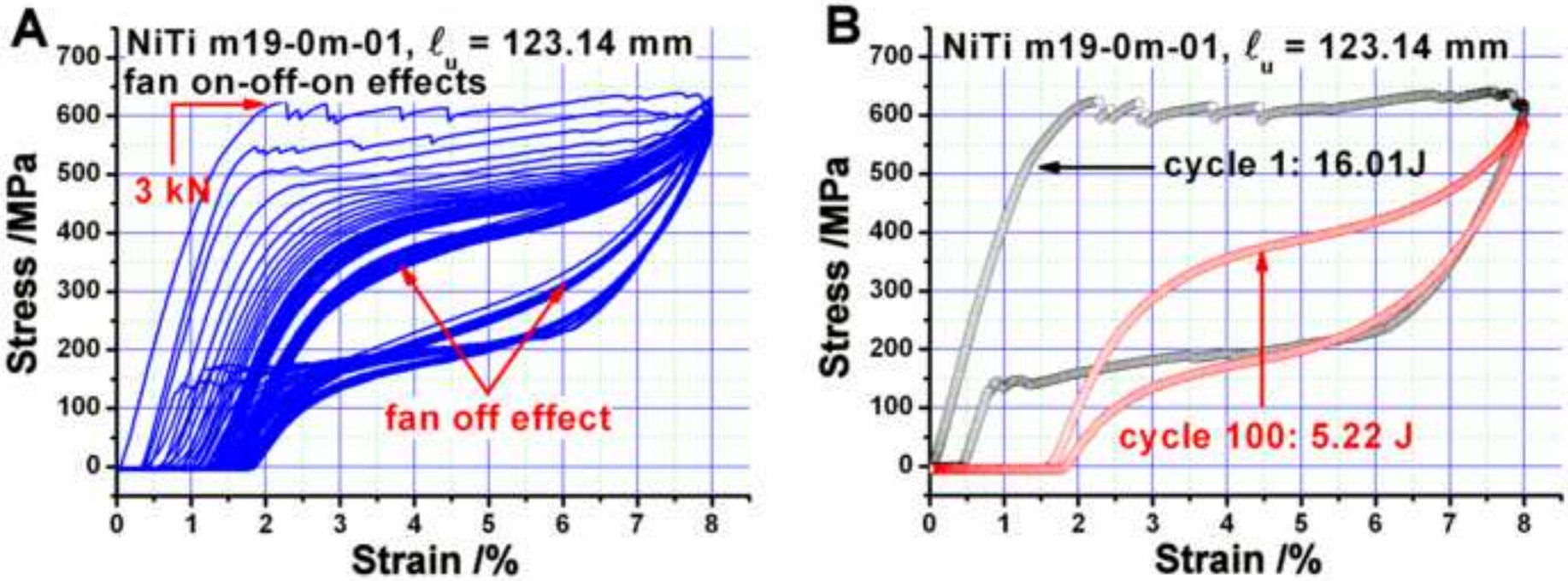

Figure 7
Click here to download high resolution image

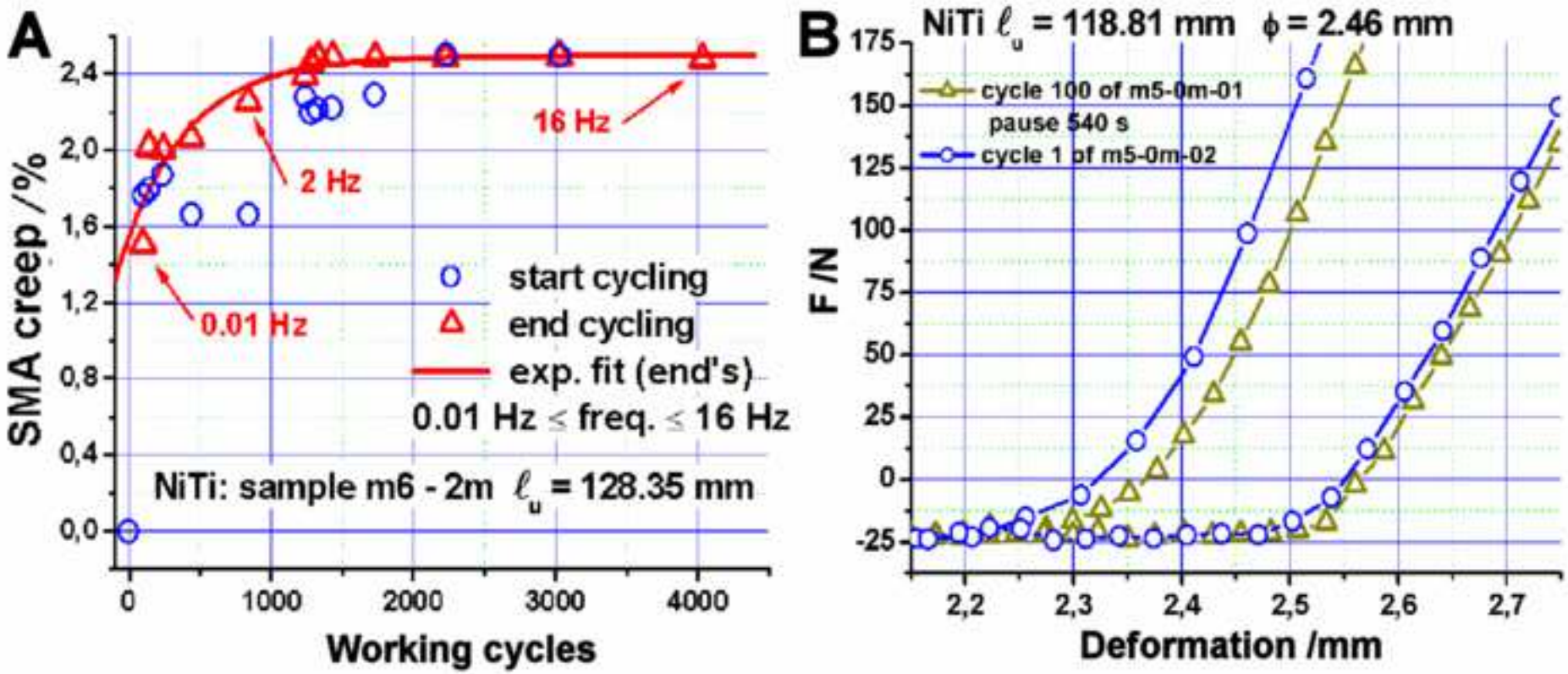

Figure 8
Click here to download high resolution image

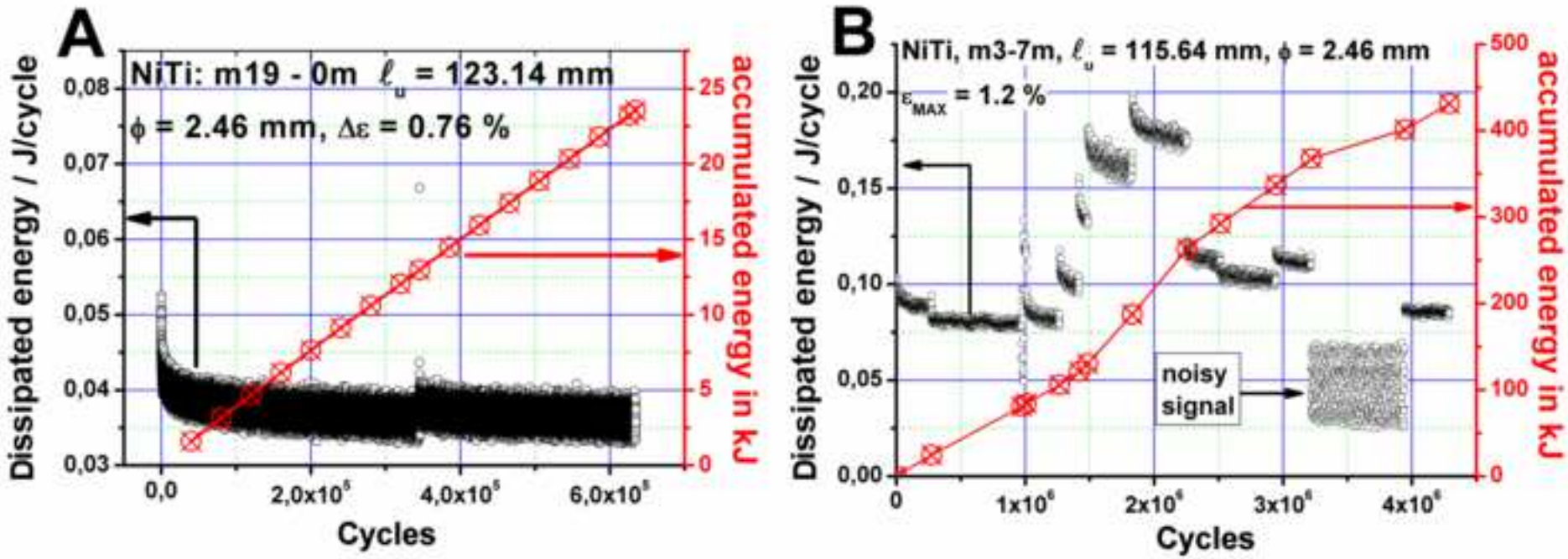

Figure 9
Click here to download high resolution image

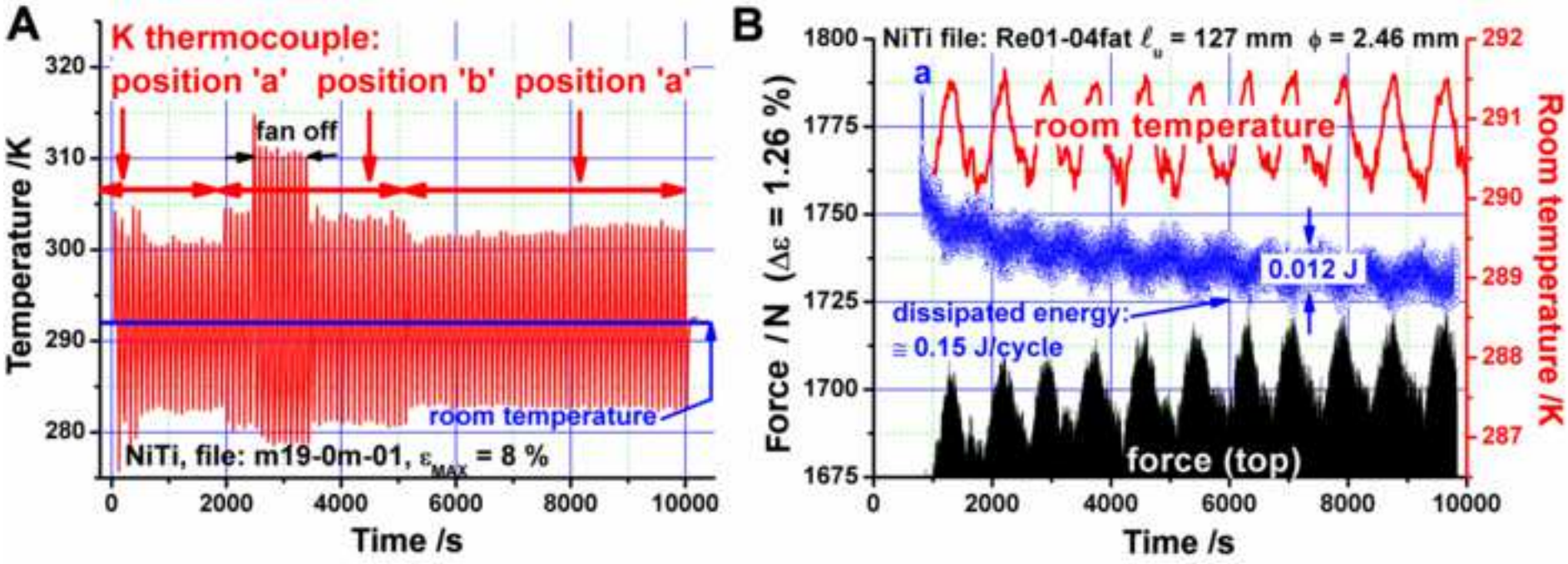

Figure 10
Click here to download high resolution image

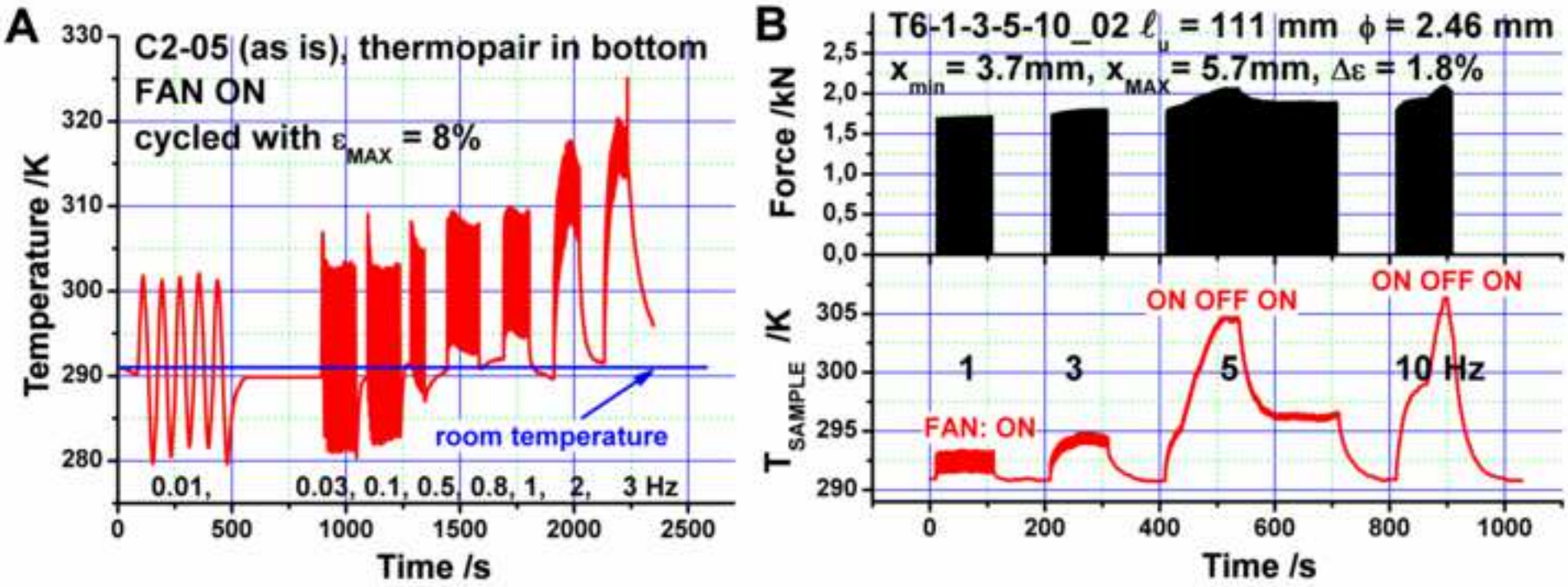

Figure 11
Click here to download high resolution image

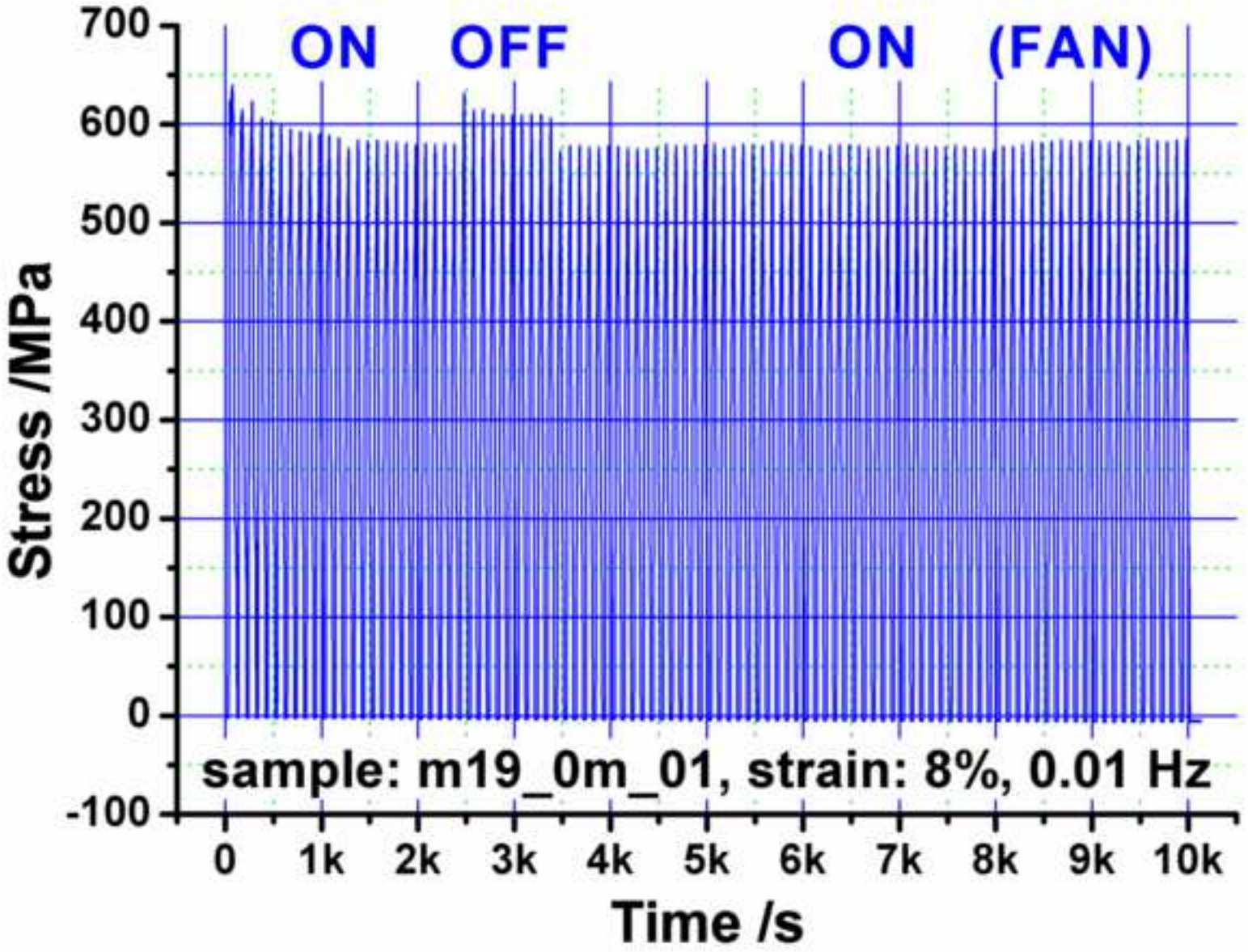

Figure 12
Click here to download high resolution image

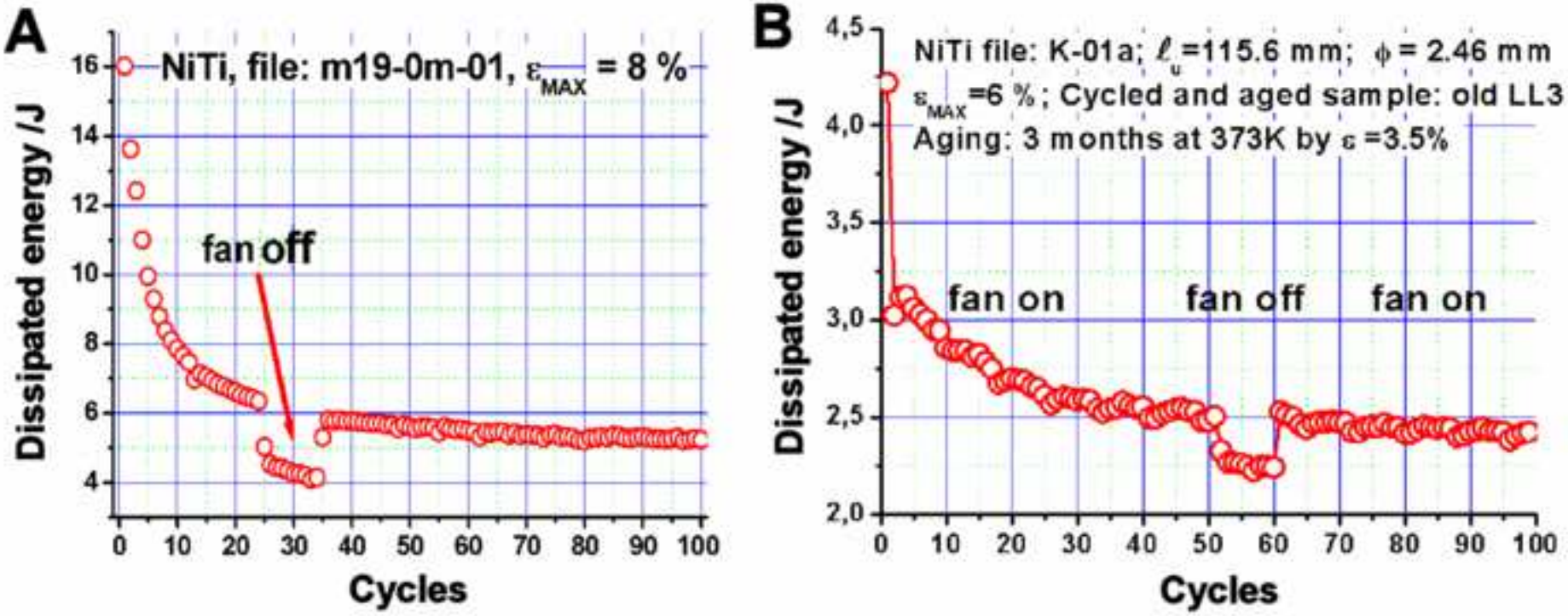

Figure 13
Click here to download high resolution image

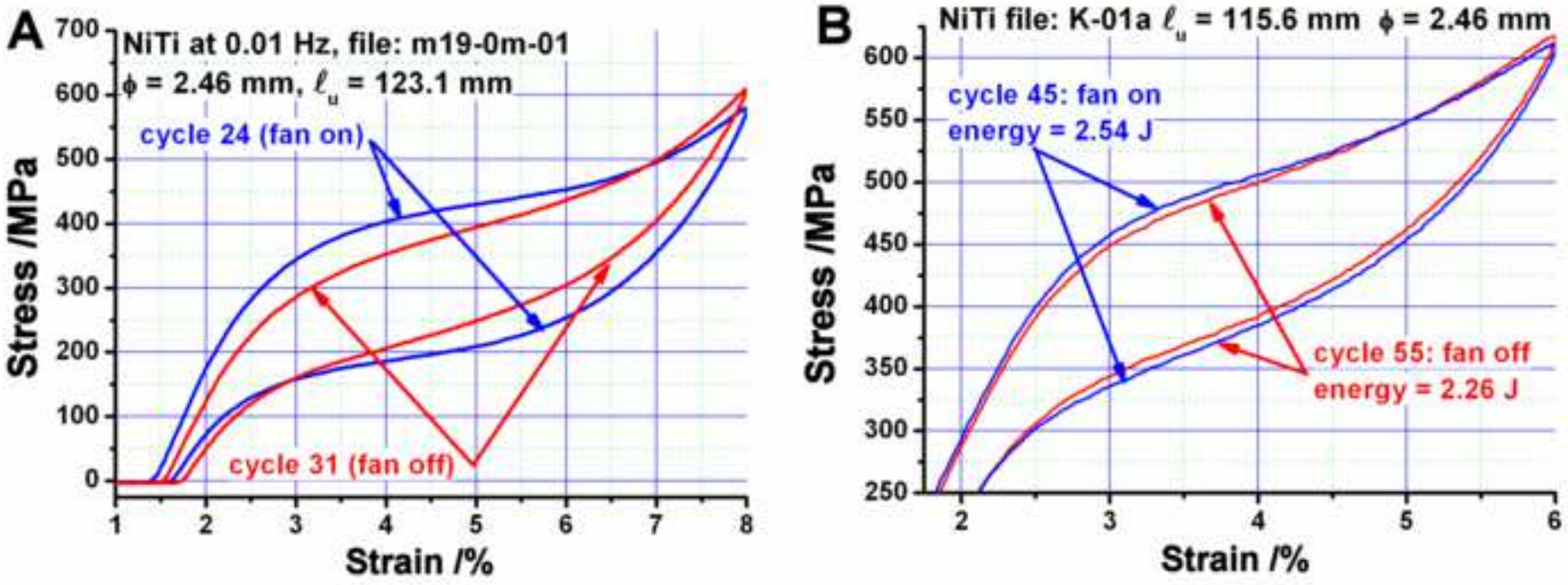

Figure 14
Click here to download high resolution image

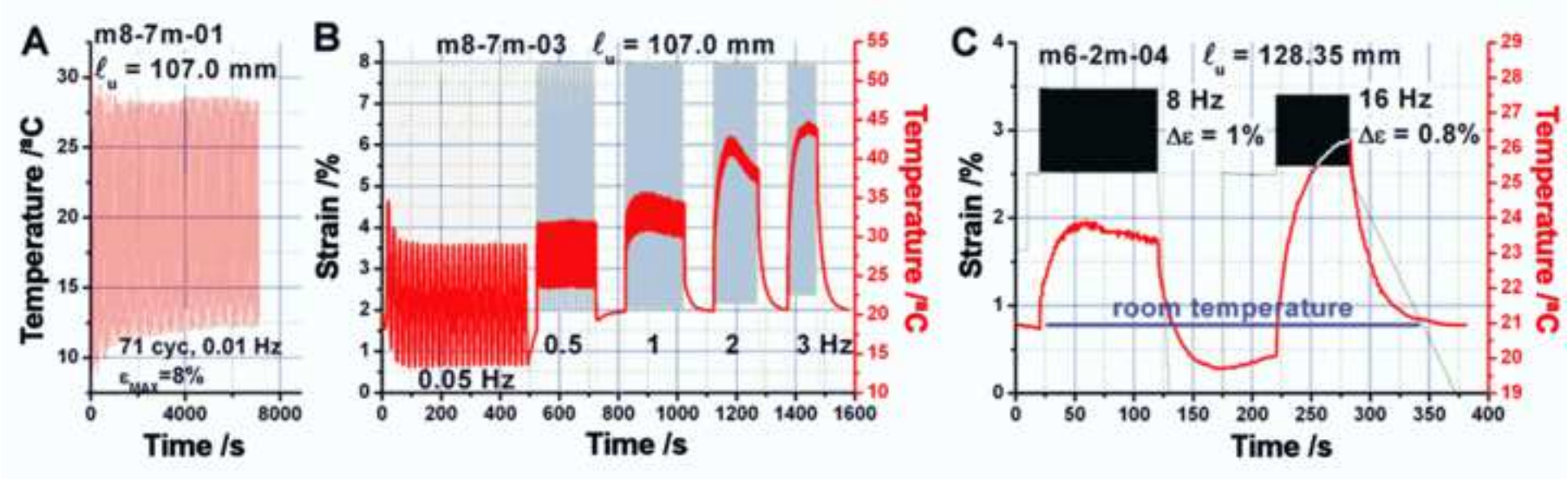

Figure 15
Click here to download high resolution image

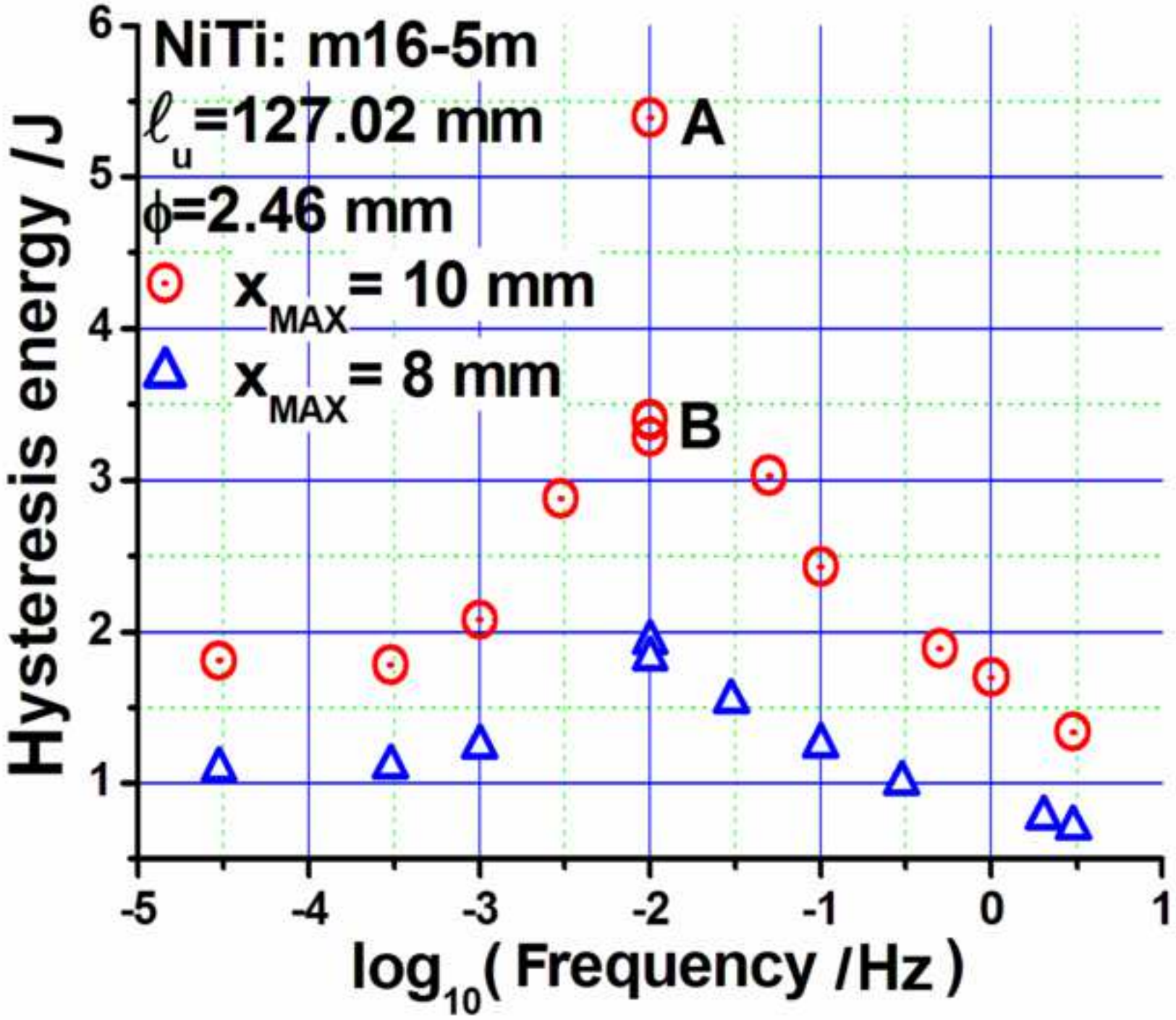

Figure 16
Click here to download high resolution image

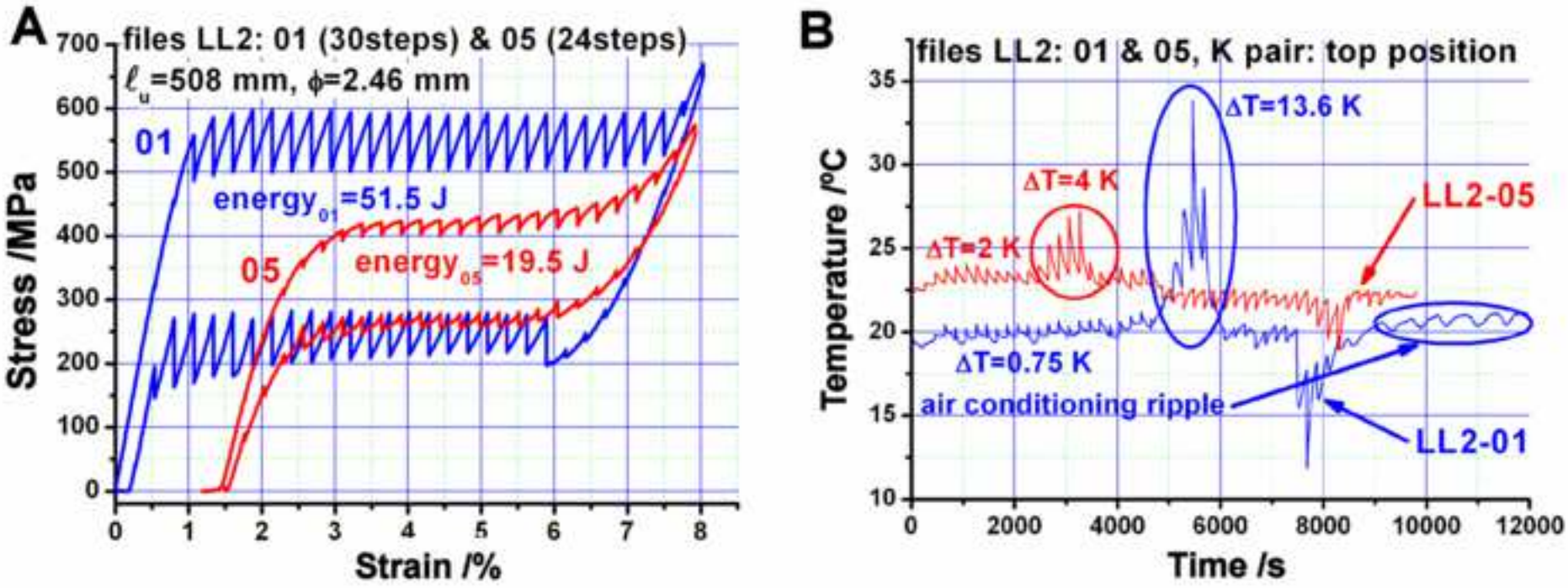

Figure 17
Click here to download high resolution image

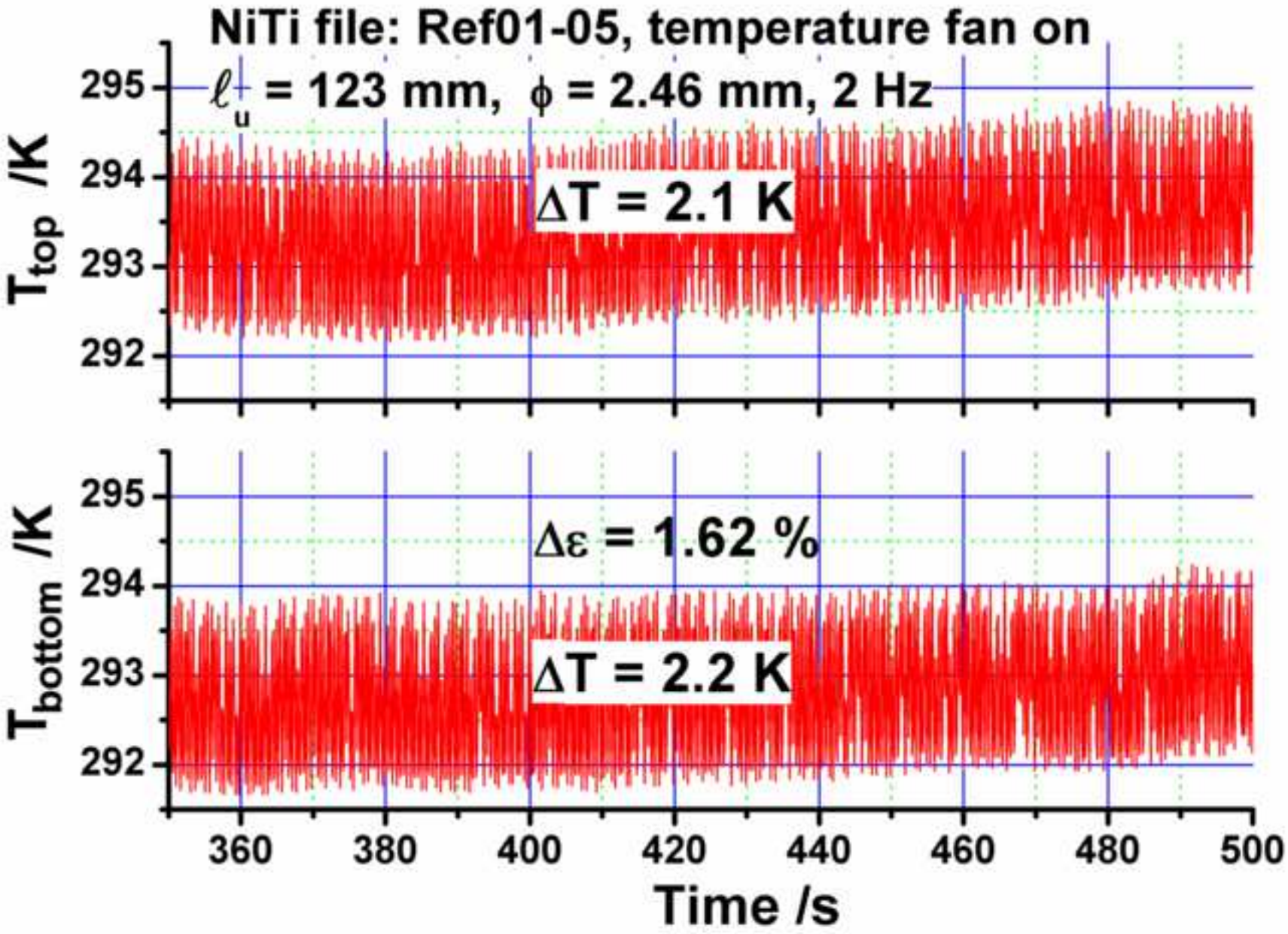

Figure18
Click here to download high resolution image

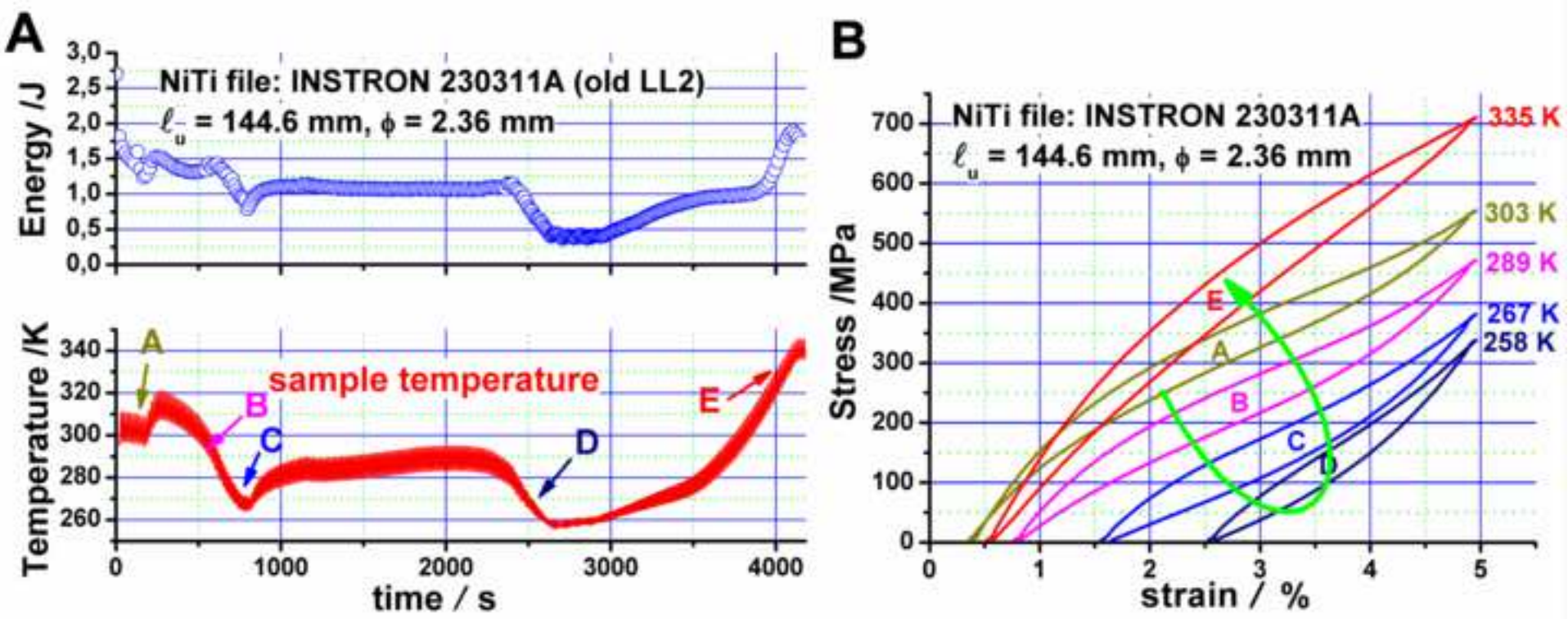

Figure19
Click here to download high resolution image

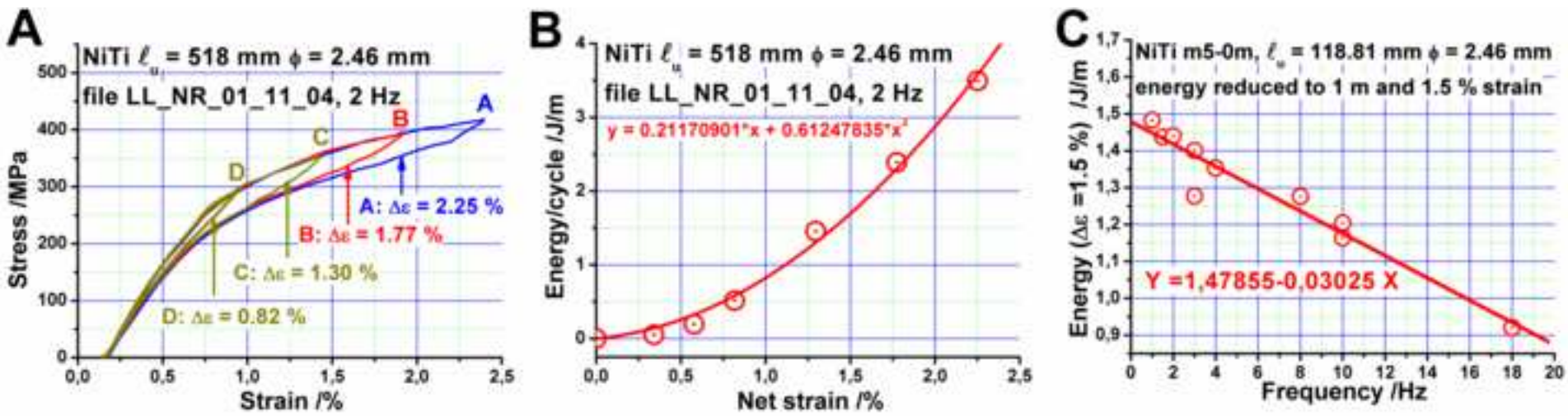

Figure20
Click here to download high resolution image

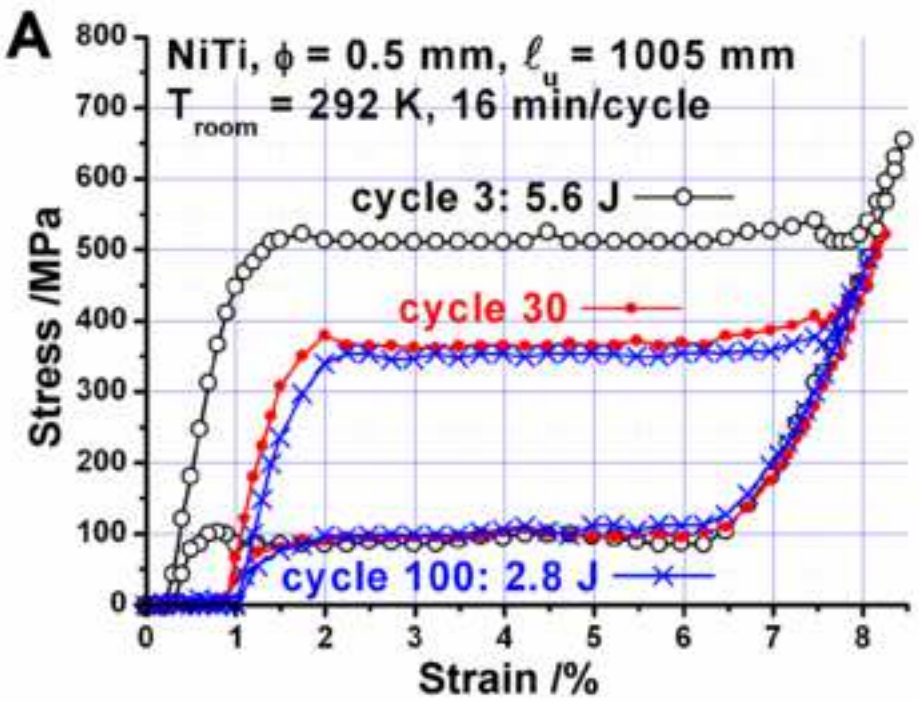

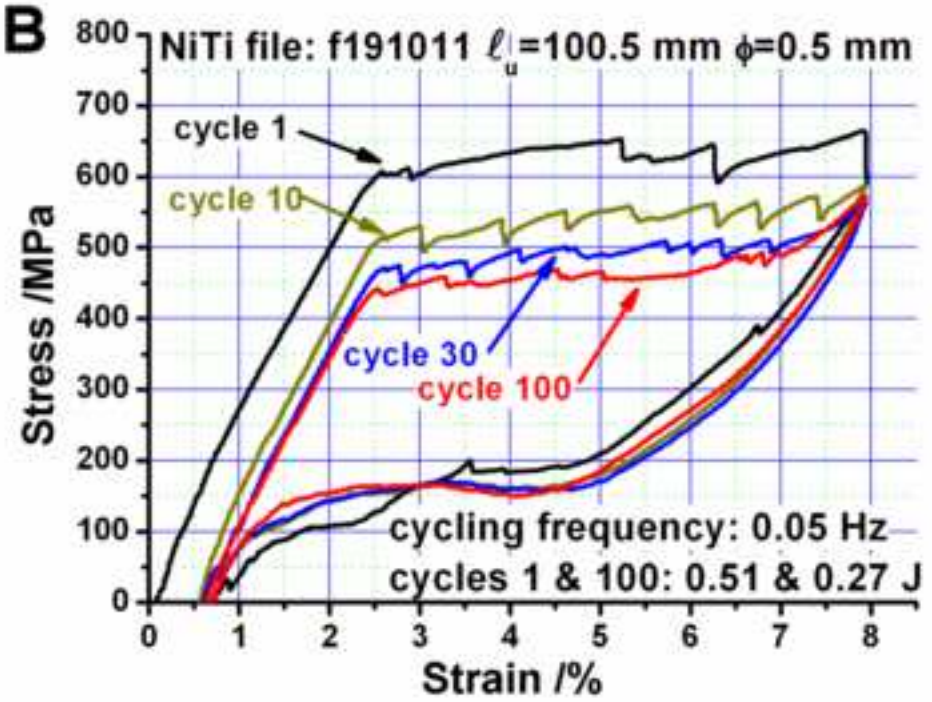

Figure21
Click here to download high resolution image

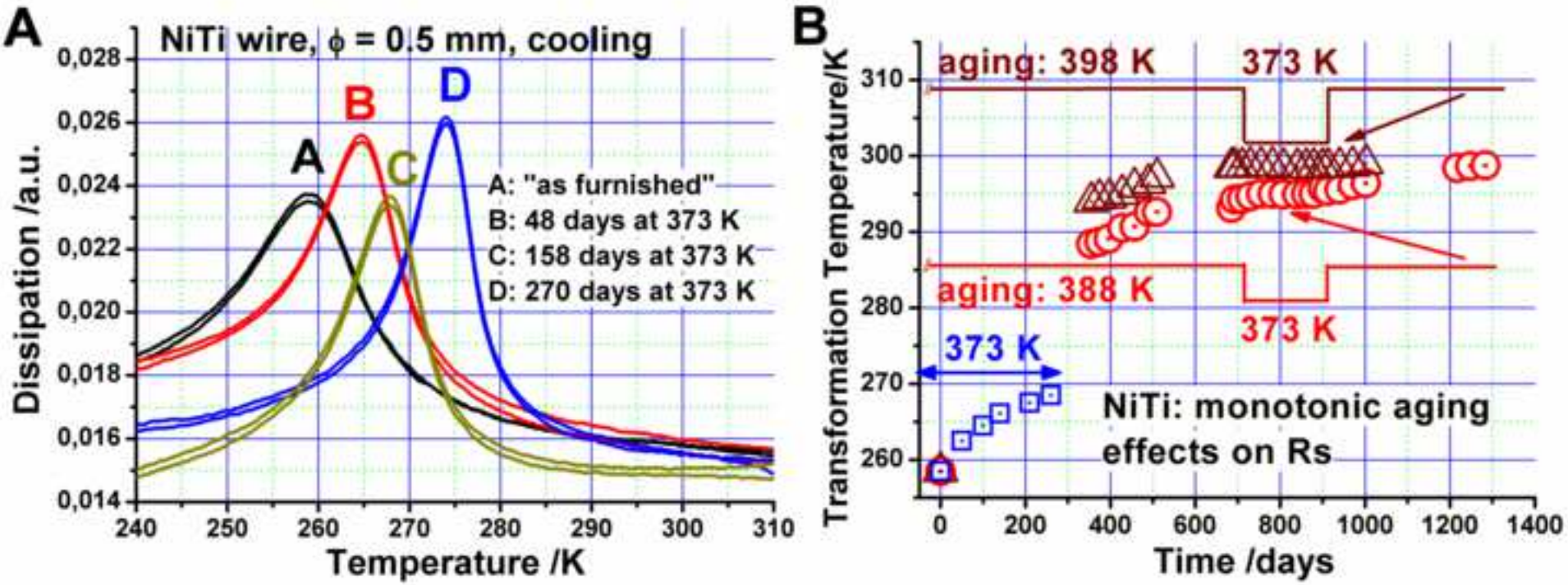

Figure22
Click here to download high resolution image

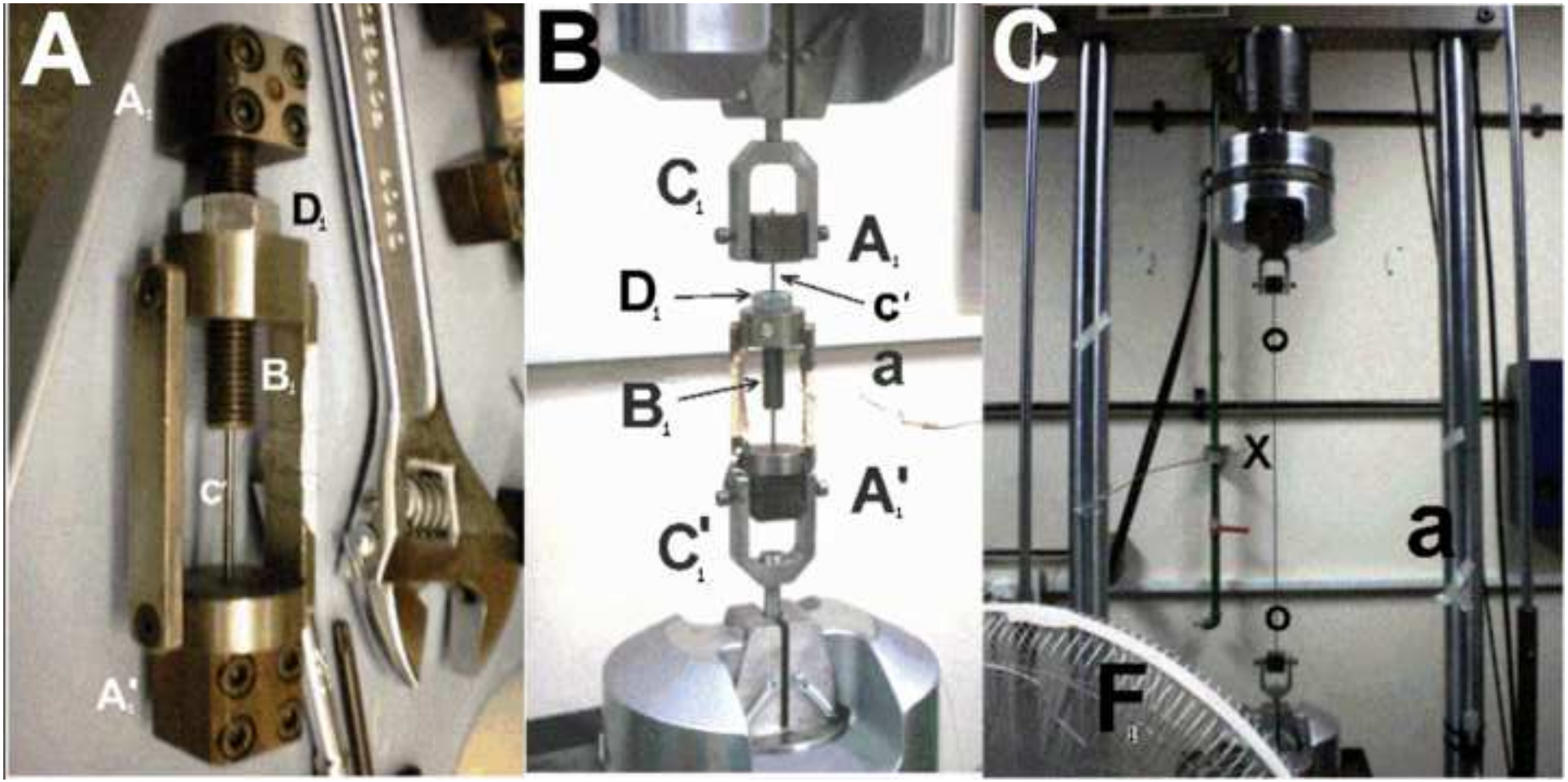

Figure23
Click here to download high resolution image

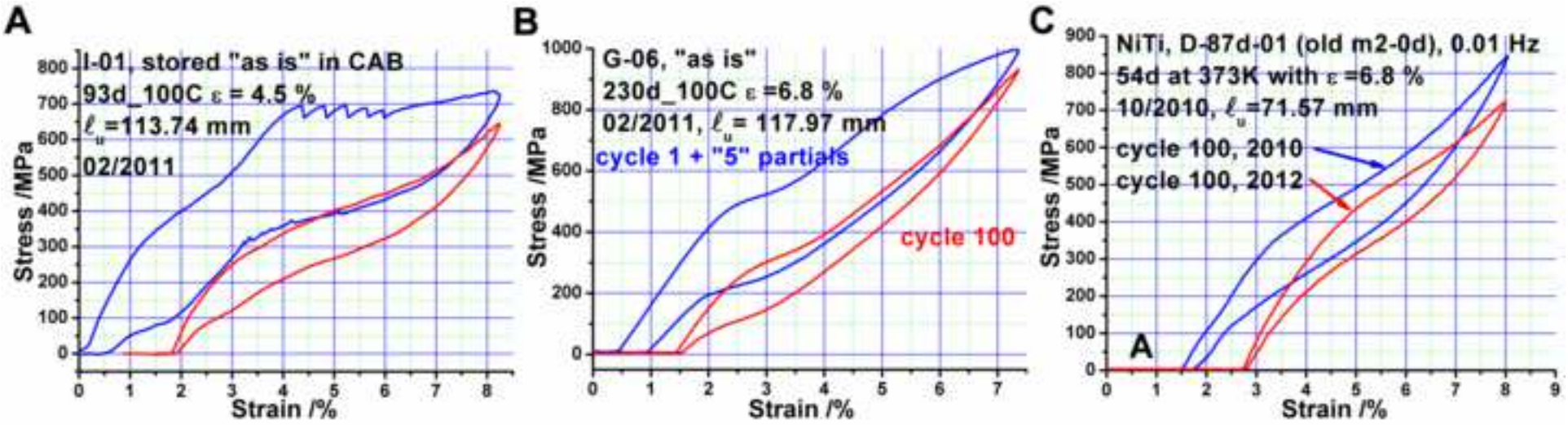

Figure24
Click here to download high resolution image

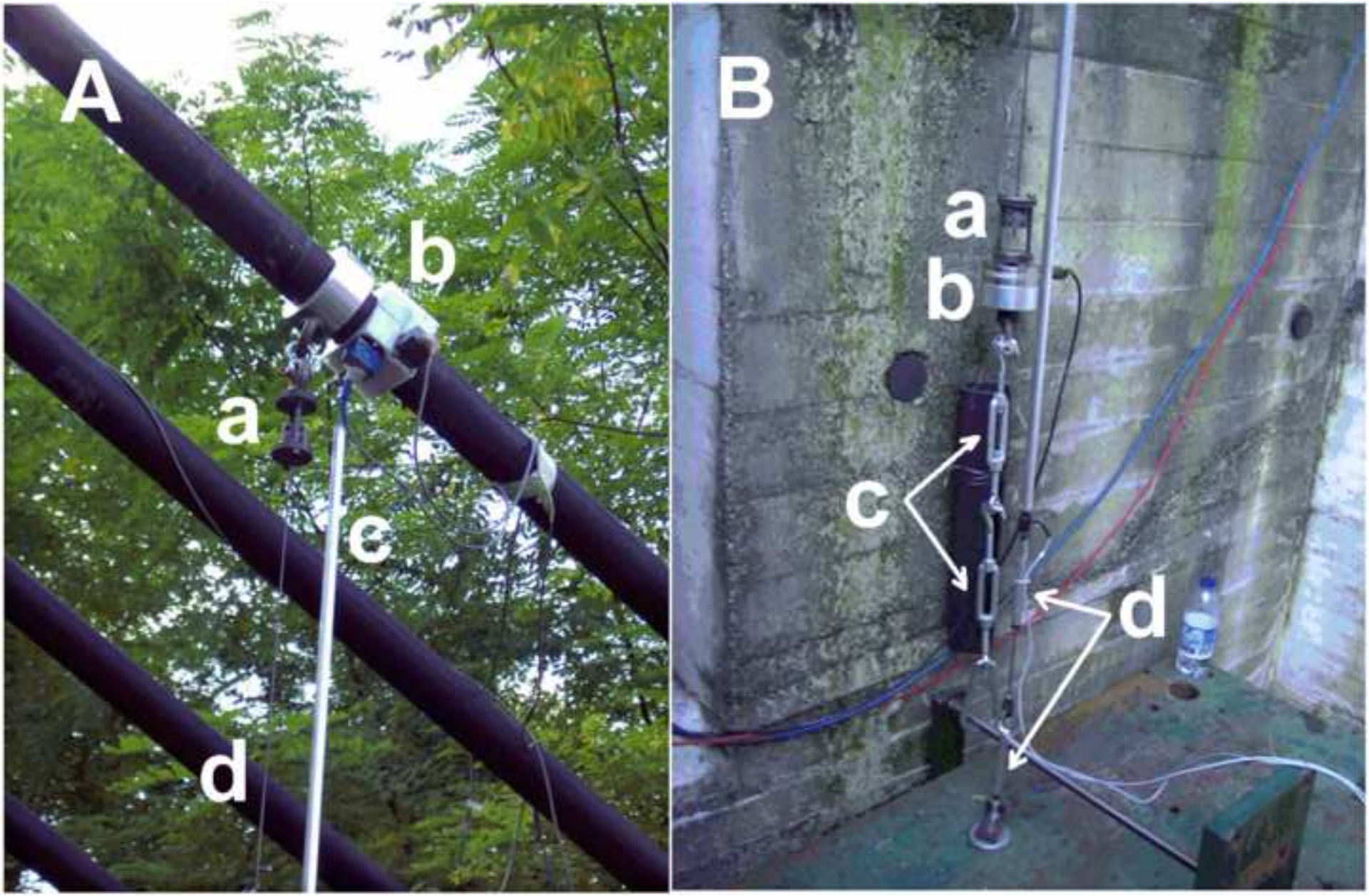

Figure25
Click here to download high resolution image

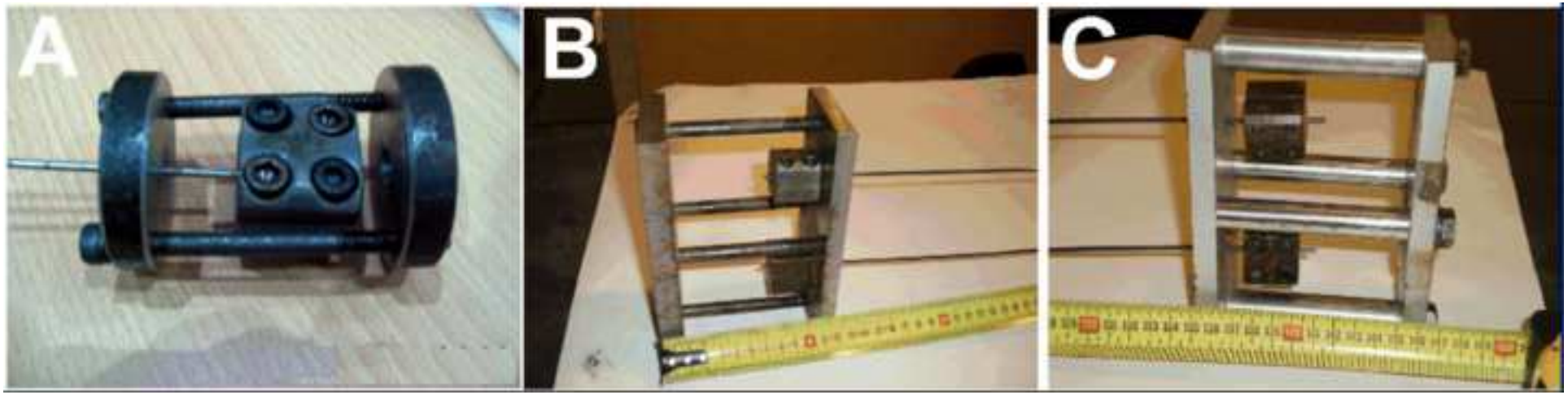

Figure26
Click here to download high resolution image

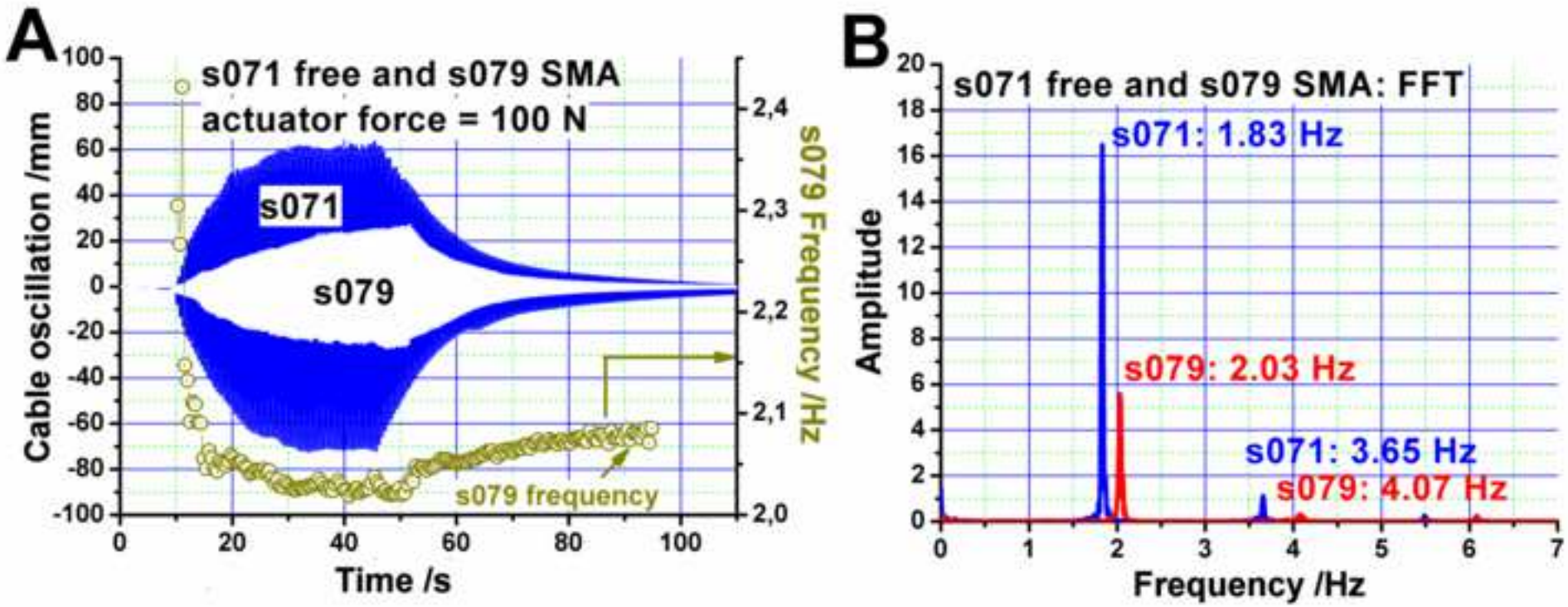

Figure27
Click here to download high resolution image

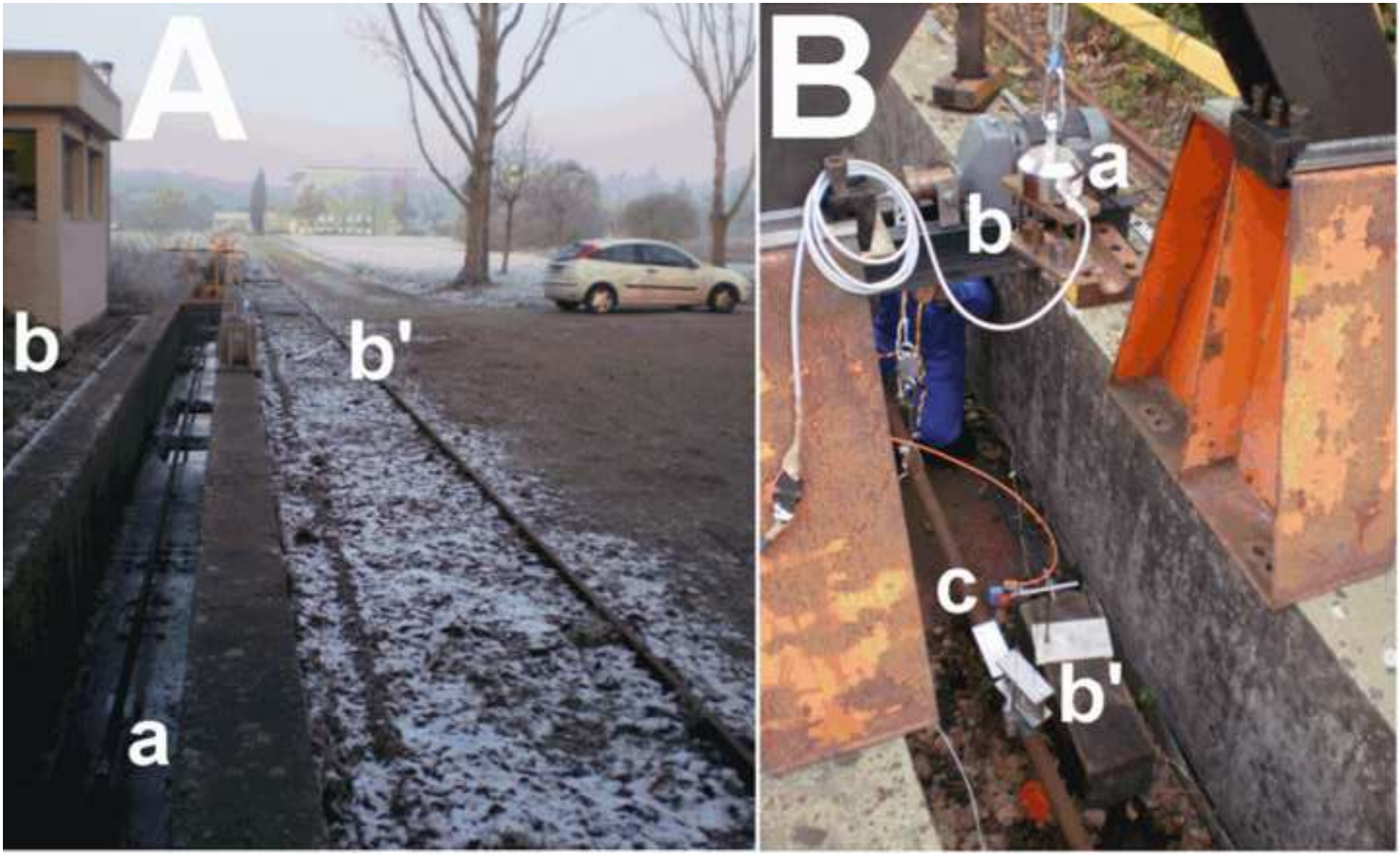

Figure28
Click here to download high resolution image

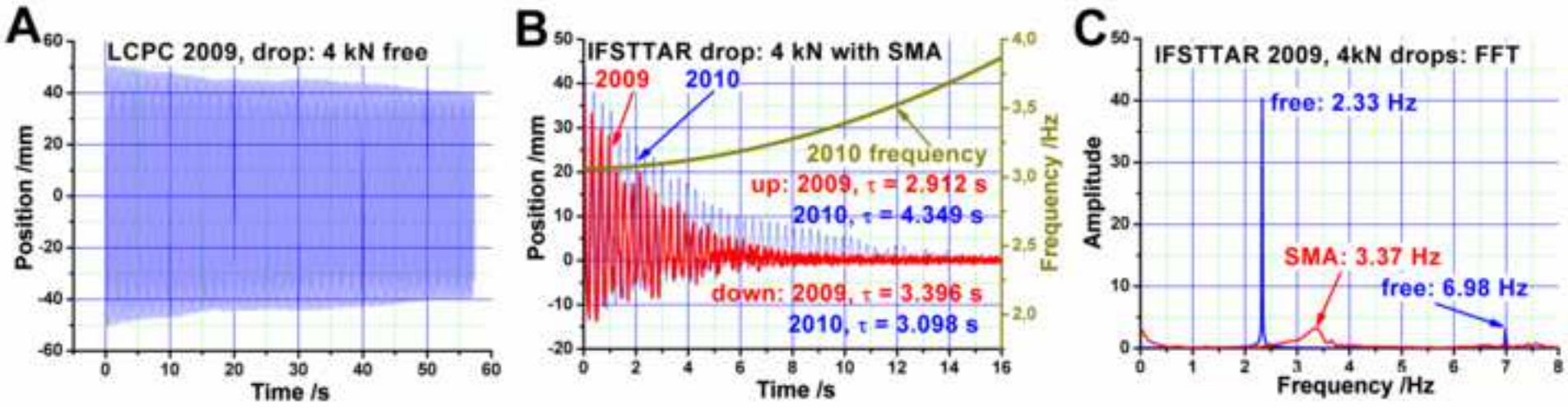

Figure29
Click here to download high resolution image

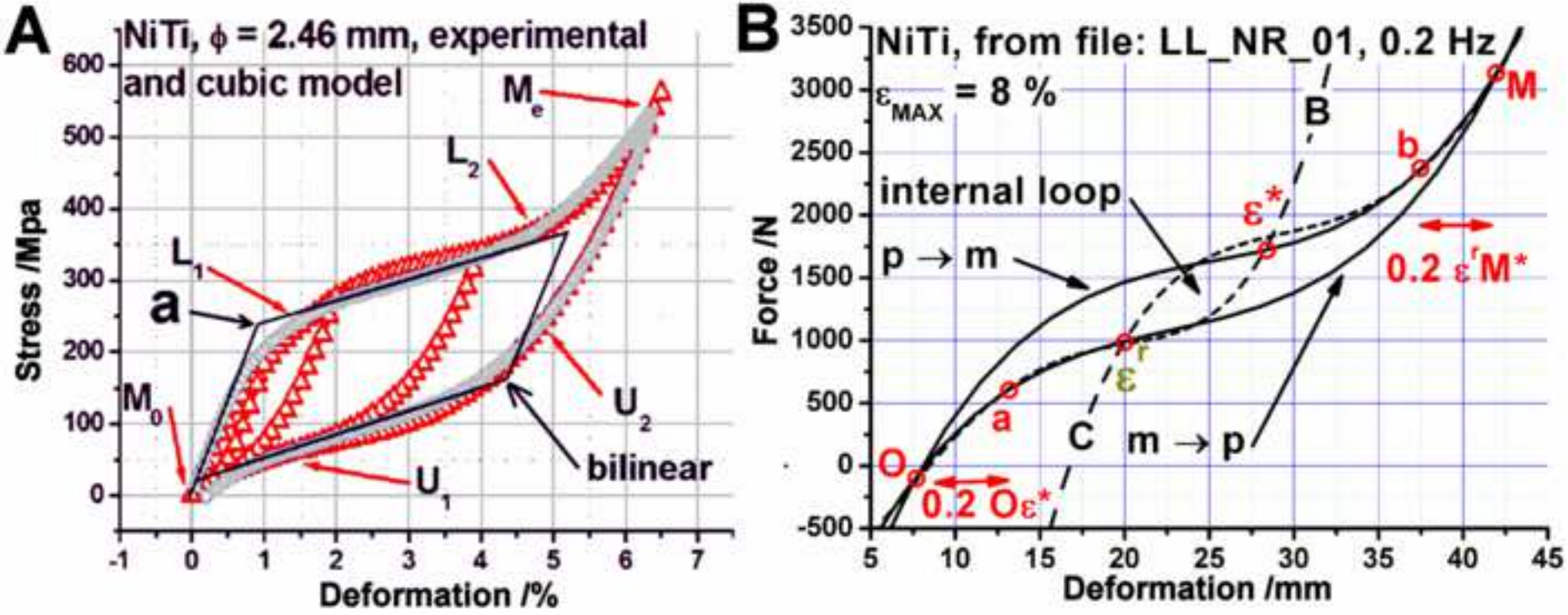

Figure30
Click here to download high resolution image

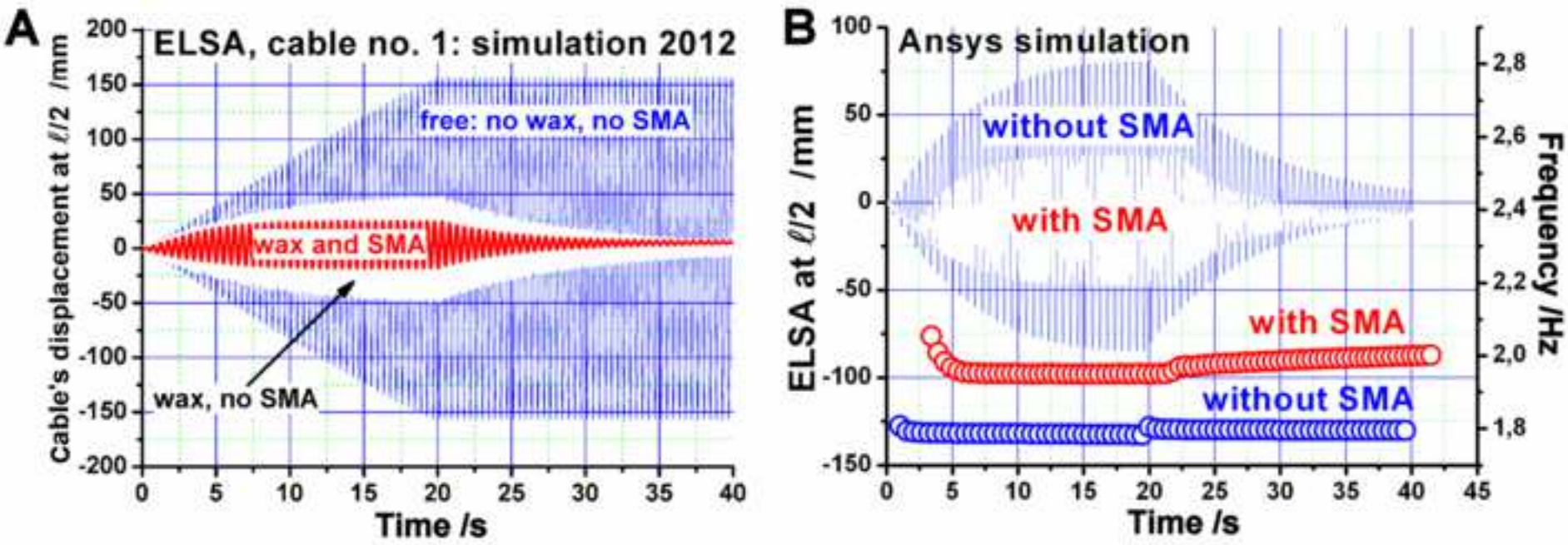

Figure31
Click here to download high resolution image

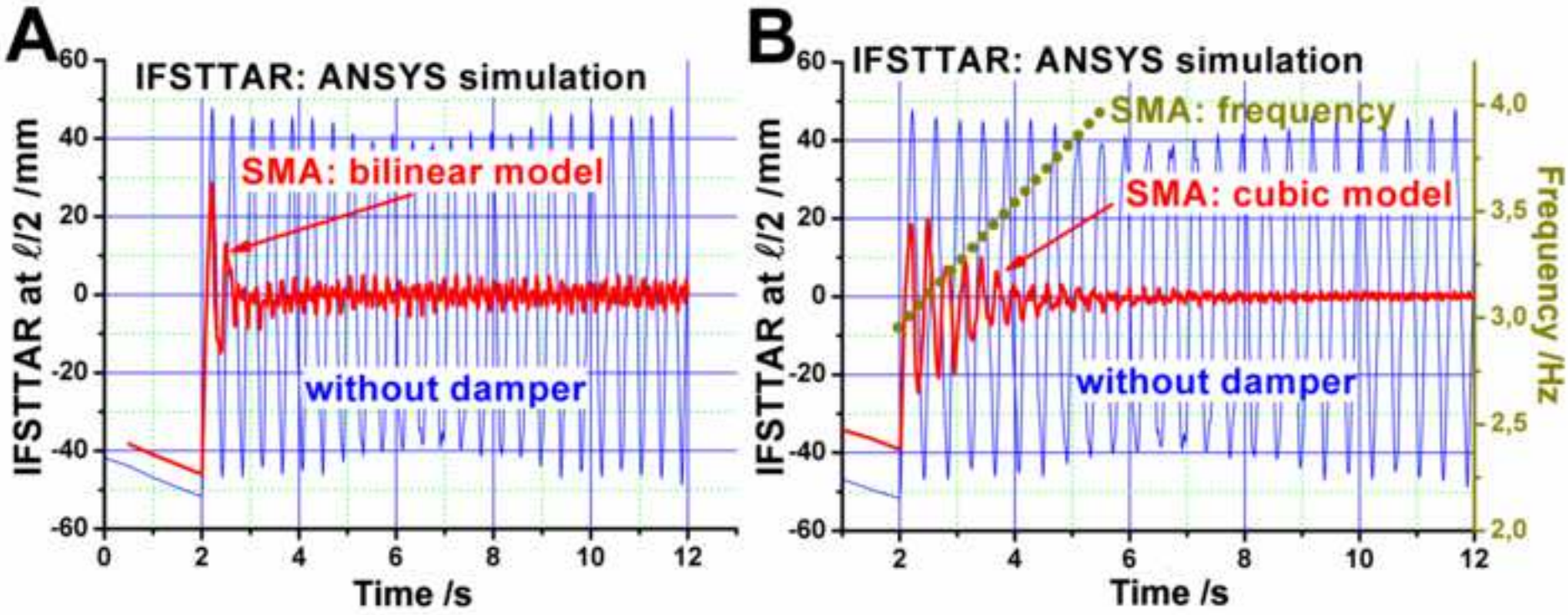

Figure32
Click here to download high resolution image

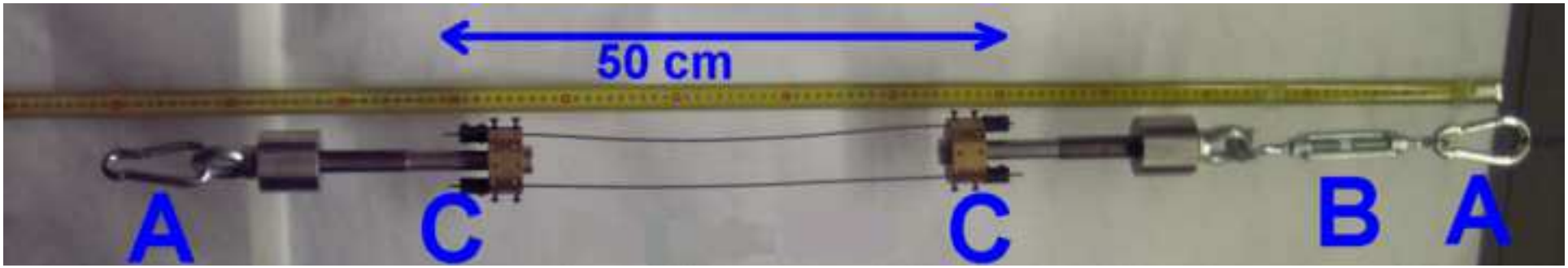

Figure 33
Click here to download high resolution image

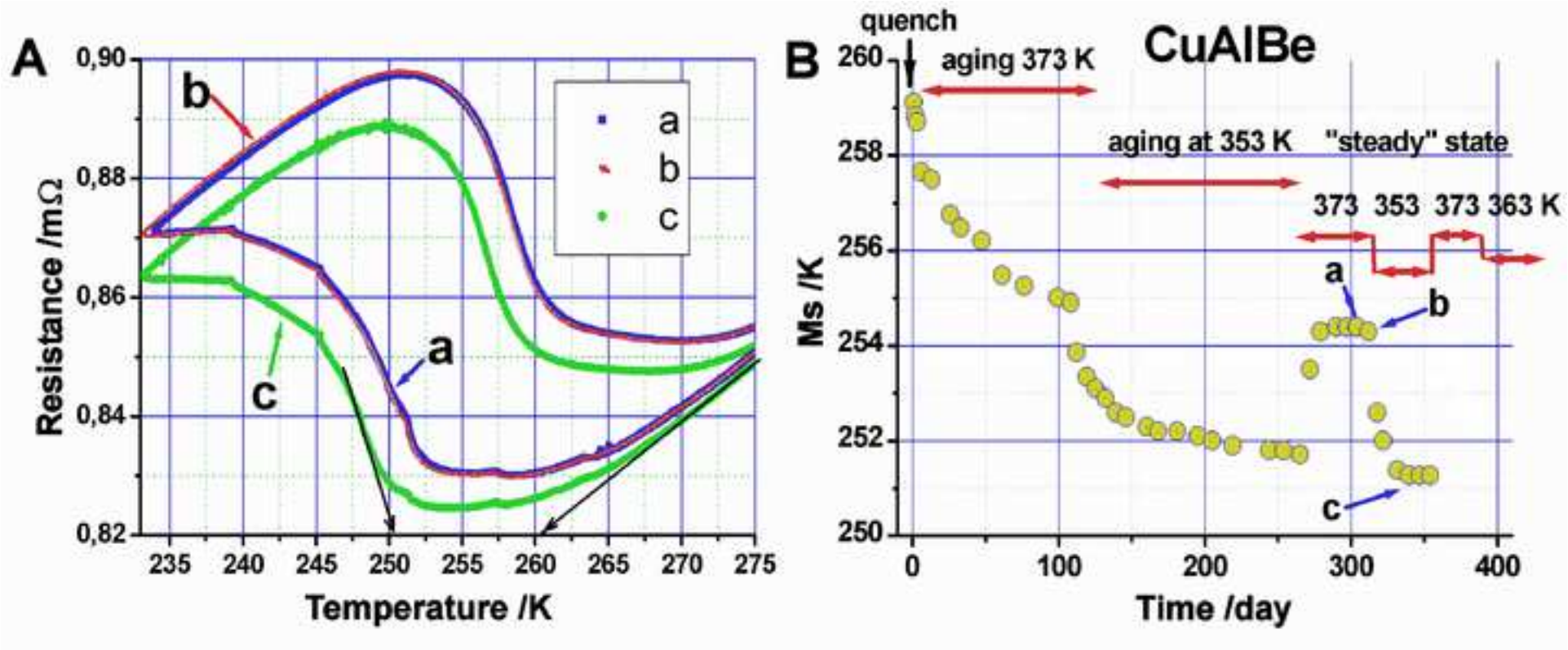

Figure34
Click here to download high resolution image

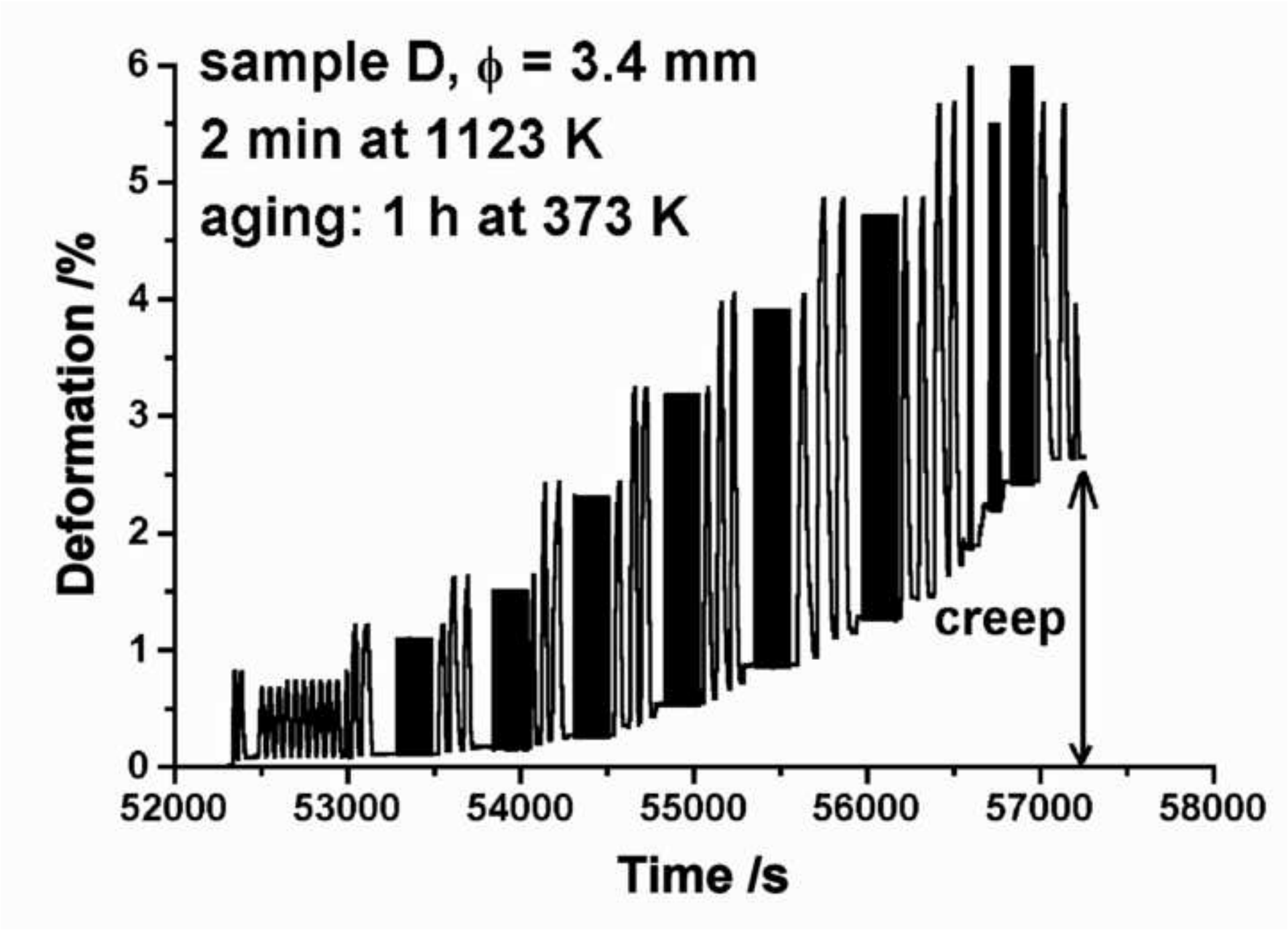

Figure35
Click here to download high resolution image

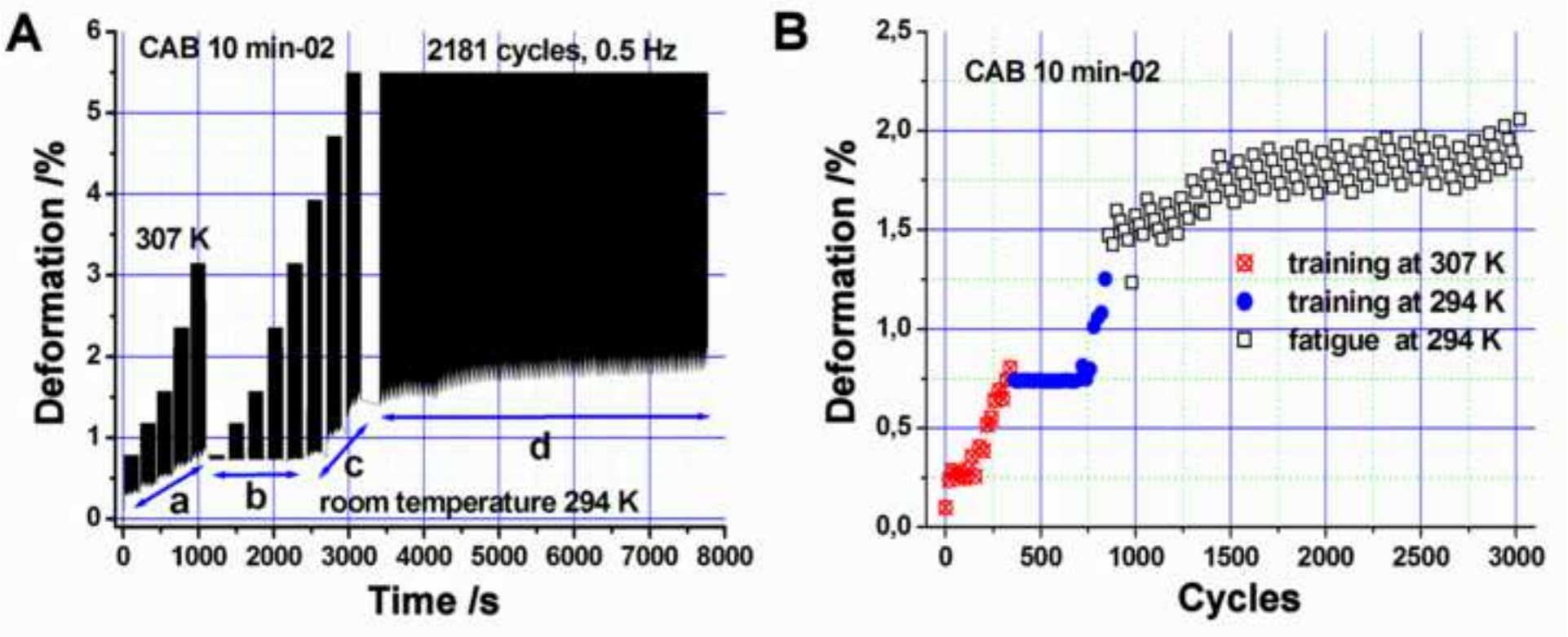

Figure36
Click here to download high resolution image

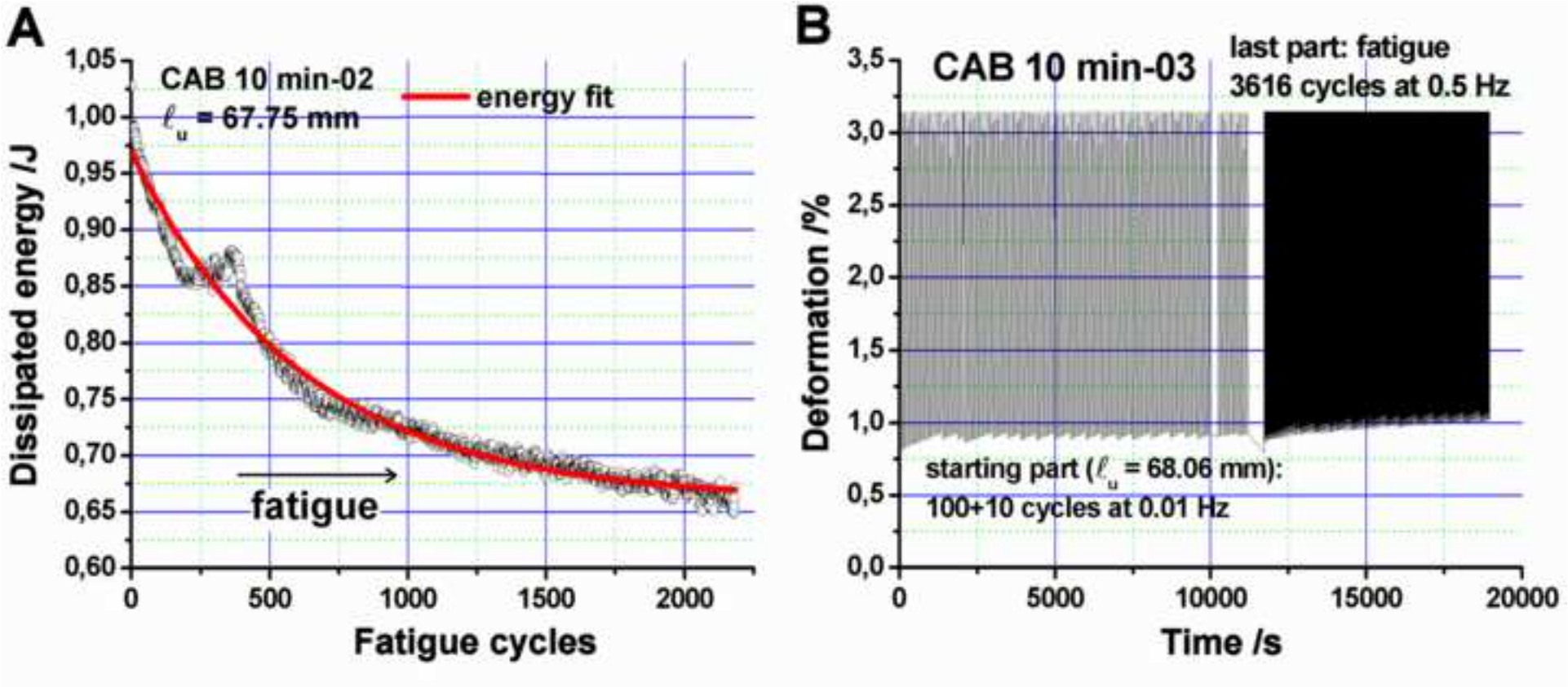

Figure37
Click here to download high resolution image

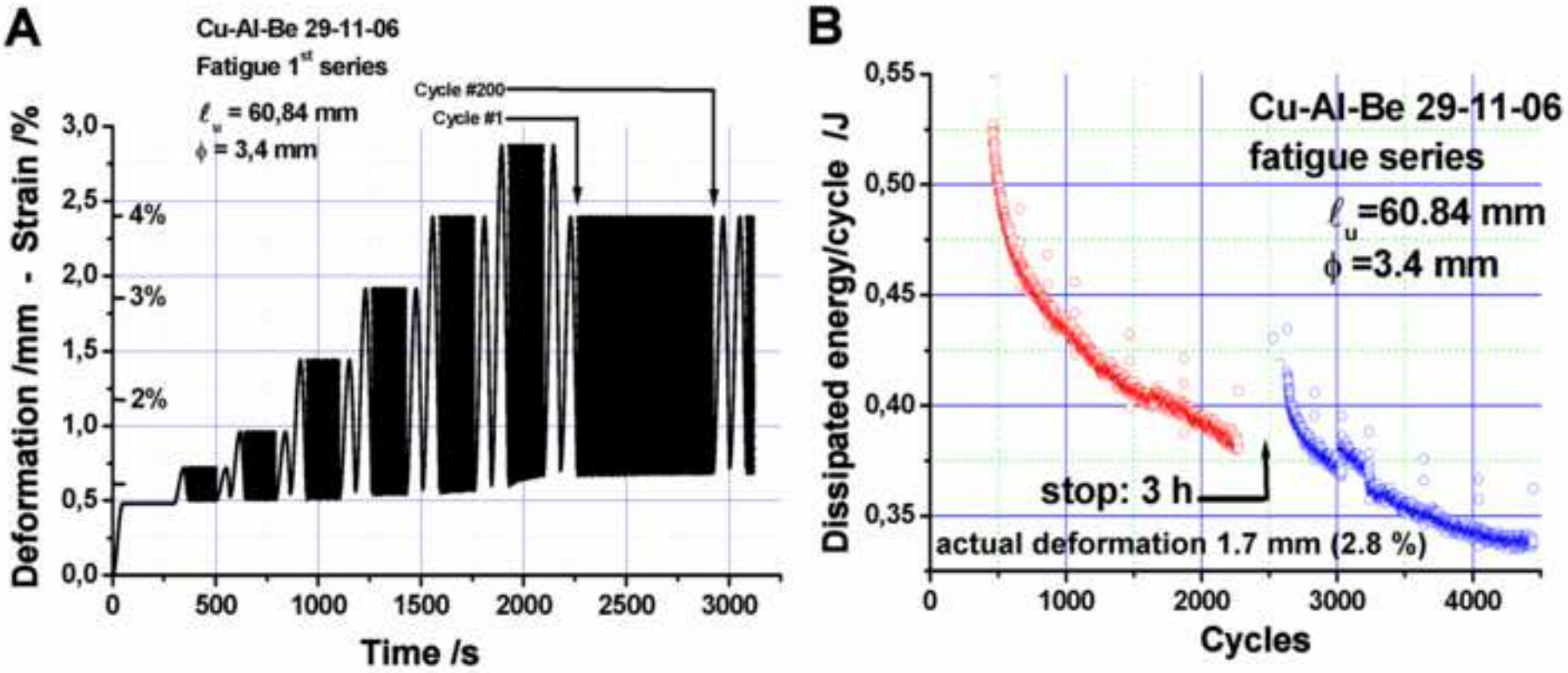

Figure38
Click here to download high resolution image

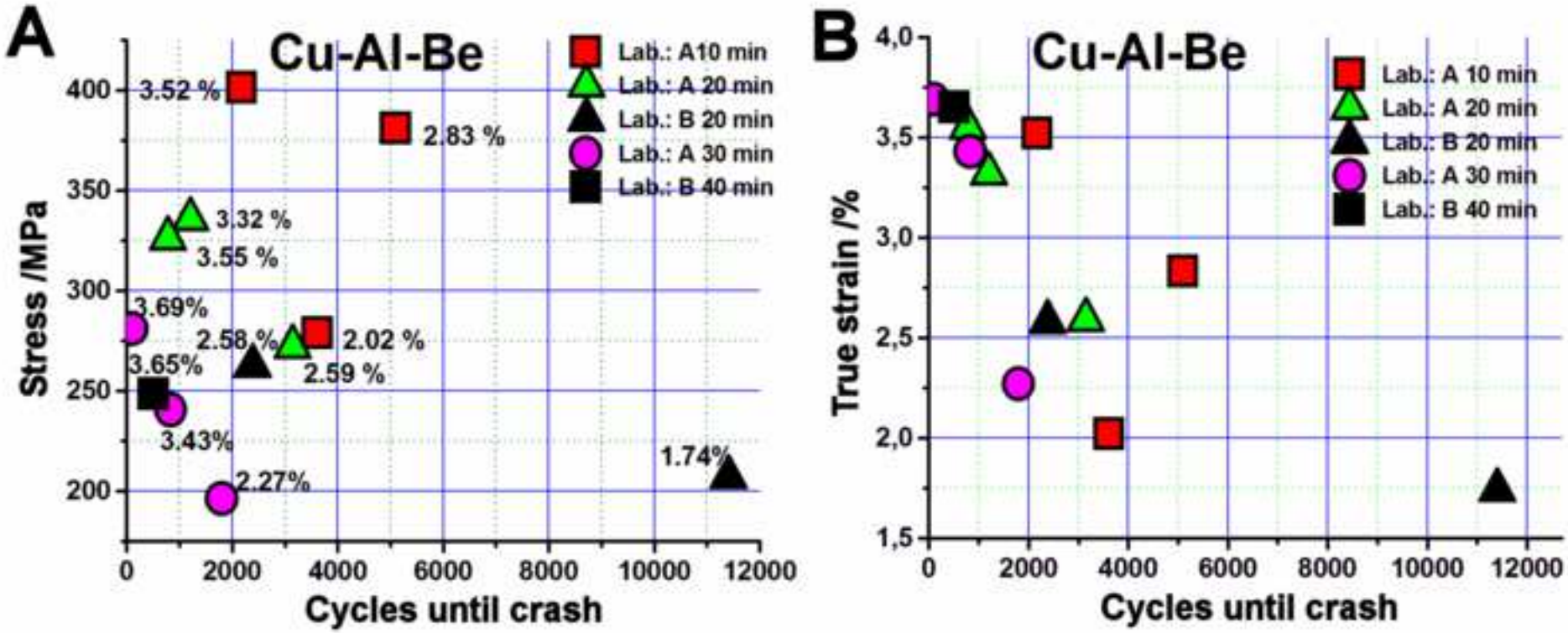

Figure39
Click here to download high resolution image

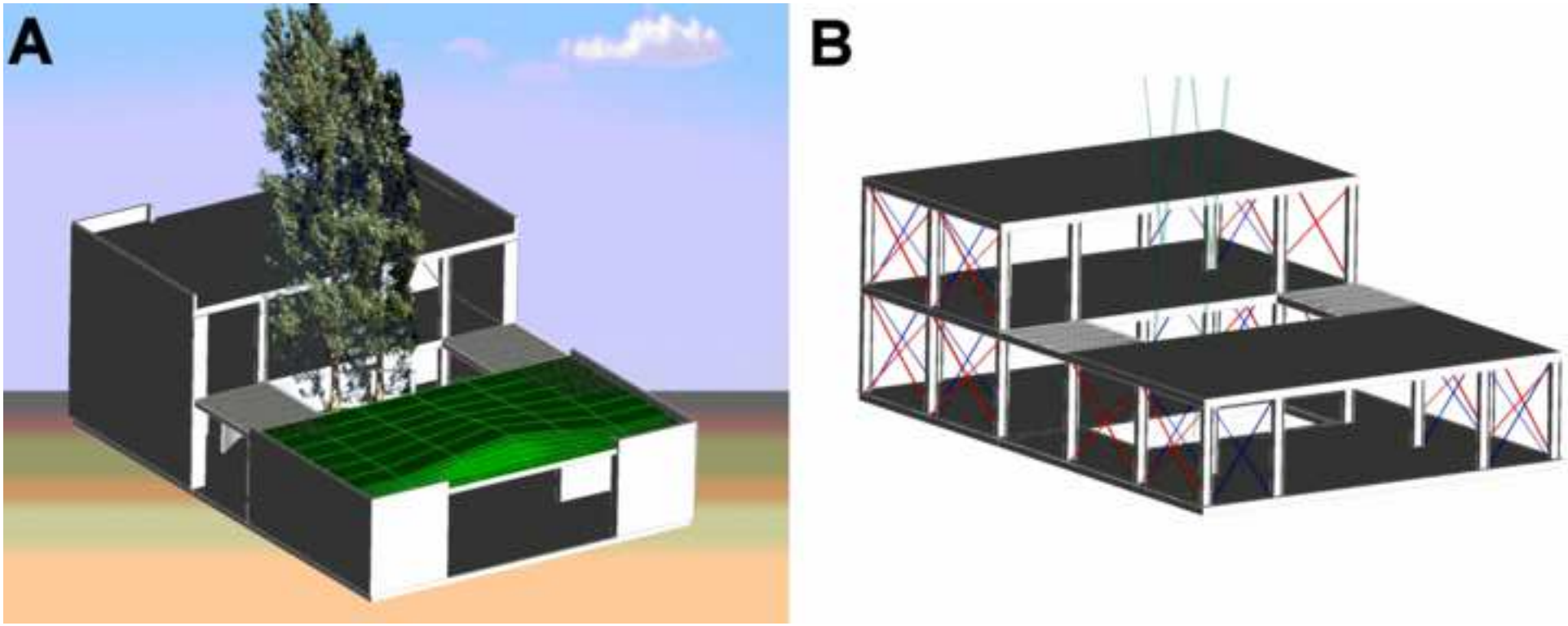

Figure40
Click here to download high resolution image

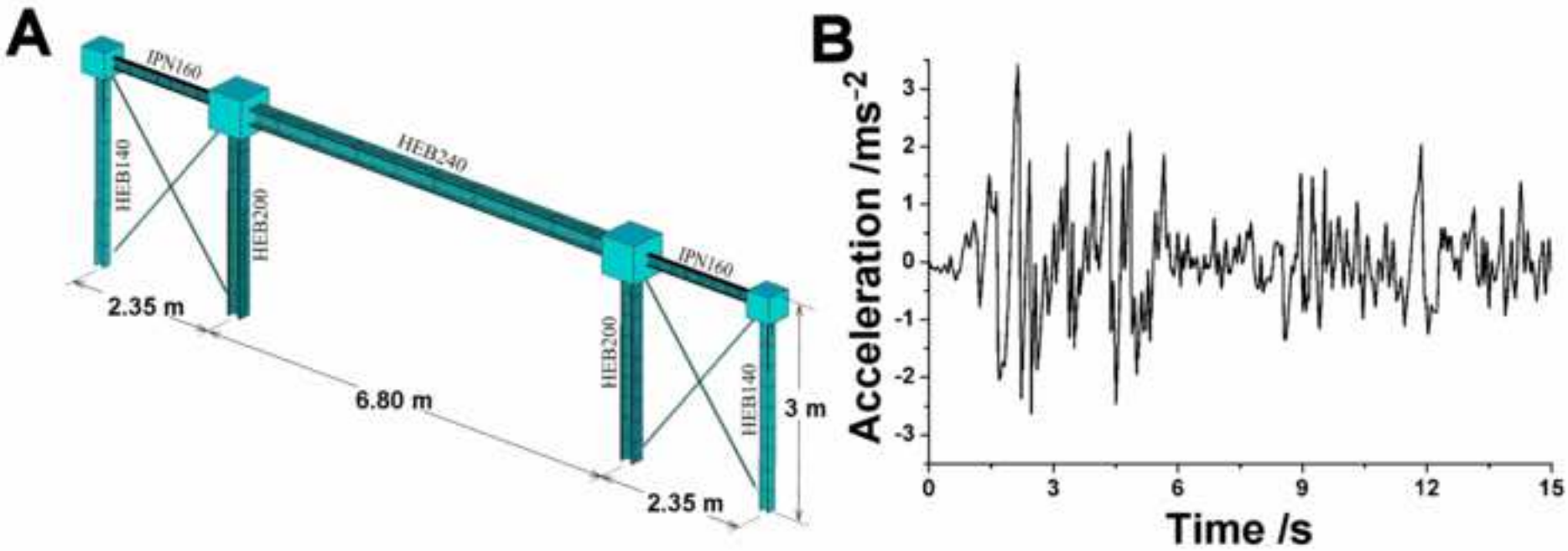

Figure41
Click here to download high resolution image

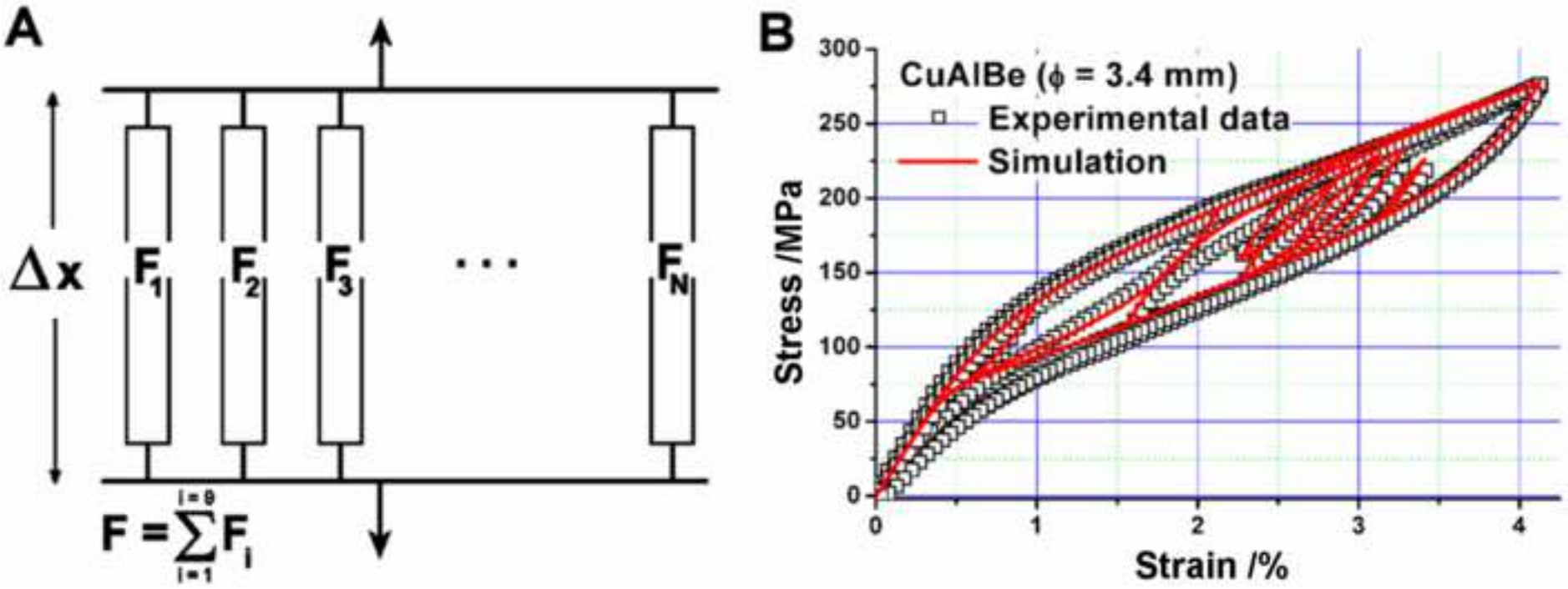

Figure42
Click here to download high resolution image

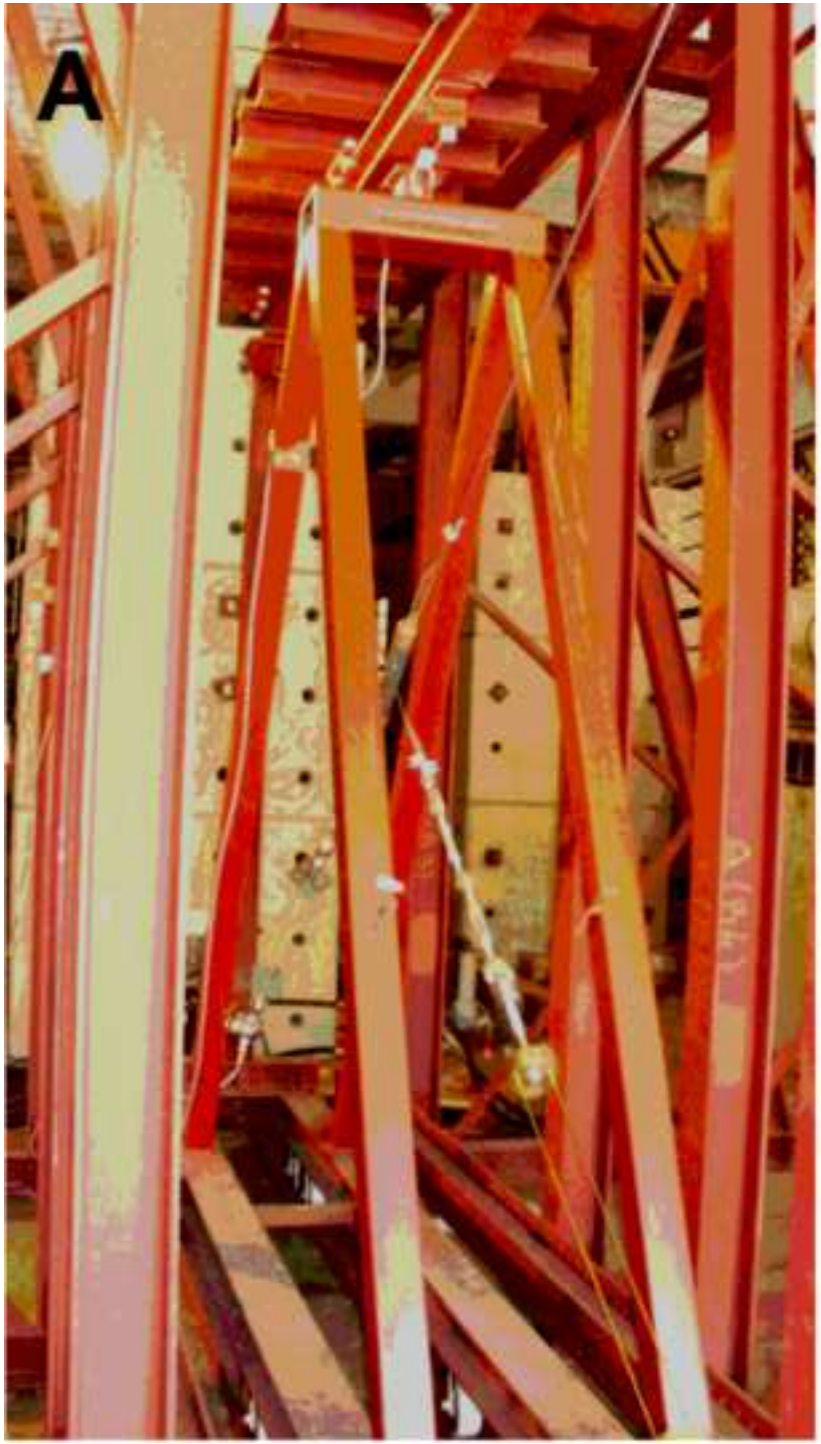

Figure43
Click here to download high resolution image

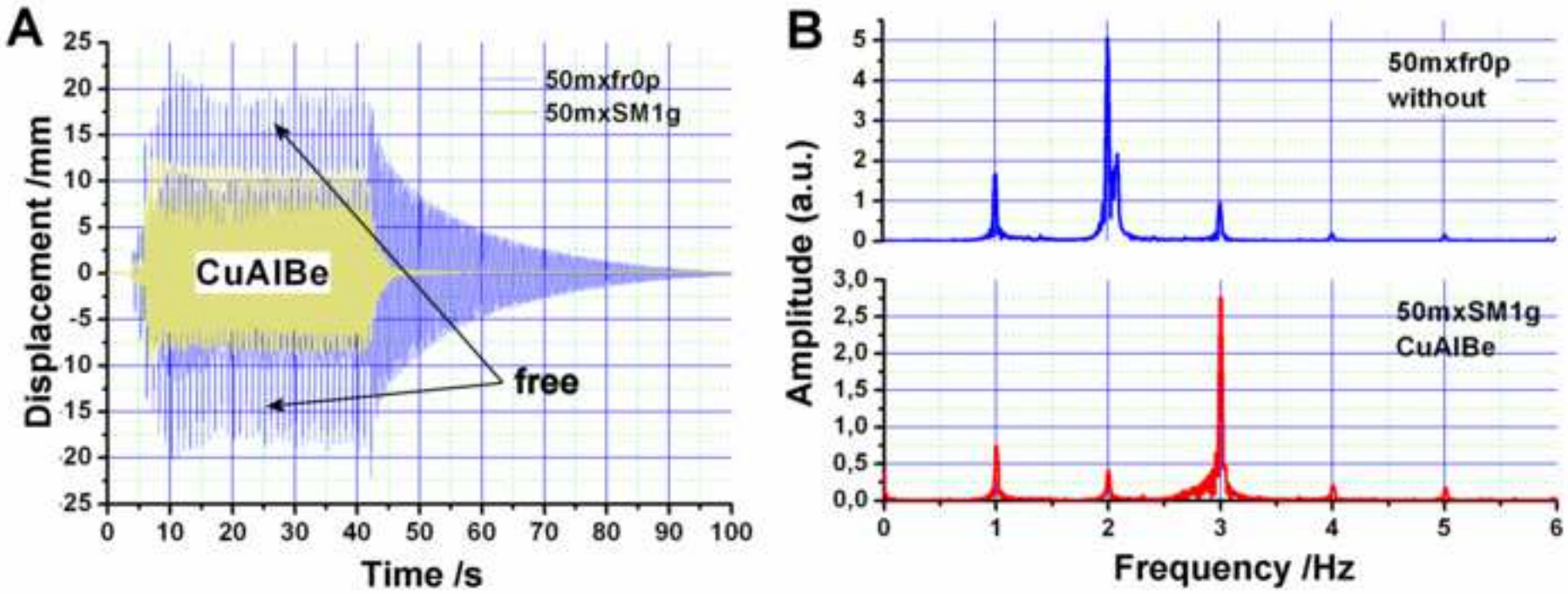

Figure44
Click here to download high resolution image

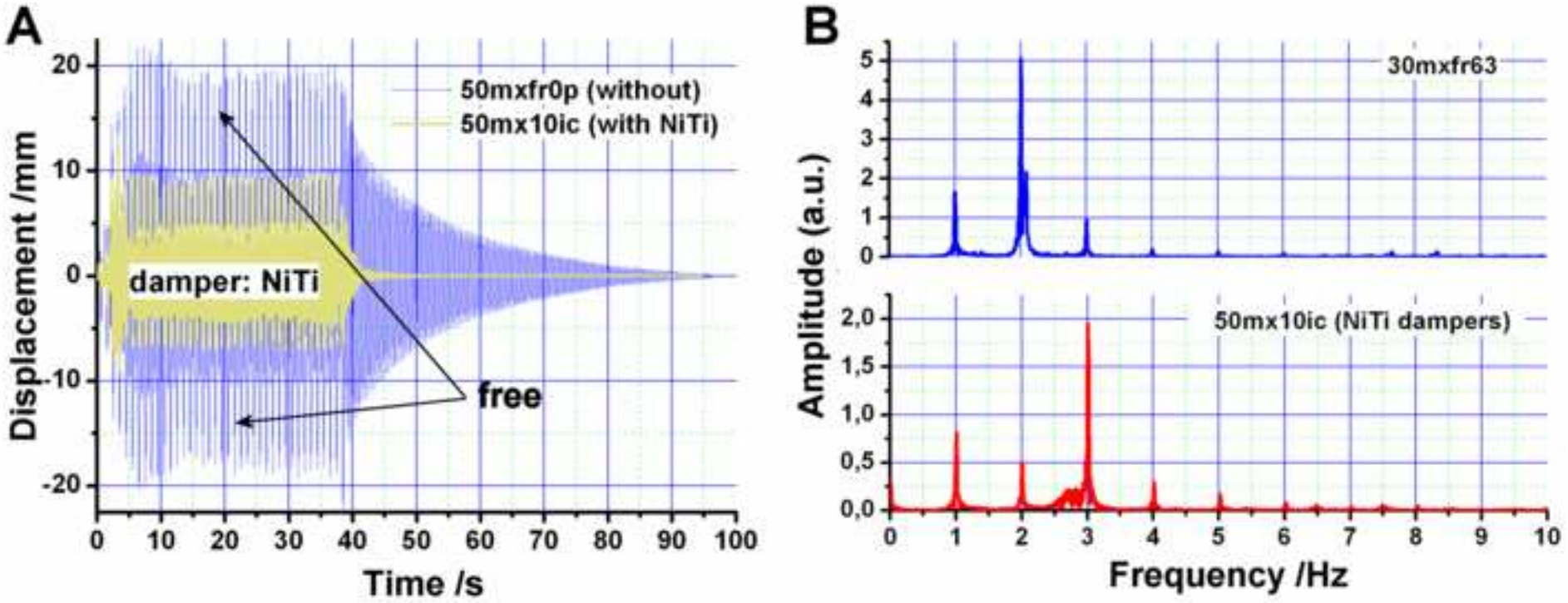

Figure45
Click here to download high resolution image

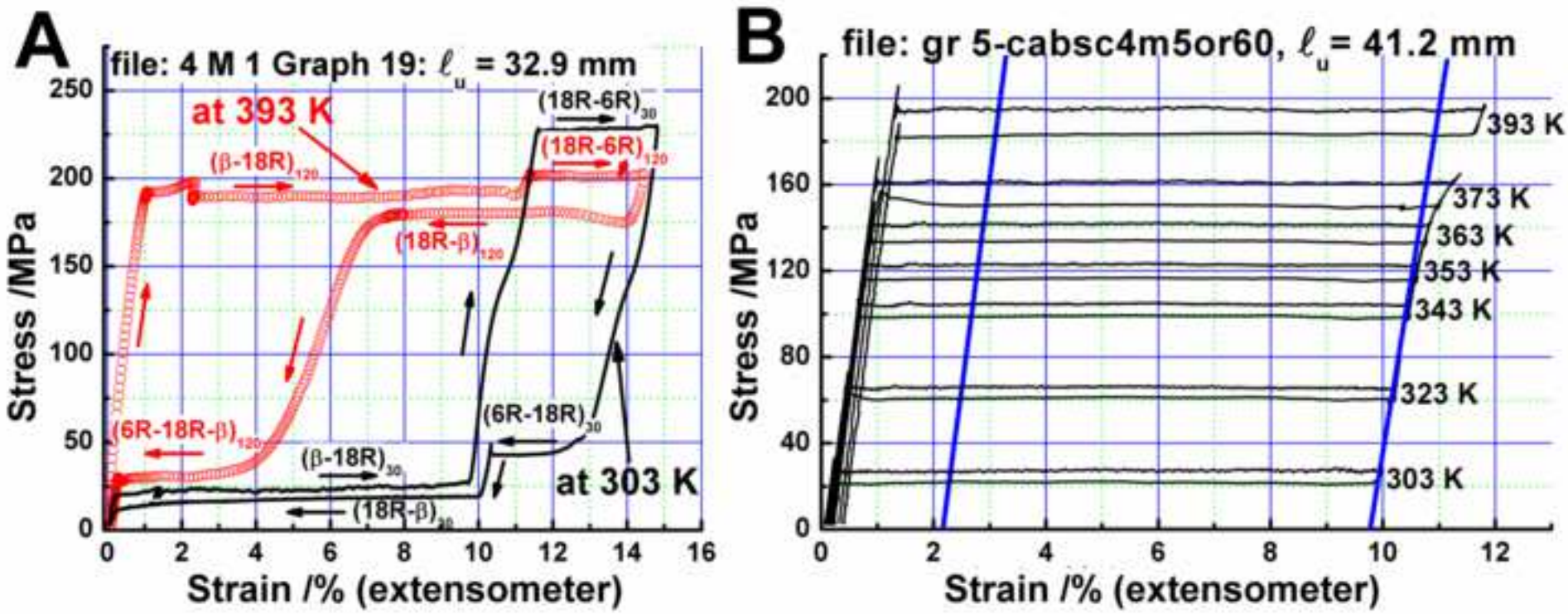

Figure46
Click here to download high resolution image

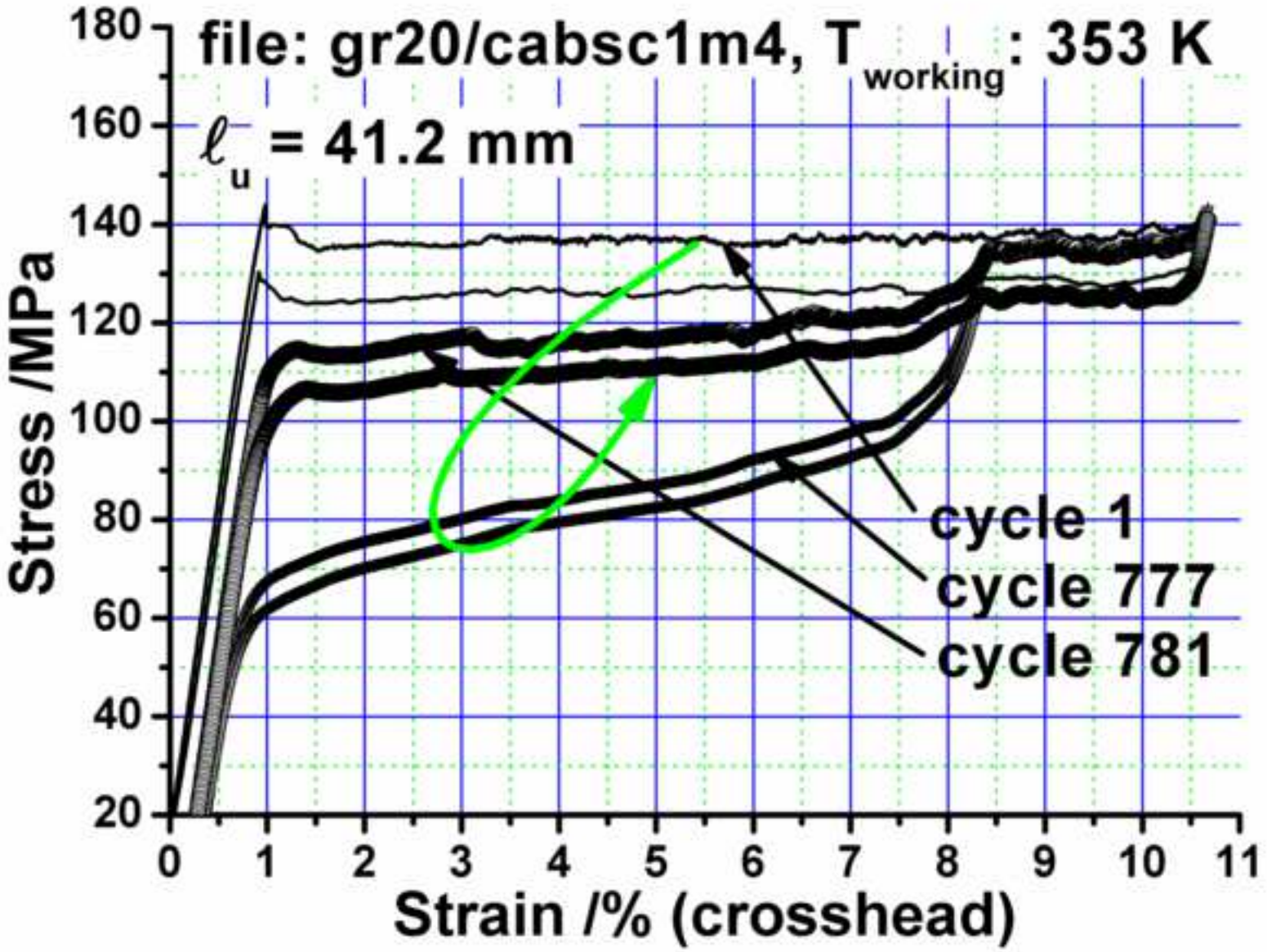

Figure47
Click here to download high resolution image

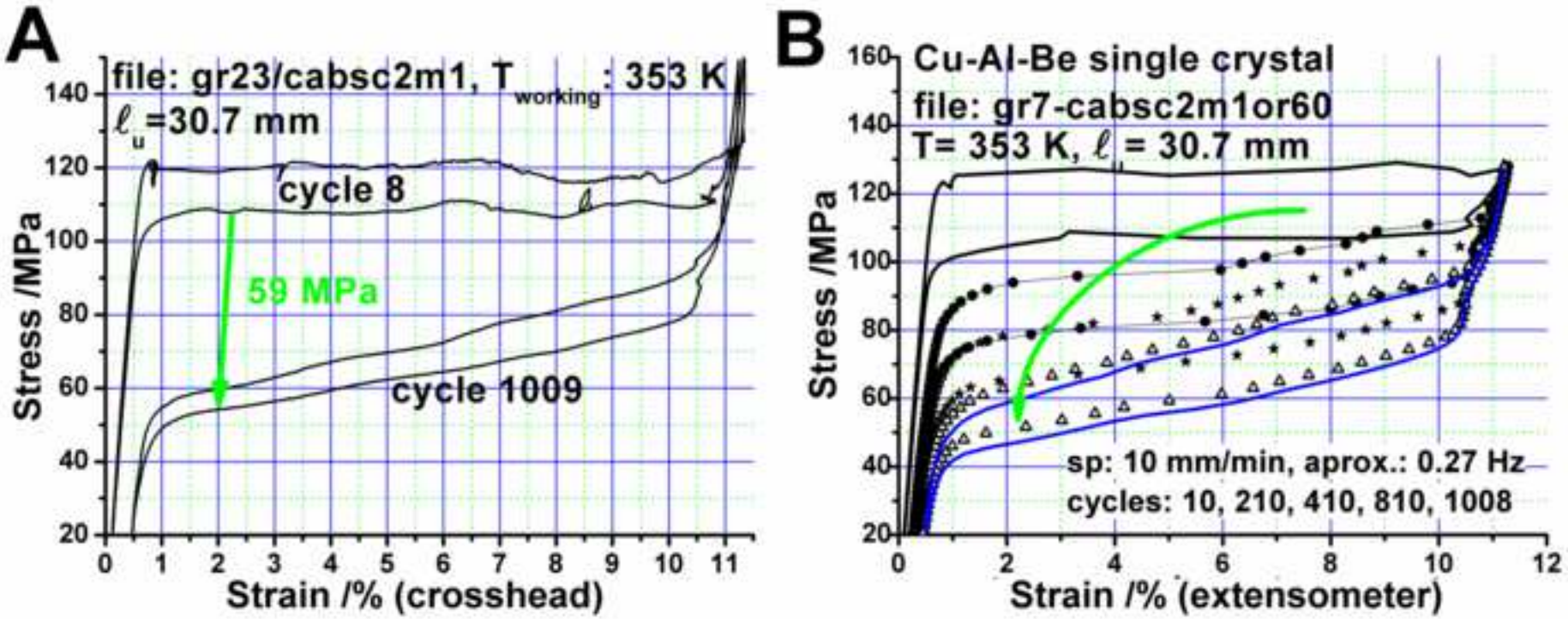

Figure48
Click here to download high resolution image

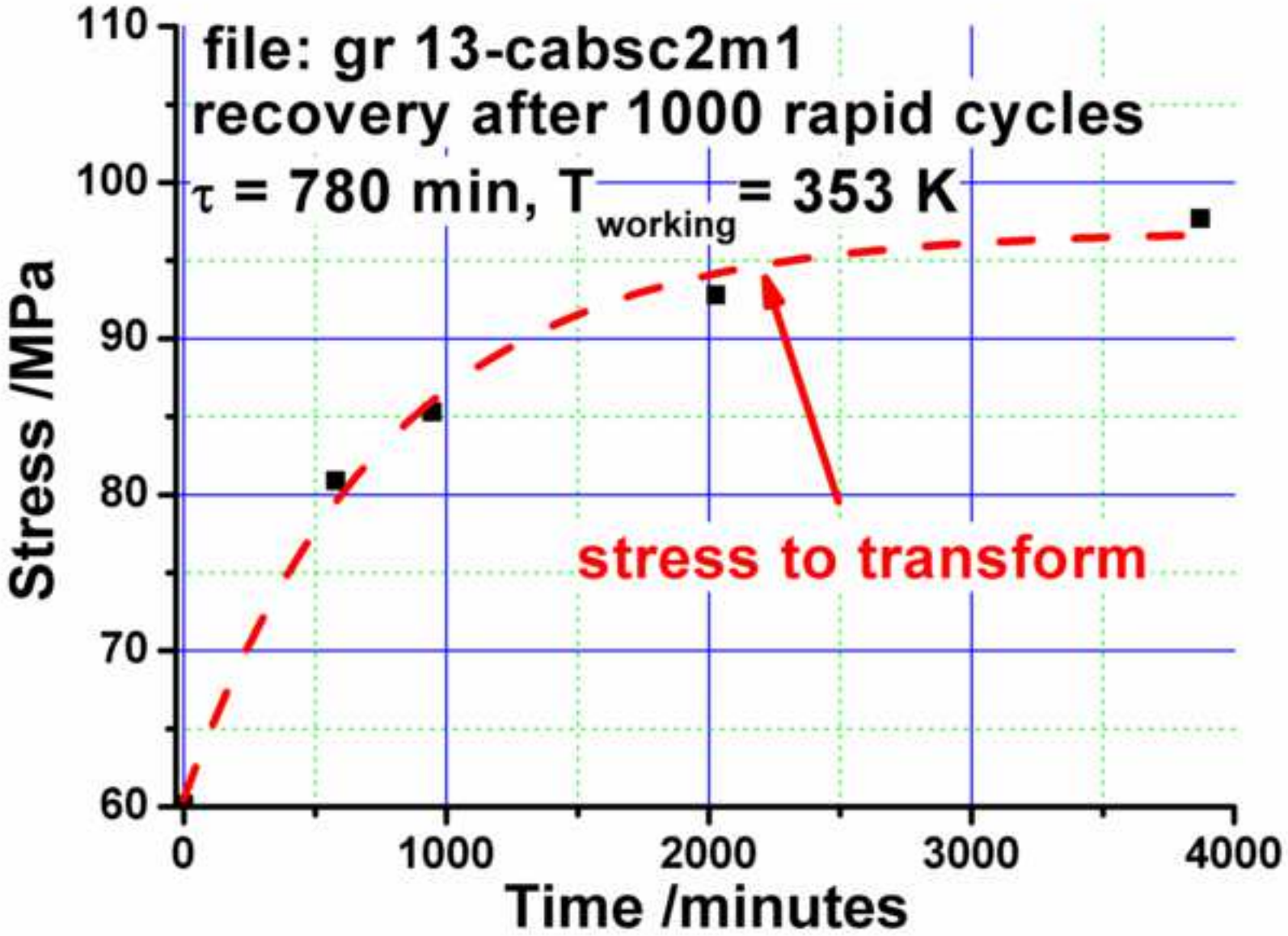

Figure49
Click here to download high resolution image

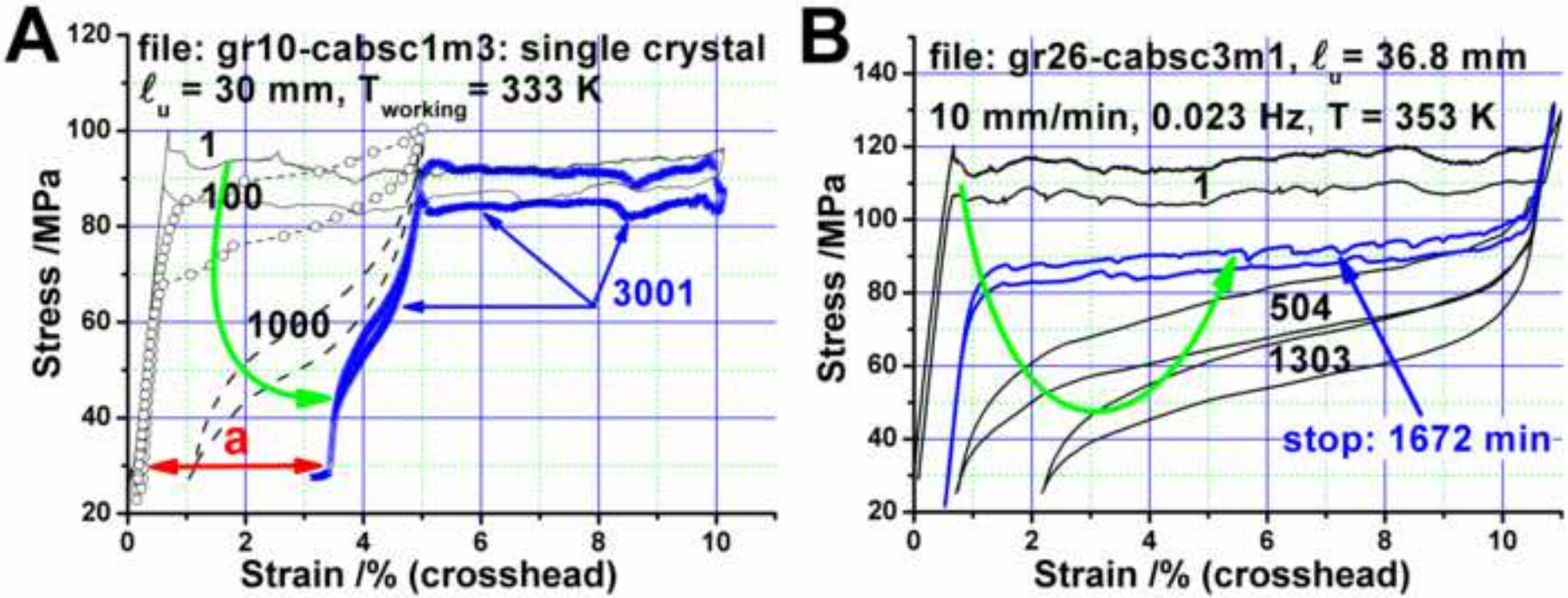

Figure50
Click here to download high resolution image

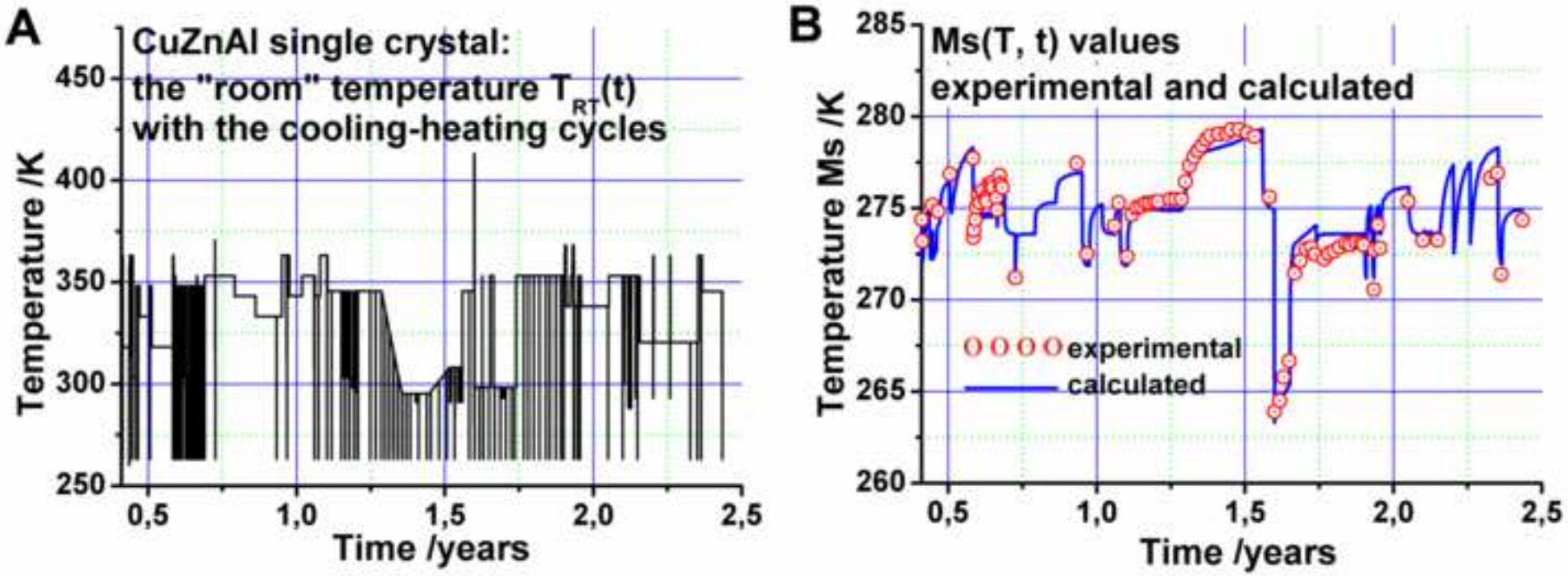

Figure 51
Click here to download high resolution image

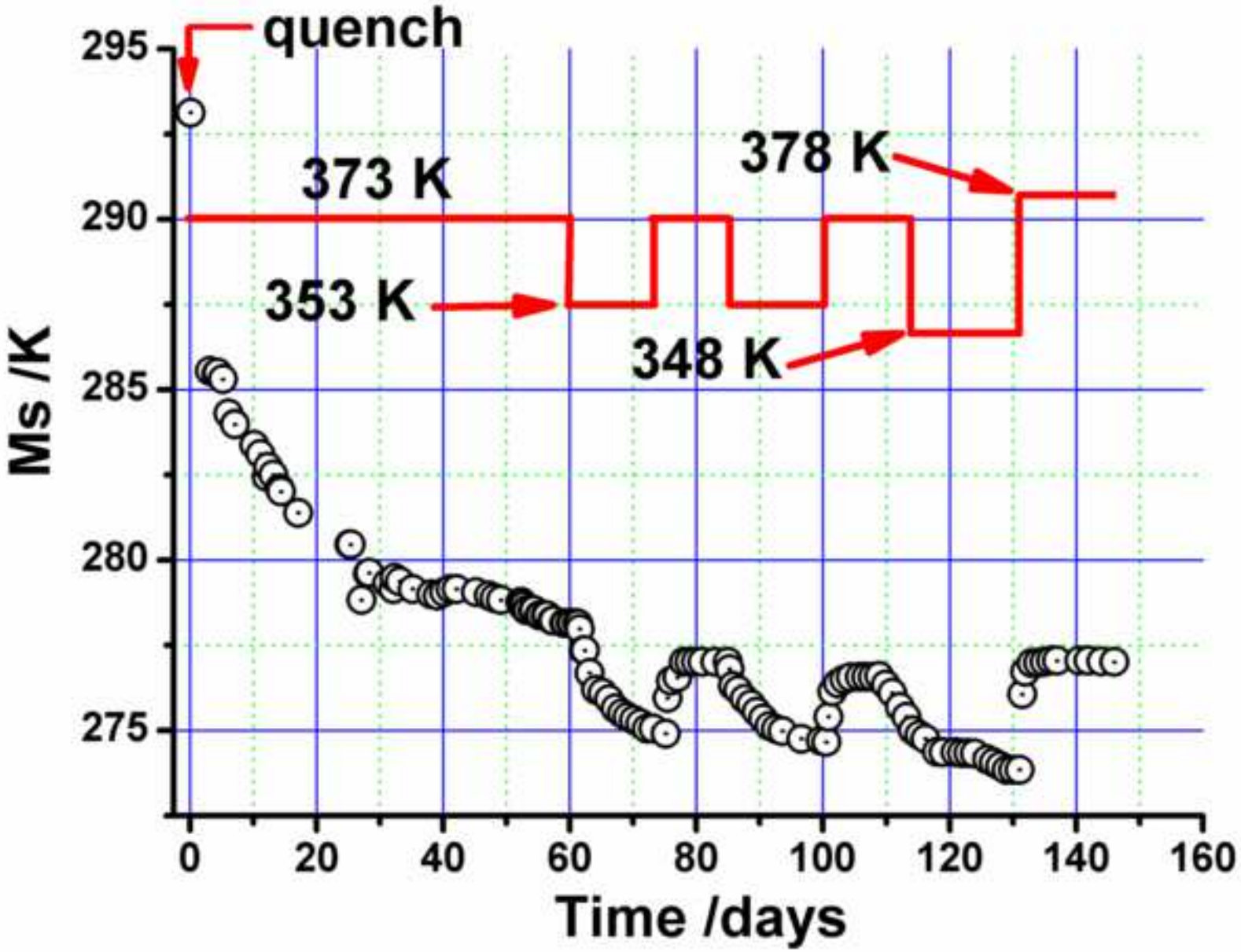

Figure52
Click here to download high resolution image

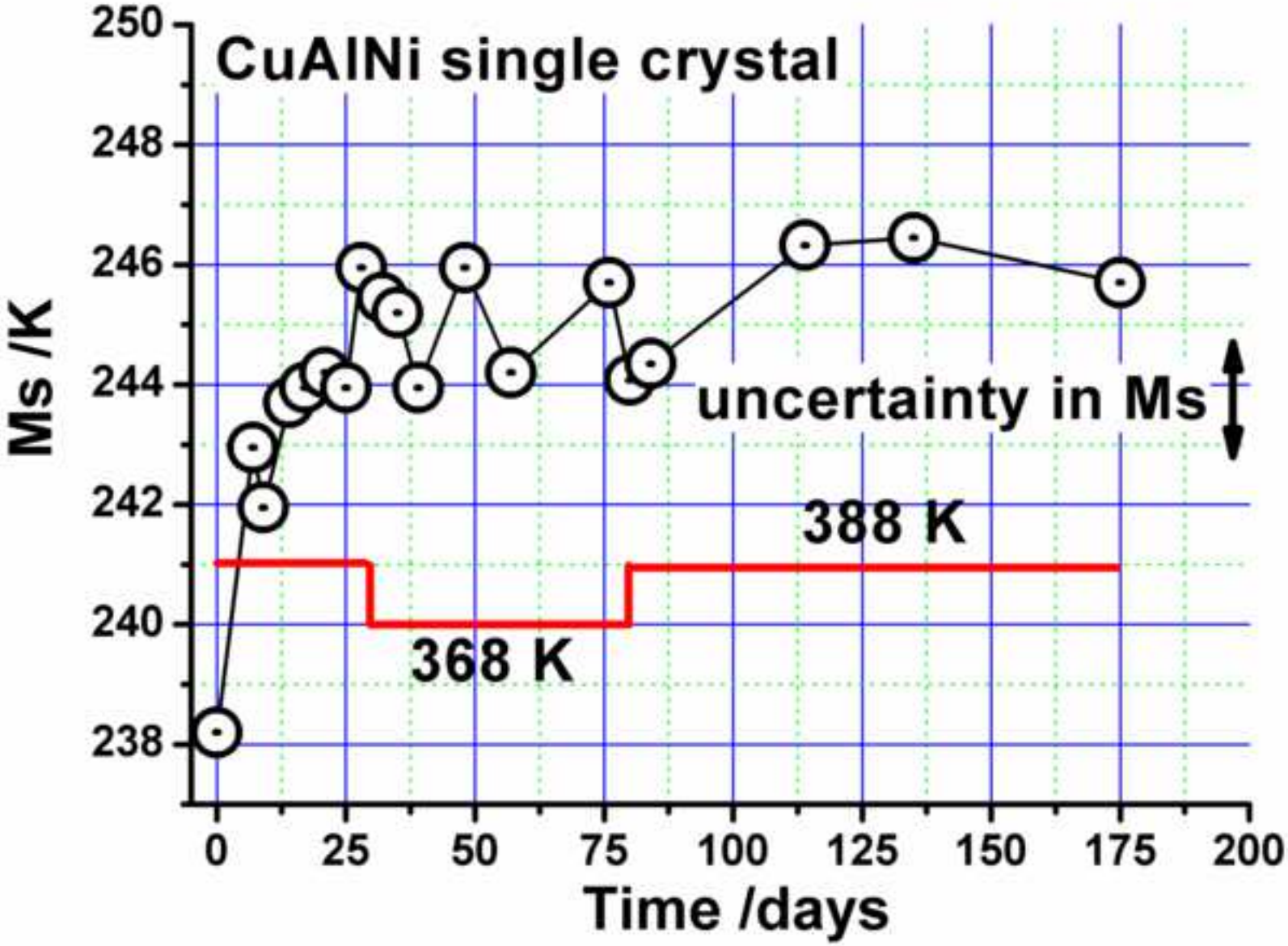

Figure53
Click here to download high resolution image

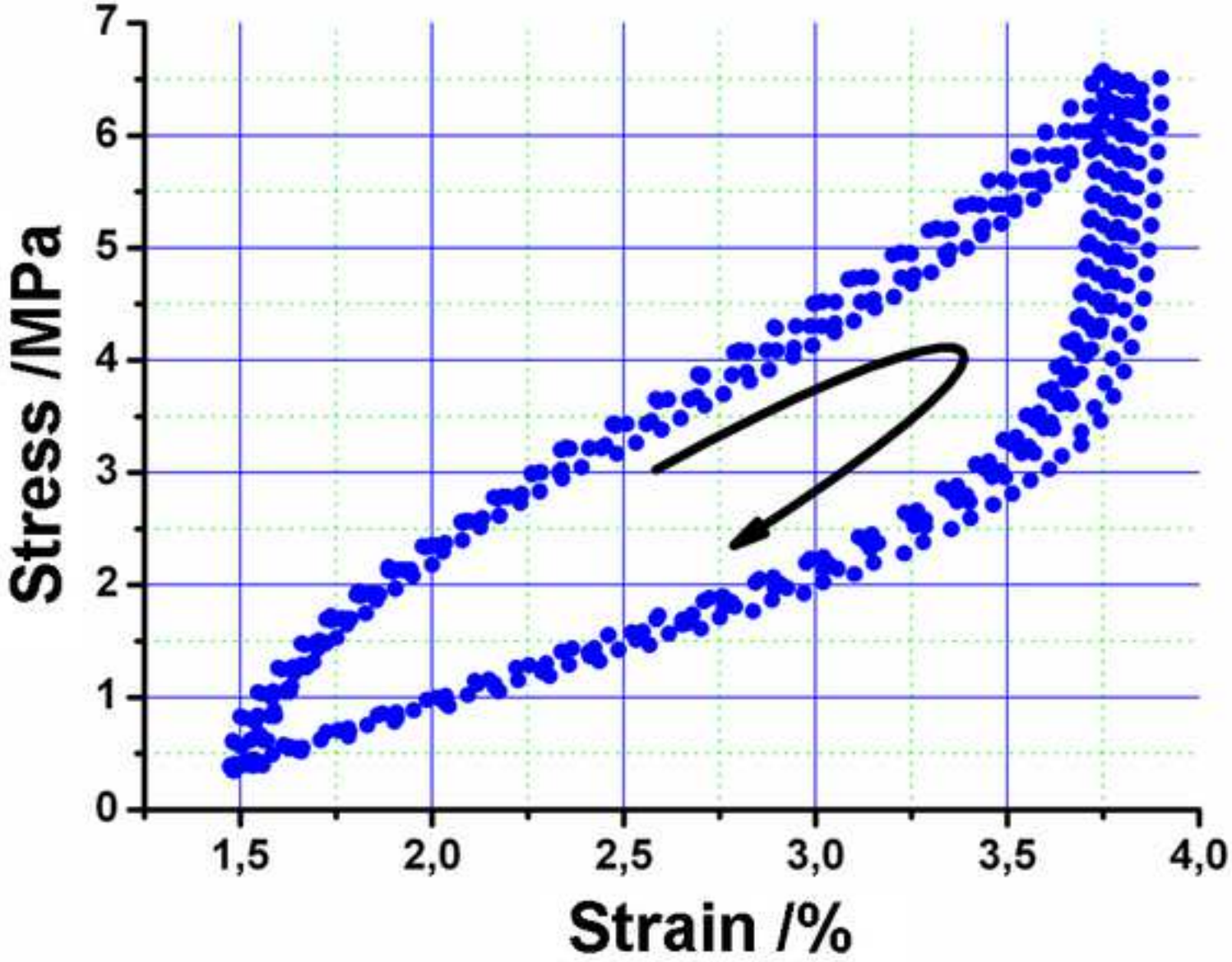

Table 1. NiTi wires of 2.46 mm diameter alloy data from the furnisher certificates. In all cases, other impurities were: H<0.005%, Fe<0.05% weight, each of the groups: (Si, Cr, Co, Mo, W, V, Nb, Al, Ba); (Zr, P, Cu, Hf, Ag, Pb, Bi, Ca); and (Mg, Sn, Cd, Zn, Sb, Sr, Na, As, Be), where in amounts of less than 0.01% weight. According to the certificates, Ti was to balance the composition.

Date	Ni % weight	C ppm weight	O ppm weight	As (fully annealed)
March, 2007	55.99	379	246	247
April, 2005	56.00	380	167	246

Table 2. Data for the cubic fits.

Point	**M_0**	**M_e**	**L_1**	**L_2**	**U_1**	**U_2**
ε (m/m)	0	0.0636	0.0166	0.043	0.0112	0.045
σ (MPa)	0	531	252	350	52	200

Table 3. Dampers in ELSA, IFSTTAR, and Pavia.

facility.	L m	SMA (wires)	length(ℓ) mm	NiTi SMA ϕ in mm	σ (cable) in MPa	traction force	f_{SMA} near	cable diameter	Δx mm	f Hz
ELSA	45	1	4140(*)	2.46	283	250 kN	1.5 kN	4*15 mm	60	2
IFSTTAR	50	2	1260(^{X})	2.46	390	1000 kN	3 kN	57 mm	50	3
Pavia	2.36	1	1229(**)	0.1	43	133.8 N	2 N	2 mm	40	5

(*) appropriate length with larger fracture life.
(^{X}) shorter length inducing reduced fracture life.
(**) fracture life that requires deeper study

Table 4

Table 4. Diffusion phenomena and asymptotic temperature effects on Ms for the CuAlBe alloy.

Parameters	**Alloy: CuAlBe [9]**
τ_1 from measures	1.95 days at 373 K
τ_1 from measures	4.63 days at 353 K
τ_1 extrapolated	116 days at 293 K
Activation Energy	5740 K
$100\Delta Ms/\Delta T_{RT}$	13.5

Table 5. Sets of modules (with their code) for the cycling procedures used in the systematic analysis of SMA creep and fatigue. (f = 0.79% in strain). The M1 was used to check mechanical setup of grips in the machine testing.

Code	**Amplitude (mm)**	**Strain (%)**	**Freq. (Hz)**	**Cycles on the samples (N)**
M1	1*f	0.79	0.50	Usually 4 or 5
M2	1.5*f	1.18	0.50	100
M3	2*f	1.57	0.50	100
M4	3*f	2.36	0.50	100
M5	4*f	3.14	0.25	50
M6	5*f	3.93	0.25	50
M7	6*f	4.71	0.25	50
M8	7*f	5.50	0.25	50

Table 6. Cu-based alloys. Calculated values of time constants (τ_1 and τ_2) and activation energies.

CuZnAl (single cristal) [39, 153, 154]	T and τ_1 373 K and 0.39 h	T and τ_2 373 K and 13.1 h	activation energy 13630 K	activation energy 10330 K
CuAlBe poly-crystal [see, Part Four]	373 K and 1.73 d	- - -	5740 K	
CuAlBe single-crystal	373 K and 0.62 d	- - -	$12*10^3$ K	- - -
CuAlNi single-crystal	388 K and 20 d (*)	- - -	$1.4*10^4$ K (*)	- - -

(*) larger uncertainty